**Micro-Computed Tomography of Primate Molars**

A Dissertation Presented

by

**Anthony Jay Olejniczak**

to

The Graduate School

in Partial fulfillment of the

Requirements

for the degree of

**Doctor of Philosophy**

in

**Anthropology**

Stony Brook University

August 2006

**Abstract of the Dissertation**

Micro-Computed Tomography of Primate Molars

by

**Anthony Jay Olejniczak**

**Doctor of Philosophy**

in

**Anthropology**

Stony Brook University

**2006**

Primate molar enamel thickness has played an important role in the taxonomic, phylogenetic, and dietary assessment of fossil teeth for nearly 90 years. Despite the frequency with which enamel thickness is discussed in paleoanthropological discourse, methods used to attain information about enamel thickness are destructive (limiting sample sizes), recording information from only a single plane of section (ignoring dimensional data that may be culled from the entire length of a tooth). In light of a growing body of published two-dimensional data on enamel thickness in primates, the dissertation presented here aims to develop a non-destructive technique capable of accurately measuring the thickness of dental enamel from a whole-crown three-dimensional perspective using modern medical imaging technology (i.e., micro-computed tomography).

Enamel thickness measurements based on microtomographic imaging are accurate (within 3.0%) compared to manually produced molar sections. The processing of radiographic images, however, introduces complications (i.e., image artifacts) into the process of measuring enamel thickness. It is demonstrated here, however, that an image filtration protocol may be applied to microtomographic dental radiographs which preserves the accuracy of the representation of dental structures, and makes these images measurable in a semi-automated fashion. Moreover, optimal scanning parameters (e.g.,

slice thickness) may be deduced for each specimen *a priori*, such that image accuracy is largely a function of tooth size and morphology.

The techniques described here were applied to primate molars (genera represented: *Hylobates*, *Symphalangus*, *Alouatta*, and *Ateles*), and several aspects of enamel morphology were recorded. Results show that 3D data are less prone to variance introduced in the preparation of specimens (i.e., section obliquity) than 2D data. Primary folivores have relatively thinner enamel than primary frugivores, and ceboids have relatively thinner enamel than hominoids. Hylobatid primates have long been considered a thin-enameled group, but this study shows that hylobatid molars are of intermediate enamel thickness. Both 2D and 3D data indicate that traditional interpretations of the enamel thickness in primate evolution should be reconsidered. The transition from thin to thick enamel in hominoid evolution has been used to diagnose great apes in the fossil record, but this demarcation is not as clear as previously thought given intermediate thickness enamel in successive outgroups (Hylobatidae and Cercopithecoidea). Enamel thickness is a reliable indicator of taxonomic affiliation when distinguishing closely-related species, but this character must be considered in light of other features of tooth morphology (e.g., the shape of the enamel-dentine junction) in order to better understand its taxonomic and phylogenetic signals.

Table of Contents

**List of Figures**

**List of Tables**

**Acknowledgements**

I wish first to express my gratitude to my dissertation advisor, Lawrence Martin, for involving me in this project, for sparking my interest in the hominoid dentition, and for support throughout my graduate school career. Lawrence showed me the value of persistence and dedication in research, for which I will always remain grateful. I wish to express my appreciation to Fred Grine, who facilitated many of the arrangements that made this dissertation possible; Fred's commitment to focusing this research on the most topical questions, and his encouragement to publish the results, have greatly enhanced not only this document but also my abilities as a researcher.

I thank Callum Ross and Stefan Judex for their invaluable contributions to this thesis, which are as far ranging as discussions about statistics, teeth, jaws, and phylogeny, to data storage, computational methods, and scanning parameters. Without such advice this work would not have been possible. I also owe a debt of gratitude to those who helped me to scan material and who taught me the basics of tomography in the process: Shiyun Xu (Stony Brook University), Heiko Temming (Max Planck Institute for Evolutionary Anthropology), and Paul Tafforeau (European Synchrotron Radiation Facility).

The majority of primate teeth scanned for this dissertation are housed in the Department of Mammalogy at the American Museum of Natural History (New York). This material is under the care of Richard Monk, who graciously permitted me to scan these jaws. Other material was provided by R. Smith (South African Museum, Cape Town), J. Botha (National Museum, Bloemfontein), and P. Holroyd (University of California Museum of Paleontology, Berkeley). Information pertaining to specimens

described in Chapter 3 was provided by E. Delson, B. Rubidge, and M. Raath.

Portions of the research presented here were funded by the Department of Human Evolution at the Max Planck Institute for Evolutionary Anthropology (Leipzig, Germany), and I am grateful to Jean-Jacques Hublin and Tanya Smith for organizing and funding these aspects of the research. Others at the Max Planck Institute supported me through critical discussions about teeth, software, and CT scanners during all phases of this research: I especially wish to thank Matt Skinner, Robin Feeney, Gert Wollny, Max von Harling, and Heiko Temming. Additional discussion, debate, and support during the writing of this dissertation from the following people is truly appreciated: Anja Deppe, Biren Patel, Mark Coleman, Jessica Lodwick, Chris Gilbert, Daria Eremina, and Ari Grossman. This thesis would never have been completed without the unending friendship and encouragement of Tanya Smith. Through staunch support and critical discussion, Tanya showed unwavering support for this project, for which I am most grateful.

Last, but not least, I wish to thank my family: Gary, Christine, Nicholas, and Amy Olejniczak. My family fostered an appreciation of education and science, and has patiently been by my side throughout the creation of this dissertation. For their love, unconditional support, understanding, and unfaltering belief in me, I remain eternally grateful.

# CHAPTER 1: INTRODUCTION

## Background

### *Objectives of the Dissertation*

Primate molar enamel morphology (including enamel thickness) has played an important role in the taxonomic, phylogenetic, and dietary assessment of fossil specimens for nearly 90 years (e.g., Miller, 1918). Despite the central role played by molar morphology in paleoprimatological and paleoanthropological discourse, modern methods used to attain information about enamel thickness are destructive (limiting sample sizes), and record information from only a single plane of section (ignoring dimensional data that may be culled the entire length of a tooth). The primary goal of this dissertation is thus to develop a method to measure enamel thickness in primate molars using micro-computed tomographic imaging. This imaging technique allows the entire molar crown to be examined and is non-destructive, thereby overcoming important limitations of current methods. The dissertation that follows describes the collection of micro-computed tomographic data, the treatment of this data (i.e., image filtration and segmentation), and the evaluation of the accuracy of this technique. Following this methodological discussion, several analyses are carried out on primate molars to demonstrate the applicability of this technique to questions about primate molar morphology.

### *Enamel Thickness*

Molar enamel morphology has long been considered central to understanding the relationships and dietary adaptations of extant and fossil primates, perhaps most notably among scholars concentrating on the hominoid superfamily. The last three decades have

seen substantial developments in the methods used to interpret the enamel character complex (enamel development, microstructure, thickness, and shape); these methods are used in investigations concentrating on a broad range of topics including dental adaptation to diet, phylogenetic reconstruction, taxonomic discrimination, and life history and development (e.g., Andrews and Martin, 1991; Macho and Spears, 1999; Dean, 2000; Schwartz, 2000; Martin et al., 2003; Smith et al., 2003). Quantitative investigations of the distribution of enamel thickness among primates were undertaken first by Gantt (1977, 1982), Kay (1981), and Martin (1983, 1985), owing in part to interest in the taxonomic status of the genus '*Ramapithecus*' at that time (now a junior synonym of *Sivapithecus*). The cumulative effect of these studies was three-fold: 1) they demonstrated the utility of enamel thickness quantification for distinguishing primate taxa; 2) they brought enamel thickness into the fold of dental characters used to interpret paleodiet; 3) they represent a sequence of methodological refinement, culminating with the method of measuring enamel thickness that is the most widely-used today (Martin, 1983, 1985).

Despite the adoption of standard methods, the destructive nature of preparing teeth for enamel thickness studies has limited the size of available samples, artificially introduced variance into measurements through slightly oblique planar (physically produced, two-dimensional) sections, and reduced the complex three-dimensional structure of molars to a two-dimensional (2D) surface from which measurements are recorded (Olejniczak, 2005). As enamel thickness measurements continue to be reported and analyzed, it is imperative to overcome these methodological obstacles so the amount of intra-individual, intra-specific, and inter-specific variation may be assessed.

Overcoming these obstacles also facilitates the study of enamel in its full three-dimensional form, thereby minimizing the dimensional loss of valuable information about enamel cap morphology. True biological variation be only be measured after artificially introduced variance is eliminated, and functional and phylogenetic signals may be more accurately assessed when non-biological variance is eliminated.

In recent years, enamel thickness has been discussed in nearly every seminal diagnosis of a hominoid taxon (e.g., Conroy et al., 1992; Begun and Kordos, 1993; White et al., 1994; Brunet et al., 1995; Leakey et al., 1995; Leakey et al., 1995; Pickford and Ishida, 1998; Asfaw et al., 1999; Haile-Selassie, 2001; Leakey et al., 2001; Senut et al., 2001; Brunet et al., 2002). Enamel thickness has also been measured in several previously described hominoid taxa (e.g., Martin and Andrews, 1984; Grine and Martin, 1988; Andrews and Martin, 1991; Beynon et al., 1998; Dean and Schrenk, 2003; Smith et al., 2003; Smith et al., 2004), and in representatives of all major extant primate radiations have been measured for enamel thickness (e.g., Shellis et al., 1998; Ulhaas et al., 1999; Martin et al., 2003; Grine et al., 2005).

Despite the emphasis placed on the taxonomic implications and potential phylogenetic signal carried in enamel thickness, there is also a growing literature describing the relationship of enamel thickness to food hardness and masticatory strain (e.g., Dumont, 1995; Spears and Crompton, 1996; Spears and Macho, 1998; Lambert et al., 1999; Macho and Spears, 1999; Shimizu, 2002; Martin et al., 2003). It is thus evident that both the capacity to masticate particular food items and a phylogenetic signal may be culled from enamel thickness measurements taken across a range of species. To date, however, no study has specifically attempted to tease apart the influences of dietary

proclivity and phylogenetic relatedness on the thickness of molar enamel in a multi-species sample (but see Ulhaas et al., 1999 and Shimizu, 2002). The discrimination of comparable functional demands from phylogenetic relatedness is critical to the interpretation of like-valued enamel thickness measurements among primate species in functional contexts. Thus, in addition to quantifying variation in enamel thickness at different levels of analysis, a second focus of enamel thickness studies has become the distinction between possible causes of variation (diet and phylogeny).

*Enamel-Dentine Junction Morphology*

The thickness of enamel is determined by the rate and duration of its secretion by ameloblasts as they migrate in a developing tooth from the inner enamel epithelium towards the future enamel surface. Amelogenesis begins at the locations of future dentine horn tips (the initial zones of mineralization) and ultimately extends towards the cervix of the tooth. The interface between the inner enamel surface and the dentine that is deposited by odontoblasts as they migrate towards the future pulp chamber is the enamel-dentine junction (EDJ). Because it is relatively independent of potential inter-individual variance in ameloblastic activity, and because its major landmarks are formed prior to enamel secretion (and perhaps are under more strict genetic control; Korenhof, 1961), the EDJ has been studied by several scholars for its potential taxonomic discriminatory power (Kraus, 1952; Korenhof, 1961; Corruccini, 1987; Sakai et al., 1965; Sakai and Hanamura, 1971, 1973a, 1973b; Olejniczak et al., 2004, in review).

Kraus (1952) reported that differences in morphology between the outer enamel surface (OES) and the EDJ prohibited precise prediction of the topography of one surface

from the other, with the exception of a few non-metrical traits (e.g., the number of major cusps). Based on a study of enamel cap "endocasts," Korenhof (1961) observed that the EDJ demonstrates a "greater measure of primitiveness" compared to the enamel surface; the EDJ may preserve vestigial cuspules, ridges, and cingula that are not apparent at the OES. Based on a lack of topographic correspondence between the OES and EDJ (Kraus, 1952), and due to perceived evolutionary conservatism, Korenhof (1961) suggested that the EDJ might be more useful than the OES for assessing phylogenetic relationships. Sakai and colleagues (e.g., Sakai et al., 1965; Sakai and Hanamura, 1971, 1973a, 1973b) published a series of analyses of EDJ topography in the Japanese dentition, documenting in detail the existence and frequency of cuspules and ridges on the EDJ and the OES of each tooth position. In the concluding installment of their series, Sakai and Hanamura (1973b) state that "characters on the dentinoenamel junction show phylogenetically more primitive or conservative conditions in relation to the exterior surface of the enamel layer", concurring with the conclusions of both Korenhof (1961) and Kraus (1952) and suggesting that EDJ morphology may be of value in phylogenetic studies.

Corruccini (1987) later employed dentine surfaces produced by enamel demineralization in a comparison of OES and EDJ topography among primates and other mammals. This study demonstrated that the EDJ sometimes is characterized by morphology that is not present in the enamel surface (e.g., paracristids in the EDJ of humans and pitheciins that do not appear at the OES), lending support to the idea that the EDJ may preserve vestigial features and that EDJ morphology may be useful for the resolution of taxonomic uncertainties and the reconstruction of phylogenetic relationships (Corruccini, 1987). Schwartz et al. (1998) found that the topography of the EDJ and OES

are not consistently correlated in fossil hominid molars with reference to the Carabelli feature. Some molars had EDJ cingula without a substantial expression at the enamel surface (and vice versa), leading them to caution against using EDJ morphology as the sole variable in phylogenetic analyses. Although Schwartz et al. (1998) suggest that EDJ morphology alone is probably not sufficient for fine taxonomic resolution, Korenhof's (1961) work indicates that it may have more discriminatory power when considered among a broader range of more distantly related taxa, and when multiple aspects of tooth morphology (e.g., EDJ topography, enamel thickness, and standard odontometric measurements) are considered simultaneously.

For instance, the combination of short dentine horns relative to tooth height and thick molar enamel has been suggested to be a key development during hominoid evolution, with implications for phylogenetic and biogeographic hypotheses regarding hominoid dispersal from Africa in the Late-Middle Miocene (Heizmann and Begun, 2001). EDJ shape characters, such as the height of the dentine horns as they relate to enamel thickness and shape (i.e., dentine penetrance), have also qualitatively been assessed and coded for parsimony analyses (e.g., Begun et al., 1997). Olejniczak et al. (2004) examined differences in EDJ landmark positions between the upper molars of several anthropoid taxa by means of a two-dimensional geometric morphometric analysis. Results indicated that significant differences in EDJ shape exist among taxa at superfamily, subfamily, generic and specific levels. In sum, the results of previous research regarding the shape of the EDJ suggest that its morphology is useful in taxonomic discrimination, and that this utility is enhanced when shape of the EDJ is

combined with other dental characteristics (e.g., enamel thickness and developmental variables).

As is the case in most previous enamel thickness studies, the morphology of the EDJ has largely been studied in two-dimensional planes of section (but see Korenhof, 1961 and Corruccini, 1987), which has limited the size of available samples due to the semi-destructive nature of this technique (discussed below). In addition to small samples, two-dimensional planes of section are limiting in that they capture only a single cross-section of a complex, three-dimensional structure, perhaps masking variation (or discriminatory power) that may be gleaned from other areas of the teeth. Moreover, the preparation of dental sections may introduce artificial variance in the form of non-homogenous cross-sectional planes (i.e., slight section obliquity). Each of these issues pertaining to dental sections is discussed below, followed by a discussion of the benefits and methodological hurdles surrounding a three-dimensional, non-destructive alternative (microtomographic imaging) for recording enamel thickness and EDJ metrics. Finally, the biological experiment conducted in Chapter 6 of this dissertation, utilizing three-dimensional microtomographic images to assess enamel thickness, dental tissue volumes and surface areas, and EDJ shape in light of phylogenetic relatedness and dietary proclivities, is introduced.

**Sample Size and Sample Bias**

In order to measure enamel thickness and EDJ shape using the standard methods developed by Martin (1983; 1985), molars are sectioned in a para-coronal plane through the tips of the mesial cusps and through the tips of the underlying dentine horns (hereafter

referred to as the *ideal plane of section*; Figure 1.1). Because of the destructive nature of this technique, only small samples of molars from extant taxa (and an even smaller number of fossil molars) are available for sectioning, limiting the assessment of both intra- and intertaxon variation.

An example of small samples masking intra-species variability in enamel thickness measurements may be found by comparing the enamel areas recorded in the ideal plane of section in molars of genus *Pan* by Martin (1983) with those from identical tooth positions reported by Shellis et al. (1998). Both Martin and Shellis et al., when examined alone, appear to have small ranges of enamel thickness values for *Pan* molars of a given tooth type. When combined, however, the range of values appears to be much greater, causing the range of *Pan*'s enamel thickness to overlap with the thin-enameled genus *Gorilla* and the intermediate-thick-enameled genus *Pongo* (based on the categories of enamel thickness erected by Martin (1983)). Bootstrap resampling procedures performed on the data for hominoid relative enamel thickness reported by Martin and Shellis et al. suggest that no less than nine molars from the upper or lower dentition should be used to estimate a species mean within 5% (this minimum was achieved by resampling enamel thickness measurements of 57 *Pan* molars and 59 *Pongo* molars; Olejniczak and Smith, unpublished).

Another consequence of small sample sizes (and, in part, sampling bias favoring large-bodied hominoids) is that certain taxa have been relatively overlooked. For instance, enamel thickness has been reported for more molars attributable to the fossil genus *Proconsul* (n=4) than to the extant genus *Hylobates* (n=2) (Martin, 1983; Walker et al., 1993; Beynon et al., 1998; Shellis et al., 1998). This is surprising given that many

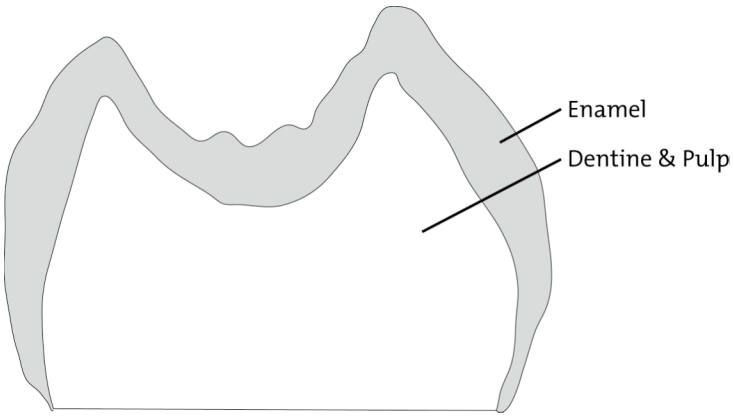


Figure 1.1: Coronal section through a molar. Relative enamel thickness in two dimensions per Martin's protocol (1983, 1985) is equal to [the area of enamel divided by the length of the EDJ] divided by [dentine area]. The area of enamel divided by the length of the EDJ yields the average straight-line distance traveled by an ameloblast during enamel secretion; dentine area is a surrogate for body size in interspecies comparisons.

cladistic approaches to understanding phylogenetic relationships of fossil hominoid primates are informed in part by the thickness of the molar enamel (e.g., Andrews and Martin, 1897a, 1991; Begun 1997). Measuring a large sample of *Hylobates* molars may shed light on the ancestral condition of the hominoid clade by polarizing the character among extant ape species. An examination of *Hylobates* enamel thickness may be especially informative for scholars of ape evolution when considered in light of published cercopithecoid (e.g., Ulhaas 1999, Grine et al., 2005) and ceboid (e.g., Martin et al., 2003) samples, which serve as second and third extant outgroups to the great ape and human clade, facilitating a more nuanced interpretation of fossil ape molars.

**Repeatability in Manually Produced Section Planes**

The precise sectioning of molars in homologous planes is difficult, and as Martin (1983) noted, any deviation from the ideal plane of section will cause enamel thickness measurements to be exaggerated (Figures 1.2 and 1.3) by increasing the apparent area of

enamel. The shape of the EDJ is also changed considerably in oblique section planes, such that the height of the dentine horns is reduced in oblique sections (Olejniczak, 2005). The result of measuring even slightly oblique sections was apparent in the study of an *Afropithecus turkanensis* molar enamel by Smith et al. (2003), who found substantial differences in enamel thickness calculated from sections that were within ~300 μm of each other. Oblique sections add variation to enamel thickness measurements, causing sample ranges to be inflated, thus confounding intra- and intertaxon comparisons by artificially increasing sample variability.

In a pilot study conducted using microtomographic imaging (mCT) machines at Stony Brook University's Department of Biomedical Engineering, serial sections at regular intervals mesial and distal to the ideal plane of section were visualized from eight primate molars of varying sizes (4-16 mm in mesial-distal length). Enamel thickness measurements taken from mCT visualization of the ideal plane of section were shown to be accurate (via post hoc comparisons) with physical sections taken through the same molars (Olejniczak, 2005). The value of enamel thickness measurements in a plane other than the ideal plane of section is contingent upon the morphology of the enamel surface and the underlying enamel-dentine junction more than on the size of the tooth, but in each case measurements within 3% of those from the ideal plane of section were recorded for at least 50 μm both mesial or distal to the ideal plane, and typically a greater distance from the ideal plane was required to find measurements that differed by more than 3% (Figure 1.4). Nonetheless, beyond approximately 150-200 μm from the ideal plane of section, measurements begin to diverge rapidly (Figure 1.4). Manually sectioning molars, where accuracy in determining the location of the ideal plane typically cannot be

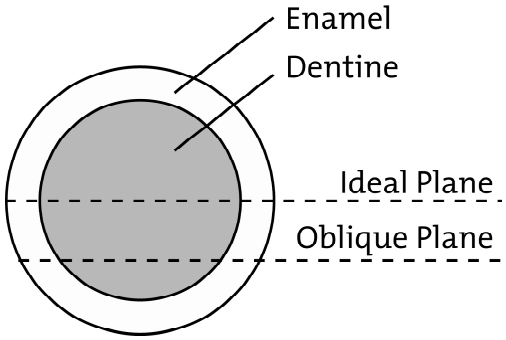


Figure 1.2: Transverse section through an idealized molar cusp. The ideal plane of section will minimize the area of enamel in cross-section and maximize the area of dentine, resulting in a lower relative enamel thickness than adjacent (i.e., non-ideal) planes of section. Redrawn after Martin (1983).

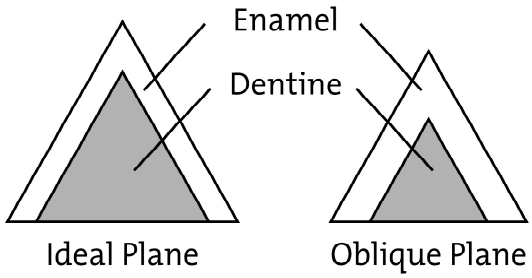


Figure 1.3: Idealized coronal section through a molar cusp. The diagram on the left depicts the ideal plane of section, in which enamel area is minimized and dentine area is maximized by virtue of sectioning the tooth through both the dentine cusp tips and the tips of the enamel cusps. The diagram on the right depicts the effects of section obliquity, where the enamel cusp tips have been sectioned, but the dentine cusp tips have not, thus increasing apparent relative enamel thickness (note also that the apparent size of the cusp has been reduced through section obliquity). Redrawn after Martin (1983).

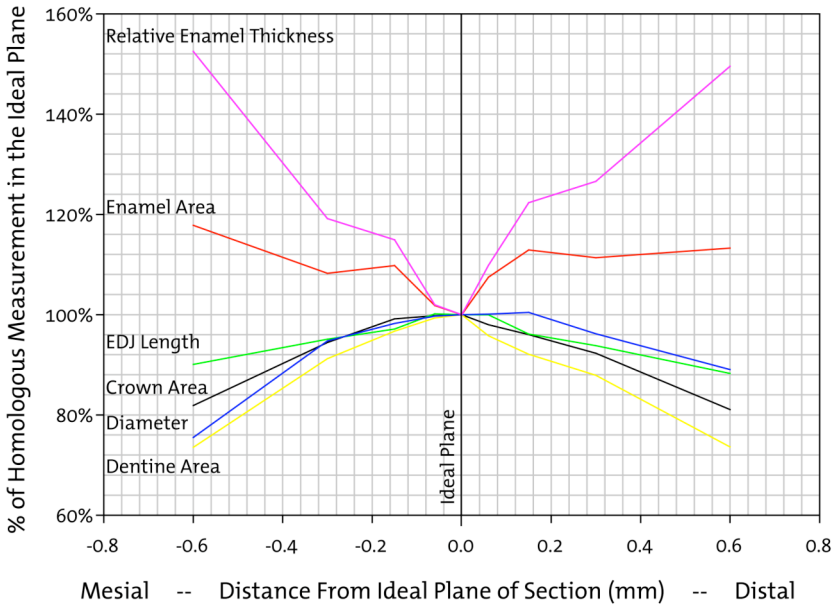


Figure 1.4: Plot showing the divergence in enamel thickness measurements from the ideal plane of section (0.0 microns on the x-axis) in a *Chiropotes* molar based on serial mCT images. Note that at approximately 50 microns from the ideal plane of section in either the mesial or distal direction, measurements begin to diverge from the ideal. "Diameter" is the distance between the two enamel cervices in cross-section.

established beyond ~200 µm, may thus impart bias towards inflated enamel thickness measurements (and reduced dentine horn height) by missing the ideal plane of section.

**Three-Dimensional Variable Correspondence to Two-Dimensional Surrogates**

A final concern regarding planar measurements is their association with volumetric measurements. Martin (1983) suggested that enamel area in the mesial ideal plane is a reasonable 2D proxy for the volume of enamel on a tooth, and that an ideal measure of the average enamel thickness of a tooth would be the volume of enamel divided by the surface area of the enamel-dentine junction. Martin's measurement protocol was therefore developed using 2D surrogates for three-dimensional phenomena (enamel area in lieu of enamel volume, dentine area in lieu of dentine volume, etc.). The

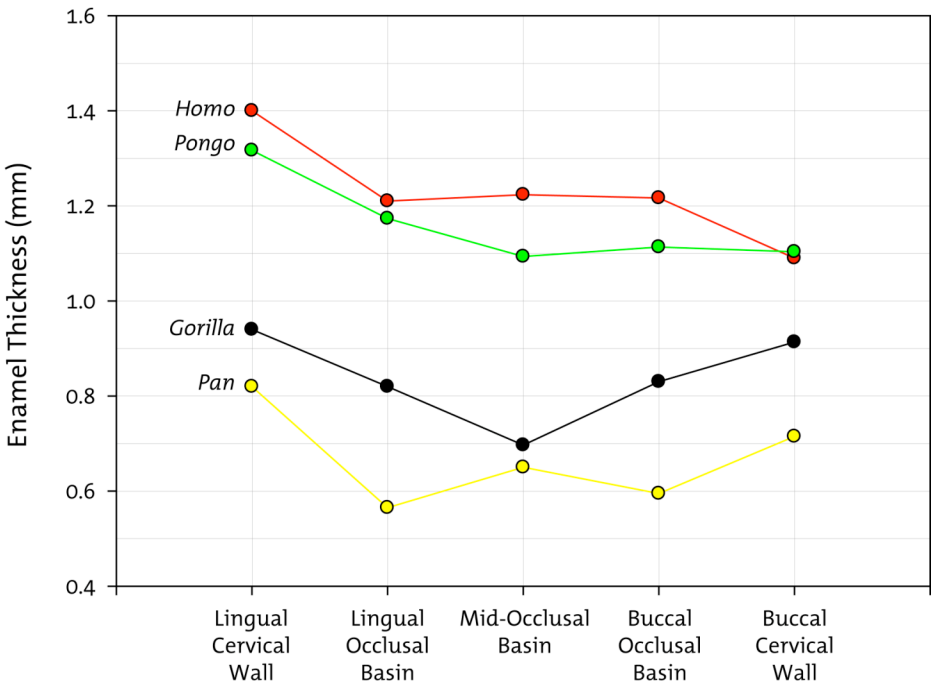


Figure 1.5: Enamel thickness patterns in hominoid maxillary molars (data taken from Martin (1983)). This plot demonstrates that enamel thickness is not constant throughout a single cross-sectional plane within a molar (see also Schwartz (2000)).

ideal plane of section ignores all morphological data along the mesial-distal axis of a molar, however, capturing only a single coronal section; moreover, several recent studies have reported data showing an uneven distribution of enamel over molar crowns, even in 2D sections (Figure 1.5) (e.g., Spears and Macho, 1998; Ulhaas et al., 1999; Schwartz, 2000; Shimizu, 2002; Martin et al., 2003). There are significant differences in enamel thickness between cusps, and between different locations on a single cusp (e.g., buccal versus lingual sides of a cusp). Both Schwartz (2000) and Ulhaas et al. (1999) found these differences to be taxon-specific, perhaps due to specific dietary regimes, indicating that a wealth of morphological information may be obtained by applying a 3D measurement technique to the entire tooth. Three-dimensional measurements must also be compared to previously published 2D measurements in order to assess the accuracy of the ideal plane in capturing some or all of the intra- and inter-species differences in

enamel cap thickness and shape, and to assess previous results based on enamel thickness measurements taken in two dimensions in light of the three-dimensional measurements they are meant to represent. Kono (2004) recently reported that enamel thickness distribution in 2D mesial ideal section planes of great apes and humans does not adequately capture the morphology of the entire tooth when compared to analogous 3D measurements. Differences in 2D and 3D measurements appeared to be due to species-specific differences in enamel thickness at locations other than the mesial section plane. Kono (2004) combined teeth from different positions in the molar row, however, as well as teeth from both the mandible and the maxilla, which may have contributed to the deviation from the best-fit regression lines in her sample due to tooth- and jaw-specific enamel and dentine distributional differences (e.g., Grine, 2004; Smith et al., 2005).

**Radiographic Methods: a Non-Destructive Alternative to Section Planes**

In order to test for species-level differences in enamel and EDJ morphology, and to generate three-dimensional measurements in sufficiently large samples for statistical analyses without destroying material, an accurate non-destructive three-dimensional visualization technique is necessary. Such a non-destructive method has the additional benefit of facilitating the accurate (and repeatable) location of ideal planes of section, thereby eliminating the variance introduced through section obliquity.

To this end, Grine has demonstrated that neither standard dental radiographs (Grine et al., 2001) nor medical CT (Grine, 1991) produce accurate measurements, despite the common employment of these technologies in enamel thickness studies (e.g., Nagatoshi, 1990; Macho and Thackeray, 1992; Molnar et al., 1993; Conroy et al., 1995;

Schwartz, 1997). Recently, other three-dimensional techniques have been suggested to be useful for enamel thickness measurements, including pulse-echo ultrasound (Yang, 1991; Feeney, 2005), TeraHz radiation (Crawley et al., 2003), and both synchrotron and standard X-ray mCT (Chaimanee et al., 2003; Gantt et al., 2003; Tafforeau, 2004; Kono, 2004; Kono and Suwa, 2005; Olejniczak and Grine, 2005; Olejniczak and Grine, 2006; Olejniczak et al., 2006; Olejniczak et al., in press).

A preliminary trial of TeraHz imaging technology revealed that only extremely thin enamel (e.g., the incisive edge of a modern human anterior tooth) can be distinguished from the underlying dentine accurately, and only with poor image quality (TPI Core System, TeraView Ltd., Cambridge, UK). Ultrasound imaging has the ability to measure thickness via the pulse echo technique, but lacks the spatial resolution to render accurate volume models (Yang, 1994; Feeney, 2005: Figures 5-8).

However, mCT analysis has produced clear images of the enamel-dentine junction (Figure 1.6) (see also Chaimanee et al., 2003; Gantt et al., 2003; Tafforeau, 2004; Kono, 2004; Olejniczak and Grine, 2005, 2006), and projects aimed at quantifying the accuracy of mCT have demonstrated the efficacy of this technique for the non-destructive visualization and measurement of enamel thickness and shape (Tafforeau, 2004; Olejniczak and Grine, 2006; Olejniczak et al., in press). A combination of custom-designed and commercial software allows accurate rendering and measurement of mCT images; the accuracy of this technique has been confirmed in a sample of primate molars and sauropsid caniniform teeth ranging in length from 4-16 mm. Experiments conducted to evaluate the accuracy of mCT systems are recounted in Chapters 3 and 4 of this

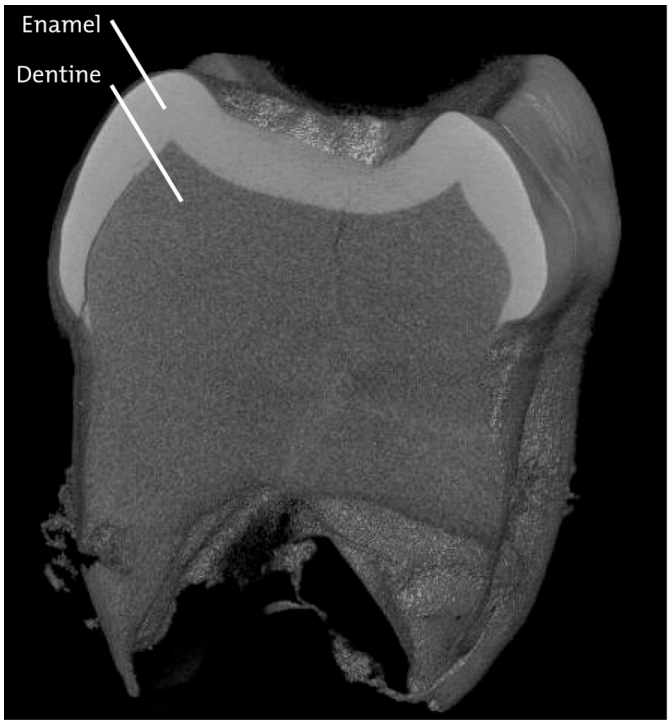


Figure 1.6: Digitally sectioned volume rendering of a *Cebus* molar made from mCT scans. The enamel and dentine are clearly distinguishable in this cross-section through the volume model, and measurements have been demonstrated to be accurate to within 10 µm compared to the physical specimen, which was sectioned after mCT scanning in order to compare linear measurements.

dissertation, and are only briefly described here as a background to the remainder of the introductory text.

Serial mCT images of molars were obtained at slice intervals ranging from 6 µm in small specimens (*Ateles, Cebus, Chiropotes*) to 10 µm in larger specimens (*Alligator*, *Crocodylus*, *Homo, Papio*). The molars were then physically sectioned, and enamel thickness measurements were recorded from a mesial ideal plane in both the physical sections and the mCT images (and in a plane traversing the long axis of the caniniform sauropsid teeth). The mCT images were found to be accurate (relative to the physical sections; see Chapter 3) to within approximately 3% for linear and area measurements. Differences in the physical and mCT measurements are most likely attributable to

difficulty in locating the ideal plane in the physical sections, whereas the mCT images could be stacked, visualized, and virtually rotated in order to locate the ideal plane to within 6-10 μm (compared to ~100-200 μm in physical sections).

**Post-Processing of mCT Images**

Microtomography thus appears to be a reliable method for quantifying enamel thickness and visualizing the enamel-dentine junction under certain circumstances (e.g., when diagenetic remineralization of fossil enamel and dentine has not caused the density of these tissues to appear the same; Olejniczak and Grine, 2006). Nonetheless, there are several obstacles that must be overcome to expedite the process of accurately measuring dental microtomographic images, most notably the presence of image noise in mCT images and the large size of mCT images in terms of computational requirements. Microtomographic datasets are serial, parallel X-Ray images at known distances from one another throughout the length of an object (discussed in Chapter 2 of this dissertation). In order to remove image noise from mCT scans, one may choose to manually draw on each of the serial images using common image manipulation software, removing pixels that are obviously not representative of the structure being visualized. However, mCT scanning produces images at such a spatial resolution (images within a stack may be only 5 μm apart), that the number of images documenting a single tooth may be over 1,500; clearly manual image cleaning is too laborious to be effective when a large sample of teeth is to be measured, and an automated approach is more efficient if its accuracy may be demonstrated.

The most common automated methods for treating image noise involve passing a filter over images (e.g., mean filter, Gaussian filter, median filter, diffusion filter, edge detection). There are hundreds of approaches to image filtration (e.g., Castle, 1996; Jähne, 1997), and the goal of most is to segment images into meaningful units. For instance, a mCT image of a tooth depicts the enamel, dentine, and pulp chamber as different shades of gray (more accurately, each tissue or space is depicted as different pixel values) because each of these tissues (or spaces) absorbs X-rays differently. If some parts of the enamel, however, are the same color (pixel value) as the underlying dentine, it becomes difficult to separate the two tissues computationally in order to measure, for instance, the thickness or volume of enamel. The image must be segmented, via some filter or combination of filters, in order to render each of the tissues as a homogenous group of pixels of roughly the same color.

A drawback to image filtration and edge detection approaches is that they may have an impact on the accuracy of the representation of a tooth. For example, edge detection may be used to isolate the dentine of a molar in a mCT image, but the edge detector may also incorporate some parts of the enamel cap that are within the same pixel value range as the dentine, thereby increasing the apparent amount of dentine and decreasing the apparent amount of enamel, which may substantially impact three-dimensional measurements of these tissues. One of the goals of this study is thus to identify and implement an image filtration protocol that cleans image noise and renders tissues homogenously without reducing the accuracy of the image's representation of the anatomy of the tooth. Chapter 5 of this dissertation contains a more thorough discussion of the image noise that is often found in dental mCT scans, and an empirically tested

method of treating serial mCT dental images to reduce this noise while maintaining accuracy before measurements are taken.

**Biological Applications Using mCT**

After developing an accurate mCT method and filtration protocol for recording three-dimensional measurements of enamel thickness, tissue volumes, and surface areas, a series of biological applications was performed on molars of carefully chosen taxa to address biological questions and to demonstrate the efficacy of the mCT technique in evaluating enamel thickness and EDJ shape in a whole-crown context. Measurements were taken on mCT scans of mandibular molars from four primate species representing two superfamilial groups and two broad dietary categories: *Hylobates syndactylus* (primary folivore) and *Hylobates muelleri* (primary soft-fruit predator) representing Hominoidea; *Alouatta seniculus* (primary folivore) and *Ateles geoffroyi* (primary soft-fruit predator) representing Atelidae. Sample sizes for individual taxa in enamel thickness studies are often less than five molars each (e.g., Shellis et al., 1998), and frequently only one molar is available for measurement in studies of fossil taxa (e.g., Andrews and Martin, 1987a; Smith et al., 2003; Dean and Shrenk, 2004, Olejniczak and Grine, 2005). The non-destructive method of this project allows for variability to be assessed in four relatively large samples (between ten and 25 molars per species). Importantly, through mCT imaging, the amplified sample variability caused by section obliquity can be quantified and eliminated, providing data ranges that allow the large body of previously reported measurements to be assessed and reinterpreted in a context of known measurement error. Chapter 6 of this dissertation documents a study of the

impact of section obliquity on enamel thickness measurements, and provides a landmark-based solution for locating repeatable homologous planes in three dimensions.

The taxa listed above were specifically chosen to facilitate comparisons between dietary groups (primary frugivore and primary folivore) and phylogenetic groups (Ceboidea and Hominoidea) allowing the effect of each on enamel and EDJ morphology to be weighed. Specifically addressed in the sample are five questions. First, whether there exists metameric variation in the molar row of the taxa studied, and if so, whether this metameric variation is species-specific or perhaps related to diet. Metamerism in the hominoid dentition has been studied by Hlusko (2000), Grine and colleagues (Grine et al., 2005; Grine, 2005), and Smith et al. (2005), and these studies concluded that mesial-to-distal gradients in enamel thickness (including the specific components of enamel thickness, such as cross-sectional enamel area) exist. Smith et al. (2005) found that differences are sufficient to warrant considering each tooth type separately when making inter-species comparisons.

A second research focus is the distinction of functional from phylogenetic signals in enamel thickness. Previous studies have been divided: some attributed differences in enamel thickness and shape primarily to dietary differences, some primarily to a phylogenetic signal (especially when considering EDJ morphology), and some to an unknown combination of both (reviewed in Schwartz, 2000). The current study explicitly addresses and quantifies the relative influence of both potential causes using general linear models as well as classificatory statistics. The choice of taxa allows both phylogenetic relatedness and dietary proclivity to be statistically controlled, ultimately acting as a test of the taxonomic utility of enamel thickness and related measurements.

The third research focus is the three-dimensional shape of the EDJ. Previous studies using geometric morphometrics (Olejniczak et al., 2004; Olejniczak et al., in press) have been conducted using two-dimensional section planes, and while the discriminatory power of the shape of the EDJ in these planes is high, it is unknown whether that signal improves or degrades when the entire length of the tooth is considered. Moreover, the distinction of congeneric species with distinct diets using EDJ shape has not been tested, and may provide a reliable means of distinguishing fossil taxa when only isolated teeth are available.

A fourth research focus is the measurement of standard two-dimensional enamel thickness variables (Martin, 1983, 1985; Grine and Martin, 1988; Beynon and Wood, 1986; Schwartz, 2000) in multiple planes of section in each tooth, and the simultaneous measurement of analogous three-dimensional data from the entire tooth crown in order to evaluate the impact of the dimensional loss of data in previous planar studies. These data provide an appropriate context (with known rates of obliquity-induced variance, as well) for the interpretation of previous 2D research in light of whole-crown morphology.

Finally, the research presented here provides important tissue thickness and distribution data from molars of genus *Hylobates*, which is the least-studied extant hominoid primate in terms of enamel thickness. As the extant outgroup to great apes and humans, *Hylobates* is in a unique position to inform discussions about the ancestral hominoid enamel thickness condition and the subsequent polarity changes in this character. The data collected in this study compliment mCT research performed on great ape and human molars (Kono 2004; Tafforeau, 2004), and serve as a comparative sample against which to gauge enamel thickness in early-to-middle Miocene fossil hominoids as

well as early fossil cercopithecoid primates (e.g., *Victoriapithecus*: Dean and Leakey, 2004).

**Specific Aims of the Project**

The primary aims of this study fall into two distinct categories: methodological aims and biological aims. The methodological aims are:

1) To test the accuracy of mCT technology in the measurement of enamel thickness, dental tissue volumes, and the visualization of the EDJ in extant and fossil teeth.
2) To assess the minimum requirements for slice thickness and image pixel resolution in order to minimize mCT costs and resultant data sizes, while preserving measurement accuracy.
3) To verify the accuracy of the mCT technique on multiple mCT systems in order to ensure the homogeneity of measurement quality when combining data from multiple scanners.
4) To develop a protocol for the filtration of noisy mCT images that does not impair the accurate measurement of the imaged dental tissues.

The biological aims of the project are:

1) To assess the intra-individual (metameric), intra-species, and inter-species variation in molar crown morphology in primate mandibular molars without the confounding effects of obliquity introduced through the physical sectioning of molars.

2) To assess the relative influence of two proposed causes of variation in enamel thickness and patterning: dietary proclivity and phylogeny.
3) To assess the utility of surrogate two-dimensional measurements of enamel thickness and shape compared to the actual three-dimensional measurements they are meant to represent.
4) To assess the power of three-dimensional EDJ landmarks in discriminating closely-related species.
5) To develop a comparative sample of *Hylobates* (including *Symphalangus*) molar enamel volume and thickness measurements for use in the polarization of enamel thickness in the evolution of the hominoid dentition.

# CHAPTER 2: BACKGROUND DISCUSSION OF CT, DIGITAL IMAGES, AND OPTIMAL IMAGE PARAMETERS

**Background to mCT**

X-ray micro-computed tomography (a.k.a. microtomography, mCT, μCT) is a relatively new technique for the visualization and measurement of small objects, including the internal structures of those objects. The physical principles of mCT scanning are similar to those of other medical imaging techniques, especially standard medical X-ray computed tomography (CT), with the notable difference that mCT is typically performed at a scale measurable in microns (rather than millimeters), resulting in finer image resolutions and slice thicknesses than standard medical CT. The process of scanning and measuring an object using mCT can be understood in three distinct phases: image acquisition, image post-processing, and image measurement and analysis. The majority of the chapters that follow focus on image post-processing, measurement, and analysis, and the principles of mCT data acquisition are only briefly described here.

The modern term *tomography* is derived from the Greek *tomos* (literally "a cutting") and *gramma* ("written words"); implicit in this etymology is that tomographic techniques document an image of a cross-section through an object (Morgan, 1983). In practice, roentgenographic tomography involves passing X-rays through an object towards a detector. X-rays are variably absorbed by different biological tissues, such that tissues absorbing few X-rays allow most of the radiation to pass through and reach the detector (these areas appear dark on X-ray images), while other tissues absorb some or all of the X-rays before they reach the detector (causing these areas of an image to appear lighter, or even white, if no X-rays pass through the object in that area).

A major advancement in radiological techniques has been the development of computed tomography (CT), which differs from conventional tomography by the use of

multiple projections in order to reconstruct a single plane of section (this technique is occasionally referred to as *reconstruction tomography*). In CT, many X-ray projections are taken through an object at varying tangential angles, and these projections are digitally reconstructed in order to produce a single image of the section based on many possible vantage points (the number of vantage points depends on the angle of rotation between the recording of each projection). The earliest attempts at CT used angle increments of 7.5 degrees (recounted in Morgan, 1983), although modern systems often use angle increments that are less than one or two degrees, facilitating highly accurate reconstructions.

Rather than visualizing only one plane of section, a series of equally spaced (i.e., serial) images may be produced by moving the X-ray source slightly after each scan (alternatively, the specimen may also be moved relative to the X-ray source). Recording many images in this way produces an *image stack*, which documents the entire object as cross-sectional images. mCT is the application of these two principles, with sub-millimeter steps between consecutive scans, and detectors that produce digital images at high pixel resolutions based on many reconstructed projections.

Finally, one of the main factors determining how well an X-ray beam may penetrate a medium is the energy at which it is accelerated (typically referred to as the "energy" of the X-ray beam). Rangayyan (2005) notes that low energy X-ray beams are absorbed at or near the skin of a human, so filters that limit the emission of low-energy X-rays are typically applied in order to prevent the unwanted irradiation of living subjects, thereby capping the low-end of the X-ray energy spectrum utilized in CT scanning. Soft tissues are typically scanned with X-rays under 30 kVp (kilo-volt-peak; a

measure of the highest energy X-ray produced given a particular voltage), while bone is typically scanned at energies between 70 and 90 kVp (Rangyyan, 2005). The dentine component of teeth absorbs X-rays of approximately the same energy as bone, and the enamel cap also is visible given this range of X-ray energies (the enamel cap observed at these energies was also later determined to be accurately portrayed; see Chapter 3). Thus, all of the scans recorded in later parts of this study were performed using X-Rays between 70 and 100 kVp.

**Background to Digital Image Stacks**

Serial-imaging techniques such as mCT involve iteratively recording cross-sectional digital images along the long axis of a specimen (the entire collection of images describing each specimen is referred to as the *image stack*). For example, the length of a molar may be traversed by the mCT X-ray source, stopping every 0.40 mm to record an image of the tooth in cross-section at that location (Figure 2.1; an actual scan would involve much smaller step increments, the number chosen here is for illustrative purposes). The distance traversed by the X-ray source between consecutive scans is called *slice thickness*. Slice thickness is known to impact the shape and appearance of mCT-based rendering of primate teeth (Figure 2.2). Increasing slice thickness is equivalent to reducing the inter-slice of the image stack, such that a greater distance must be interpolated between slices. Because a "slice" does not actually have a thickness, the thickness of each image representing a slice must be extrapolated by giving that slice a depth component.

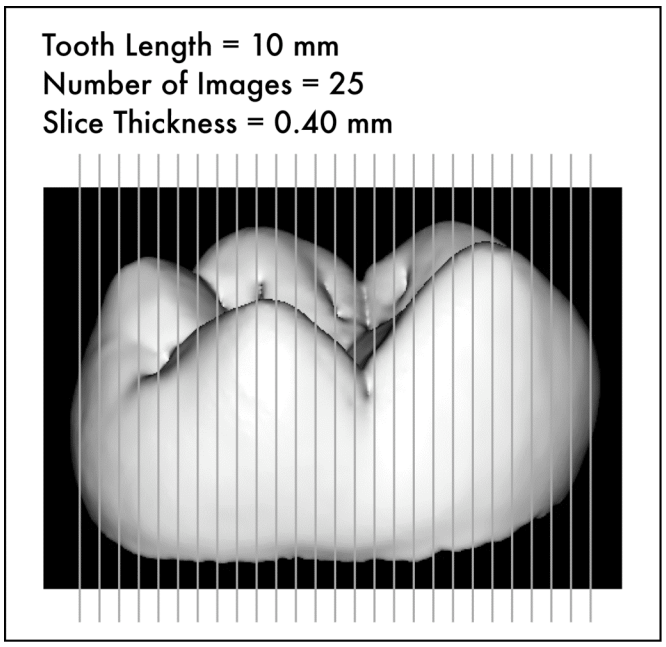


Figure 2.1: Schematic demonstrating slice thickness in a hypothetical scan of a *Symphalangus* molar (slices depicted here are thicker than they would be in typical scanning for illustrative purposes). Each line through the tooth represents a location where the mCT X-ray source took an image. In this case, the length of the tooth is 10 mm, and 25 images were taken, resulting in a slice thickness of 0.40 mm.

The resultant digital image produced at each slice location is comprised of some number of square pixels of known dimension (*e.g.*, each pixel may be 10.5 x 10.5 μm). The number of pixels within an image is known as *image resolution*, and also serves to calibrate measurements taken on that image because the size of the pixels is known (Figure 2.3). For example, each of the serial images may be 15 x 15 pixels, so given a pixel dimension of 6 x 6 μm, the image is known to be 90 x 90 μm (Figure 2.3). The pixel dimension of the image thus serves to calibrate measurements of the objects contained within each image (e.g., the area of the enamel cap).

Slice thickness also acts as a depth parameter for the serial images. For instance, if slice thickness in an image stack is 6 μm, and each image is comprised of pixels that are 6 x 6 μm, then each pixel may be considered a cube (called a *voxel*, derived from the

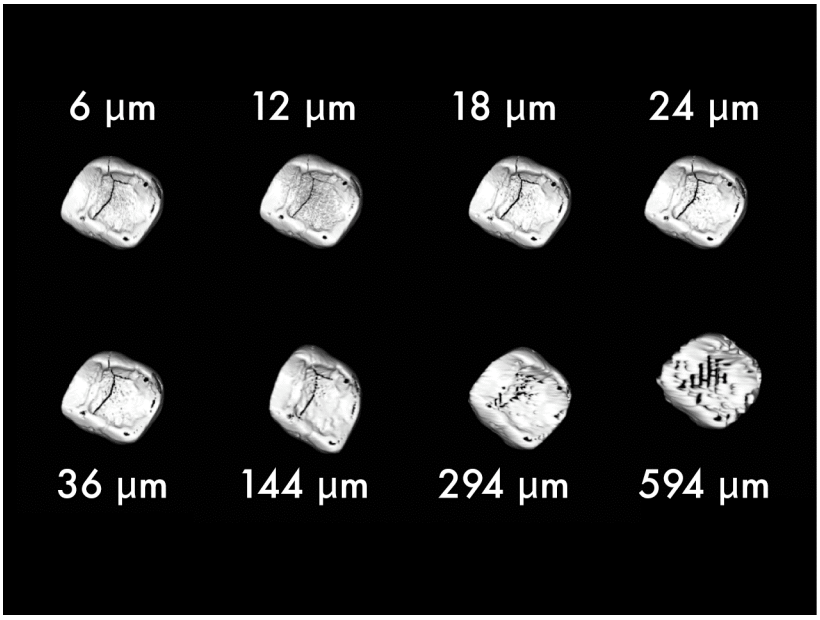


Figure 2.2: Surface models of an *Ateles paniscus* molar generated from image stacks with varying slice thicknesses. The tooth was worn and broken prior to scanning (note the pools of dentine at the cusp tips and post mortem cracks). The quality of the model's representation of the tooth is reduced when models are based on thicker slices, which require software to interpolate increasing amounts of missing (unscanned) morphology.

term *volumetric pixel*) that is 6 x 6 x 6 µm. In this way, each cross-sectional image is actually a cubic rectangle (Figure 2.3).Slice thickness and image resolution have a substantial impact on one's ability to manipulate and measure image stacks in three dimensions due to computational limitations. For instance, the image stack of a single *Symphalangus syndactylus* molar scanned for this study is approximately 3.6 GB in size when LZW compressed (compression is discussed below; this example assumes 8-bit TIF images), and requires 85.3 GB of random access memory (RAM) to manipulate in three dimensions at an image resolution of 2048 x 2048 pixels. If one reduces the resolution of each image in the stack by 75% to 512 x 512 pixels, the required RAM is reduced to 6 GB, enabling standard desktop computers to manipulate and measure the image stack with only minor modification to memory handling settings (Figure 2.4). An alternative

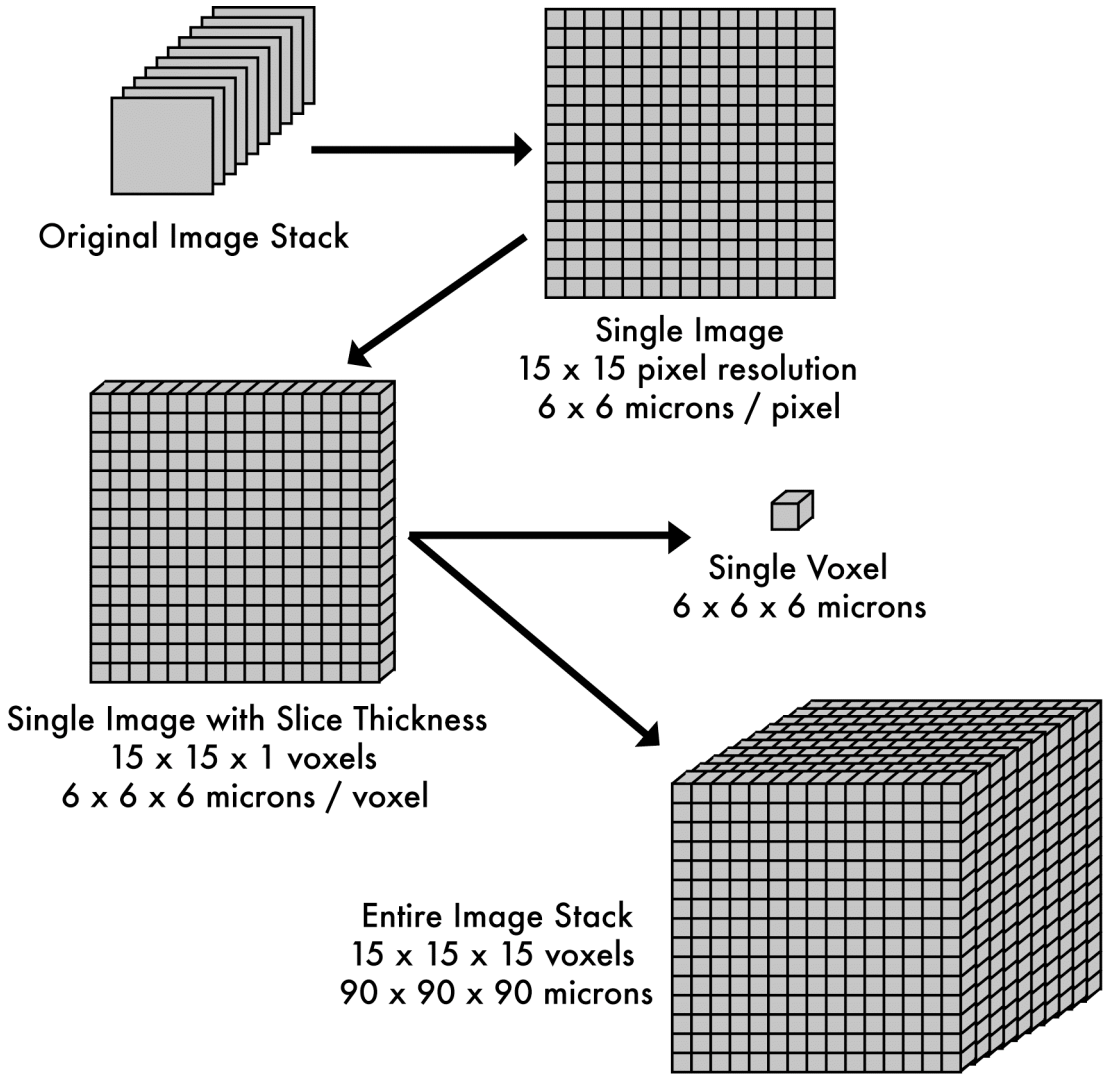


Figure 2.3: Schematic describing the different levels of data used in analysis of mCT image stacks. The original image stack contains the serial cross-sectional images. Each single image from within that stack is of known dimension, because the number of pixels and the size of each pixel are known. The slice thickness is used to turn each image into a cubic rectangle comprised of voxels, or three-dimensional pixels, the smallest volumetric units in the mCT image stack. The entire volume is visualized by giving each image from the original stack a thickness, and then viewing the resultant voxels in three-dimensions.

to reducing image resolution is to record fewer images during the scanning process, which is equivalent to increasing the slice thickness. Thus, a compromise between image quality (minimizing slice thickness and maximizing image resolution) and computational ability (increasing slice thickness and reducing image resolution) is sought in order to ensure that mCT scanning is not only accurate, but also viable for researchers without access to costly computational facilities.

In the course of establishing an analysis protocol for the experiments described in the remainder of this dissertation, several computer systems were evaluated to determine how best to carry out analyses in terms of both accuracy and cost. Ultimately, two computer systems were assembled from readily available components in order to carry out the experiments that follow. The first is an Intel-based PC running a Windows XP operating system that was used primarily to run VoxBlast 3D software (Vaytek, Inc., Fairfield, IA, USA) for the purposes of re-orienting image stacks relative to a user-defined plane of section (e.g., perpendicular to the best-fit plane containing the four major dentine horn tips). This system has a 3.3 GHz processor (overclocked) and 4 GB of random access memory. The second system, used for all of the measurements recorded in later sections of this dissertation as well as for programming image filters, rendering movies and still images, and modifying image stacks, was a dual-processor (2.5 GHz each) Apple Power PC with 8 GB of RAM running OS X Server Edition. The combination of these systems, with several external hard drives for data storage, was sufficient to carry out analyses at the optimal image stack settings in order to ensure accuracy.

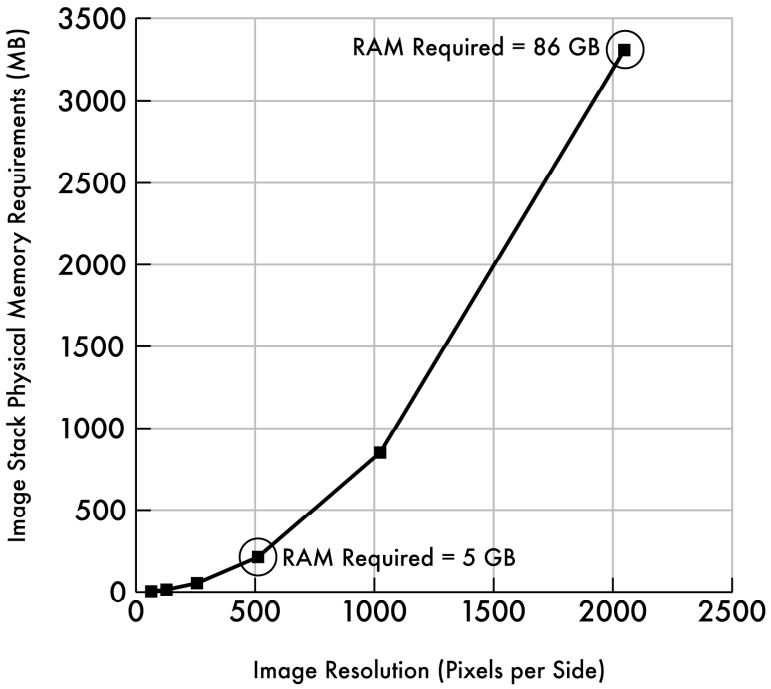


Figure 2.4: Plot depicting the physical memory required to store an image stack versus the resolution of the images in that stack, based on a Symphalangus syndactylus molar (the pattern depicted here is similar for any image stack, only the absolute values change). In the case of images stored at 2048 x 2048 pixels at 8-bite per pixel, which occupy 3.31 GB of hard drive space, approximately 86 GB of RAM are required to manipulate and measure the image stack in three dimensions. When the images are reduced in resolution to 512 x 512 pixels, the required RAM is reduced to approximately 5 GB. Due to the hardware limitations of modern desktop computers, smaller images are preferred because of one's ability to manipulate them with standard computational facilities. The research presented here demonstrates that reducing the size of the image stack (either by recording fewer images through or by reducing the resolution of those images) may have a substantial impact on measurements and should be avoided to ensure measurement accuracy.

Several types of files pertinent to medial imaging exist, the most common of which are "tagged image file format" (TIF) and "digital imaging and communications in medicine" (DICOM) files. TIF files typically have a one-to-one correspondence between mCT slices and images (each TIF file is a single cross-sectional image captured by the mCT apparatus). DICOM files have the advantage of containing all of the images within an image stack in a single file (although it is possible to arrange TIF files in a similar manner). Despite the relative simplicity of DICOM files in terms of transferring only a

single file between systems, individual slice-by-slice TIF files were used in this study because, among the several software packages used to measure the mCT scans, TIF was the only format common to all of them. This reduced the number of image file type conversions that had to be made in order to analyze a single tooth. A second reason that TIF files were chosen is that they more explicitly adhere to typical bitmapped file format protocols available in common programming environments used for filter programming (e.g., Appendices A and B). TIF files are typically either 8-bits per pixel or 16-bits per pixel; for the purposes of this study 8-bits per pixel TIF images were used in order to reduce file size.

The image files produced by the ScanCo system used throughout this study were LZW compressed prior to transferring the images from the mCT on-board system to the computers used for analysis in order to increase file transfer speed as well as to reduce the total hard-drive space required to store the images. LZW compression (a.k.a. Lempel-Ziv Welch compression) is a lossless compression method, so this process did not reduce the quality of the images (Welch, 1984) and was deemed superior to alternative, lossy compression schemes (*lossy* is a computer science term describing a process in which data are irretrievably removed during compression). Pitas (1993) describes the process of LZW compression, and offers C-language code for the implementation of both image compression and decompression following the LZW model. Compression and decompression were accomplished in this study through the use of GraphicConvertor software (Lemke Software, GmbH, Germany).

One final consideration regarding the use of radiographic images such as those produced via mCT is the *pixel value*. Each pixel in every image (assuming hereafter that images

are 8-bits per pixel) has an associated value, ranging from 0 to 255. A pixel value of 0 indicates that the pixel is black; a pixel value of 255 indicates that the pixel is white. Pixel values between 1 and 254 indicate that the pixel is some shade of gray, with the low end of the range indicating darker values of gray and the higher end of the range indicating brighter shades (Figure 2.5). Pixel value is a function of how many X-rays penetrated that area of the scanned object and were therefore recorded by the mCT's X-ray detector; the hydroxyapatite crystals comprising the enamel cap (which appears nearly white in mCT images) absorb more X-rays than the underlying dentine (which appears grey in mCT images). Pixel values are useful not only in visually interpreting the image stacks produced by mCT scanning, but also in the computer-based identification of tissues (i.e., image segmentation), where software may be used to automatically associate all of the nearly white pixels with one another, thus identifying the enamel cap, for example. Because each pixel corresponds to a three-dimensional voxel of known volume (when slice thickness is considered), pixel value threshold segmentation is a crucial step in calculating tissue volumes (see also Chapter 5 of this dissertation).

**An Experiment to Determine Optimal Image Dimensions and Slice Thickness**

In order to reduce the memory required to store mCT images and to minimize the cost of scanning, it is necessary to determine the settings for both slice thickness and image pixel size that provide the required resolution at the smallest file size (see also Olejniczak et al., in press). To this end, an experiment was conducted on a small pilot sample. The sample studied contained molars from a taxonomically broad range of primates (Table 2.1); these taxa are known from previous two-dimensional analyses to

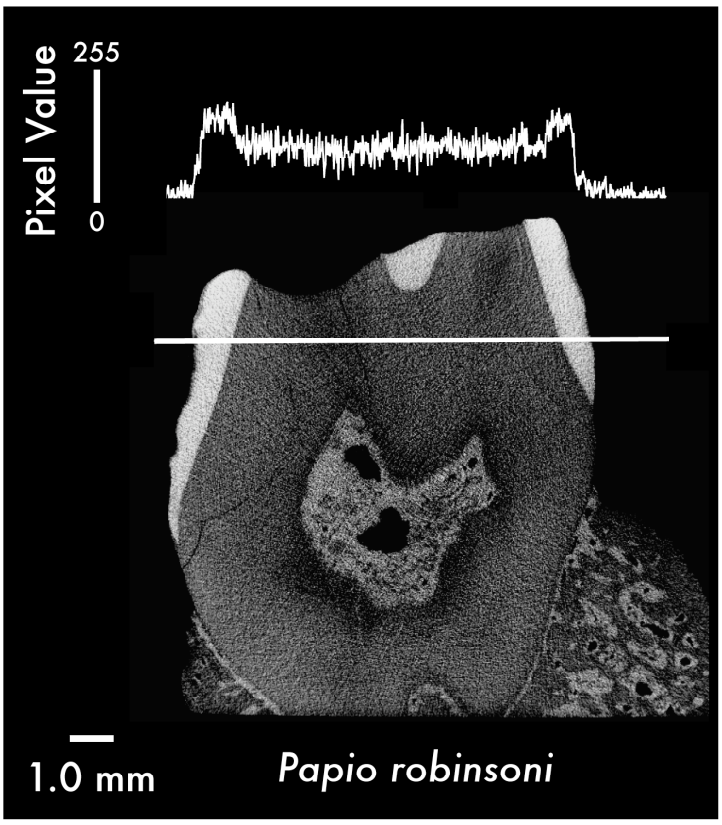


Figure 2.5: Cross-section through a molar of the fossil taxon *Papio robinsoni* (approximately 2.0 Myr old; E. Delson, pers. com.) derived from mCT scanning. The white line through the molar specifies a region of interest, and the pixel value plot above shows the pixel values along that line (0 is black and 255 is white). The enamel pixels show a peak compared to the pixels representing the dentine, demonstrating that mCT is able to resolve dental tissues in this Pliocene fossil tooth.

exhibit a range of enamel thicknesses and enamel cap shapes (Martin, 1985; Shellis et al., 1998; Ulhaas et al., 1999; Schwartz, 2000; Martin et al., 2003; Olejniczak et al., 2004). Each molar was scanned using a Scanco uCT 20 system (Scanco Medical, Switzerland). The thinnest possible slices were taken, and images with the highest possible resolution were acquired for each specimen. These parameters are partially dependent upon the size of the individual specimen as it limits the diameter of the mCT gantry that will accommodate this size; slice thickness and image resolution for each specimen are reported in Table 2.1. Scanning resulted in an image stack for each specimen comprised

*Table 2.1: Study sample composition and scanning parameters.*

| Taxon | Tooth | Voxel Cubic Dimension (mm) | Image Resolution (pixels) | Number of Images |
|---|---|---|---|---|
| *Ateles geoffroyi* | $M_1$ | 0,011 | 2048x2048 | 756 |
| *Ateles paniscus* | $M_1$ | 0,006 | 2048x2048 | 1097 |
| *Cebus apella* | $M_2$ | 0,006 | 2048x2048 | 663 |
| *Homo sapiens* | $M^3$ | 0,010 | 2048x2048 | 1314 |
| *Homo sapiens* | $dm_1$ | 0,008 | 2048x2048 | 839 |
| *Homo sapiens* | $M_3$ | 0,008 | 2048x2048 | 1589 |
| *Papio ursinus* | $M^2$ | 0,010 | 2048x2048 | 1449 |
| *Symphalangus syndactylus* | $M_2$ | 0,010 | 2048x2048 | 847 |
| *Symphalangus syndactylus* | $M_2$ | 0,010 | 2048x2048 | 834 |
| *Symphalangus syndactylus* | $M_1$ | 0,010 | 2048x2048 | 807 |

of serial compressed TIF images, which were uncompressed prior to analysis, and converted using NIH ImageJ software to unsigned character raw image format for volumetric analysis using Slicer3D software.

In order to assess the impact of different slice thicknesses on computer-based measurements of mCT scans, the volume of the enamel cap in each specimen was measured at 15 different slice thicknesses (because slices themselves have no thickness, this was accomplished by removing every other slice in order to double the length that must be interpolated between each slice). The range of slice thicknesses corresponded to the lowest possible thickness based on the mCT machine's capability on the low end, up to 1.00 mm on the high end. For example, a molar scanned at a slice thickness of 0.01 mm had volume measurements taken at the following 15 slice thicknesses for comparison: 0.01 mm, 0.02 mm, 0.03 mm, 0.04 mm, 0.05 mm, 0.06 mm, 0.07 mm, 0.08 mm, 0.09 mm, 0.10 mm, 0.20 mm, 0.30 mm, 0.40 mm, 0.50 mm, and 1.00 mm. Volume measurements were performed using Slicer3D software, ensuring that identical pixel threshold values were assigned to the image stack during each measurement of the

enamel volume. The volume of the enamel cap was calculated for each tooth at each slice thickness, and the length of the specimen was also noted in order to create the index [slice thickness / specimen length]. Using this percentage, slice thickness may be viewed as a function of tooth size, allowing a researcher to choose the thickest possible slices that still yield an accurate (within 1%) measurement of volumes, given the size of the tooth as the only parameter known a priori. Because scanning is both time-consuming and expensive, selecting the maximum slice thickness that provides accurate measurements is important, and an effective way to reduce the resultant file size.

A single cross-sectional image from within each specimen's image stack also was examined at the highest resolution per the ScanCo uCT 20's camera (2048 x 2048 pixels). Images were deliberately chosen from the center of each image stack so that both enamel and dentine were visible. NIH ImageJ software was employed to threshold the image, so that only enamel pixels were visible. The area of enamel was calculated by counting the number of pixels describing the enamel (the number of thresholded pixels) and multiplying this number by the area of a single pixel. This process was repeated on each image five more times, after halving the resolution each time. Thus the area of enamel was recorded for each tooth cross-section at the following image resolutions: 2048 x 2048, 1024 x 1024, 512 x 512, 256 x 256, 128 x 128, and 64 x 64 pixels. Because pixels in the original image are of a known length and width, halving the resolution is equivalent to quadrupling the area of each pixel (i.e., when 2048 pixels at 10 μm per side are represented as 1024 pixels, the size of each pixel become 20 μm per side). In this way, the study described here is actually better characterized as a determination of the optimal pixel size rather then the optimal number of pixels. Identical thresholding was

used for all six measurements of each tooth image. Finally, the 2048 x 2048 pixel image was printed and the hard-copy output was measured using a digitizing tablet interfaced with SigmaScan Pro software (v5.0, SPSS, Inc.).

Table 2.2 shows the slice thickness at which volume measurements were 1% different than those recorded from the thinnest slices possible. Table 2.2 also reports a percentage calculation of slice thickness versus the specimen length (mesio-distal crown diameter). Results of the slice thickness experiment suggest that volume is a rather robust measurement, such that a slice thickness of 8% of the length of the specimen, on average, results in scans that are accurate to within 1% of the best possible (thinnest) scans for that specimen (Table 2.2). Moreover, there is no trend for thin-enameled species (e.g., *Ateles paniscus*) to require more scans than thickly enameled species (e.g., *Cebus apella*) in order to achieve measurement accuracy, nor is there a relationship between specimen length and required slice thickness.

Results of the image resolution experiment indicate that area measurements taken on images to which identical thresholding algorithms had been applied tend to become less similar to the actual area value (as measured by digitization) as resolution is decreased (that is to say, accuracy decreased as the size of the pixels expressed in mm increased). Table 2.3 depicts the value of enamel area obtained by digitization for each tooth section, and the percent difference of computer-based measurements of the same section at different pixel resolutions. There is a wide range of percent differences from the digitized area value, but the general trend is towards decreased measurement accuracy (i.e., increased percent differences from the value obtained via digitization) with larger pixels. The average percent difference of all the specimens at a given resolution is

*Table 2.2: Slice thickness at which volume measurement is 1% different than ideal.*

| Specimen | Tooth | Thickness at 1% Different (mm) | Slice Thickness / Specimen Length |
|---|---|---|---|
| *Ateles geoffroyi* | $M_1$ | 0,42 | 9,83% |
| *Ateles paniscus* | $M_1$ | 0,30 | 4,55% |
| *Cebus apella* | $M_2$ | 0,60 | 15,08% |
| *Homo sapiens* | $M^3$ | 0,80 | 7,60% |
| *Homo sapiens* | $dm_1$ | 0,80 | 11,76% |
| *Homo sapiens* | $M_3$ | 1,00 | 6,29% |
| *Papio ursinus* | $M^2$ | 0,50 | 3,45% |
| *Symphalangus syndactylus* | $M_2$ | 0,50 | 5,90% |
| *Symphalangus syndactylus* | $M_2$ | 1,00 | 11,90% |
| *Symphalangus syndactylus* | $M_1$ | 0,60 | 7,43% |
| Mean | | | 8,38% |

approximately 1.5 times the percent difference at the previous (better) resolution: from 2.00% at 1024 x 1024 pixels, to 2.79% at 512 x 512 pixels, to 4.57% at 256 x 256 pixels, and so on. The digitized values were almost always closest to the values obtained via thresholded pixel counts at 2048 x 2048 pixels, suggesting that the smallest possible pixels produce the most accurate measurements compared to a hand-digitization standard (less than 1.00% measurement difference).

Results of the experiments conducted here suggest that while image resolution should be maximized in order to achieve automated image measurement accuracy (e.g., counting pixels or voxels after thresholding to measure areas and volumes, respectively), slice thickness may be sacrificed while maintaining accurate measurements in some cases. That is, enamel volume may be calculated accurately in permanent human molars with slices that are between 0.80 and 1.00 mm thick, even though it is possible to achieve slice thicknesses of 0.008 mm for these specimens. However, because of its three-dimensional nature, volume is less influenced by shape irregularities caused by interpolation of thicker slices than two-dimensional measurements such as areas or distances. For instance, in the case where the precise location of dentine horns in a mCT stack is not possible because of poor image resolution (i.e., the tip of the horn appears as

*Table 2.3: Enamel area from digitization (mm^2) and thresholding (% different than digitization) at different pixel counts.*

| Taxon | Tooth | Digitized Area (mm^2) | 2048x2048 | 1024x1024 | 512x512 | 256x256 | 128x128 | 64x64 |
|---|---|---|---|---|---|---|---|---|
| *Ateles geoffroyi* | $M_1$ | 1.56 | 0.64% | 4.49% | 8.33% | 9.62% | 25.00% | 44.23% |
| *Ateles paniscus* | $M_1$ | 2.14 | 0.00% | 1.40% | 2.34% | 4.67% | 10.28% | 22.43% |
| *Cebus apella* | $M_2$ | 3.54 | 0.28% | 0.85% | 0.56% | 0.85% | 2.54% | 7.34% |
| *Homo sapiens* | $M^3$ | 17.68 | 0.79% | 1.81% | 1.92% | 5.77% | 4.07% | 1.41% |
| *Homo sapiens* | $dm_1$ | 8.42 | 1.07% | 1.19% | 0.48% | 0.24% | 2.85% | 12.00% |
| *Homo sapiens* | $M_3$ | 40.52 | 0.79% | 1.16% | 1.23% | 9.45% | 12.22% | 8.66% |
| *Papio ursinus* | $M^2$ | 21.90 | 1.92% | 4.20% | 4.93% | 4.89% | 6.62% | 10.68% |
| *Symphalangus syndactylus* | $M_2$ | 9.12 | 0.22% | 4.50% | 7.13% | 6.69% | 5.92% | 6.80% |
| *Symphalangus syndactylus* | $M_2$ | 9.11 | 0.66% | 0.11% | 0.33% | 1.43% | 3.84% | 5.60% |
| *Symphalangus syndactylus* | $M_1$ | 11.00 | 1.00% | 0.27% | 0.64% | 2.09% | 4.55% | 7.82% |
| Mean | | | 0.74% | 2.00% | 2.79% | 4.57% | 7.79% | 12.70% |

a fuzzy gray that could belong to enamel or dentine), the linear distance between two of the dentine horns may not be known accurately. Having included a small section of each dentine horn tip in the enamel volume measurement, however, will only add a small amount of enamel relative to the volume of the entire cap, resulting in a volume measurement that is similar to that which does not include the tips of the dentine horns. In a previous analysis, it was found that a slice thickness ranging from 0.006 mm to 0.010 mm facilitates accurate measurements of distances within mCT image stacks of primate teeth (Olejniczak and Grine, 2006), suggesting that volumes and distances necessitate different slice thicknesses in order to ensure measurement accuracy. The slice thicknesses reported here (Table 2.2) thus serve only as maximum thicknesses to permit the accurate measurement of enamel volumes, and these guidelines are adhered to in all of the experiments discussed in later sections of this dissertation.

# CHAPTER 3: PROOF OF CONCEPT IN RECENT AND FOSSIL MATERIAL

## Introduction

Several studies have examined the repeatability of measurements (and inter- and intra-individual errors in locating landmarks) from mCT images of trabecular bone (e.g., Durand and Rüegsegger, 1991; Balto et al., 2000), tooth root canals (Peters. et al., 2000), and tooth enamel (Avishai et al., 2004). To date, however, the only studies that have attempted to assess the accuracy of measurements derived from high-resolution X-ray computed tomography have been conducted with reference to trabecular bone (Kuhn et al., 1990; Müller et al., 1996, 1998; Hildebrand et al., 1999; Fajardo et al., 2002), periapical and periradicular alveolar bone destruction (Balto et al., 2000; von Stechow et al., 2003), the diameters of tooth root canals (Rhodes et al., 1999), and cortical bone porosity (Cooper et al., 2004).

Kuhn et al. (1990), Müller et al. (1996, 1998), Hildebrand et al. (1999) and Fajardo et al. (2002) observed negligible differences between measurements derived from mCT images and those obtained using traditional or stereological techniques applied to histological thin sections. Percentage differences between mCT and histological values reported by these studies ranged between lows of 0.88 to 1.17 (Müller et al., 1996) and highs of 2.5 to 6.1 (Müller et al., 1996), depending upon the type of physical section examined. Balto et al. (2000) and von Stechow et al. (2003) also reported negligible differences between measurements obtained from mCT and histological sections of periapical and periradicular bone. Rhodes et al. (1999) similarly reported very high correlations between the values recorded for the diameters of tooth root canals from mCT images and physical sections. Cooper et al. (2004) compared measurements obtained by mCT to those recorded from micro-radiographs of cortical bone, and while the two

methods produced similarities, relatively poor results were obtained for measurements of pore density. Unfortunately, it is not possible to ascertain the source of this discrepancy or its deviation from values derived from physical sections because histological preparations were not measured directly. Fajardo et al. (2002) concluded that mCT can accurately reconstruct the complex architecture of trabecular bone, although slight alterations in threshold values greatly affected the morphometric data.

The only mCT studies that have been directed explicitly at the resolution of dental hard tissues (e.g., Avashai et al., 2004; McErlain et al., 2004) have not involved comparisons of measurements derived from mCT and physical sections. McErlain et al. (2004) examined a single tooth from a 420-year-old Late Iron Age site in Cambodia, and simply commented that they were clearly able to visually differentiate the hard tissue components, which were displayed with "exceptional clarity." The study by Avishai et al. (2004) examined individual error rates in locating landmarks (and resultant measurements) in a series of tooth germs derived from archaeological contexts.

Thus, although mCT is potentially a powerful tool by which to obtain information on enamel thickness in a non-destructive manner, its efficacy for this purpose has yet to be demonstrated. It is necessary to establish the validity of enamel thickness measurements obtained using mCT before these data are employed to answer questions of evolutionary interest. The purpose of the present experiment was to establish the accuracy of high-resolution mCT measurements of enamel thickness in teeth of differing size, enamel thickness, and degree of mineralization. Towards this end, measurements were obtained from mCT scans that had not undergone any image artifact corrections (as this may impact measurements) to those obtained from physical sections of the same

specimens, in a sample comprised of teeth that vary in size, enamel thickness, and mineralization. Dental sections were measured using standard techniques (printing the images and measuring them using a digitizing tablet) in order to make results comparable to previously published studies. Measurements taken directly from digitization were compared to those taken directly on the three-dimensional models in order to assess the comparability of these measurement protocols.

**Materials and Methods**

Twelve isolated teeth that varied in size, absolute enamel thickness, and degree of mineralization were chosen for study (Table 3.1). One of the modern human molars (depicted in Figure 3.1) was embedded in a cylinder of methyl methacrylate. Although the absolute sizes of the teeth differed somewhat, all were chosen for their ability to be accommodated within the specimen tubes of the mCT system that was used (μCT 40, Scanco Medical, Switzerland). These tubes range from 13 mm to 35 mm in diameter. Beyond this, the extant primate and sauropsid specimens were selected on the basis of published values (Dauphin, 1987; Sato et al., 1988; Shellis et al., 1998; Martin et al., 2003; Grine, 2004a; Grine et al., 2005) and personal observations of enamel thickness, such that a range of thin- to thick-enameled teeth was represented. The three fossil teeth were chosen on the basis of absolute enamel thickness and geological age, with the latter expected to exhibit some degree of correlation with degree of diagenetic re-mineralization.

In order to generate a three-dimensional model of each tooth, every specimen was scanned in its entirety using a fan-beam-type desktop mCT system (μCT 40, Scanco

*Table 3.1: Study sample and average published measurements.*

| Taxon | Age | Tooth | BCD* (mm) | Maximum Lateral Linear Enamel Thickness (mm) |
|---|---|---|---|---|
| *Alligator mississipiensis* | Recent | Caniniform | 6.60 | 0.14 |
| *Ateles paniscus* | Recent | $LM_1$ | 4.20 | 0.40 |
| *Cebus apella* | Recent | $LM_2$ | 4.50 | 0.90 |
| *Chiropotes satanus* | Recent | $LM_1$ | 2.70 | 0.30 |
| *Crocodylus palustris* | Recent | Caniniform | 6.70 | 0.24 |
| *Diademodon tetragonus* | c. 241 Myr | Maxillary Molariform | 8.90 | 0.05 |
| *Homo sapiens* | Recent | $LM^3$ | 10.90 | 0.60 |
| *Homo sapiens* | Recent | $RM_3$ | 8.90 | 2.20 |
| *Homo sapiens* | Recent | $Ldm_1$ | 5.90 | 0.70 |
| *Moschops capensis* | c. 263 Myr | Incisor | 8.50 | 0.36 |
| *Papio robinsoni* | c. 2.0 Myr | $LM_2$ | 10.00 | 0.90 |
| *Papio ursinus* | Recent | $LM^2$ | 12.70 | 1.70 |

* Bi-cervical diameter.

Medical, Switzerland). The diameter of the specimen tubes used, as well as the voxel dimensions and number of slices produced, are given in Table 3.2. All scans were output with 2048 x 2048 pixels per image and 8-bits per pixel; the resultant voxels were isometric (having identical length, width, and depth). Each scan used the same settings for voltage and amperage, and the acquisition time for each slice was 4-7 seconds, with a reconstruction time of approximately 24 seconds per slice at an angular increment of 0.36 degrees.

After the mCT scanning of each tooth was complete, the specimens were prepared for physical sectioning following established methods (e.g., Martin, 1983; Martin et al., 2003; Grine, 2002, 2004b, 2005). The tips of the two mesial cusps (protocone and paracone, or metaconid and protoconid) of the primate molars were marked with a spot of permanent ink. An equivalent procedure was employed for the sauropsid and therapsid teeth, taking into account the fact that, because they differ morphologically from the primate molars, a homologous plane is not available. In these instances, a series of anatomical landmarks and pseudo-landmarks (e.g., cusp tips, cervical margins) was identified in order to define the location of the plane of section (discussed below). The

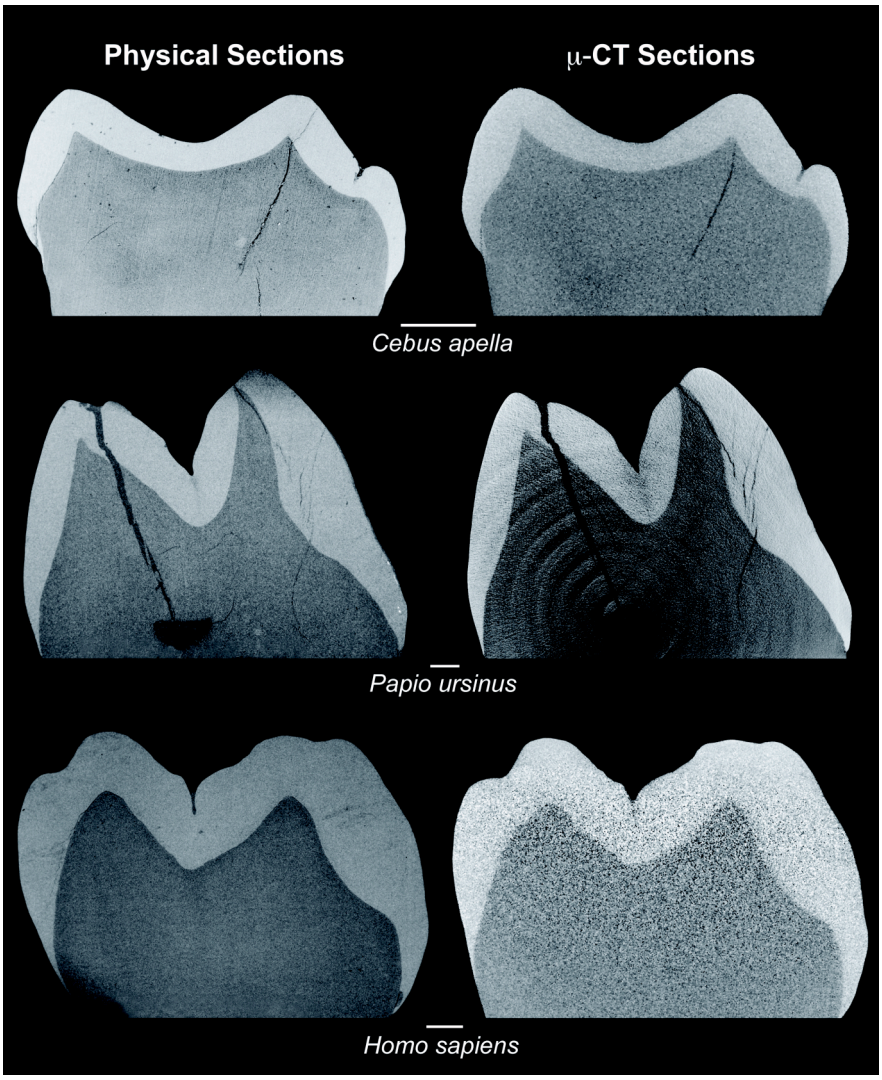


Figure 3.1: Scanning electron micrographs (left) and mCT images of the same cross-section through three of the primate molars examined. Scale bar is 1 mm.

*Table 3.2: mCT scanning protocol.*

| Taxon | Tooth | Tube Diameter (mm) | Voxel Dimension (microns) | Post-Processing Pixel Resolution (microns) | Scan Length (mm) |
|---|---|---|---|---|---|
| *Ateles paniscus* | $LM_1$ | 12,3 | 6,0 | 24,0 | 6,6 |
| *Cebus apella* | $LM_2$ | 12,3 | 6,0 | 24,0 | 4,0 |
| *Chiropotes satanus* | $LM_1$ | 12,3 | 6,0 | 24,0 | 4,6 |
| *Homo sapiens* | $LM^3$ | 16,4 | 8,0 | 32,0 | 10,5 |
| *Homo sapiens* | $Ldm_1$ | 16,4 | 8,0 | 32,0 | 6,8 |
| *Homo sapiens* | $RM_3$ | 20,5 | 10,0 | 40,0 | 15,9 |
| *Papio ursinus* | $LM^2$ | 20,5 | 10,0 | 40,0 | 14,5 |
| *Crocodylus palustris* | Caniniform | 20,5 | 10,0 | 40,0 | 3,4 |
| *Alligator mississipiensis* | Caniniform | 20,5 | 10,0 | 40,0 | 3,4 |
| *Diademodon tetragonus* | Molariform | 16,4 | 8,0 | 32,0 | 16,2 |
| *Moschops capensis* | Incisor | 35,0 | 17,5 | 70,0 | 1,1 |
| *Papio robinsoni* | $LM_2$ | 20,5 | 10,0 | 40,0 | 15,7 |

crown was then embedded in epoxy, and sectioned with a 0.15 mm diamond-wafering blade (Buehler Isomet). The blade was positioned immediately distal to the ink marks to ensure that the mesial crown block included both dentine horns. This block face was ground with 400-grade paper and polished with a sequence of diamond pastes to 0.25 μm (Buehler Microcloth) to obtain a topography-free buccolingual (BL) section that traversed the tips of both dentine horns (in the case of the primate molars). The polished surface was lightly etched with 0.5% $H_3PO_4$ for 15 seconds to remove any smeared enamel, ultrasonicated in distilled $H_2O$, mounted on a stub and coated with silver for examination by scanning electron microscopy (AMRAY 1810). These specimens were examined at 25 kV in either secondary or, more commonly, back-scattered electron mode. Micrographs were recorded using Polaroid Type 55 P/N film at magnifications between 7.5x and 11.0x depending upon the size of the specimen; working distance was kept under 27 mm to ensure accurate magnification. Enlargements of the micrographs were used for measurement.

In order to compare measurements recorded from the physical sections to those obtained by mCT, stacked image sequences of each tooth derived from mCT scanning were imported into the VoxBlast software program (Vaytek, Inc.) to create three-dimensional reconstructions of the crown. The size of the mCT image file at the slice thicknesses used here (3.0-10.0 GB for each image stack in this study) imposes certain hardware limitations, so image stacks were stored at a resolution of 512 x 512 pixels (the same pixel dimensions used by Kono, 2004) rather than the 2048 x 2048 pixels generated by the mCT unit. No visual loss of image quality was seen after the adjustment. Because the slice thickness of the scans was preserved, the pixel length and height was effectively four times the slice thickness, and voxels were therefore no longer isometric.

VoxBlast software allows user-defined planes of section to be created, and these can pass through the three-dimensional reconstructions at any orientation. Using two enamel cusp tips as landmarks (in the case of the primate molars), a buccolingual section was made through each tooth model, attempting to capture the same plane as was located in the physical sections. An iterative (slice-by-slice) technique was employed to refine the location of this plane of section based on visual comparison of the SEM micrographs to the mCT model. Anatomical landmarks unique to a particular plane (e.g., cracks in the enamel or dentine, distinct pulp chamber morphology, distinct dentine topography) were identified in order to match the mCT section to the physical section. After locating the desired plane of section in the mCT model, the image of this plane was exported and printed at its resolution based on our post-processing technique (512 x 512 pixels). Two images representing the same plane of section were thus available for comparison for

each specimen: one generated by physical sectioning and one generated by mCT (Figure 3.1).

As mCT analysis of teeth becomes commonplace, the measurement of dental tissues using software alone (rather than digitizing a printed image) is likely also tobecome widespread. Therefore, measurements were compared using both techniques in order to examine whether substantial measurement differences exist between them. First measuring the teeth using a digitizing tablet served to control potential sources of measurement error by ensuring that identical techniques were used to measure all images in this study (SEM micrographs and printed mCT sections). Digitization also made the method of analysis used here comparable to that of previous studies. Following digitized measurements with on-screen measurements sought to establish whether these two techniques may be reliably compared (e.g., when comparing published data recorded using a digitization tablet to those taken directly on mCT models). Certain measurements that are based on anatomical landmarks (e.g., the thickness of enamel between the dentin horn tip and the enamel cusp tip) were recorded on the mCT images for three of the specimens using VoxBlast software. These values were compared to measurements obtained by digitizing the printed images.

Measurements describing the thickness of enamel relative to other dental dimensions were recorded for each primate molar (Figure 3.2), following the protocol established by Martin (1983). These include the area of coronal dentine and pulp (b), the area of the enamel cap (c), and the bi-cervical diameter (BCD). Eleven measurements describing the linear thickness of enamel at various locations across the molar crown were also recorded for each primate tooth. Because different absolute enamel thicknesses

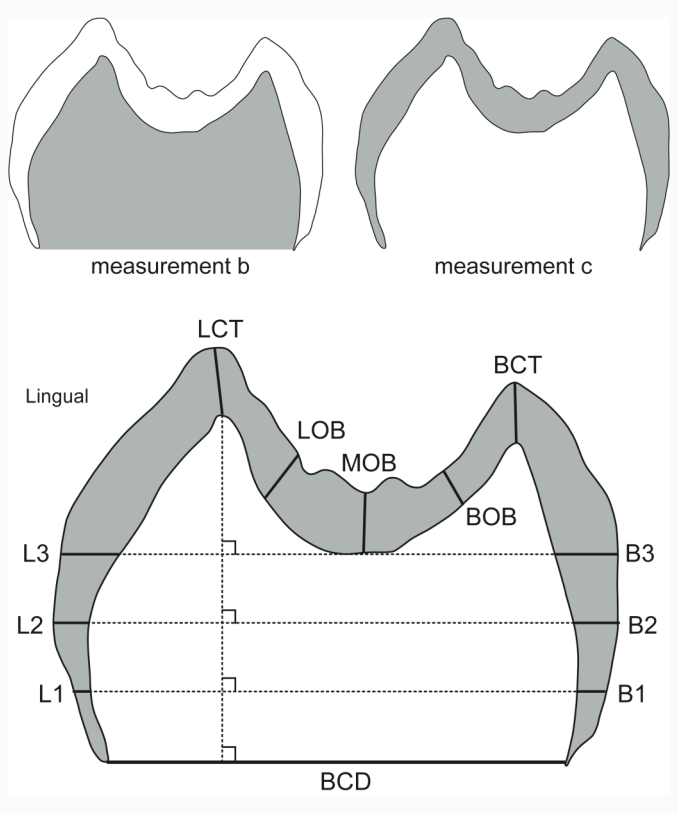


Figure 3.2: Schematic diagram of the enamel thickness measurements recorded in the primate teeth examined. Measurement b is the area of dentine (including the area of the pulp chamber, if present in the section) contained within the enamel cap (in mm2). Measurement c is the area of enamel in cross-section (in mm2). BCD is the bi-cervical diameter, the distance between the two enamel cervices (in mm). LCT and BCT are the linear thicknesses of enamel between the dentine horn apex and the enamel cusp tip in the lingual and buccal cusps, respectively (in mm). LOB, MOB, and BOB are the maximum radial enamel thickness in the lingual cusp occlusal basin, the mid-occlusal basin, and the buccal cusp occlusal basin, respectively (in mm). L1-L3 and B1-B3 are defined as the thickness of enamel at three evenly spaced intervals between the bi-cervical diameter and the lowest point of the enamel-dentine junction in the mid-occlusal basin, parallel to the bi-cervical diameter.

are accompanied by differential rates of error using standard CT methods (Grine, 1991; Spoor et al., 1993), the linear measures were devised to examine whether areas of thick and thin enamel in an individual tooth yield comparable rates of measurement error using mCT. In the case of the fossil cercopithecoid molar, the plane of section on which measurements were recorded coursed through the distal cusps due to post-mortem

breakage of the mesial half of the tooth. The morphology of extant sauropsid and fossil therapsid teeth is not comparable to that of primates, so a unique set of linear enamel thickness measurements was defined for comparing the two planes of section for each of these teeth (Figure 3.3).

All measurements were recorded on enlargements of physical section micrographs and the printed mCT sections using SigmaScan software (Systat Software, Inc.) interfaced with a SummaSketch III digitizing tablet (CalComp, Inc.). Values were recorded to the nearest 0.1 mm (or 0.1 $mm^2$). Measurements derived from scanning electron microscopy were calibrated using the measurement scale printed on the micrographs. Measurements derived from mCT models were calibrated by the bi-cervical diameter of the image. This was determined using VoxBlast, as the number of pixels spanning the bi-cervical diameter related to the pixel size in microns. In order to minimize intra-observer error, each measurement was recorded three times, and the mean of these three trials was recorded as the value. In order to avoid the potentially confounding effect of image manipulation on the resulting measurements, images were not enhanced to eliminate scan artefacts (e.g., the ring artefacts evident in the *Papio ursinus* scan in Figure 3.1), or by sharpening borders through the use of automated image filtering techniques.

The relative difference in density (and therefore X-ray absorption) of enamel and dentine impacts directly the ability of mCT (or any X-ray based radiographic technique) to distinguish these tissues. The relative absorption of dentine and enamel were measured with OsiriX software (v1.6, Rosset et al., 2004) on an Apple Macintosh computer. A single mCT cross-section of each fossil tooth, the two sauropsid teeth, and

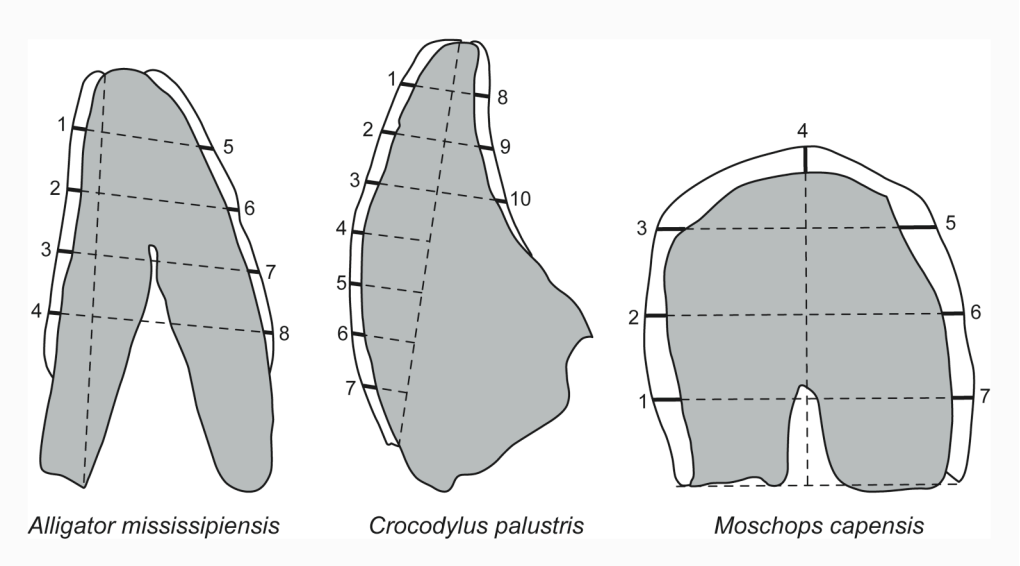


Figure 3.3: Schematic diagram of the measurements recorded on the sauropsid and therapsid teeth examined in this study (not drawn to scale). Each measurement point was determined by first identifying two landmarks on each tooth (e.g., the labial enamel cervix and the cusp tip in the *Crocodylus* tooth) which form a reference line, and then drawing perpendicular lines through the crown at equally spaced intervals along this line, measuring the thickness of enamel where each perpendicular courses through the enamel cap.

an extant primate molar were analyzed using OsiriX by tracing a Region of Interest (ROI) line over the cross-section, ensuring that the line traversed both the enamel and dentine. The value of each pixel crossed by the line (0 for black pixels, 255 for white pixels, and between 0 and 255 for shades of gray) was exported into a spreadsheet and plotted against its location on the line. The resulting charts were superimposed onto the mCT images of the teeth (Figure 3.4). Substantial differences in the pixel values for enamel and dentine imply that they are heterogeneous in their density and therefore discernable for measurement, whereas like-valued pixels for enamel and dentine are not distinguishable by the mCT scanner.

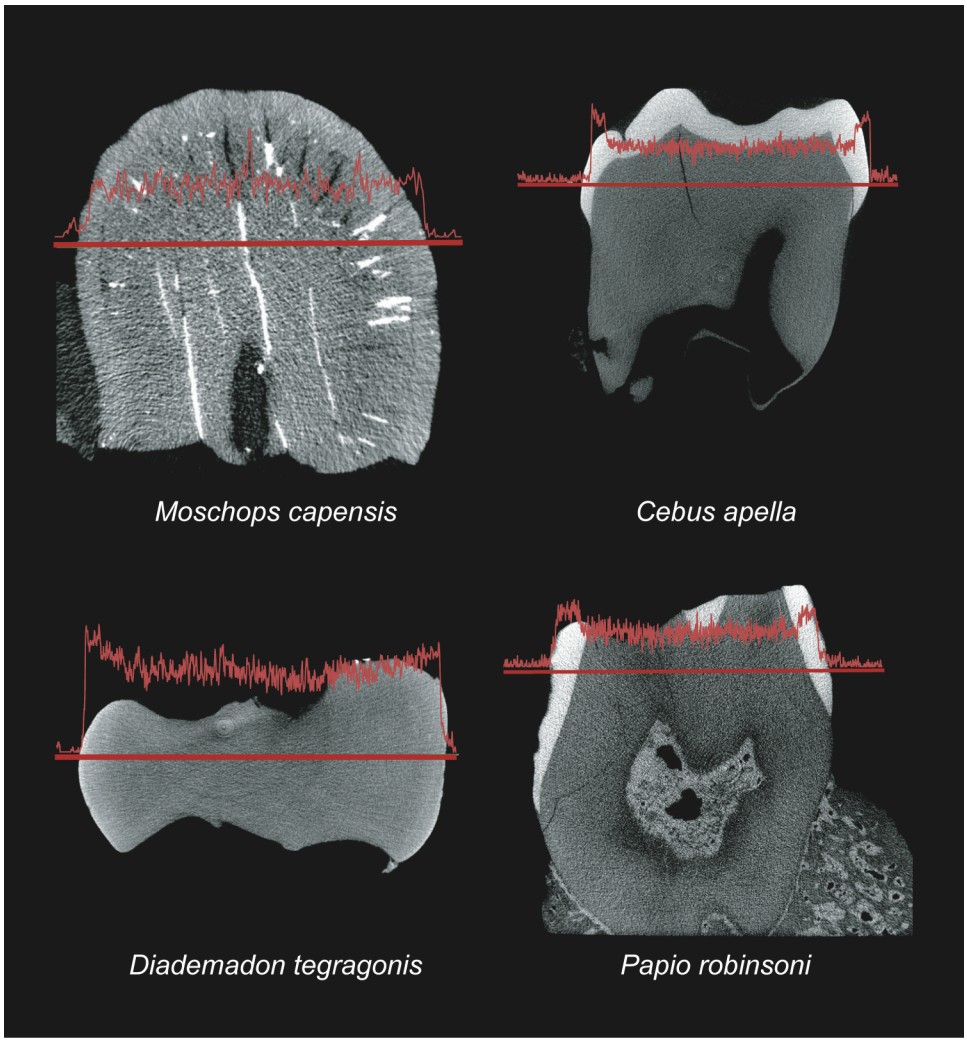


Figure 3.4: Plots of the pixel values along region of interest lines in representative teeth. The height of the red line corresponds to the value of the pixels along the base line (higher values indicate a color value that is closer to white, lower values indicate closer to black). Note that in the extant *Cebus apella* molar and the fossil *Papio robinsoni* molar, the enamel clearly has higher pixel values than the dentine. Neither of the therapsid teeth show a clear difference between enamel and dentine, although a post-mortem fissure propagated between the enamel and dentine of the *Moschops capensis* incisor allows the two tissues to be separated for measurement.

**Results**

Among the recent primate and sauropsid teeth, the enamel-dentine junction and outer enamel surface (hence the thickness of enamel) were clearly visible (e.g., Figures 3.1 and 3.4). Scans of the modern human tooth that had been embedded in methyl methacrylate had more image noise than the other specimens, although measurements did not seem to be affected. Comparisons between the measurements derived from mCT images and physical sections are presented in Tables 3.3 and 3.4. The percentage difference between the mCT-derived and the physical section-derived measurements, expressed as an average of the 130 total measurements recorded, was 3.52% across the extant sample. As can be seen from the tables, there was no tendency for smaller teeth (e.g., *Ateles paniscus* mean difference = 2.89%) to have more or less percentage difference between measurements than larger teeth (e.g., *Papio ursinus* mean difference = 2.96%). There was no tendency for thick-enameled teeth (e.g., *Homo sapiens* $M^3$ mean difference = 4.66%) to have less measurement difference than thin-enameled teeth (e.g., *Chiropotes satanus* $M_1$ mean difference = 4.71%). Moreover, there was no consistent pattern of mCT measurements being either smaller or larger than those taken on physical sections.

Across the different measurements taken, there is no obvious trend towards thinner regions of enamel being more prone to differences in measurements than thicker areas of the same tooth among the recent primate specimens. Measurements L1, L2, and L3, which represent the linear thickness of lingual enamel from nearer to the cervix to nearer to the cusp, respectively, showed an overall decrease in percent difference, although the same was not true for buccal measurements. Moreover, the increase from

*Table 3.3: Values of measurements and percent differences between physical and mCT sections in recent primate teeth.*

| | *Ateles paniscus* | | | *Cebus apella* | | | *Chiropotes satanus* | | | *Homo sapiens* $M^3$ | | | *Homo sapiens* $M_3$ | | | *Homo sapiens* $dm_2$ | | | *Papio ursinus* | | |
|---|---|---|---|---|---|---|---|---|---|---|---|---|---|---|---|---|---|---|---|---|---|
| Measurement | mCT | Physical | % Diff. | mCT | Physical | % Diff. | mCT | Physical | % Diff. | mCT | Physical | % Diff. | mCT | Physical | % Diff. | mCT | Physical | % Diff. | mCT | Physical | % Diff. |
| b | 12.27 | 12.20 | 0.57% | 7.49 | 7.27 | 3.03% | 5.68 | 5.50 | 3.27% | 29.76 | 30.70 | 3.06% | 39.14 | 40.99 | 4.51% | 27.59 | 28.45 | 3.02% | 65.10 | 65.81 | 1.08% |
| c | 2.72 | 2.69 | 1.12% | 3.67 | 3.57 | 2.80% | 1.42 | 1.32 | 7.58% | 25.70 | 25.54 | 0.63% | 30.29 | 30.57 | 0.92% | 7.65 | 7.83 | 2.30% | 40.45 | 40.78 | 0.81% |
| BCD | 4.25 | 4.19 | 1.43% | 4.64 | 4.55 | 1.98% | 2.88 | 2.74 | 5.11% | 10.27 | 10.87 | 5.52% | 9.38 | 8.87 | 5.75% | 5.65 | 5.90 | 4.24% | 11.83 | 12.68 | 6.70% |
| LCT | 0.22 | 0.21 | 4.76% | 0.57 | 0.57 | 0.00% | 0.16 | 0.16 | 0.00% | 1.94 | 2.03 | 4.43% | 1.68 | 1.60 | 5.00% | 0.22 | 0.21 | 4.76% | n/a | n/a | n/a |
| LOB | 0.24 | 0.24 | 0.00% | 0.48 | 0.48 | 0.00% | 0.15 | 0.14 | 7.14% | 1.45 | 1.49 | 2.68% | 1.54 | 1.62 | 4.94% | 0.44 | 0.42 | 4.76% | 1.23 | 1.27 | 3.15% |
| MOB | 0.35 | 0.33 | 6.06% | 0.40 | 0.39 | 2.56% | 0.21 | 0.19 | 10.53% | 0.90 | 0.89 | 1.12% | 1.47 | 1.55 | 5.16% | 0.36 | 0.35 | 2.86% | 1.79 | 1.86 | 3.76% |
| BOB | 0.29 | 0.28 | 3.57% | 0.45 | 0.46 | 2.17% | 0.09 | 0.09 | 0.00% | 2.29 | 2.34 | 2.14% | 1.65 | 1.81 | 8.84% | 0.39 | 0.39 | 0.00% | 1.44 | 1.44 | 0.00% |
| BCT | n/a | n/a | n/a | 0.56 | 0.55 | 1.82% | n/a | n/a | n/a | 1.98 | 1.98 | n/a | 1.74 | 1.63 | 6.75% | 0.41 | 0.40 | 2.50% | 1.47 | 1.46 | 0.68% |
| L1 | 0.23 | 0.24 | 4.17% | 0.18 | 0.17 | 5.88% | 0.16 | 0.17 | 5.88% | n/a | n/a | n/a | 0.27 | 0.29 | 6.90% | 0.37 | 0.39 | 5.13% | 0.85 | 0.87 | 2.30% |
| L2 | 0.31 | 0.30 | 3.33% | 0.31 | 0.29 | 6.90% | 0.18 | 0.18 | 0.00% | n/a | n/a | n/a | 0.78 | 0.76 | 2.63% | 0.52 | 0.56 | 7.14% | 1.55 | 1.63 | 4.91% |
| L3 | 0.39 | 0.40 | 2.50% | 0.52 | 0.50 | 4.00% | 0.19 | 0.18 | 5.56% | 0.44 | 0.42 | 4.76% | 1.23 | 1.22 | 0.82% | 0.58 | 0.60 | 3.33% | 2.36 | 2.50 | 5.60% |
| B1 | n/a | n/a | n/a | 0.18 | 0.19 | 5.26% | 0.14 | 0.13 | 7.69% | n/a | n/a | n/a | 0.45 | 0.46 | 2.17% | 0.33 | 0.35 | 5.71% | 0.43 | 0.44 | 2.27% |
| B2 | 0.23 | 0.22 | 4.55% | 0.27 | 0.27 | 0.00% | 0.20 | 0.19 | 5.26% | 0.30 | 0.30 | 0.00% | 0.86 | 0.88 | 2.27% | 0.57 | 0.56 | 1.79% | 0.90 | 0.93 | 3.23% |
| B3 | 0.37 | 0.38 | 2.63% | 0.93 | 0.89 | 4.49% | 0.30 | 0.31 | 3.23% | 0.53 | 0.55 | 3.64% | 2.04 | 2.23 | 8.52% | 0.71 | 0.74 | 4.05% | 1.20 | 1.25 | 4.00% |
| Average (Absolute Value) | | | 2.89% | | | 2.92% | | | 4.71% | | | 2.80% | | | 4.66% | | | 3.69% | | | 2.96% |

*Table 3.4: Values of measurements and percent differences between physical and mCT sections in the recent sauropsid teeth.*

| | *Alligator mississipiensis* | | | *Crocodylis palustris* | | |
|---|---|---|---|---|---|---|
| Measurement | mCT | Physical | % Diff. | mCT | Physical | % Diff. |
| 1 | 0.15 | 0.14 | 7.14% | 0.18 | 0.19 | 5.26% |
| 2 | 0.05 | 0.05 | 0.00% | 0.24 | 0.24 | 0.00% |
| 3 | 0.11 | 0.12 | 8.33% | 0.20 | 0.21 | 4.76% |
| 4 | 0.07 | 0.06 | 16.67% | 0.18 | 0.17 | 5.88% |
| 5 | 0.15 | 0.16 | 6.25% | 0.14 | 0.15 | 6.67% |
| 6 | 0.11 | 0.11 | 0.00% | 0.17 | 0.16 | 6.25% |
| 7 | 0.09 | 0.09 | 0.00% | 0.13 | 0.13 | 0.00% |
| 8 | 0.04 | 0.04 | 0.00% | 0.15 | 0.17 | 11.76% |
| 9 | | | | 0.17 | 0.16 | 6.25% |
| 10 | | | | 0.13 | 0.12 | 8.33% |
| Average (Absolute Value) | | | 4.80% | | | 5.52% |

L1 to L3 was not substantial, although samples are not large enough to facilitate statistical comparisons. Area measurements (measurements b and c) tend to have lower percent differences than linear enamel thickness measurements.

Recording distance measurements using known landmarks on the computer screen (i.e., directly on mCT volume models in VoxBlast) did not result in substantially different measurements from those obtained by digitizing printed images (Table 3.5). There is, on average, from 2.60% to 3.50% difference between measurements taken on-screen and those using a digitizing tablet. These differences accord with those between the mCT prints and physical sections, as noted above.

There is a substantial difference between the ability of computer software (e.g., OsiriX, VoxBlast) and the human eye to distinguish enamel from dentine if scans are not

*Table 3.5: Comparison between measurements recorded on-screen using software and those recorded on printed images using a digitizing tablet.*

| | *Homo sapiens* $RM_3$ | | | *Papio ursinus* $LM^2$ | | | *Cebus apella* $LM_2$ | | |
|---|---|---|---|---|---|---|---|---|---|
| Measurement | On-Screen | Digitizer | % Diff. | On-Screen | Digitizer | % Diff. | On-Screen | Digitizer | % Diff. |
| LCT | 1.68 | 1.62 | 3.70% | n/a | n/a | n/a | 0.57 | 0.54 | 5.56% |
| BCT | 1.74 | 1.68 | 3.57% | 1.47 | 1.39 | 5.76% | 0.56 | 0.58 | 3.45% |
| MOB | 1.47 | 1.43 | 2.80% | 1.79 | 1.73 | 3.47% | 0.40 | 0.42 | 4.76% |
| BCD | 9.38 | 9.41 | 0.32% | 11.83 | 11.79 | 0.34% | 4.64 | 4.65 | 0.22% |
| Average (Absolute Value) | | | 2.60% | | | 3.19% | | | 3.50% |

first treated with some segmentation routine or image filters. Figure 3.5 depicts the physical and mCT derived sections of the *Alligator* tooth, in which one can readily differentiate enamel from the underlying dentine. Also depicted is an ROI line through the same tooth, demonstrating that although the very thin enamel (as thin as 40 μm; Table 3.4) on the lingual surface is visible to the eye, the software is unable to distinguish the value of the enamel pixels from those of the dentine using unfiltered scans. This problem becomes important if computer software alone is used to record measurements, such as the volume of the enamel cap. A volume rendering of the *Alligator* tooth is depicted in Figure 3.5; this demonstrates that although enamel is visible to the human eye on the lingual surface of the tooth, software alone (without any tissue segmentation) is incapable of differentiating it from the underlying dentine.

With regard to the mCT images of the fossil teeth (Table 3.6), there is less contrast along the ROI line in the 2.0 Myr-old *Papio robinsoni* molar (Figure 3.4) than among the extant specimens. Nevertheless, the enamel cap was clearly visible on this fossil baboon crown in comparison to the substantially older Karoo fossils. Enamel could barely be distinguished from the underlying dentine in the *Moschops capensis* incisor, and this distinction was accentuated somewhat by their partial physical separation along a post-mortem fissure (Figure 3.4). The *Diademodon tetragonus* tooth crown was a

*Table 3.6: Values of measurements and percent differences between physical and mCT sections in fossil teeth.*

| | *Moschops capensis* | | | *Papio robinsoni* | | |
|---|---|---|---|---|---|---|
| Measurement | mCT | Physical | % Diff. | mCT | Physical | % Diff. |
| 1.00 | 0.32 | 0.33 | 3.03% | | | |
| 2.00 | 0.33 | 0.34 | 2.94% | | | |
| 3.00 | 0.26 | 0.27 | 3.70% | | | |
| 4.00 | 0.27 | 0.28 | 3.57% | | | |
| 5.00 | 0.32 | 0.33 | 3.03% | | | |
| 6.00 | 0.33 | 0.36 | 8.33% | | | |
| 7.00 | 0.32 | 0.33 | 3.03% | | | |
| BCD | | | | 10.13 | 10.01 | 1.20% |
| L1 | | | | 0.63 | 0.61 | 3.28% |
| L2 | | | | 0.59 | 0.63 | 6.35% |
| L3 | | | | 0.63 | 0.60 | 5.00% |
| B1 | | | | 0.42 | 0.40 | 5.00% |
| B2 | | | | 0.82 | 0.84 | 2.38% |
| B3 | | | | 0.92 | 0.91 | 1.10% |
| Average (Absolute Value) | | | 3.95% | | | 3.47% |

homogenous gray across the entire scan; in this case, mCT was incapable of clearly distinguishing enamel from dentine (Figure 3.4).

The 2.0 Myr-old *Papio robinsoni* molar demonstrates that enamel and dentine can be differentiated by mCT in a fossil when the enamel is of moderate thickness (0.5-1.0 mm). The relative inability of mCT to differentiate between enamel and dentine in the *Moschops* tooth, and its total inability to do so in the *Diademodon* tooth, may reflect the comparatively greater degree of fossilization (i.e., re-mineralization) of the enamel (and especially dentine) in these Karoo specimens. A molar attributable to *Homo neanderthalensis* has also been studied, demonstrating that even thin cervical enamel in a fossil tooth may be visualized (Olejniczak and Grine, 2005).

However, geochronological age does not account entirely for differences in the ability of mCT to visualize enamel. The *Diademodon* tooth is approximately 22 Myr younger than the *Moschops* incisor. Despite its relative age, it is possible to visualize the enamel cap of the *Moschops* specimen, whereas it is totally invisible to mCT in *Diademodon*. It is possible that diagenetic alteration, which may be (to some degree)

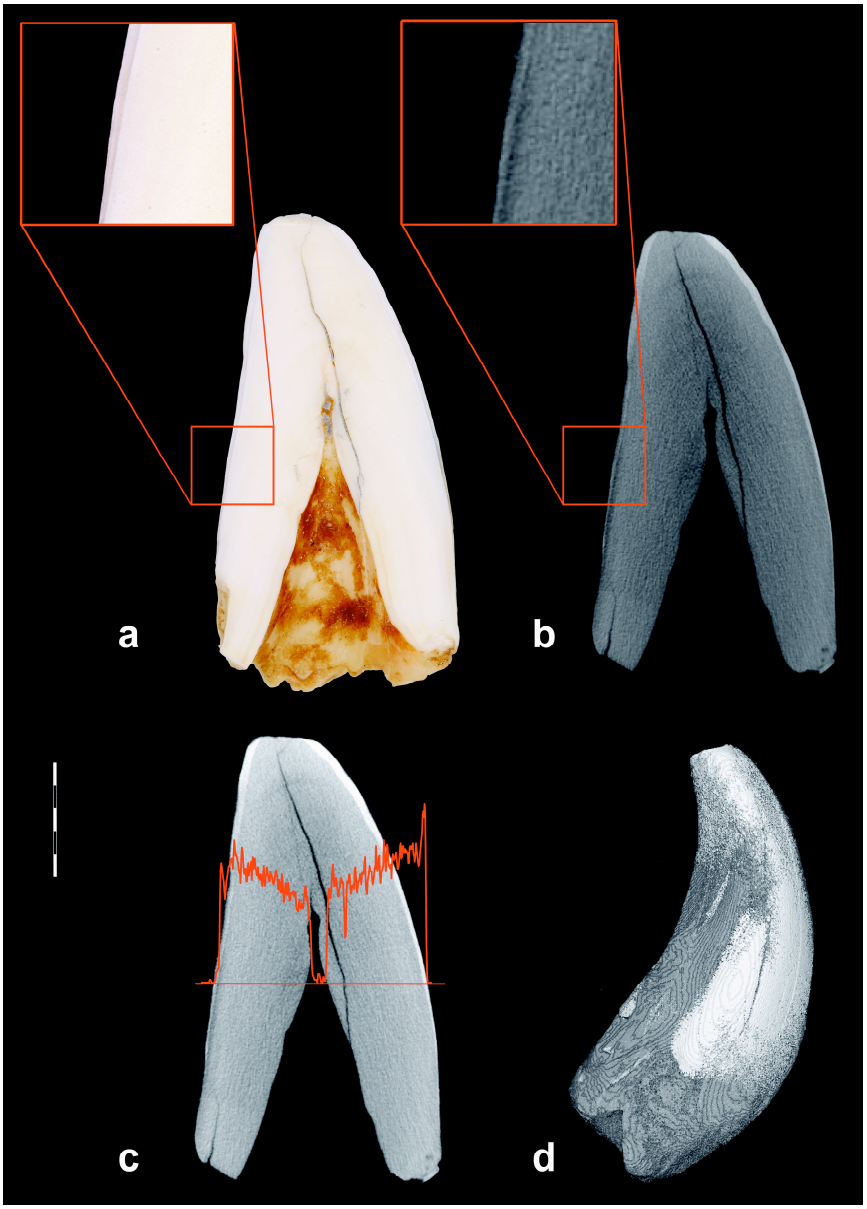


Figure 3.5: Different visualizations of an *Alligator* tooth; scale bar at left is 5 mm and applies to images a-c (image d is not to scale). a) physical section with enlargement (box) showing the lingual enamel, b) mCT derived section through the same plane with enlargement (box) showing that the lingual enamel can be differentiated from the underlying dentine by the human eye, c) an ROI line demonstrating that while the thicker enamel on the labial side of the tooth can be differentiated by segmentation software as a peak in the intensity of the pixel values at the right side of the line, the thin enamel on the lingual surface of the tooth cannot be differentiated (note the absence of any intensity peak at left), d) a 3-D computer volume rendering of the tooth, demonstrating that the enamel on the lingual surface is not distinguished from the underlying dentine by segmentation software.

independent of geological age, may have differentially affected the *Moschops* and *Diademodon* teeth such that the re-mineralized dentine and enamel are of a more homogeneous structural composition in the former. In order to investigate this possibility, these two teeth were subjected to energy dispersive x-ray microanalysis to investigate the composition of the dentine and enamel. The physical section faces of each specimen were examined in a LEO 1550 (LEO/Zeiss) SEM equipped with an EDAX Sapphire Si(Li) detector and Phoenix analyzer (EDAX, Inc.) at 15 kV, zero tilt, a 4.1 take-off, and a working distance of 8.0 mm. The results of these analyses are depicted graphically in Figure 3.6. In the *Moschops* incisor, the dentine and enamel have essentially identical proportions of calcium and phosphorous (i.e., typical calcium phosphate), and they differ only in the amount of silicon present. In the *Diademodon* tooth, while calcium and phosphorous predominate the mineral chemistry of the dentine, the enamel is wholly lacking in phosphorous (it also exhibits some manganese). Thus, the dentine and enamel are dissimilar to one another in chemical composition in both specimens, although diagenetic alteration has not been the same in each. The introduction of silicon into the dentine compartment of the *Moschops* incisor (presumably in the form of quartz) might be expected to affect the mCT X-ray beam attenuation as much as the diagenetic loss of phosphorous from the enamel compartment of the *Diademodon* crown, which suggests an increase in porosity.

This appears to suggest that neither geological age *per se*, nor the differential diagenetic alteration of the chemical composition of the enamel and dentine adequately explain the differences in the ability of mCT to visualize the enamel caps of the two therapsid teeth. Rather, the difference between them in the detection of enamel via mCT

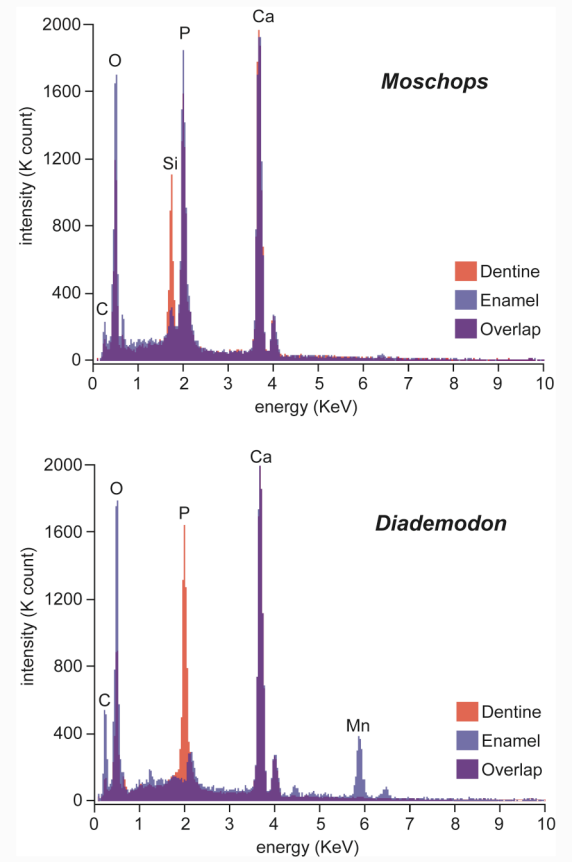


Figure 3.6. Energy dispersive X-ray microanalysis of enamel and dentine in the fossil therapsid teeth. Note that the composition of the enamel and dentine in Moschops are virtually identical except in the higher concentration of phosphorus in the former and the presence of silica in the latter. In *Diademodon*, the enamel and dentine differ in the presence of manganese in the former and the almost total absence of phosphorus in the latter.

seems to be related principally to its absolute thickness. Enamel in *Moschops* is approximately six times thicker than in *Diademodon* (~0.30 mm in *Moschops*, versus ~0.05 mm in *Diademodon*). However, the inability of mCT to resolve the enamel cap in *Moschops* as clearly as in recent and substantially younger fossil teeth may be related to the diagenetic alterations of the dentine in the former.

**Discussion**

The percent differences (mean = 3.52%) reported here between enamel thickness measurements derived from mCT scans and physical sections of recent teeth are significantly improved over standard CT procedures (7-34%: Grine, 1991) and especially over lateral dental radiographs (15-115%: Grine et al., 2001). The percent differences obtained here are comparable to those recorded in studies comparing mCT scans and physical sections of trabecular bone (Müller et al., 1996, 1998). This indicates that mCT is a valuable technique for the non-destructive assessment of enamel thickness in extant primate teeth. Figure 3.1 demonstrates the similarity between mCT and physical sections measured in this study, where only slight differences in the shapes of these sections are apparent.

The percent difference for the measurements reported here apparently does not relate to the thickness of the enamel or the size of a given specimen (Tables 3.3 and 3.4). The differences perhaps are due to human error in the process of measuring the photographs and printed images of the sections, rather than any inherent differences in the comparability of the two sections measured for each tooth or to any other factor having to do with specimen size or thickness.

Although distances measured on the computer screen by way of drawing lines did not differ substantially from those taken by hand using a digitizing tablet (Table 3.5), the mCT technology used here does appear to be limited in its ability to distinguish enamel from dentine when the enamel is very thin and/or these two dental tissues have undergone diagenetic alteration. Thus, the extant sauropsid teeth and the *Ateles* and *Chiropotes* molars examined here demonstrate that mCT is capable of differentiating between

enamel and dentine in recent specimens with thin enamel (as thin as 0.04 mm in the *Alligator* tooth). However, as is evident from the ROI line across the *Alligator* tooth (Figure 3.5), whereas the pixel values clearly differentiate the thicker enamel, the extremely thin lingual enamel (c. 0.04 mm) is not clearly distinguished from the adjacent dentine. Thus, it would appear that absolutely thin enamel (less than ~0.10 mm) is difficult to resolve adequately with mCT based on pixel values alone. Nevertheless, while it is not distinguished from dentine based on pixel values, the thin lingual enamel of the *Alligator* tooth is visible to the human eye in the mCT scans (e.g., Figure 3.5). Since the comparably thin enamel of the *Diademodon* is not visible in terms of pixel values or to the human eye, this problem appears to be exacerbated by diagenetic processes involved in fossilization. It is possible that other mCT systems, such as industrial mCT (e.g., Bush et al., 2004) and synchrotron mCT (Tafforeau, 2004; Olejniczak et al., 2006) may be better suited to imaging very thinly enameled fossils.

The poor visualization of enamel by mCT in the c. 250 Myr-old therapsids compared to the c. 2.0 Myr-old papionin, and the somewhat lower contrast in pixels along the ROI in these specimens compared to recent teeth, suggest that diagenetic alteration, which may differ substantially with geochronological age, may have an impact on visualization based on mCT scanning. On the other hand, the differences in detection by mCT of the enamel caps of the two therapsid specimens suggest that the absolute thickness of enamel (0.30 mm in *Moschops* versus 0.05 mm in *Diademodon*) is a more problematic issue. Finally, the ability of segmentation software to distinguish enamel and dentine differs in some cases from the ability of the human eye to detect the same two tissues. The thin enamel of the *Alligator* tooth (e.g., Figure 3.5) demonstrates that while

the human eye may detect and measure thin enamel on mCT scans, computer-automated tissue segmentation (based on pixel shade values) may fail to do so. Thus, the measurement of enamel thickness based on mCT scans by means of computer software alone may exacerbate the two problems of thin enamel and re-mineralization via diagenesis. In sum, provided that enamel and dentine have not undergone substantial diagenetic remineralization, and that enamel is sufficiently thick, mCT provides accurate images of the tooth crown.

# CHAPTER 4: A COMPARISON OF CT SYSTEMS FOR SCANNING DENTAL MATERIALS

## Introduction

The previous chapter demonstrated that modern mCT techniques facilitate the accurate imaging and measurement of internal dental structures provided that teeth have not undergone severe diagenetic remineralization and that enamel is sufficiently thick. As similar non-destructive studies become commonplace, it is inevitable that several different types and name brands of mCT systems will be utilized in the measurement of recent and fossil primate teeth (e.g., conventional laboratory mCT and synchrotron mCT; Olejniczak et al., 2006). While the accuracy of laboratory mCT (Olejniczak and Grine, 2006) and synchrotron mCT (Tafforeau, 2004) have been independently established by examining physically-produced sections and mCT sections from the same specimens, fundamental differences between techniques have been shown to lead to differences in image quality (Tafforeau, 2004; Olejniczak et al., 2006; Tafforeau et al., 2006), which may result in differences in measurements. In order to explore this artefactual variation, and to determine whether combining measurements from multiple mCT systems in future meta-analyses is justified in light of potential inter-system variance, identical measurements on mCT images of a small sample of teeth scanned with different mCT systems were compared.

In order to explore inter-system variance, five teeth (Table 4.1; Figure 4.1) were scanned using some combination of three different mCT systems: the Scanco μCT 40 (Department of Biomedical Engineering, Stony Brook University), the SkyScan 1172 (Department of Human Evolution, Max Planck Institute for Evolutionary Anthropology), and the ID 19 beam-line (European Synchrotron Radiation Facility). Only one specimen

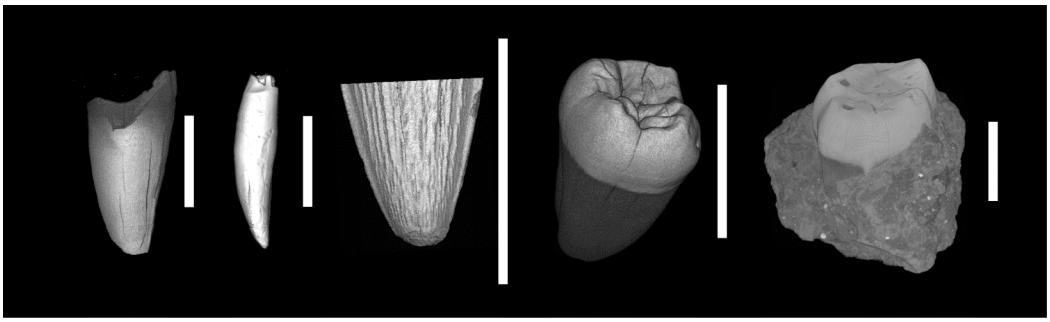

Figure 4.1: Volume models of the five specimens scanned on multiple scanners in this study. From left to right, the specimens are: *Alligator*, *Diademodon*, *Gavial*, *Homo*, and *Pongo*. The scale bar is 1.0 cm in each instance.

(*Alligator mississippiensis*) was available for measurement using the Scanco system, although the *Pongo* tooth was scanned on this system to produce a pixel value plot.

Although the Scanco and SkyScan machines are similar (with the exception of a higher energy used in producing X-rays by the SkyScan machine), the synchrotron facility has several fundamental differences. These differences are thoroughly recounted by Tafforeau et al. (2006), and they are briefly summarized here. First, the phenomenon of "beam hardening" is greatly reduced using synchrotron microtomography. Beam hardening is manifest as a blurring of tissue boundaries, and is caused by the differential absorption of X-rays from various parts of the polychromatic X-ray spectrum. Unlike standard laboratory mCT machines, the synchrotron facility produces monochromatic X-rays, effectively eliminating beam hardening. A second difference is that synchrotron mCT is more effective at detecting edges in diagenetically remineralized materials (e.g., the enamel-dentine junction of a fossil tooth) through the use of phase contrast techniques. Standard absorption techniques may not produce images in which the difference between enamel and dentine are detectible (see also Chapter 3, above). Phase contrast, which is available only using synchrotron mCT, relies on long distances

*Table 4.1: Specimens scanned by multiple mCT systems.*

| Taxon | Tooth Type | Notes |
|---|---|---|
| *Pongo pygmaeus* | Maxillary Molar | ca. 130 Kya |
| *Homo sapiens* | Mandibular Molar | Recent |
| *Alligator mississippiensis* | Caniniform Tooth | Recent |
| *Diademodon tetragonus* | Molariform Tooth | ca. 180 Mya |
| *Gavial* | Caniniform Tooth | Recent |

between the X-ray source and the object scanned (i.e., 145 m on the ID-19 beamline) and long distances between the object being scanned and the detector (i.e., 0.5 m on the ID-19 beamline). These long distances, combined with a high-resolution detector, allow for the edges of different tissues to be located based on X-ray interference patterns that are not detected using standard absorption methods. These edges may be superimposed onto the absorption scan, and two tissues with nearly the same density may then be identified (Tafforeau et al., 2006).

**Materials and Methods**

A tooth-specific set of measurements was recorded on each of the image stacks from the different mCT systems, following the tooth-specific protocol described for the sauropsid teeth measured in Chapter 3 of this dissertation. The specific linear measurement locations for each tooth appear in Table 4.2. Measurements were recorded on a single area of each tooth, and included the volume, linear thickness (in three locations), and surface area of that area or section of the tooth (or some combination of these measures). In the case of he *Diademodon* tooth, root dentine was measured in lieu of enamel. All measurements were collected using OsiriX (v1.6, Rosset et al., 2004) and VoxBlast (Vaytek, Inc.) software. The pixel value histogram of each image stack was also recorded to compare the locations of peaks and troughs representing enamel, dentine,

*Table 4.2: Definitions of the three linear measurements (L1-L3).*

| Measurement | Definition |
|---|---|
| *Alligator* L1 | Length of the entire tooth |
| *Alligator* L2 | Distance between apical-most points at the tooth base |
| *Alligator* L3 | Width at mid-point of pulp chamber |
| *Homo* L1 | Length |
| *Homo* L2 | Breadth |
| *Homo* L3 | Buccal enamel cusp tip distance |
| *Gavial* L1 | Circumference at 1 mm apical to cusp tip |
| *Gavial* L2 | Circumference at 2 mm apical to cusp tip |
| *Gavial* L3 | Circumference at 3 mm apical to cusp tip |
| *Diademodon* L1* | Length |
| *Diademodon* L2* | Breadth at 1/3 length apical to cusp tip |
| *Diademodon* L3* | Breadth at 2/3 length apical to cusp tip |
| *Pongo* L1 | Length |
| *Pongo* L2 | Breadth |
| *Pongo* L3 | Distance between two buccal cusp tips |

and background noise, allowing comparisons of the relative ease of tissue segmentation in images recorded using the different mCT systems. The thickness of slices and pixel dimensions were kept constant (or as close to equal between systems as possible) in order to isolate measurement variation due to machine differences rather than voxel dimension.

**Results**

The measurements recorded in this study are reported in Table 4.3, and the average percent differences between systems for each measurement type are reported in Table 4.4. Results indicate that measurements taken on all three systems appear to be comparable (less than 3.0% different between machines in all cases). Volumes are the most stable measurements, with the lowest percentage difference among systems. Linear measurements and surface areas both show between 2% and 3% measurement differences; unlike volumes, these measurement types require human decisions about the locations of landmarks, potentially introducing measurement error and increasing apparent percentage differences.

Despite the relative similarity of measurements across systems, there is a notably sharper quality of images produced by synchrotron scanning, due in part to the

*Table 4.3: Results of measurements of scans recorded using different systems.*

| | | Volume | Surface Area | Linear 1 | Linear 2 | Linear 3 |
|---|---|---|---|---|---|---|
| | | mm^3 | mm^2 | mm | mm | mm |
| *Alligator* | Scanco | 51.54 | 498.94 | 22.56 | 10.59 | 3.49 |
| | Skyscan | 51.32 | 499.60 | 22.74 | 10.63 | 3.47 |
| | Synchrotron | 51.57 | 501.79 | 23.63 | 10.48 | 3.51 |
| *Homo* | Scanco | n/a | n/a | n/a | n/a | n/a |
| | Skyscan | 195.97 | 433.52 | 10.48 | 9.21 | 5.00 |
| | Synchrotron | 196.09 | 435.84 | 10.11 | 9.45 | 4.98 |
| *Gavial* | Scanco | n/a | n/a | n/a | n/a | n/a |
| | Skyscan | n/a | n/a | 3.77 | 6.47 | 9.23 |
| | Synchrotron | n/a | n/a | 3.96 | 6.98 | 9.94 |
| *Diademodon* | Scanco | n/a | n/a | n/a | n/a | n/a |
| | Skyscan | 249.90 | 258.30 | 20.45 | 4.73 | 5.43 |
| | Synchrotron | 255.46 | 276.69 | 21.39 | 4.66 | 5.38 |
| *Pongo* | Scanco | n/a | n/a | n/a | n/a | n/a |
| | Skyscan | 604.59 | 875.15 | 7.53 | 7.30 | 5.36 |
| | Synchrotron | 608.54 | 881.79 | 7.73 | 7.35 | 5.25 |

*Table 4.4: The percent difference between scanners for each measurement group.*

| Measurement Group | SkyScan v. Scanco | SkyScan v. Synchrotron | ScanCo v. Synchrotron |
|---|---|---|---|
| Linear % Difference | 0.58% | 2.98% | 2.05% |
| Surface Area % Difference | 0.43% | 2.09% | 0.57% |
| Volume % Difference | 0.13% | 0.84% | 0.07% |
| Mean % Difference | 0.46% | 2.43% | 1.36% |

monochromatic beam used in this technique, whereby images are produced with fewer artefacts and with more distinct tissues (e.g., Figure 4.2). Pixel value histograms demonstrate that the synchrotron produces more homogenous tissue groups as well (a comprehensive discussion of pixel value histograms appears in Chapter 5 of this document). Figure 4.3 depicts the three-dimensional pixel value histograms for the same specimen (*Pongo*) produced by all three mCT scanners (before any attempt at tissue segmentation); the same histogram pattern was identified in all of the specimens examined. The SkyScan system's histogram shows only a faint separation of the enamel from the dentine; the enamel appears as a slight "hump" in the curve at approximately pixel value 130. The Scanco system's histogram shows no separation between enamel and dentine. The synchrotron, however, has produced a separate peak of enamel pixels, and even shows a slight difference (in the form of two distinct peaks) between dentine and the surrounding matrix and fossilized maxilla.

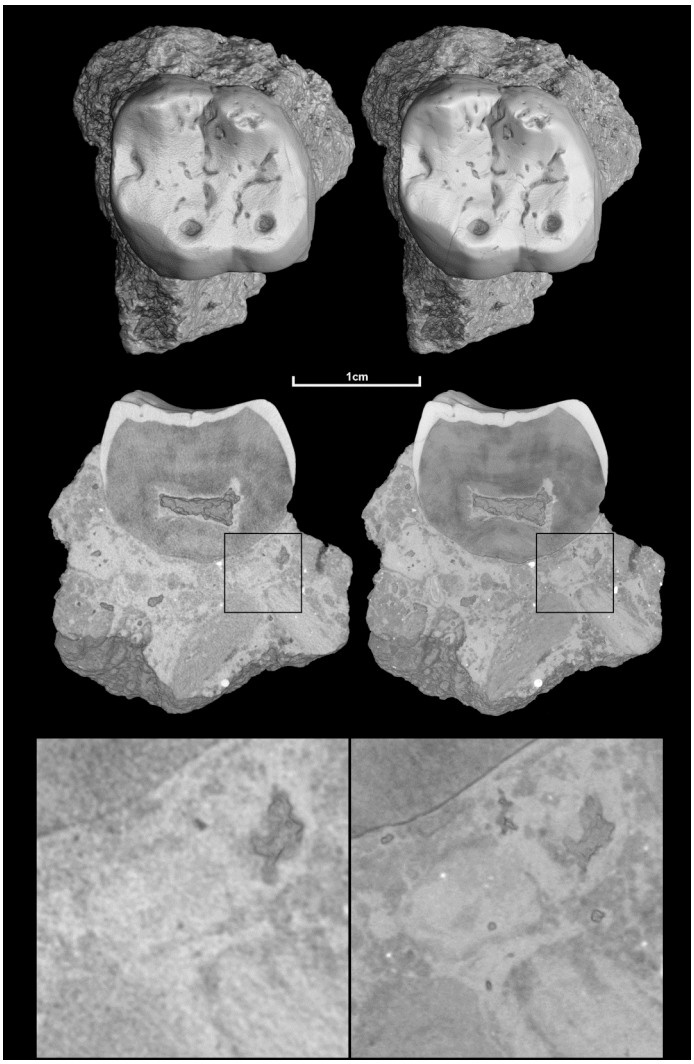


Figure 4.2: Comparison of synchrotron mCT (right) and laboratory mCT (mCT) volume models and cross-sections. The synchrotron model has fewer occlusal artefacts, and in cross-section the synchrotron images appear shaper, of approximately the same quality as a histological section. The laboratory mCT section appears more pixilated and with less distinct features despite being scanned at the same pixel resolution and slice thickness. This figure is reproduced courtesy of Paul Tafforeau.

## Discussion

Having clearly separated tissues based on pixel values expedites the tedious process of tissue segmentation, in which the unique tissues in each image stack are rendered homogenous in order to facilitate accurate measurement. The synchrotron

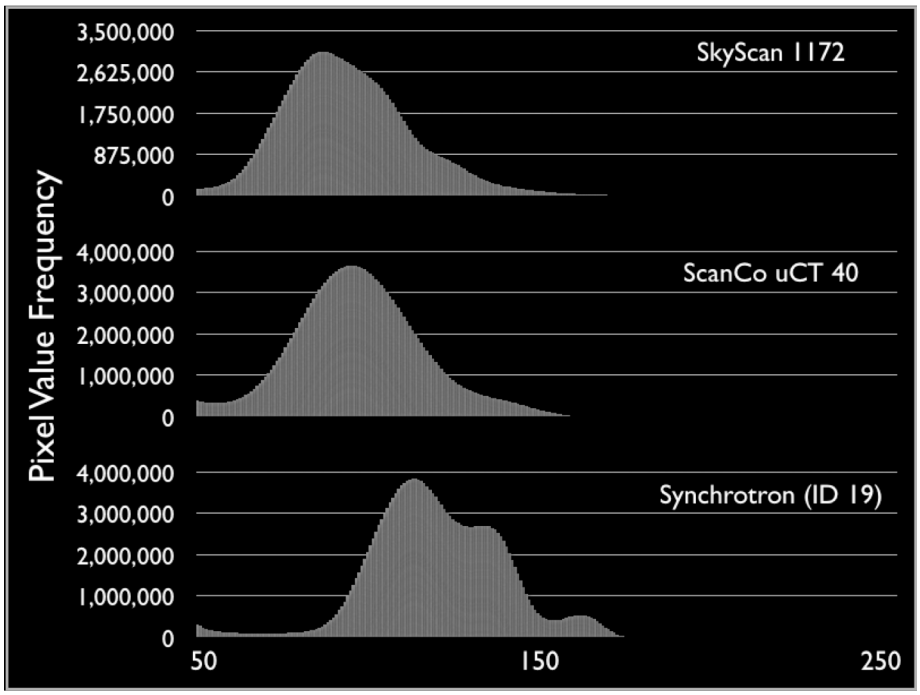


Figure 4.3: Pixel value histograms of the *Pongo* specimen from each of the three systems on which it was scanned. The numbers at the bottom of the plot are the pixel value (values below 50 have been eliminated to remove background noise pixels from actual biological tissues). The SkyScan system histogram shows a slight break at the right of the distribution, where enamel is separated from dentine, matrix, and maxilla. The Scanco system histogram does not show any discrimination between tissues. The synchrotron shows a separate peak for enamel, as well as two distinct peaks separating dentine from the surrounding matrix and maxilla. Because of the discrepancy in underlying pixel values, the synchrotron image stack is much easier to segment into unique tissues for the purpose of recording measurements.

clearly produces the cleanest images prior to segmentation, making this method of scanning superior to the laboratory scanners. Moreover, the synchrotron is capable of imaging fossilized teeth that the standard laboratory scanners would not be able to visualize (Tafforeau et al., 2006). Nonetheless, when identical segmenting techniques were applied to all of the image stacks, accurate measurements may be derived from all systems, as demonstrated by the percentage differences between measurements recorded on each system (Table 4.3). Combining measurements of teeth from multiple mCT

systems presupposes that measurements from each system are comparable, and the research presented here indicates that this is the case (within 3%).

# CHAPTER 5: PRE-ANALYSIS IMAGE PREPARATION

**Image Noise, Segmentation, and Filtering**

Images derived via mCT scanning often have background noise and pixels with values other than the tissue (or space) they are meant to represent (Figure 5.1). Background noise in digital images is roughly analogous to the speckling sometimes manifest in standard photography (i.e., luminance noise). Dental images obtained via mCT scanning have the background noise typically associated with medical imaging, but there is also occasionally a bridge of "false dentine" filling the concavities at the enamel surface between cusp tips (apparent at the enamel surface in Figure 5.1). Moreover, the specimen tube containing the specimen being scanned is apparent in the resultant images from some scanners (including the ScanCo μCT 40, ScanCo Medical, Switzerland, one of the scanners used to derive data for this study). A large literature outside the scope of this text describes the physics of medical imaging and the causes of background noise and related image phenomena; the interested reader is directed to the volume by Hendee and Ritenour (2002).

The process of tissue measurement in mCT scans requires that each tissue is approximately homogenous in its pixel values, or at least that no two tissues have overlapping ranges of pixel values; it is also critical that air, both in the background of the image and within any biological spaces (e.g., the pulp cavity of a molar), is relatively uniform in pixel value. That is to say, background noise should be eliminated in order to take accurate measurements of digital images, and also in order to divide the images into their constituent tissues (e.g., enamel and dentine). The process of converting original, sometimes noisy images derived from mCT scanning into clean images where each tissue of interest is represented by a homogenous range of pixel values is termed *segmentation*,

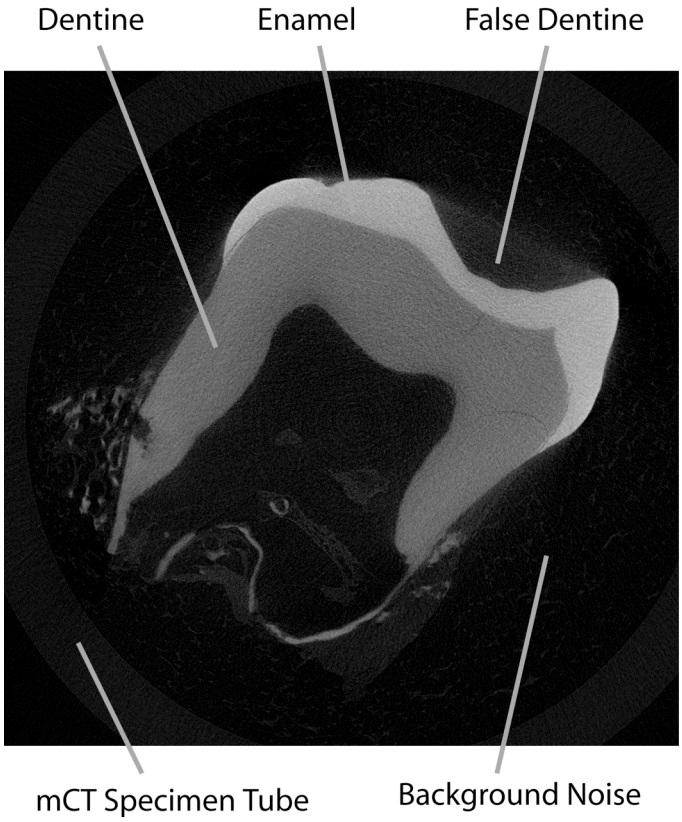


Figure 5.1: A single image from a mCT-derived image stack of a *Cebus apella* molar. The enamel and dentine are indicated, as are three image phenomena pertinent to the study of mCT images of teeth: typical mCT background noise, the tube that holds the specimen in the mCT gantry, and the "false dentine" layer manifest at the outer enamel surface (so-called because these pixels sometimes take the same value as dentine pixels, representing a challenge for dental image segmentation).

and typically involves the application of digital filters to each image in the stack. Castleman (1996) defines image segmentation as the process "that partitions a digital image into disjoint (non-overlapping) regions." In images of teeth, the objects of interest are enamel and dentine.

Several approaches to image segmentation exist, and they can be roughly divided into three categories (following Castleman, 1996): 1) the region approach, 2) the boundary approach, and 3) the edge-detection approach. The region approach examines each pixel in an image, and attempts to classify that pixel as part of a larger group, or *region* (e.g., a white pixel within the enamel cap would be classified as enamel because

of the nature of the surrounding pixels, and its own pixel value). The boundary approach attempts to locate the boundaries between different regions (e.g., the enamel-dentine junction or the enamel-air interface). The edge-detection approach attempts to locate the edges of homogenous tissue groups, and then to link these edge pixels together in order to create a continuous border surrounding the object.

The simplest type of segmentation, called *threshold segmentation*, is a regional approach. In thresholding a digital image, the pixel values are used in order to determine the values typically associated with certain objects in the image (e.g., the value of enamel pixels in an 8-bit grayscale image may be between 200 and 255, while dentine pixels have values between 100 and 200). With this knowledge in mind, one can simply eliminate all of the pixels with values below 200 from the image (i.e., set their pixel values to zero causing them to be black), and one is left with an image of only the enamel (Figure 5.2). Unfortunately, in many cases the boundary between the pixel values of certain objects is blurred, such that some pixels representing dentine have values in the range associated with enamel, and *vice versa* (Figure 5.2, bottom pane). Background noise also poses a problem, as it is often of the same pixel values as dentine. If background noise and pixel value overlap between tissues is not substantial, a simple neighborhood-based noise removal algorithm may clean the image sufficiently for measurement.

Thus, while threshold segmentation is an elegant solution to separating tissues in mCT images of teeth, the tissues themselves must be made to be homogenous in pixel values before thresholding. Experimentation with several types of image filters (e.g., those presented by Pitas, 1993) revealed that a significant portion of background noise

Original image

Image After Threshold Segmentation

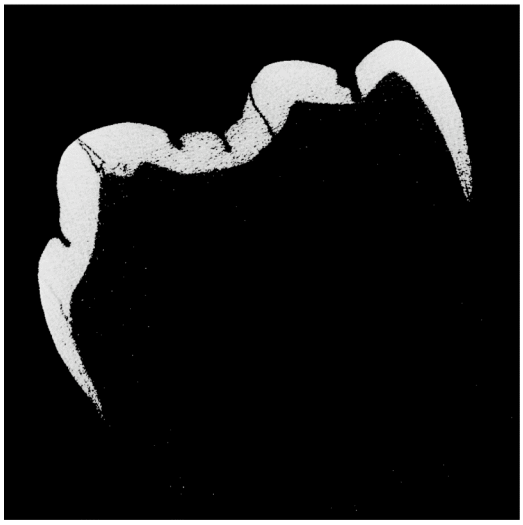

Figure 5.2: Comparison of an original mCT image of a *Symphalangus syndactylus* lower second molar and the same image after threshold segmentation. While threshold segmentation identifies nearly all of the pixels correctly, there are some holes in the thresholded enamel cap, especially near the cervices, and there are some pixels in the area that was only occupied by dentine. Threshold segmentation is a powerful tool for extracting tissues, but those tissues must be made to be homogenous and of a unique pixel value range before threshold segmentation can be completely successful.

may be eliminated, and that enamel pixels may be made to be more distinct from dentine pixels, by passing a median filter over the images. The median filter is a reliable method of cleansing images of background noise so long as less than 50% of the pixels represent image noise (Pitas, 1993). A simple median filter works by examining each pixel in an image in turn, and replacing that pixel with the median pixel value of its 8-neighbor group (Figure 5.3). This has the effect of replacing outlying pixel values (e.g., single pixels with very high values resident in the dentine) with a more likely representation of their actual value, as defined by their neighbors. The median filter does, however, have a significant drawback to its use in the study of mCT images of teeth: the filter lightens black (or very dark) pixels that border lighter pixels (such as the enamel air interface) thereby increasing the apparent number of pixels representing the brighter structure (Figure 5.4). The median filter also fails to recognize large regions of tissues that may have erroneously low or high pixel values; the occlusal basin of some teeth in mCT scans appears as a uniformly dark area, the color of dentine, although it is actually representative of enamel (or in some cases, air). The median filter thus must be supplemented by another approach, such as edge detection, in order to be of use in cleansing dental mCT images of their noise, and the accuracy of the median filter must be assessed in light of its potential to obfuscate tissue boundaries.

Another method of image segmentation, which is adept at locating edges, is a diffusion filter. There are several types of diffusion filters (e.g., inhomogeneous diffusion, biased diffusion, anisotropic diffusion), but they all have two key elements in common: the filters 1) preserve information about the location of the edges of objects, while 2) smoothing the regions contained within those edges (Jähne, 1997). Edge-

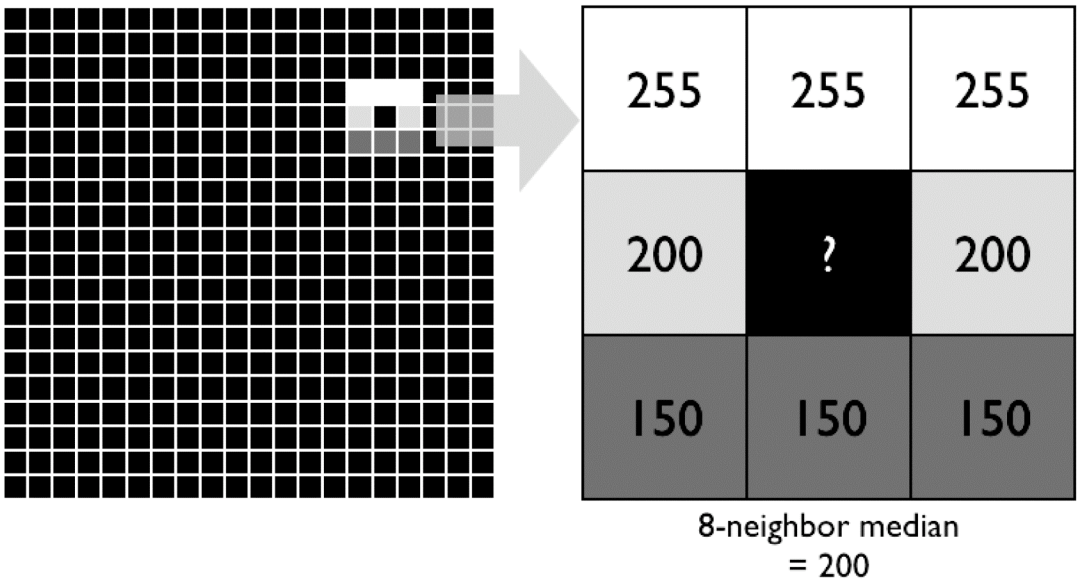


Figure 5.3: Explanation of the median filter. In the image at left (borders have been drawn between the pixels for illustrative purposes), the pixel in the center of those of varying shades of gray is the object of interest; this area of the image has been expanded to the right. The pixel in question will be replaced by the median of the surrounding eight pixels (its 8-neighborhood), which in this case is 200. Thus the previously black pixel will be replaced by a relatively bright shade of gray; the median filter has great power in its ability to correct single-pixel outliers due to image noise, as this example illustrates.

detection is a relatively simple process in digital images of teeth (especially of the enamel cap) when background noise and inhomogeneous tissue pixel values are randomly dispersed, and it follows a straightforward process: the image is examined pixel-by-pixel until an edge is discovered (e.g., a white pixel that is partially surrounded by black pixels must represent enamel at the air-enamel interface), then that edge is followed until the original pixel is arrived at again, thereby demarcating the edges of the object of interest.

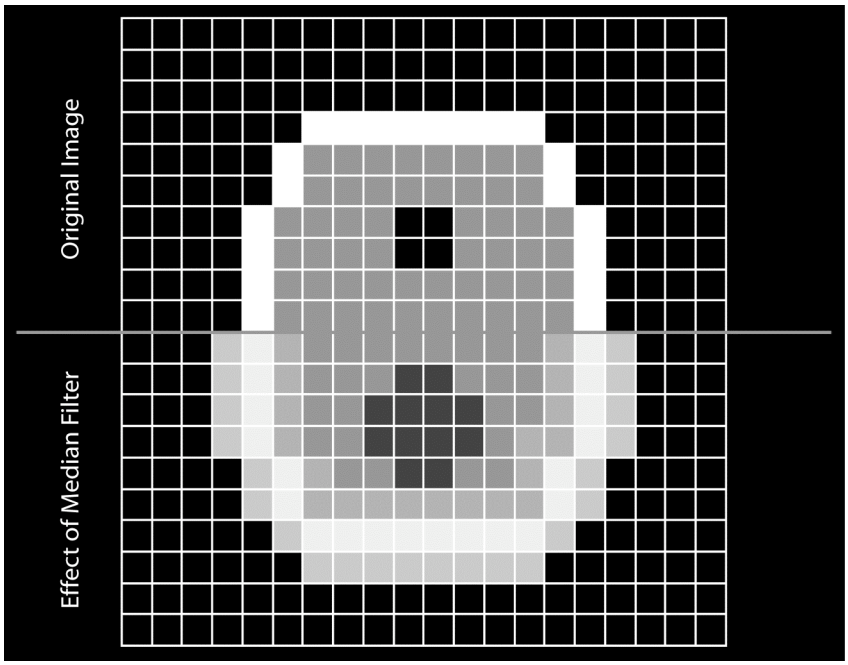


Figure 5.4: Hypothetical impact of applying a median filter to a transverse mCT image of a molar cross-section. The half of the image on top shows the lateral enamel, in white, the dentine as gray, and a bit of the pulp chamber in black. The bottom half of the image is a mirror image of the top half, but showing the effect that a median filter may have on the image. The white enamel pixels are blurred into the surrounding air, creating a gray layer surrounding the tooth; the small pulp chamber has also been closed by blurring of the dentine pixels. The result of the median filter's blurring of brighter pixels into the darker surroundings may render measurements taken on filtered images inaccurate in that brighter areas are exaggerated.

The process then reiterates, storing the information about the location of the edges it has previously discovered, until the edges of all of the objects in the image are discovered.

After the edge-discovery phase, a diffusion filter then smoothes the area contained within each boundary. The smoothing process is unique to each type of diffusion filter, such that an inhomogeneous diffusion filter, for instance, smooth objects more at the center of the image and less as an edge is approached. The anisotropic diffusion filter, however, smoothes an object without regard to the direction of the edges, but has the negative effect of potentially obscuring sharp edges as the edge may also be the subject

of some smoothing. Because the enamel of mCT scans of teeth is characterized sometimes by beam hardening artifacts, in which the outer enamel pixels are brighter than the inner enamel pixels, the anisotropic diffusion is more appropriate than the inhomogeneous diffusion filter in order to remedy the overall inconsistency in pixel values near the edge of the object. Nonetheless, like the median filter, the impact of blurring the edges of bright objects into the surrounding dark pixels must be measured in order to assess the impact of this filtration technique on measurement accuracy. Because it is necessary to homogenize dental tissues prior to automated measurement of volumes and surface areas, an experiment was conducted to determine whether the two proposed image filtering techniques (median filter and anisotropic diffusion filter) significantly impact measurements of dental mCT images.

**An Experiment to Determine the Impact of Median and Anisotropic Diffusion Filters on Measurements**

In order to assess whether the application of the median filter, the anisotropic diffusion filter, or the combination of both filters has an impact on measurements of digital images of teeth, nine individual mCT images were examined, including primates with both thick and thin enamel (Figure 5.5). Each of the images was stored as an uncompressed, cropped, 8-bit grayscale, tagged image file format picture (TIF); 8-bit images contain pixels that may be one of 256 different values (a value of zero indicates a black pixel, a value of 255 indicates a white pixel, and values in between indicate some shade of gray). The relative scale of each image in this experiment compared to the other images is not relevant to the measurements (the pixels are of known dimension in each

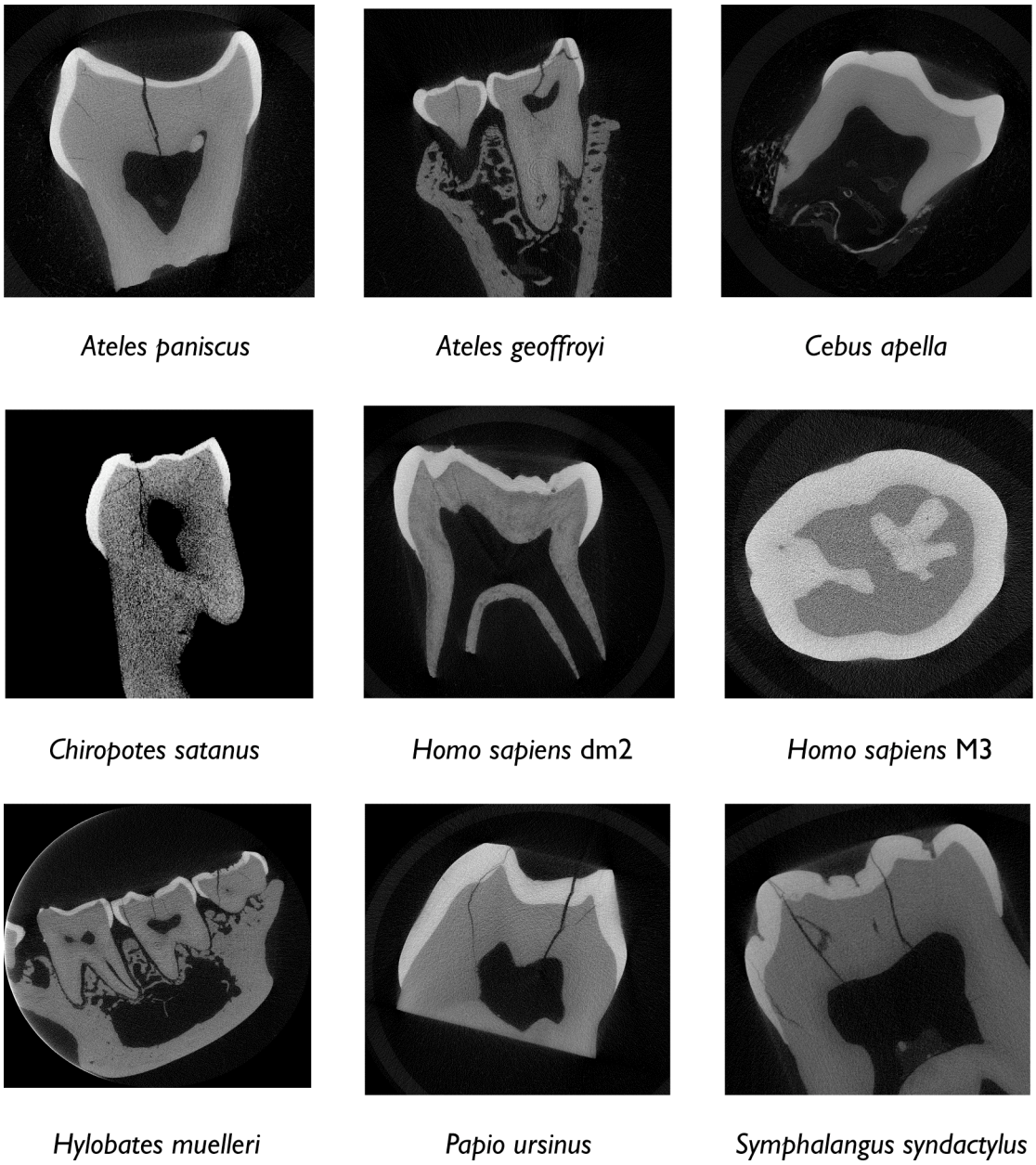


Figure 5.5: The sample of primate molar mCT scans used in the image filtration experiment. The sample represents a variety of primate species, as well as a variety of scan orientations (e.g., the permanent mandibular Homo sapiens third molar is scanned in a transverse orientation, several individual teeth were scanned in a paracoronal orientation, and two images represent sections through mandibles containing multiple molars).

image). To make the figures more clear, images are shown in which all the teeth of roughly equal size rather than at an actual comparative scale.

A uniform set of measurements for each image was recorded, including the bi-cervical diameter, the thickness of enamel at each cusp tip (although no attempt was made to resection the image stacks in order to locate ideal planes of section and actual dentine horn tips, as re-orienting image stacks causes the resultant images to consist of interpolated pixel values, which would introduce a potential source of error into measurements), and the total area of enamel (based on thresholded pixel values). Cuspal enamel thickness measurements were made on the left-most cusp first, then on the next cusp to the right, and so forth, as specific planes of section were not located prior to measurements. Each image's pixel value histogram was also recorded. For images where multiple teeth are present, the measurements were recorded in all teeth (although the enamel area is the entire area of enamel within the image). In the transversely oriented human third permanent molar, the area of enamel, the maximum mesio-distal length of both enamel and dentine, and the maximum bucco-lingual breadth of both enamel and dentine were recorded. All of the measurements were recorded digitally with the aid of software (NIH ImageJ); differences between measurements from printed images using a digitizing tablet and those taken directly on-screen have been found to be insignificant (Olejniczak and Grine, 2006).

Each image was then subjected to a median filter (the median pixel value was calculated from a 3 x 3 pixel neighborhood) and the measurements were re-recorded. The median filter was programmed in the Xcode environment (v. 2.0) using the Objective-C programming language; the source code for this method appears as

Appendix A. The original images were then subjected to coherence-enhancing anisotropic diffusion (available as a filter in Adobe PhotoShop CS), and the measurements were again recorded. Finally, the original images were subjected to both the median filter and then the anisotropic diffusion filter, and the measurements were recorded again. All measurements were recorded three times, and the average of the three trials was taken to be the actual measurement.

The percent difference between measurements recorded before and after filtering was examined in order to assess the impact of these filters on measurements. Finally, the pixel value histograms of these images were qualitatively compared in order to determine the impact of the filters on the overall tissue homogeneity. Figure 5.6 depicts the original image, the image after median filtering, the image after anisotropic diffusion, and the image after both median and anisotropic diffusion filtering in one of the specimens in order to illustrate the visual effect of applying the filters.

Results of the measurements are reported in Tables 5.1-5.9. Results indicate that there is little difference between linear measurements of enamel thickness or the bi-cervical diameter (recorded using the line tool in NIH ImageJ). Moreover, there is no observable pattern that might suggest a directional difference between median or anisotropic images and the original image. This indicates that the measurement difference is due in part to error introduced through manually recorded on-screen measurements rather than any inherent property of the filtered images.

It is of considerable importance for automated measurements of dental tissues that the area of enamel (recorded by image thresholding) does not deviate substantially from the result obtained using the original images. This suggests that the filtering process,

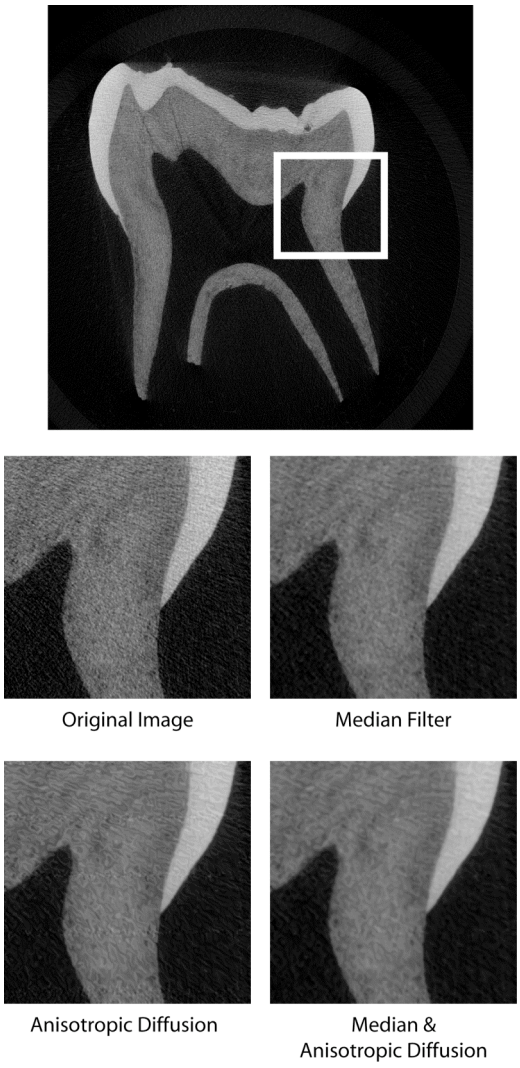


Figure 5.6: Examples of the filters used in this study; the tooth depicted is a *Homo sapiens* lower second deciduous molar. The image above shows the entire original image and the area that has been enlarged below. The enlargements below show the original image, the image after median filtration, the image after anisotropic diffusion, and the image after both median and anisotropic diffusion filters have been applied.

while rendering images easier to measure, does not impact automated measurements of cross-sectional areas (and therefore volumes). The lack of measurement differences in spite of the aforementioned edge blurring caused by both the median and anisotropic diffusion filters may be due to the blurred pixels at the borders having very low pixel

*Table 5.1: Measurements of filtered images of the Ateles paniscus molar.*

| | Oiginal Image | Median Filter | % Diff. | Anisotropic Diffusion | % Diff. | Both Filters | % Diff. |
|---|---|---|---|---|---|---|---|
| Enamel Area (mm^2) | 55.7 | 55.7 | 0.00% | 55.7 | 0.00% | 55.7 | 0.00% |
| Bicervical Diameter (mm) | 4.17 | 4.12 | -1.20% | 4.17 | 0.00% | 4.17 | 0.00% |
| Cusp Thickness 1 (mm) | 0.27 | 0.28 | 3.70% | 0.27 | 0.00% | 0.28 | 3.70% |
| Cusp Thickness 2 (mm) | 0.29 | 0.3 | 3.45% | 0.29 | 0.00% | 0.29 | 0.00% |

*Table 5.2: Measurements of filtered images of the Ateles geoffroyi molars.*

| | Oiginal Image | Median Filter | % Diff. | Anisotropic Diffusion | % Diff. | Both Filters | % Diff. |
|---|---|---|---|---|---|---|---|
| Enamel Area (mm^2) | 163.8 | 163.8 | 0.00% | 163.8 | 0.00% | 163.8 | 0.00% |
| Bicervical Diameter 1 (mm) | 1.67 | 1.66 | -0.60% | 1.67 | 0.00% | 1.67 | 0.00% |
| Bicervical Diameter 2 (mm) | 3.38 | 3.38 | 0.00% | 3.39 | 0.30% | 3.39 | 0.30% |
| Cusp Thickness 1 (mm) | 0.47 | 0.46 | -2.13% | 0.48 | 2.13% | 0.48 | 2.13% |
| Cusp Thickness 2 (mm) | 0.26 | 0.26 | 0.00% | 0.26 | 0.00% | 0.26 | 0.00% |
| Cusp Thickness 3 (mm) | 0.21 | 0.21 | 0.00% | 0.21 | 0.00% | 0.21 | 0.00% |

*Table 5.3: Measurements of filtered images of the Cebus apella molar.*

| | Oiginal Image | Median Filter | % Diff. | Anisotropic Diffusion | % Diff. | Both Filters | % Diff. |
|---|---|---|---|---|---|---|---|
| Enamel Area (mm^2) | 70.9 | 70.8 | -0.14% | 70.8 | -0.14% | 70.8 | -0.14% |
| Bicervical Diameter (mm) | 4.45 | 4.45 | 0.00% | 4.47 | 0.45% | 4.47 | 0.45% |
| Cusp Thickness 1 (mm) | 0.58 | 0.57 | -1.72% | 0.58 | 0.00% | 0.59 | 1.72% |
| Cusp Thickness 2 (mm) | 0.91 | 0.91 | 0.00% | 0.91 | 0.00% | 0.91 | 0.00% |

*Table 5.4 Measurements of filtered images of the Chiropotes satanus molar.*

| | Oiginal Image | Median Filter | % Diff. | Anisotropic Diffusion | % Diff. | Both Filters | % Diff. |
|---|---|---|---|---|---|---|---|
| Enamel Area (mm^2) | 53.1 | 53.1 | 0.00% | 53.1 | 0.00% | 53.1 | 0.00% |
| Bicervical Diameter (mm) | 3.16 | 3.17 | 0.32% | 3.16 | 0.00% | 3.17 | 0.32% |
| Cusp Thickness 1 (mm) | 0.31 | 0.30 | -3.23% | 0.31 | 0.00% | 0.30 | -3.23% |
| Cusp Thickness 2 (mm) | 0.19 | 0.19 | 0.00% | 0.19 | 0.00% | 0.19 | 0.00% |

*Table 5.5: Measurements of filtered images of the Homo sapiens deciduous molar.*

| | Oiginal Image | Median Filter | % Diff. | Anisotropic Diffusion | % Diff. | Both Filters | % Diff. |
|---|---|---|---|---|---|---|---|
| Enamel Area (mm^2) | 161.4 | 161.4 | 0.00% | 161.4 | 0.00% | 161.4 | 0.00% |
| Bicervical Diameter (mm) | 4.17 | 4.17 | 0.00% | 4.17 | 0.00% | 4.17 | 0.00% |
| Cusp Thickness 1 (mm) | 0.63 | 0.64 | 1.59% | 0.64 | 1.59% | 0.64 | 1.59% |
| Cusp Thickness 2 (mm) | 0.73 | 0.74 | 1.37% | 0.74 | 1.37% | 0.74 | 1.37% |

*Table 5.6: Measurements of filtered images of the Homo sapiens permanent molar.*

| | Oiginal Image | Median Filter | % Diff. | Anisotropic Diffusion | % Diff. | Both Filters | % Diff. |
|---|---|---|---|---|---|---|---|
| Enamel Area (mm^2) | 232.3 | 232.3 | 0.00% | 232.3 | 0.00% | 232.3 | 0.00% |
| Enamel Max Length (mm) | 13.11 | 13.11 | 0.00% | 13.11 | 0.00% | 13.11 | 0.00% |
| Dentine Max Length (mm) | 9.81 | 9.81 | 0.00% | 9.81 | 0.00% | 9.81 | 0.00% |
| Enamel Max Breadth (mm) | 10.78 | 10.78 | 0.00% | 10.78 | 0.00% | 10.78 | 0.00% |
| Dentine Max Breadth (mm) | 7.31 | 7.31 | 0.00% | 7.31 | 0.00% | 7.31 | 0.00% |

*Table 5.7: Measurements of filtered images of the Hylobates muelleri molar.*

| | Oiginal Image | Median Filter | % Diff. | Anisotropic Diffusion | % Diff. | Both Filters | % Diff. |
|---|---|---|---|---|---|---|---|
| Enamel Area (mm^2) | 419.4 | 419.4 | 0.00% | 419.4 | 0.00% | 419.4 | 0.00% |
| Bicervical Diameter 1 (mm) | 4.43 | 4.43 | 0.00% | 4.43 | 0.00% | 4.43 | 0.00% |
| Bicervical Diameter 2 (mm) | 4.64 | 4.65 | 0.22% | 4.64 | 0.00% | 4.65 | 0.22% |
| Bicervical Diameter 3 (mm) | 4.07 | 4.07 | 0.00% | 4.07 | 0.00% | 4.07 | 0.00% |
| Cusp Thickness 1 (mm) | 0.48 | 0.47 | -2.08% | 0.49 | 2.08% | 0.47 | -2.08% |
| Cusp Thickness 2 (mm) | 0.40 | 0.41 | 2.50% | 0.40 | 0.00% | 0.41 | 2.50% |
| Cusp Thickness 3 (mm) | 0.38 | 0.38 | 0.00% | 0.38 | 0.00% | 0.38 | 0.00% |
| Cusp Thickness 4 (mm) | 0.52 | 0.51 | -1.92% | 0.52 | 0.00% | 0.51 | -1.92% |

*Table 5.8: Measurements of filtered images of the Papio ursinus molar.*

| | Oiginal Image | Median Filter | % Diff. | Anisotropic Diffusion | % Diff. | Both Filters | % Diff. |
|---|---|---|---|---|---|---|---|
| Enamel Area (mm^2) | 272,9 | 272,9 | 0,00% | 272,8 | -0,04% | 272,8 | -0,04% |
| Bicervical Diameter (mm) | 11,61 | 11,61 | 0,00% | 11,63 | 0,17% | 11,61 | 0,00% |
| Cusp Thickness 1 (mm) | 1,11 | 1,11 | 0,00% | 1,1 | -0,90% | 1,11 | 0,00% |
| Cusp Thickness 2 (mm) | 1,77 | 1,77 | 0,00% | 1,75 | -1,13% | 1,75 | -1,13% |

*Table 5.9: Measurements of filtered images of the Symphalangus syndactylus molar.*

| | Oiginal Image | Median Filter | % Diff. | Anisotropic Diffusion | % Diff. | Both Filters | % Diff. |
|---|---|---|---|---|---|---|---|
| Enamel Area (mm^2) | 85.4 | 85.4 | 0.00% | 85.4 | 0.00% | 85.4 | 0.00% |
| Bicervical Diameter (mm) | 7.55 | 7.53 | -0.26% | 7.54 | -0.13% | 7.54 | -0.13% |
| Cusp Thickness 1 (mm) | 0.83 | 0.85 | 2.41% | 0.84 | 1.20% | 0.85 | 2.41% |
| Cusp Thickness 2 (mm) | 0.85 | 0.89 | 4.71% | 0.86 | 1.18% | 0.89 | 4.71% |

values (although higher than the values they began with), so they were still below the threshold value used to separate enamel from the rest of the image. It may be further extrapolated that the enamel surface area (i.e., the outer enamel surface area plus the enamel-dentine junction surface area) is also not affected by image filtering. This may be inferred because the enamel area has not changed, suggesting that the same number of pixels was counted as enamel in all the images (area is a function of the number of pixels multiplied by the size of each pixel in square mm), and that the number of pixels at the border of the enamel (the surfaces) must also be the same. None of the three filtering techniques (median, anisotropic diffusion, and the combination of these two filters) appears to have any greater deviation from the original image measurements than any other. This finding is supported by the results of the pixel value histogram analysis discussed below, in which the three filtering regimens demonstrate roughly equally disparate pixel value regions for dentine and enamel.

Results of the analysis of image pixel value histograms indicate that the combination of the median and anisotropic diffusion filters is successful at distinguishing those pixels representing dentine from those representing enamel. Figure 5.7 depicts a typical pixel value histogram, in which three individual peaks represent background pixels, dentine pixels, and enamel pixels. The vast majority of pixels are black (representing air), represent background noise, or represent the plastic tube in which specimens are placed prior to mCT scanning. The lower panel of Figure 5.7 shows a close-up view of that portion of the pixel value histogram that contains pixels above a value of 50, thereby eliminating much of the air, background noise, and specimen tube signal, and facilitating a better view of the pixel peaks representing dentine and enamel.

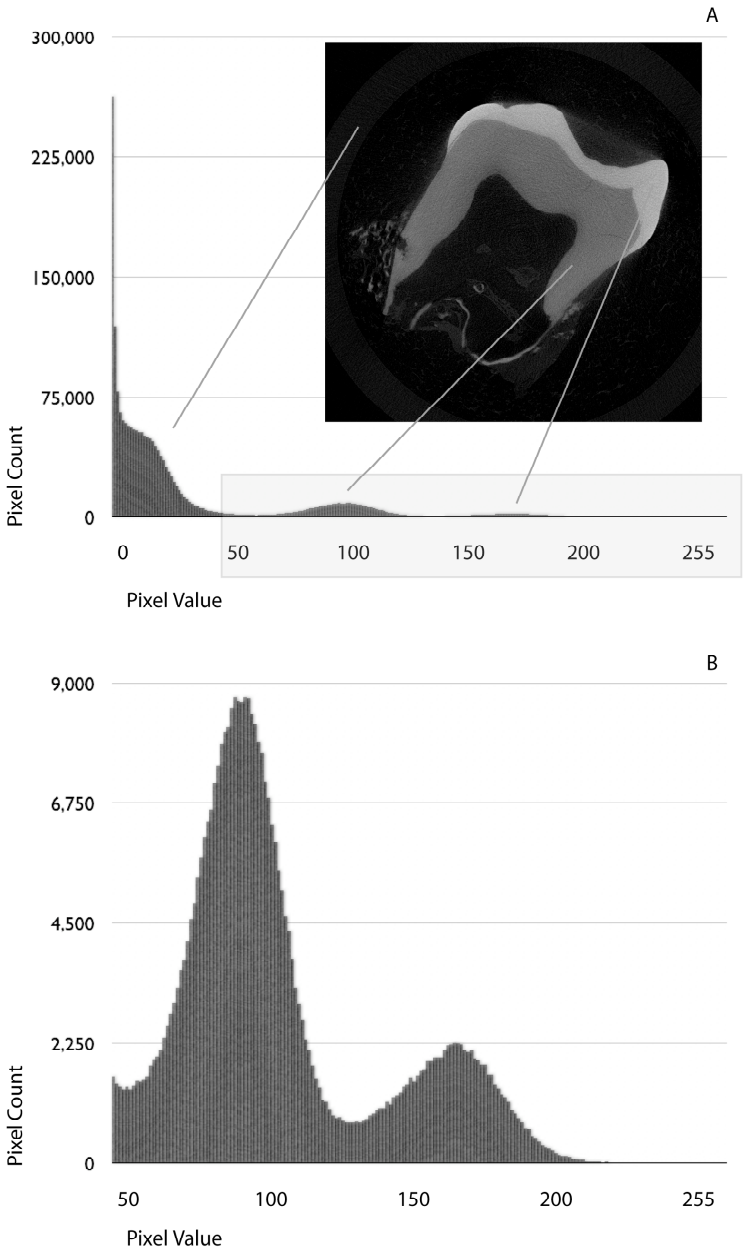


Figure 5.7. Description of pixel plot histograms. In figure 5.7A, the count of pixels with low values is quite high (the peak at the left side of the histogram), and these low pixels represent air (pixel value zero), background noise, and the mCT specimen tube. The majority of pixels in this image represent air, so the histogram bar at position zero is much taller than the other bars. The bars in the center of the histogram depict the counts of pixels that represent dentine, which have a lower value than enamel pixels and a higher value than background noise. The bars depicting the counts of pixels representing enamel appear at the right of the histogram, as enamel pixels are the brightest objects in the image. Figure 5.7B is a close-up image of the box in 5.7A; this image shows the same data as in 5.7A, but beginning at pixel value 50 in order to eliminate the peak at left representing background noise and air.

In an ideal situation, there is a complete separation between the portions of the graph representing dentine and those representing enamel, rather than the trough seen in Figure 5.7b; in this case, one could simply eliminate all of the pixels below the enamel portion of the graph from an image via thresholding, effectively creating an image of only the enamel portion of the tooth. With all but enamel eliminated, measurements are quite easy to take, as all of the visible (non-zero) pixels represent the tissue of interest.

Figure 5.8 depicts the pixel value histogram of the *Papio ursinus* molar cross-section (beginning at pixel value 50), as well as the histograms of the median filtered image, the anisotropic diffusion filtered image, and the image subjected to both median filtering and anisotropic diffusion. There is clearly a lower trough between the enamel and dentine portions of the histogram in the filtered images than in the original image, suggesting that the application of these filters allows the two tissues to be separated more easily via simple thresholding than in the former. The lowest trough between enamel and dentine pixels occurs in the histogram of image to which both filters were applied, and this is true in the case of every image of a tooth (or teeth) examined in this experiment.

As an additional experiment to test that a combination of the median filter and anisotropic diffusion renders enamel and dentine as relatively homogenous pixel groups in mCT images, a particularly poorly defined image was chosen as a test of the method. This image is of a lower first molar of an anatomically modern human fossil from South Africa (SAM AP 6242; see Grine 2000), and was recently analyzed in order to compare dental tissue volumes to more recent modern humans (Smith et al., in review). In measuring the tooth it was apparent that standard thresholding and other basic segmentation techniques could not adequately separate the enamel from the dentine, as

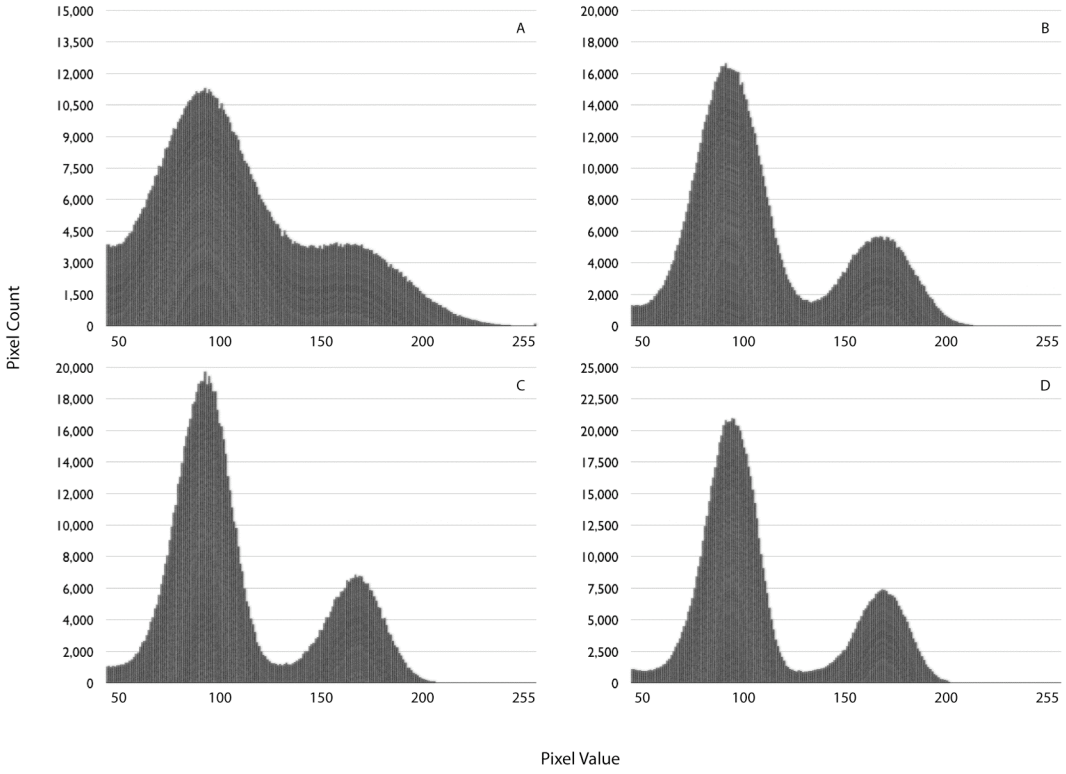


Figure 5.8: Pixel plot histograms of the *Papio ursinus* molar mCT image measured in the study of image filters. Each of the histograms begins at the pixel value 50 (not the entire range of 0-255) in order to highlight that range of pixels depicting enamel and dentine rather than background noise and space. In figure 5.8A, the original image's pixel value histogram is shown; while there is a trough between the dentine and enamel pixels, this trough is substantially less well-defined than in the other histograms. Figure 5.8B and 5.8C depict the pixel value histograms of the median and anisotropic diffusion filtered images, respectively; in these plots, the trough between enamel and denting is better defined than in the histogram of the original image. Figure 5.8D shows the pixel value histogram of the image subjected to both the median and the anisotropic diffusion filters; in this image, the distinction between enamel and dentine pixels is the greatest, suggesting that the combination of these two filters is the most useful for segmenting the two

much of the occlusal enamel was similar in pixel value to the dentine, and *vice versa* (Figure 5.9A).

Figures 5.9B and 5.9C show a close-up of a poorly defined area of the tooth as originally manifested in the mCT scan, and after median filtering and anisotropic diffusion. Figure 5.9D shows the result of thresholding the original image (i.e.,

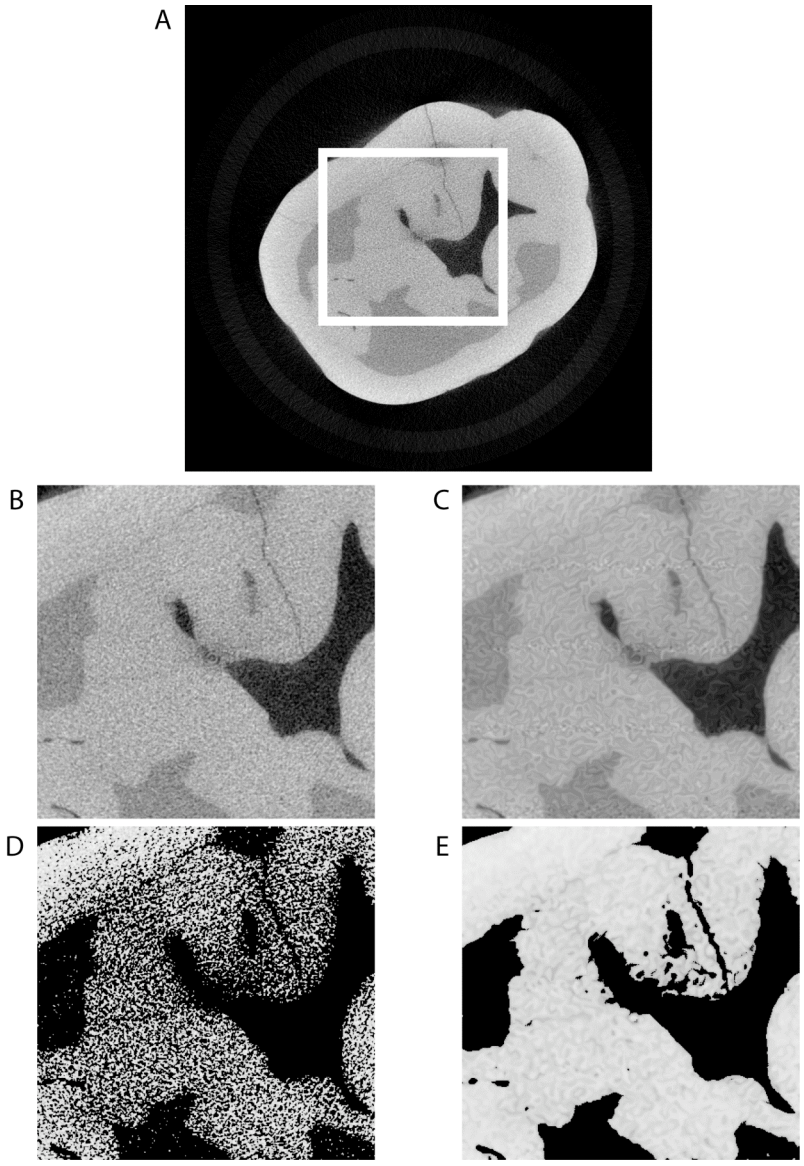


Figure 5.9: Images depicting a fossil modern human lower first molar (SAM AP 6242). The original image appears as figure 5.9A, and the inset shows a particularly poorly defined area of the image. Figures 5.9B and 5.9C show the inset region in its original form and after the filtering approach described in the text, respectively. Figures 5.9D and 5.9E show the results of identical thresholding regimens on original and filtered images. The results of thresholding the filtered image are clearly superior in that the enamel is homogenized with only a few holes (which can easily be filled using standard 3D measurement algorithms), while the dentine has been completely removed, making 3D measurements relatively easy to record.

eliminating pixels below a certain value in order to remove the dentine component), and it can clearly be seen that much of the enamel is also removed, and many pixels representing dentine remain; the underlying pixel value histogram depicts a strong overlap between the pixel values of these tissues. Figure 5.9E, however, depicts an image using the same thresholding settings as applied to the image that had been filtered, and the result is clearly better (i.e., there are no dentine pixels left in the image, and relatively few holes appear in the enamel). The small holes that appear in the enamel may be readily patched using a flood fill algorithm or through erosion and dilation algorithms available in 3D analysis software packages; such a neighborhood-based noise removal algorithm may easily be programmed, and such a method appears as Appendix B. Thus it appears that even in the most poorly defined mCT scans, the combination of median filtering and anisotropic diffusion provides a simple means to modify and correct the underlying pixel value histogram and render the images measurable using standard techniques.

When combined with the results of the measurement portion of this experiment (the image filters do not have a substantial impact on measurements), it is clear that filtering images in order to segment dental tissues is a fruitful process. All of the image stacks treated in later parts of this study have thus been subjected to both median and anisotropic diffusion filtration in order to homogenize tissues, greatly enhancing the efficiency of recording 3D measurements such as volumes and surface areas.

# CHAPTER 6: MOLAR CROSS-SECTION ORIENTATION AND AN ANALYSIS OF SECTION OBLIQUITY

**Standard Techniques for the Generation of Molar Sections: Orientation and Obliquity**

Studies of enamel thickness are typically performed on cross-sections of molars that are produced using histological methods, or by grinding the tooth to the location of the desired plane and then polishing that surface (e.g., Martin, 1983, 1985; Beynon et al., 1998; Shellis et al., 1998; Ulhaas et al., 1999; Grine 2002, 2005; Martin et al., 2003; Smith et al., 2003, 2004). The exact location of the desired plane of section (hereafter referred to as the "ideal plane of section") is defined following Martin (1983) as that plane which courses through the tips of the dentine horns of the mesial cusps (e.g., in a mandibular molar, the protoconid and metaconid) and is perpendicular to the cervical margin of the tooth (Figure 6.1). Ideal planes that course through dentine horn tips of other cusps are also possible (the distal ideal plane through the hypoconid and entoconid, the buccal ideal plane through the protoconid and hypoconid, and the lingual ideal plane through the metaconid and entoconid). Planes that course diagonally through a molar in occlusal view have also been studied, (the ideal plane coursing through the protoconid and the entoconid dentine horn tips, or the ideal plane coursing through the metaconid and the hypoconid of dentine horn tips); such diagonal planes were generated (in addition to the four planes discussed above) by Tafforeau (2004) in his study of enamel thickness using synchrotron mCT.

It is well-documented that planes of section that are anything other than ideal (that is, planes which do not course through the tips of the dentine horns or that are not perpendicular to the cervical margin) may yield different enamel thickness measurements

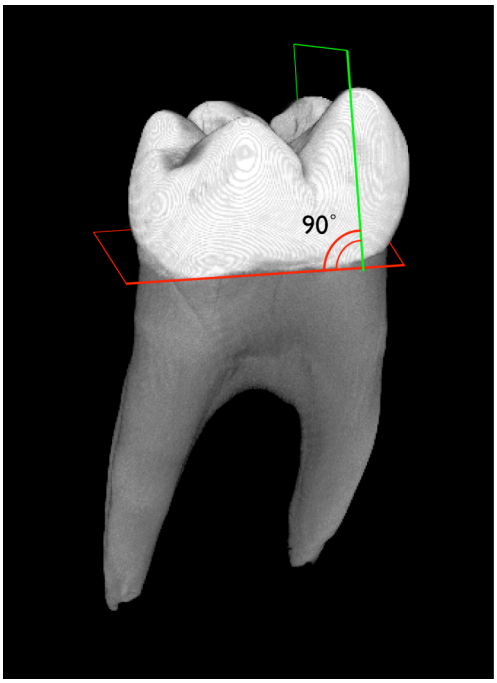


Figure 6.1: Schematic depicting the location of the ideal plane of section (green square) as defined by Martin (1983). This plane of section should be perpendicular to the cervical margin of the tooth (depicted as the red square) and also course through the tips of two dentine horns. Because the dentine horns are not visible at the time of sectioning, it is difficult to locate them exactly.

than the ideal plane (e.g., Martin, 1983; Dean and Schrenk, 2003; Smith et al., 2003; Olejniczak, 2005). Non-ideal sections result from two types of section obliquity: 1) *angular obliquity*, whereby the dentine horns are traversed but the plane of section is not perpendicular to the cervical margin, and 2) *mesio-distal obliquity*, whereby the plane is perpendicular to the cervical margin but courses either mesial or distal to the dentine horn tips (Figure 6.2). These two types of obliquity can appear in the same physically produced section.

The reason some sections are oblique is attributable to both the inability to see the exact location of the dentine horns before sectioning, and the non-linear (often sinuous) path of the cervical margin (Figure 6.3). For instance, when grinding through a molar, it is common to arrive at the dentine horn of one cusp before the other dentine horn is

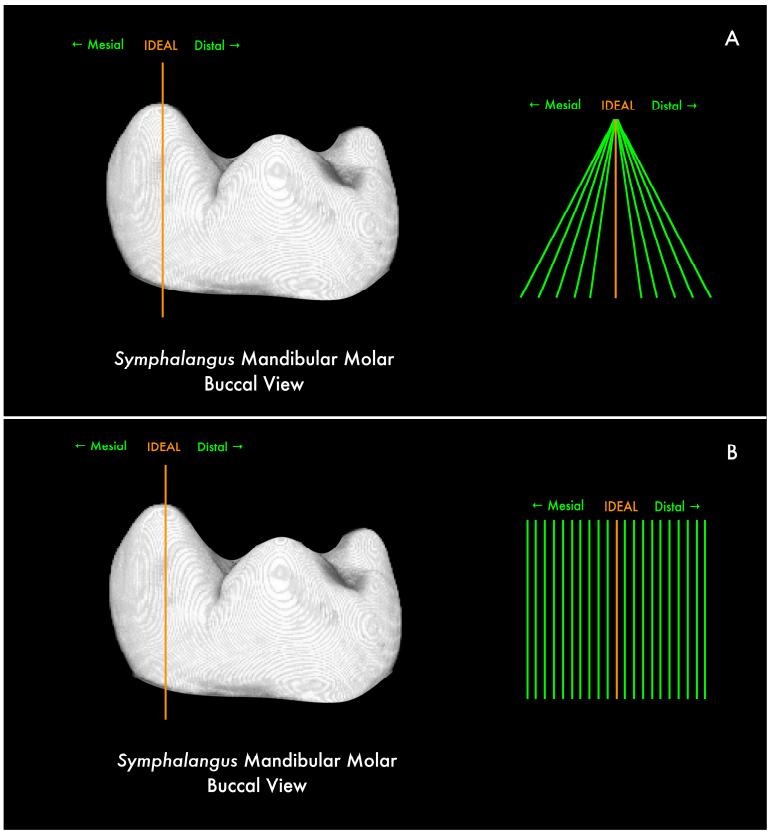


Figure 6.2: Depiction of angular (A) and mesio-distal (B) obliquity. The orange lines represent the ideal plane of section. The diagrams at right show the locations of oblique planes of section (green lines) with reference to the ideal plane.

reached. In this case, further grinding will cause the dentine horn that has been located to be obliterated, and not grinding further prevents visualizing the morphology of the other dentine horn. Grinding only one side of the tooth in order to locate the second dentine horn results in a beveled, non-planar surface, which does not lend itself to photography or scanning electron microscopy (techniques commonly used to produce measurable pictures in enamel thickness studies). Moreover, the cervical margin of a tooth is non-linear and tends to extend further apically on one side of a molar than the other, although this pattern is not uniform across species or individuals within a species (Figure 6.3); in many cases the human eye is a reliable gauge of what is "perpendicular" to the cervical margin, although this is a judgment which may not be made identically by two different

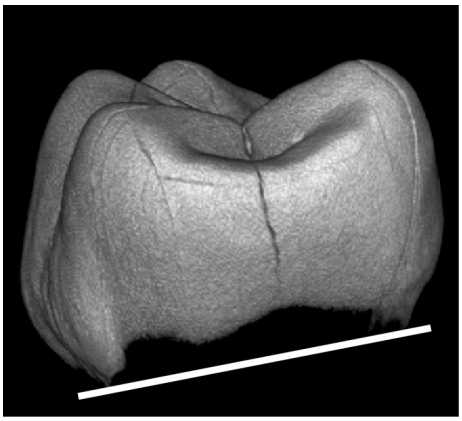

Figure 6.3: Volume rendering of a *Symphalangus syndactylus* lower molar enamel cap. The white line represents a straight-line approximation of the cervical margin, which is actually a complex, non-linear tissue interface.

researchers. The cervical margin of fossil molars is frequently broken, further complicating this method.

The result of section obliquity of either the mesio-distal or the angular type is the same: enamel thickness is exaggerated, and the area of dentine is reduced (Figure 6.4; see also Martin, 1983; Dean and Schrenk 2003; Smith et al., 2003). Obliquity thus impacts enamel thickness measurements by inflating linear, average, and relative measurements, acting as an added source of variance in the measurements of the resultant molar sections. Ideally, the manufacturing of planes of section would be repeatable and resultant planes of section would be exactly homogenous between individuals and species; section obliquity prevents these goals from being achieved. Moreover, there is no margin of error in the production of sections; once a section is made, little can be done to alter that section, and alternative sections that may be closer to ideal often cannot be located (one cannot simply begin again if an error is made).

The use of mCT technology seems to be an ideal approach to recording planes of section without destroying material, and has the benefit of being repeatable; because

mCT models are not destroyed in the production of sections, multiple attempts may be made to locate the ideal plane. Computer rendered mCT volume models allow for the true locations of dentine horn tips to be located and exactly homogenous planes of section to be recorded for multiple individuals, while controlling for section obliquity and effectively eliminating this source of variance from the resultant data. Nonetheless, one of the same obstacles to locating ideal planes of section in real molars applies to mCT models as well: the definition of an ideal plane, as it is currently understood, does not account for the true, non-linear, shape of the cervical margin, leaving only the two dentine horn tips of interest as reliable landmarks with which to define the plane.

The standard equation for a geometric plane with non-zero normal vector $n = (a, b, c)$ is:

$$ax + by + cz + d = 0.$$

Inherent in this definition is that the coefficients $a$, $b$, $c$, and $d$, are known in order to locate the plane; alternatively, one must know the location of no less than three Cartesian points $(x, y, z)$ on the plane in order to determine its coefficients. The latter strategy (locate three points to define the plane) is appropriate for the current purpose. Since only the two dentine horn tips may be reliably located (the cervical margin is not a single landmark, nor is it a straight line, and it is often broken or cracked in fossil specimens and dry museum specimens), a third point must be located. To this end, two strategies using mCT data have emerged recently (Tafforeau, 2004; Suwa and Kono, 2005).

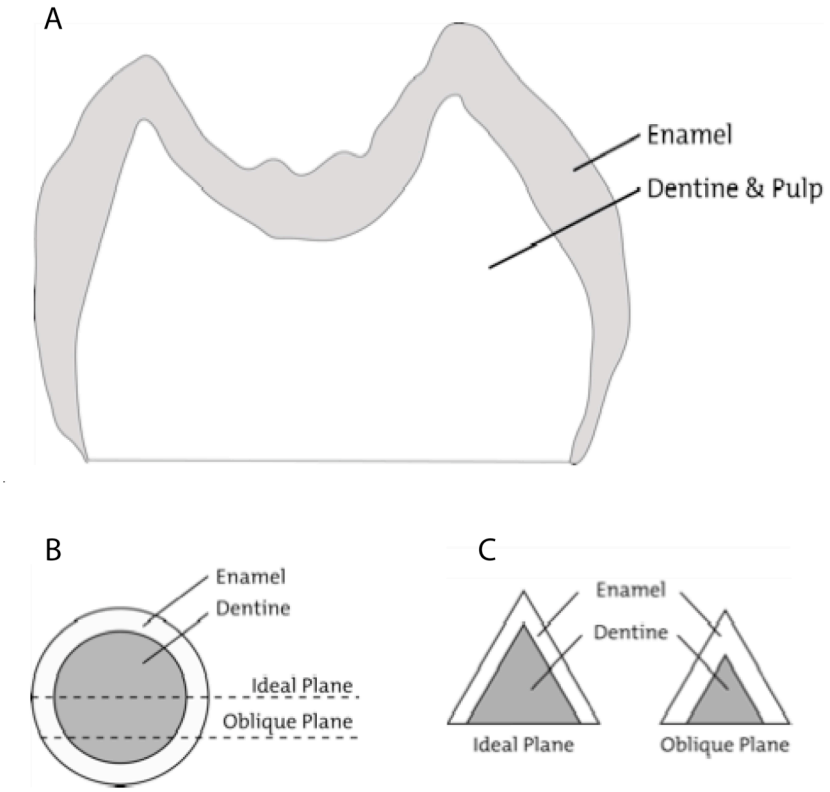


Figure 6.4: Schematic of the ideal plane of section in a molar (6.4A). The boxes below represent a transverse cross-section through a cusp (6.4B), showing the impact of mesio-distal obliquity on the relative amounts of enamel and dentine that are visible, and a coronal section through a cusp (6.4C) showing the impact of angular obliquity on the relative quantities of enamel and dentine in the section. In both cases, the relative amount of enamel increases when obliquity is present.

**Recent mCT Methods for Ideal Plane Production**

Suwa and Kono (2005; Kono, 2004) located ideal planes of section in mCT models by first devising a reference plane, to which the ideal planes could be defined as perpendicular. In order to locate this reference plane, models of each tooth were rendered, and the maximum area occupied in occlusal view (after an iterative oscillation of the model to various occlusal positions) was taken as the orientation of the reference plane. Perpendicular planes to the reference plane were then erected and made to contain two dentine horn tips, thereby creating ideal planes of section.

In creating these ideal planes of section, however, Suwa and Kono's method incorporates a measure of enamel thickness, and therefore is not independent of the measurements of interest. Great ape and human molars have disparate enamel thicknesses at their lateral perimeters (e.g., Martin, 1983; Schwartz, 2000; Martin et al., 2003; Grine, 2005); enamel is thicker on the "functional" cusp lateral walls (i.e., the mandibular buccal cusps or the maxillary lingual cusps). The pattern of enamel thickness on the lateral walls of cusps is not consistent within species (Schwartz, 2000; Martin et al., 2003), nor is it consistent between conspecific individuals (Martin, 1983: Appendix A). Thus, when viewed in occlusal orientation, the maximum area of molars is dependent upon enamel thickness (therefore not an independent measurement), and is also defined differently in different individuals and in different taxa.

Tafforeau (2004) reviewed Suwa and Kono's methods in his study of enamel thickness in hominoid primates using synchrotron mCT, and developed two alternative techniques for ideal plane orientation that are independent of enamel thickness. His first method for locating ideal planes of section relied on orienting each molar in an approximately equivalent manner, and then measuring the morphology of the cervical margin of each tooth in order to reorient the teeth in a standard way. Tafforeau (2004) began by orienting the volume model of each molar in an occlusal position; the model was rotated 90˚ such that the lingual surface was visible. A straight line was plotted along the cervical margin of the lingual aspect of the molar, which Tafforeau called the average line of the cervix. The angle between this line and a horizontal line (with reference to the occlusal surface of the tooth) was then calculated. The model was rotated 180˚ and the same measurement was calculated on the buccal side. The average

of these two angles was used to correct the position of the volume model, such that the cervical margins of the lingual and buccal sides were made to be as close to horizontal as possible. In order to orient the tooth on its mesio-distal axis, the same technique was applied to the cervical margin of these two faces.

An alternative method used by Tafforeau (2004), in light of the high degree of variation he found in the location of the enamel cervix, is the location of dentine horn tips for model orientation. Tafforeau developed a system of animation, wherein a volume model of the dentine component of the molar crown is oscillated until the best-fit plane containing the dentine horns of the major cusps was captured. This plane was then used as a reference for generating sections, such that any perpendicular plane that also contained the tips of two dentine horns was said to be an ideal plane of section. Tafforeau (2004) found that his system of animation was repeatable, with resultant orientations that differed by less than 1˚ in retrials.

In light of the difficulty in fitting a plane to the cervical margin, as well as the need for independence of measurements, Tafforeau's method of using dentine horn tips may be judged to be superior among the previously discussed techniques; this technique is also consistent with Martin's (1983) original definition, such that the dentine horns are the basis for the location of the planes. Discussed below, I have made a modification to Tafforeau's method, such that it is simpler (does not require animation) and relies on only three dentine horn tips, making it applicable to taxa without major cusps of relatively similar height.

An earlier version of this method, developed during pilot work, utilized the dentine horn tips of all four major cusps. A best-fit plane was iteratively fit to these four

points using the least squares method, and this plane was taken to be the perpendicular to the ideal planes. It became apparent, however, that there is great discrepancy between the height of the entoconid and the other three cusps in many taxa (including those examined in Chapter 7 of this dissertation), caused the reference plane to tilt towards the disto-lingual aspect of the molar, substantially impacting the morphology of the resultant ideal planes. The protoconid, hypoconid, and metaconid were of similar height in all taxa examined in the present study, and the resultant ideal planes were not oblique to the cervical margin based on visual inspection of the mCT models; thus, only these three cusps were used to produce reference plane in all cases.

**A Modification of Tafforeau's (2004) Reference Plane**

To avoid the use of a measurement of interest (enamel thickness) in the definition of the reference plane, to avoid using an approximation of the cervical margin, and to avoid generating oblique planes due to great differences in cusp height, a strategy is developed that relies on only type 1 landmarks (*sensu* Bookstein, 1997). These landmarks are available on all molars, represent homologous morphological features, and can be located reliably by multiple researchers examining the same specimen. Other than enamel cusp tips, dentine horn tips represent the only type 1 landmarks available on a wide range of molars from different species (nearly all primate lower molars have four major cusps (and often a hypoconulid), but the presence and location of other features is taxon-specific; (e.g., the accentuated intercuspal crests associated with folivory). The method proposed here, following Tafforeau (2004), relies solely on the location of dentine horn tips to define a reference plane for recording ideal sections. To produce a

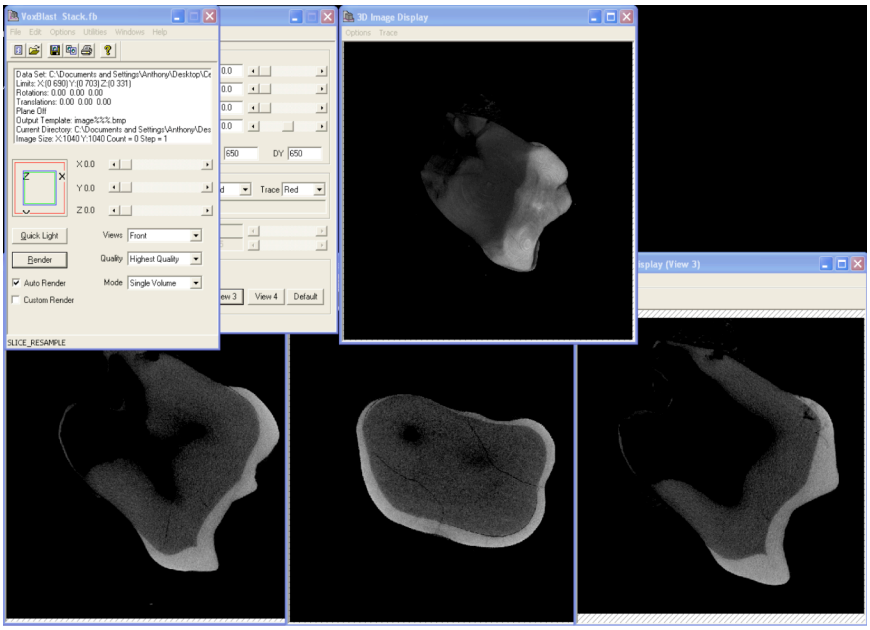


Figure 6.5: A screen capture of VoxBlast software (Vaytek, Inc.) showing multiple slice planes taken from a volume model of a *Cebus apella* molar. By iteratively scrolling through the model's slice planes, specific landmarks (e.g., dentine horn tips) may be located and their position recorded.

reference plane, VoxBlast software (Vaytek, Inc.) was used to render a volume model of each tooth, and to simultaneously visualize planes of section within that model (Figure 6.5).

The Cartesian coordinates of three dentine horn tips (protoconid, metaconid, and hypoconid) were recorded by inspecting individual planes of section until the most occlusal point of dentine at each cusp was captured in a plane (Figure 6.6); the orientation of the image stack was then adjusted to be parallel to the plane containing those three dentine horn tips (Figure 6.7). With the image stack now parallel to the reference plane, the single image containing all three dentine horn tips of interest was located by simply scrolling through the images. The orientation of the image stack was then adjusted again, such that the images were perpendicular to their current orientation (i.e., perpendicular to the reference plane), and finally another rotation of the image stack so that in addition to

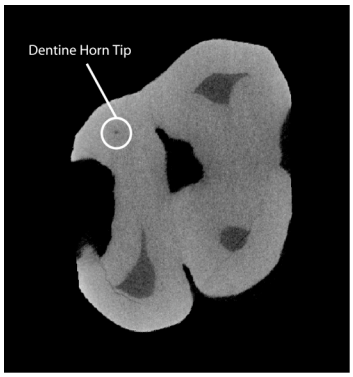


Figure 6.6: Re-sliced image from within a model of a *Cebus apella* lower molar showing the tip of a dentine horn (within the white circle, the dentine horn tip is the small dot of dark pixels in the center).

being perpendicular to the reference plane, a single image also coursed through two dentine horn tips. In this way, any pair of dentine horn tips could appear in an image that is perpendicular to the reference plane; that is, any ideal plane of section could be located with reference to the plane containing the dentine horn tips (Figure 6.7). In sum, this method utilizes two landmarks and a perpendicular in order to produce ideal sections with reference to a plane that is defined by three landmarks. Visual comparisons to ideal sections produced using standard methods show that the virtual planes closely approximate the plane of section found using traditional methods (Figure 6.8; see also Olejniczak and Grine, 2006).

As noted by Tafforeau (2004), a primary advantage of the mCT-derived planes described here is that they have no component of variance due to human judgment about the location of the cervical margin or the dentine horn tips, so human-induced section obliquity effectively has been controlled. The planes also rely solely on anatomical landmarks that multiple researchers will define and locate identically, effectively eliminating inter-observer error in the location of sections, rendering the method repeatable. Moreover, this method does not rely on enamel thickness, nor the location of

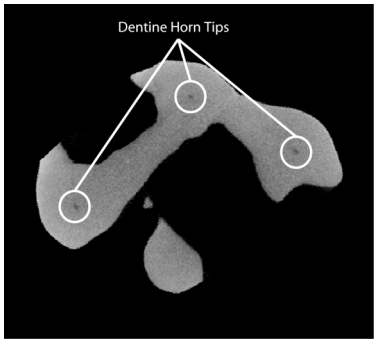


Figure 6.7: Re-sliced image from within a model of a *Cebus apella* lower molar showing the tips of all three dentine horns (inside white circles) that are used in order to generate ideal sections.

the cervical margin of the tooth, thus circumventing the issues discussed above with reference to the methods of Suwa and Kono (2005), and the original definition of ideal planes put forth by Martin (1983).

**Quantification and Analysis of Section Obliquity**

Several authors have noted that measurements recorded from an oblique (non-ideal) section may be different from those recorded in the ideal section (Martin, 1983; Dean and Schrenk 2003; Smith et al., 2003; Olejniczak, 2005), but the impact of section obliquity on measurements has not been systematically quantified. One of the goals of the research presented here is to assess the impact of section obliquity on enamel thickness measurements, such that previously published research may be interpreted in light of a known degree of variance introduced by non-ideal sections.To evaluate the impact of obliquity on cross-sectional measurements, a small sample of primate molars (n = 11) was scanned with high-resolution mCT (Scanco μCT 20, Scanco Medical AG, Switzerland). The molars represented small- and large-bodied primates, with thick and thin enameled taxa represented (Table 6.1). Models of each molar were virtually

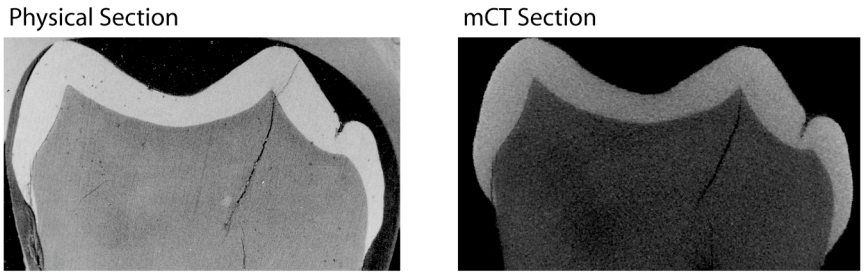


Figure 6.8: Comparison of an ideal plane of section created using the methods described in this chapter (right) to the physically produced section (scanning electron micrograph at left) of the same specimen. The mCT plane of section differs slightly from that of the same tooth presented in Olejniczak and Grine (2006) and Chapter 3 of this dissertation, as the goal in those studies was to locate the identical plane of section using physical sectioning and mCT, whereas the goal here is to compare a physical section to an ideal mCT section that has been created without regard to the physical section, using the methods described in this chapter.

sectioned in mesial ideal planes, controlled mesio-distal oblique planes (Figure 6.2), and controlled angular oblique planes (Figure 6.2). The dentine horn tips of the three tallest cusps were used to create a reference plane from which to locate ideal planes, per the methods above.

Measurements recorded in each section appear in Figure 6.9 and include the area of the enamel cap, the area of dentine (including pulp), the bi-cervical diameter, the height of both dentine horns, the thickness of enamel at both cusps, the length of the enamel-dentine junction, and the relative enamel thickness index (following Martin, 1983). Figures 6.10 and 6.11 demonstrate visually the impact of the two types of obliquity on molar sections.

Results indicate that measurements recorded from oblique sections yield substantially different measurements than those from an ideal section, and that large differences in measurements can be found at small distances from the ideal plane (~50-100 microns). In the figures that follow, the z-score of each measurement has been

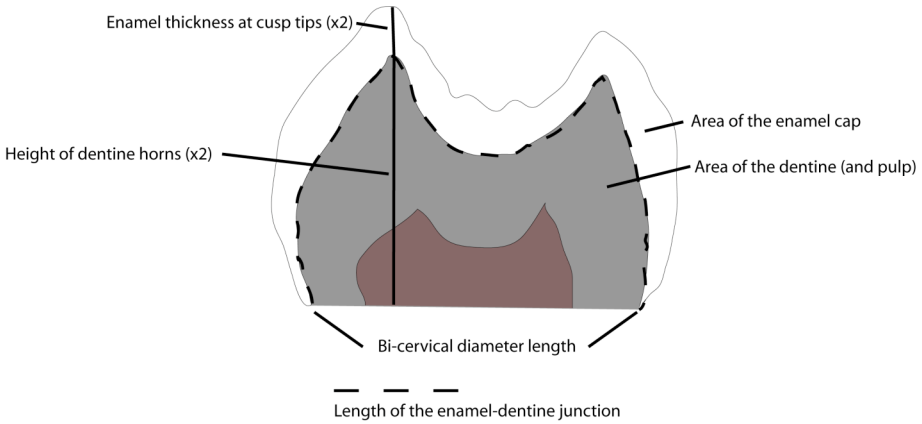


Figure 6.9: Schematic of an ideal cross-section through the mesial cusps of a molar showing the measurements recorded in the obliquity experiment.

plotted in order to equalize the scale of each measurement to ease visual comparisons. Z-scores (which are equal to the observed measurement minus the mean, then divided by the standard deviation) have the added benefit of rendering data in standard deviation units; for example, a score of 1.0 indicates a measurement that is exactly one standard deviation above the mean, or a score of -2.0 indicates a measurement that is exactly two standard deviations below the mean.

Figure 6.12 depicts the impact of angular and mesio-distal obliquity on linear measurements. Angular obliquity has the effect of reducing apparent crown height, thereby reducing the height of the enamel cusps and of the dentine horns. Mesio-distal obliquity, however, shows a pattern in which enamel thickness increases mesially and decreases distally along the molar; the opposite pattern is reflected in the measurements of dentine horn height. As was the case in angular obliquity, these results can be explained in terms of reduced apparent crown height; the height of the section decreases as the molar is traversed in the mesial direction. In the distal direction, the cusps reduce

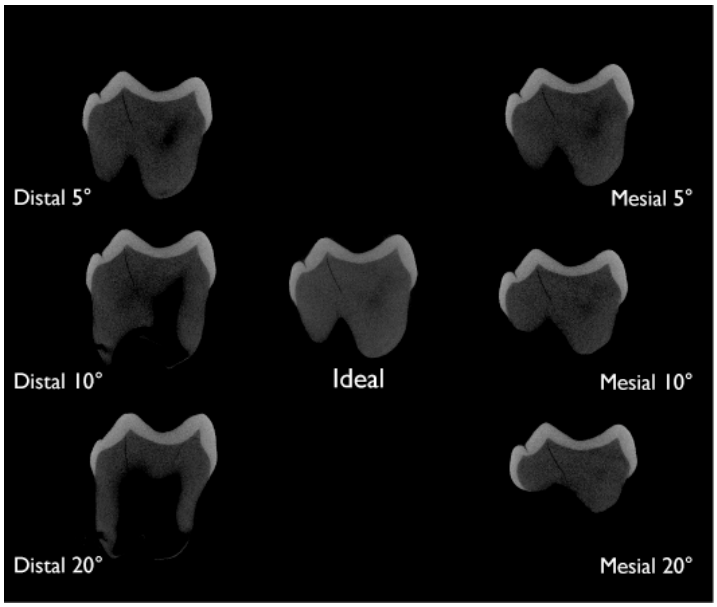


Figure 6.10: mCT derived cross-sections through a *Cebus apella* lower molar. The image in the center is the ideal plane of section, and the other images represent varying degrees of angular obliquity.

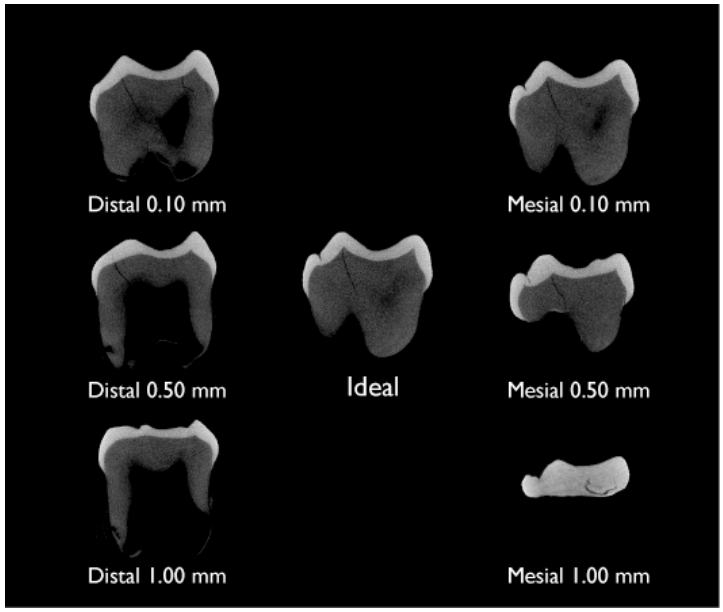


Figure 6.11: mCT derived cross-sections through a *Cebus apella* lower molar. The image in the center is the ideal plane of section, and the other images represent varying distances of mesio-distal obliquity.

*Table 6.1: Specimens examined in the study of section obliquity.*

| Taxon | Sample Size | Morphology / Notes |
|---|---|---|
| *Homo sapiens* | 1 | Large, thick enamel, bunodont. |
| *Symphalangys syndactyuls* | 7 | Medium size, thin enamel. |
| *Chiropotes satanus* | 1 | Small, thin enamel, short dentine horns. |
| *Papio ursinus* | 1 | Thick enamel, tall horns, bilophodont. |
| *Cebus apella* | 1 | Small, thick enamel, bunodont. |

in height as they slope towards the occlusal basin, thus reducing the perceived enamel thickness.

Figure 6.13 depicts the impact of angular and mesio-distal obliquity on area measurements. Angular obliquity again is seen to reduce the apparent size of the cross-section in either the mesial or distal direction, thereby reducing all area measurements. Mesio-distal obliquity, as is the case among linear measurements, decreases the apparent size of the crown mesially, resulting in reduced areas, and increase the size of the crown distally, resulting in larger areas.

Figure 6.14 depicts the impact of angular and mesio-distal obliquity on the lengths of the enamel-dentine junction and the bi-cervical diameter, as well as the relative enamel thickness index. After a series of up and down transitions, angular obliquity tends, ultimately, to reduce the two length measurements and to increase the relative enamel thickness index. The reduction in lengths may again be attributed to the reduced apparent size of the tooth when sectioned at an angle to the ideal plane. The increase in relative enamel thickness may be attributable to the relative increase in the area of enamel that is being captured in cross-section versus the area of dentine (see Figure 6.13), following Martin's (1983) prediction. Mesio-distal obliquity shows that relative enamel thickness increases in the mesial direction, as predicted from the behavior of enamel and dentine area, but decreases in the distal direction. This decrease is attributable to the lack of cusp definition in distal sections, such that only the occlusal basin is visualized and the

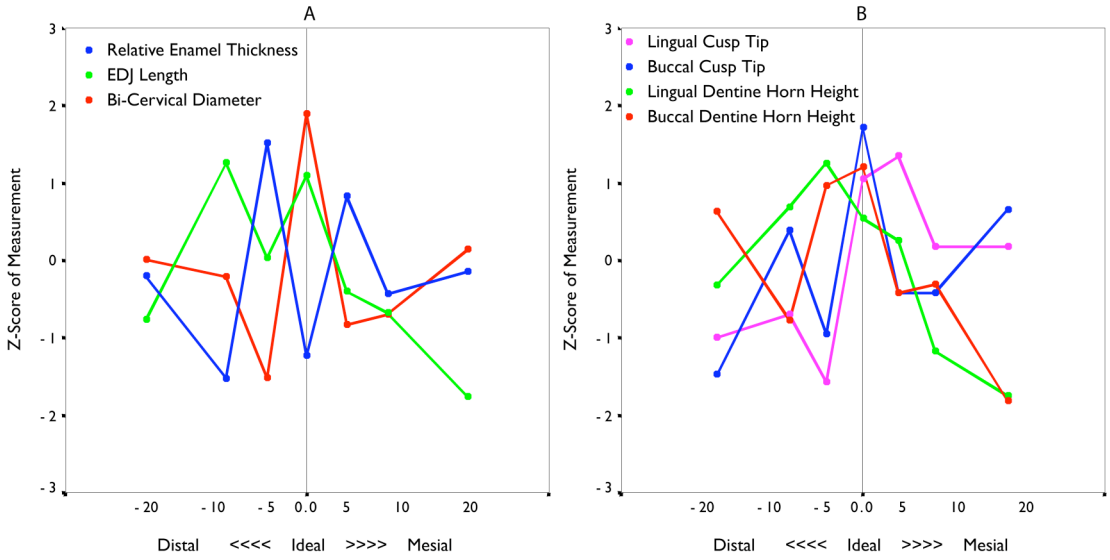


Figure 6.12: Plots depicting the z-scores of linear measurements at the ideal section, in angular oblique sections (A), and in mesio-distal oblique sections (B). The units on the abscissa in figure 6.12A are angles, and in figure 6.12B they are mm.

majority of the section is occupied by dentine and pulp with a partial "ring" of enamel around it.

In sum, measurements are clearly seen to deviate at oblique angles and along the mesio-distal axis of the tooth. The rapidity with which the measures increase or decrease is not consistent, but in most cases angular deviations of more than 5˚ produce measurements that are more than 5% different than ideal. In terms of mesio-distal obliquity, tooth size plays a role in how quickly the measurements begin to atrophy, but even when the largest teeth are considered, there appears to be a window of error that is less than 1.0 mm in order to ensure measurements that are within 5% of the ideal.

The plots presented above do not immediately render data published using traditional methods to be without validity. This is because previous workers have taken great care to produce sections as accurately as possible, and the human eye is a relatively accurate judge of the location of perpendicular planes (e.g., Figure 6.8). The existence of

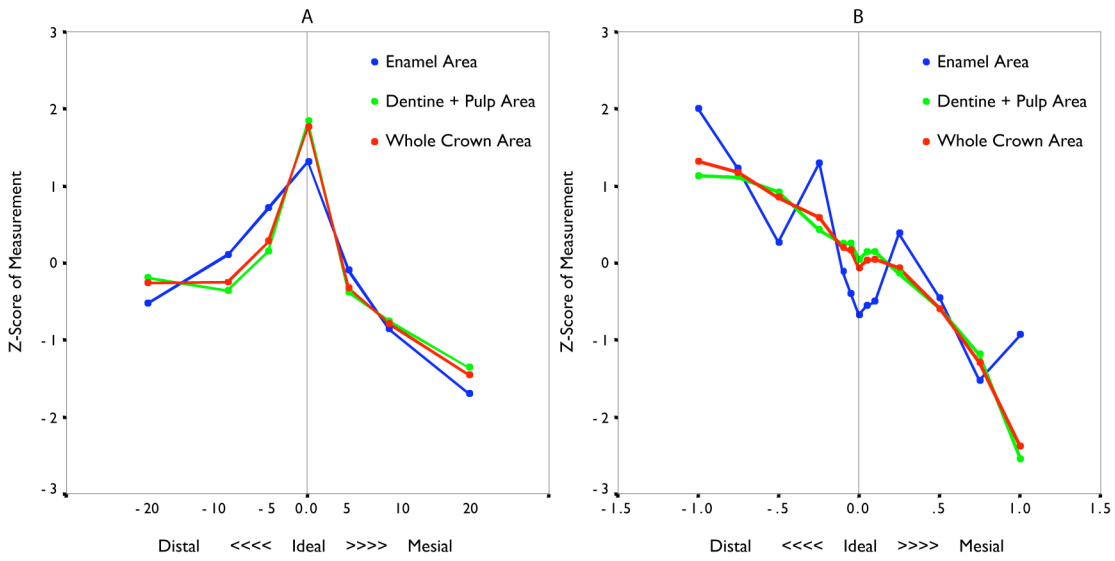


Figure 6.13: Plots depicting the z-scores of area measurements at the ideal section, in angular oblique sections (A), and in mesio-distal oblique sections (B). The units on the abscissa in figure 6.13A are angles, and in figure 6.13B they are mm.

artificially inflated or deflated measurements in previous studies, however, means that the distribution of these measurements should be treated as having an element of variation that is not accounted for by biological variation. The means and standard deviations from these samples should perhaps be treated as floating within a confidence interval rather than as fixed numbers.

Moreover, samples of physical sections created for comparisons of tooth types or comparisons between taxa are likely to contain approximately the same level of artificial variance (assuming variation caused by obliquity is randomly introduced into samples), rendering them suitable for statistical comparison with each other. Nonetheless, mCT studies can produce distributions of measurements that do not have this added source of variance, and the discrepancy between the two techniques should be treated with caution when measurements recorded using both of them are combined. It is recommended that future researchers wishing to section teeth (e.g., for studies where dental development

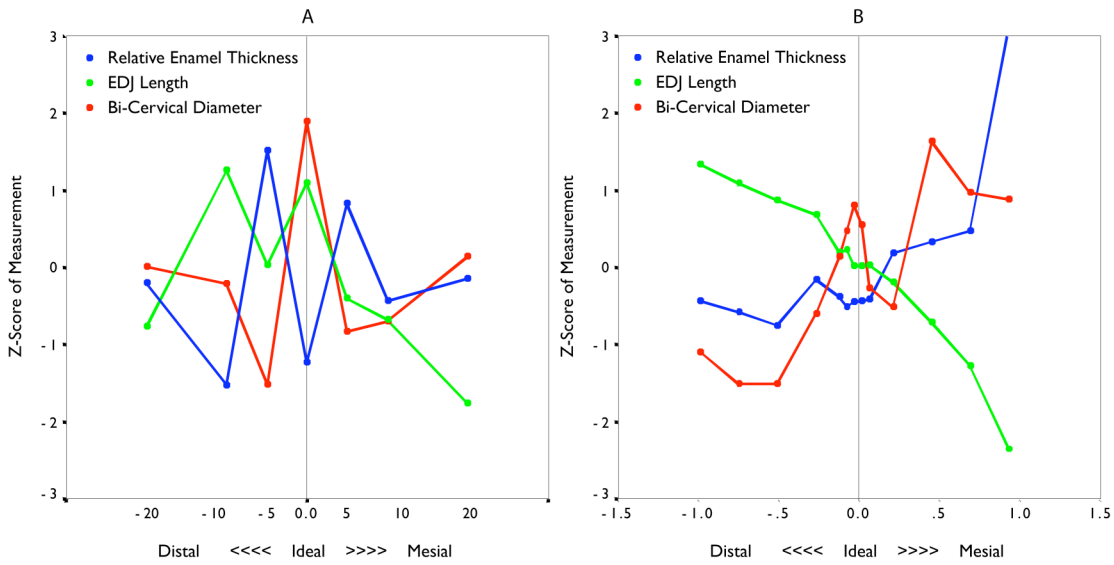


Figure 6.14: Plots depicting the z-scores of the enamel-dentine junction length, the bi-cervical diameter, and the relative enamel thickness index at the ideal section, in angular oblique sections (A), and in mesio-distal oblique sections (B). The units on the abscissa in figure 6.14A are angles, and in figure 6.14B they are mm.

and enamel thickness will be compared) first have the teeth mCT scanned; the scans may then be used to produce ideal planes of section, and these virtual models may be used as guides for making equivalent physical sections without the confounding effects of section obliquity.

## Conclusions

Generating ideal planes of section using mCT models of teeth is useful for the comparison of mCT-derived data to previously published measurements using traditional methods, and it is also useful in the analysis of worn teeth where three-dimensional reconstruction of worn areas is difficult compared to two-dimensional reconstructions (Tafforeau, 2004). Planes of section created using mCT models necessitate a reference plane for orientation. Previously published methods have defined this reference plane in different ways, but these methods are either not entirely independent of the enamel

thickness to be measured (Suwa and Kono, 2005), or they rely on planar approximations of a complex, three-dimensional structure (Tafforeau, 2004). The method presented here shows that a plane defined by only three points that are available in each tooth, and that are reliable in terms of inter-observer measurement differences, may be used in order to generate homologous and repeatable ideal planes of section. Finally, because the impact of section obliquity on measurements of enamel thickness is severe at small deviations from the ideal plane, it is recommended that future researchers who wish to section teeth first mCT scan the specimens in order to drive the ideal planes of section virtually. Morphological landmarks from the virtual models should then be used to guide the physical sectioning process.

# CHAPTER 7: BIOLOGICAL APPLICATIONS OF MICROTOMOGRAPHY

## Introduction

Chapter 1 of this dissertation introduced a series of analyses that may be performed using mCT scans of primate molars, and provided a brief review of the literature pertaining to these areas of study. These areas of inquiry include the comparison of (relative) enamel thickness in closely related species with differing diets, the assessment of enamel-dentine junction morphology and outer enamel surface morphology (by way of enamel and dentine polygons), and the assessment of metameric variation in enamel thickness. The remainder of this dissertation covers each of these topics, employing a comparatively large sample of primate molars (n = 73) representing two closely related species dyads from two superfamilies.

The study samples and the mCT scanning protocol used to produce virtual sections and models of each tooth are described first. As several of the individual measurements recorded are used in examining more than one question, the next section is devoted to describing the entire set of measurements recorded on each tooth. The first question is then addressed: is there any evidence of sexual dimorphism in enamel thickness measurements? The answer to this question will determine whether multi-sex samples may be combined in the other analyses. Next, the issue of metamerism is explored to assess whether there is a gradient from the M1-M3 in any of the three-dimensional measurements or in the enamel thickness indices.

The next section examines the correspondence of two- and three-dimensional measurements, and describes an experiment testing the validity of the assumption that mesial ideal planes are accurate proxies for total crown morphology. Next, the specific enamel thickness conditions of the species studied are examined in light of previous

models of the evolution of molar enamel thickness in primates, and a new interpretation of the polarity of this character in hominoid evolution is offered. The final two sections are experiments designed to detect possible functional signals in enamel thickness and patterning, and to examine the relative utility of the enamel-dentine junction compared to the enamel surface in terms of the utility of occlusal polygons and cuspal angles.

**Study Samples and Scanning Protocol**

Nearly any multi-species sample allows for metamerism, the correspondence of two- and three-dimensional measurements, and the discriminatory power of occlusal and dentine polygons to be investigated. An examination of the relative influence of phylogenetic relatedness and dietary proclivity, however, requires a careful choice of taxa. Two species were chosen from family Atelidae, and two from family Hylobatidae, thus facilitating comparisons between two phylogenetically distinct primate groups. Within each superfamilial species dyad, one primary frugivore (*Hylobates muelleri* and *Ateles geoffroyi*) and one primary folivore (*Symphalangus syndactylus* and *Alouatta seniculus*) were chosen, allowing for the influence of diet on molar morphology to be assessed. Nearly all primates incorporate some amount of both fruit and leaves into their diet, rendering it impossible to test differences between an obligatory folivore and an obligatory frugivore. Nonetheless, data from field studies indicate that *Hylobates muelleri* (Leighton, 1987) and *Ateles geoffroyi* (Chapman and Chapman, 1991) diets consist of substantially greater proportions of fruit than of leaves, and that the diets of *Symphalangus syndactylus* (Gittins and Raemaekers, 1980) and *Alouatta seniculus* (Neville et al., 1998) consist of substantially more leaves than fruit. Moreover, the

primary folivore in each group is substantially larger in terms of body mass than the primary frugivore (e.g., Smith and Jungers, 1997; Fleagle, 1999). Body mass in primates is often correlated with diet, and more folivorous primate speces are larger than closely-related species that are more frugivorous (Fleagle, 1999).

The choice of taxa for inclusion in this study is also a function of the available anthropoid primate familial dyads representing primary folivores and primary frugivores (anthropoids were specifically chosen due to their relavence to existing debates about the evolution of enamel thickness). Among hominoids, *Gorilla* and *Pan* are not generally considered to be sister taxa (e.g., Ruvolo, 1997), and the size of their mandibles precludes scanning using laboratory mCT machines. Hylobatids, however, show a broad dietary range, and a suitable dyad may be chosen from this group. Cercopithecoids do not offer any con-familial frugivore-folivore dyads (the majority of cercopithecine primary folivores belong to the monophyletic Colobinae). Among ceboids, the only family containing both primary folivores and primary frugivores is the Atelidae. There is also a conspicuous absence of thick-enameled hard-object feeders and gramnivores in the study sample (e.g., *Cebus apella*, *Papio ursinus*). The selection of folivores and frugivores rather than gramnivores was predicated on external factors; the size of the mCT gantry, for instance, facilitates a mandibular width at M3 of no more than 11 cm, prohibiting great apes, humans, and gramnivorous cercopithecoids such as baboons or mangabeys. Moreover, there is no example of explicit soft- and hard-object feeding species within the same phylogenetic family group among primates, while closely-related folivore-frugivore species dyads are more common (see discussion above; Martin et al., 2003: Appendix B). Finally, the specific species chosen here were based in part on the availability of

relatively unworn mandibular molars that could be loaned from American Museum of Natural History (New York, USA) for mCT scanning.

An additional benefit of including two hylobatid species is that enamel thickness studies have traditionally focused on hominoid evolution, yet few hylobatid molars (n = 2; Martin (1983), Shellis et al. (1998)) have been studied. This group may provide additional insight into the nature and polarity of the evolution of enamel thickness among hominoid primates.

Table 7.1 lists the species, the individual mandibular specimens (the catalogue number from the American Museum of Natural History), the number of teeth at each mandibular molar position scanned from each mandible, the sex of each individual, and the resultant voxel size from mCT scanning. Each specimen was transported from the American Museum of Natural History to the Department of Biomechanical Engineering at Stony Brook University for mCT scanning. All specimens were scanned using a Scanco vivaCT 40 (Scanco Medical AG, Switzerland) at 70 kVp (85 mA). A 2k detector was used, resulting in reconstructed images that were 2048 x 2048 pixels. In accordance with the experimentally derived optimal slice thickness and image resolution parameters discussed in Chapter 2 of this dissertation, all scanning was done at resolutions that produced voxels between 0.0100 mm and 0.0175 mm per side (Table 7.1). The reconstructed images were LZW compressed tagged image file format (TIF) images, which were transferred via FTP to another location for storage, backup, decompression, and analysis (discussed in Chapter 5 of this dissertation).

Specimens were placed in the mCT gantry with the most anterior part of the mandible inserted first; each mandible was secured using foam and tape in order to

*Table 7.1: The Study Sample and mCT Resolution.*

| Taxon | AMNH Cat. # | Sex | M1 | M2 | M3 | Total Teeth | Voxel (microns) |
|---|---|---|---|---|---|---|---|
| *Alouatta seniculus* | 33074 | F | 1 | 1 | 1 | 3 | 15.00 |
| *Alouatta seniculus* | 129415 | M | 1 | | | 1 | 10.50 |
| *Alouatta seniculus* | 94139 | F | | 1 | 1 | 2 | 15.00 |
| *Alouatta seniculus* | 73553 | F | 1 | 1 | 1 | 3 | 17.50 |
| *Alouatta seniculus* | 73548 | F | | 1 | 1 | 2 | 15.00 |
| *Alouatta seniculus* | 239857 | F | 1 | 1 | 1 | 3 | 17.50 |
| *Alouatta seniculus* | 33063 | F | | 1 | 1 | 2 | 12.50 |
| *Alouatta seniculus* | 32145 | M | 1 | 1 | | 2 | 12.50 |
| *Alouatta seniculus* | 23347 | U | 1 | 1 | | 2 | 12.50 |
| ***Alouatta* Total** | | | **6** | **8** | **6** | **20** | |
| *Ateles geoffroyi* | 123282 | U | 1 | 1 | 1 | 3 | 12.50 |
| *Ateles geoffroyi* | 176649 | U | 1 | 1 | 1 | 3 | 12.50 |
| *Ateles geoffroyi* | 172171 | F | 1 | 1 | 1 | 3 | 12.50 |
| *Ateles geoffroyi* | 14484 | F | 1 | 1 | 1 | 3 | 12.50 |
| *Ateles geoffroyi* | 172170 | U | 1 | 1 | 1 | 3 | 12.50 |
| *Ateles geoffroyi* | 17220 | M | | 1 | 1 | 2 | 10.50 |
| *Ateles geoffroyi* | 17222 | F | | 1 | 1 | 2 | 10.50 |
| *Ateles geoffroyi* | 123283 | M | 1 | 1 | | 2 | 10.50 |
| *Ateles geoffroyi* | 29844 | M | 1 | 1 | | 2 | 10.50 |
| *Ateles geoffroyi* | 11074 | F | 1 | 1 | | 2 | 10.50 |
| ***Ateles* Total** | | | **8** | **10** | **7** | **25** | |
| *Hylobates muelleri* | 106781 | F | 1 | 1 | 1 | 3 | 12.50 |
| *Hylobates muelleri* | 103725 | F | 1 | 1 | 1 | 3 | 10.50 |
| *Hylobates muelleri* | 103726 | M | 1 | 1 | | 2 | 10.50 |
| *Hylobates muelleri* | 106328 | F | 1 | 1 | 1 | 3 | 10.50 |
| ***Hylobates* Total** | | | **4** | **4** | **3** | **11** | |
| *Symphalangus syndactylus* | 102724 | M | | 1 | | 1 | 12.50 |
| *Symphalangus syndactylus* | 102729 | M | | 1 | | 1 | 10.01 |
| *Symphalangus syndactylus* | 102189 | M | | 1 | 1 | 2 | 10.50 |
| *Symphalangus syndactylus* | 102722 | F | 1 | 1 | | 2 | 10.50 |
| *Symphalangus syndactylus* | 106582 | F | | 1 | | 1 | 10.50 |
| *Symphalangus syndactylus* | 102191 | F | 1 | 1 | | 2 | 15.00 |
| *Symphalangus syndactylus* | 102193 | M | 1 | 1 | 1 | 3 | 15.00 |
| *Symphalangus syndactylus* | 100048 | M | 1 | | | 1 | 10.01 |
| *Symphalangus syndactylus* | 201316 | U | 1 | 1 | | 2 | 12.50 |
| *Symphalangus syndactylus* | 102197 | F | | 1 | 1 | 2 | 15.00 |
| ***Symphalangus* Total** | | | **5** | **9** | **3** | **17** | |
| **Sample Total** | | | **23** | **31** | **19** | **73** | |

prevent vibration during scanning, as entire mandibles could not be fully accommodated in the gantry due to the height of the ascending rami. The focal tooth was located using the X-ray apparatus interfaced with an on-board computer system, and the area of scanning was limited to scan only this tooth (rather than the entirety of the portion of the mandible inserted into the gantry) in order to minimize the number of scans recorded, as well as both scanning and projection reconstruction times. If more than one tooth from a given mandible was to be recorded, this area was expanded in order to encompass all of the teeth of interest in a single scan. Molars from either the left or right side of an individual were scanned; in no cases were both left and right molars from the same individual scanned.

Images containing multiple teeth were later cropped in order to isolate each tooth as a unique image stack for filtering, measurement, and analysis. After scanning, transferring, decompression, and cropping, the image stack representing each tooth was filtered using both a median and an anisotropic diffusion filter (see Chapter 5 of this dissertation), and imported into VoxBlast (Vaytek, Inc.) for reorientation of the image stack parallel to the basal plane, as well as to locate and record the ideal planes of section for two-dimensional measurements (see Chapter 6 of this dissertation).

**Measurements Recorded**

Because unworn or lightly worn teeth were chosen for analysis, a complete set of measurements was available to be recorded on every tooth. In some cases, minor reconstructions were made where light attrition was apparent. The measurements recorded fall into three groups: 1) planar image measurements in ideal planes of section

following Martin (1983); 2) three-dimensional volumes and surface areas following Kono (2004) and Tafforeau (2004), in addition to some newly derived measurements; and 3) Cartesian coordinates describing the locations of enamel cusp tips, dentine horn tips, and the tips of pulp horns (i.e., the most occlusal point at which the pulp chamber extends at each cusp. From the third set of measurements, the true three-dimensional thickness of enamel cusp tips and the underlying dentine horns were derived, and the occlusal polygon and its associated intercuspal angles (following Bailey, 2004), which serve to discriminate modern *Homo* molars from Neandertal molars, was also recorded. These coordinates also allow for the shape of the dentine component of the molar crown to be quantified, which is regarding by some as having taxonomic value (e.g., Korenhof, 1960; Olejniczak et al., 2004).

*Two-Dimensional Measurements*

Two ideal planes of section were recorded: the mesial ideal plane (coursing through the dentine horn tips of the metaconid and the protoconid) and the distal ideal plane (coursing through the dentine horn tips of the hypoconid and the entoconid). The discussion of ideal plane location in Chapter 6 provides the basis for the identification of these planes using VoxBlast software (Vaytek, Inc.); the planes were recorded perpendicular to the plane defined by the dentine horn tips of the protoconid, metaconid, and hypoconid. Buccal and lingual ideal planes were not recorded due to their relatively oblique orientation, which is caused by substantial height differences between the shorter metaconid and the taller protoconid and hypoconid; these planes are also difficult to record in small, bulbous teeth where the buccal and lingual sides "curl under" the crown

because the cervix is compressed laterally. In this case, a ring of continuous enamel is created by taking a buccal or lingual section, and these sections are not useful for the present study, which assumes the presence of a bi-cervical diameter in each section. Once the mesial and distal ideal planes were produced, the following measurements (which follow Martin (1983)) were recorded using a digitizing tablet interfaced with SigmaScan software (SPSS Science, Inc.) (Figure 7.1):

1. The total area of the molar crown, in $mm^2$ (measurement *tota*). The total area of the molar crown above he bi-cervical diameter (see below).
2. The area of the enamel cap, in $mm^2$ (measurement *c*).
3. The area of coronal dentine (including pulp) contained within the enamel cap, in $mm^2$ (measurement *b*). This measurement is calculated as the total area of the crown (*tota*) minus the total area of enamel (*c*).
4. The bi-cervical diameter, in mm (measurement *bcd*).
5. The length of the enamel-dentine junction, in mm (measurement *e*).
6. Seven linear enamel thicknesses, in mm (measurements *e1 – e7*).
7. Average enamel thickness, in mm (measurement *aet*). This is the average straight-line distance between the enamel-dentine junction and the outer enamel surface, calculated as the quotient of enamel area (*c*) and enamel-dentine junction length (*e*): *aet* = [*c* / *e*].
8. Relative enamel thickness, a scale-free measurement (measurement *ret*). This is the average thickness of enamel (*aet*) scaled by a surrogate for tooth size (dentine area, measurement *b*), as in: *ret* = [*aet* / sqrt(*b*)] * 100. The square root of dentine area is used in order to eliminate the mm units from the result (as is appropriate in

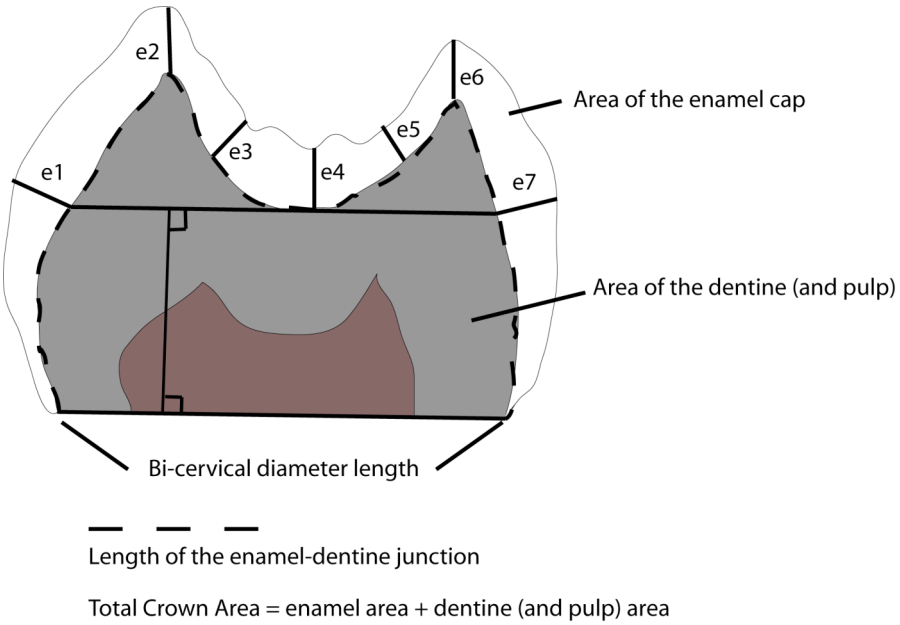


Figure 7.1: Schematic of a molar cross-section demonstrating the mesial and distal ideal plane measurements recorded in this study.

scaling equations); the result is multiplied by 100 in order to produce a scale above 1.0 for ease of comparison. Martin (1983) found that this is the most appropriate measurement for interspecies comparisons, where the size of each species' teeth must be taken into account.

The calculated values above were all performed using SPSS syntax (v11.0.4 for the Macintosh, SPSS Science, Inc.). A prefix of either *mes* (indicating mesial) or *dis* (indicating distal) was placed before each variable name in order to indicate whether the calculation is being performed on the mesial or distal ideal plane of section. The syntax text used in producing the calculated measurements appears in Appendix C. All of the two-dimensional measurements recorded in this study appear in appendices D and E.

*Three-Dimensional Measurements*

Martin (1983) noted that the two-dimensional enamel thickness measurements he derived were basically surrogate measurements in light of not having sufficiently accurate technology at the time of his writing in order to produce complete three-dimensional renderings and measurements of the molar crown and its internal structures. In this way, the area of the enamel cap in cross-section (measurement *c*) represents the volume of the enamel cap, the length of the enamel dentine junction in cross-section (measurement *e*) represents the surface area of the enamel-dentine junction, and so on. Thus in addition to quantifying the molar morphology of the focal taxa in three dimensions to attempt to discriminate dietary proclivity from phylogenetic propinquity, a major impetus of the present study is to compare three-dimensional measurements of molar morphology to planar sections in order to quantify differences due to not having the third, mesial-to-distal dimension in previous planar studies. The measurements recorded are as follows, borrowing from both Kono (2004) and Tafforeau (2004), and making additions and changes to their measurements as noted:

1. The volume of the enamel cap, in $mm^3$ (Figure7.2; measurement *evol*). This measurement was made using Slicer3D software, after homogenizing the enamel cap pixel values via median and anisotropic diffusion filtering (see Chapter 5 of this dissertation). The enamel above the basal plane (see below) was selected via thresholding; any errors in the threshold process were detected and fixed (i.e., parts of the dentine or background that were also selected as part of the thresholded region were de-selected, and any holes in the enamel cap were filled with the thresholded values). Slicer3D then counts the number of thresholded

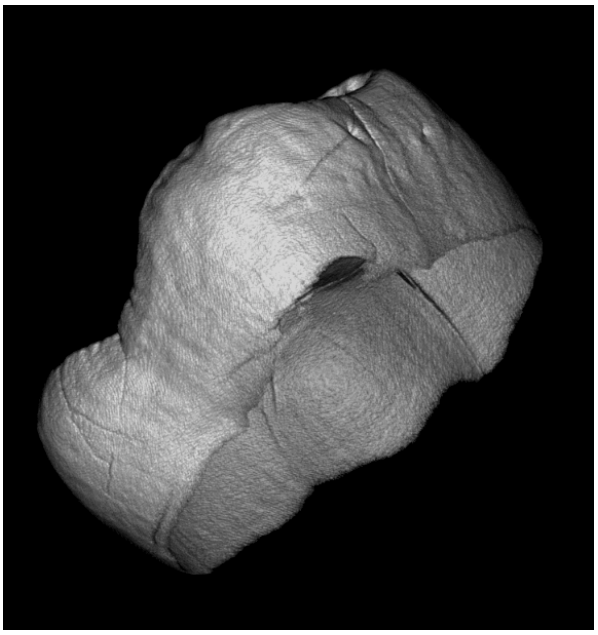

Figure 7.2: Volume rendering of the enamel cap of a *Pongo* molar. The dentine component of the tooth has been removed via segmentation.

voxels and multiplies by the cubic (volumetric) dimension of each voxel. For instance, if 100 voxels are selected, and each voxel is 0.5 x 0.5 x 0.5 mm, then the enamel volume is said to be [100 x 0.5 mm x 0.5 mm x 0.5 mm] = 12.5 $mm^3$.

2. The volume of the entire crown, in $mm^3$ (Figure 7.3; measurement *totvol*). This measurement was made using Slicer3D software. The entire crown, above the basal plane, was selected via thresholding; any errors in the threshold process were detected and fixed as above for measurement *evol*. Slicer3D then counts the number of thresholded voxels and multiplies by the cubic (volumetric) dimension of each voxel, as in measurement *evol*, above, thus yielding the volume of the total crown.
3. The volume of coronal dentine (including the pulp contained within the enamel cap), in $mm^3$ (measurement *dvol*). This measurement is calculated as the

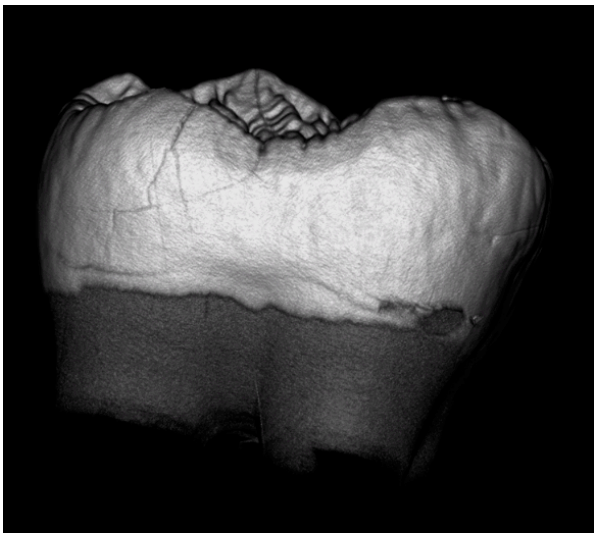

Figure 7.3: Volume rendering of the entire crown of a *Pongo* molar. Inferior to the cervical margin of the molar, the dentine component of the tooth can be seen as a darker shade of gray. Only the dentine contained within the enamel cap is measured as part of the total crown volume (i.e., the root dentine is not measured).

difference between the total crown volume (*totvol*) and the enamel volume (*evol*), as in: *dvol* = [*totvol* – *evol*].

4. The area of the basal plane, in $mm^2$ (Figure 7.4; measurement *basarea*). This measurement is the three-dimensional counterpart to the bi-cervical diameter (measurement *bcd*). In order to locate this plane, the image stack representing each tooth was imported into VoxBlast software (Vaytek, Inc.). The most apical plane of section containing a continuous ring of enamel at the cervix of the tooth was located. By definition, there is only one such plane, so no human decision regarding the orientation of this plane must be made. Next, the linear distance between this plane and the most apical plane that is both parallel to the continuous ring of enamel and which contains the most apical extension of enamel was calculated. Then, the mid-point between this plane and the plane containing a continuous ring was fit to the model, and it is this plane (midway between the

plane containing a continuous ring of enamel and that which contains the most apical extension of enamel) that is regarded as the basal plane (Figure 7.4). An important difference exists between the plane as defined here and as defined by Kono (2004). Kono used the plane of section containing the most apical continuous ring of enamel, thus Kono's plane cuts off the dentine associated with the entirety of any enamel extensions. As enamel extensions are highly variable, this may be regarded as a decision that reduces variation in dentine volume due to enamel extensions (as the basal plane is moved apically, the volume of dentine recorded above this plane increases substantially). Nonetheless, in the taxa examined in the present study, there was a particular pattern of enamel extension that was manifest in a majority of cases: the enamel extended apically at the buccal and lingual convexities of the teeth, and eliminating these extensions would result in the removal of a substantial volume of enamel. Thus, the choice was made to include one half of the length of the apical enamel extensions as a compromise between including too much dentine in the volume calculation because of the extensions, and too little dentine. With these considerations in mind, the basal area was defined at the midpoint between the plane containing a continuous ring of enamel and that containing the most apical extension of enamel. Once this plane was located, the image was exported and its planar area measured using NIH ImageJ software.

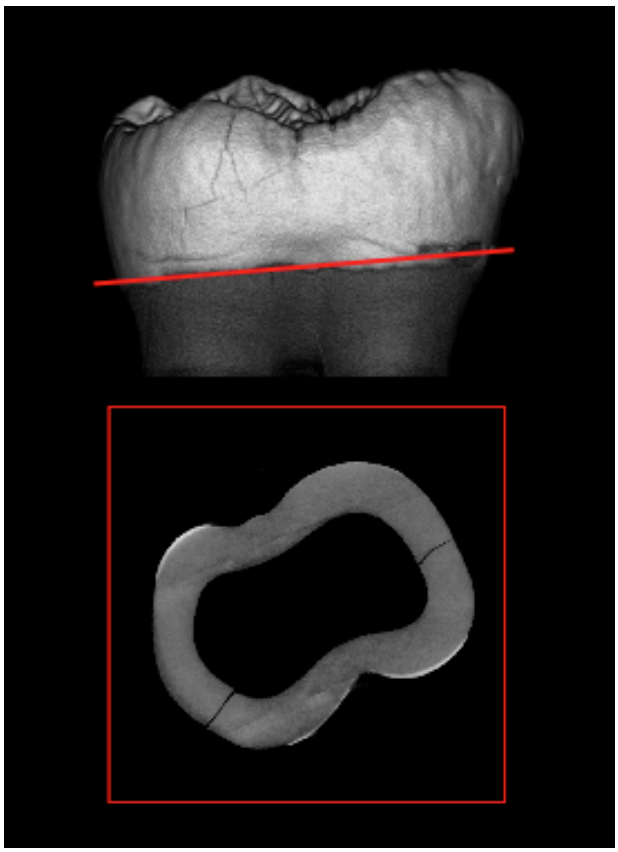

Figure 7.4: The same volume rendering of the entire crown of a *Pongo* molar as in Figure 7.3. The red square in the top image marks the location of the basal plane; this plane is shown in the lower image, where the cervical extensions of enamel may be seen in some areas at the periphery.

5. The surface area of the entire crown, in $mm^3$ (measurement *totsa*). This measurement was made using Slicer3D software. The entire crown, above the basal plane, was selected via thresholding; any errors in the threshold process were detected and fixed as above for measurements *evol* and *dvol*. A surface model of the entire crown was produced (using smoothing and decimation values of 20 and 1, respectively). After creation of the surface model, the total surface area of the model was measured and recorded.
6. The surface area of the outer enamel surface (OES), in $mm^2$ (measurement *oessa*). This measurement represents the entire surface area of the OES, and it is

calculated from other measurements. The surface area of the whole crown can be thought of as the basal area plus the surface area of the OES, and so the total crown surface area (*totsa*) minus the basal area (*basarea*) was calculated in order to produce *oessa*.

7. The total enamel surface area, in $mm^2$ (measurement *totesa*). This measurement represents the entire enamel cap surface area, which is defined as the OES surface area (*oessa*) plus the enamel-dentine junction surface area (see below). This measurement was made using Slicer3D software. The entire enamel cap above the basal plane was selected via thresholding; any errors in the threshold process were detected and fixed as above for measurement *evol*. A surface model of the entire enamel cap was produced (using smoothing and decimation values of 20 and 1, respectively). After creation of the surface model, the total surface area of the model (*totesa*) was measured and recorded.
8. The surface area of the enamel-dentine junction, in $mm^2$ (measurement *edjesa*). This measurement represents the entire surface area of the EDJ (the internal aspect of the enamel cap or the external aspect of the coronal dentine); this is a calculated measurement. Because the total enamel surface area (*totesa*) is known, as is the OES surface area (*oessa*), *edjsa* may be calculated by subtracting *oessa* from *totesa*.
9. Average enamel thickness, in mm (measurement *aet3d*). As is the case in its two-dimensional counterpart, the average enamel thickness is the average straight-line distance between the enamel-dentine junction and the outer enamel surface. This

is calculated as the quotient of the enamel volume (*evol*) and the enamel-dentine junction surface area (*edjsa*): *aet3d* = [*evol* / *edjsa*].

10. Relative enamel thickness, a scale-free measurement (measurement *ret3d*). As in two-dimensional *ret*, this is the average enamel thickness (*aet3d*) scaled by a the dentine core volume in order to make scaled, size-free comparisons: *ret3d* = [*aet3d* / cubert(*dvol*)]*100. The cube root is used in order to make the result scale-free as is appropriate for interspecies comparisons; the result is multiplied by 100 for ease of interpretation, setting the scale of the results above 1.0.

The calculated values above were all performed using SPSS syntax (v11.0.4 for the Macintosh, SPSS Science, Inc.). The syntax used in producing the calculated measurements appears in Appendix C. All of the three-dimensional measurements recorded in this study appear in Appendix F.

*Cartesian Coordinates and Related Measurements*

In addition to the planar and three-dimensional measurements discussed above, the locations (expressed in Cartesian coordinates) of twelve anatomical landmarks were located on each molar, using VoxBlast software (Vaytek, Inc.). These coordinates included the location of the four major enamel cusp tips, the location of the dentine horn tips of each of the four major cusps, and the tip of the pulp horn associated with each cusp (the pulp chamber of molars follows roughly the same contour as the enamel-dentine junction; at the location of each cusp, a small "horn" of pulp extends towards the cusp tip). Dentine thickness may then be measured as the distance between the pulp horn and the dentine horn of a particular cusp, in the same way that enamel thickness may be

measured as the distance from the dentine horn tip to the enamel cusp tip. From these Cartesian coordinates, each intercuspal distance was calculated, as well as each inter-cuspal angle (e.g., the protoconid angle is defined as the angle at the vertex of lines connecting the metaconid to the protoconid, and the protoconid to the hypoconid). These measurements were repeated using the dentine horn tips. Finally, the landmarks collected were used to make inter-taxon comparisons of the shape of the polygon formed by connecting the dentine horns in each taxon, and the shape of the polygon formed by the enamel cusp tips, serving as a comparison of the relative efficacy of the enamel-dentine junction and the outer enamel surface to discriminate species. The calculated values above were all performed using SPSS syntax (v11.0.4 for the Macintosh, SPSS Science, Inc.). The syntax used in producing the calculated measurements appears in Appendix C. All of the measurements calculated from Cartesian coordinates in this study appear in appendices G-J.

**Sexual Dimorphism in Three-Dimensional Enamel Thickness Measurements**

Odontometric analyses have shown that molars of humans and other primates display varying degrees of sexual dimorphism in terms of their length and breadth (e.g., appendices within Swindler, 2005). Nonetheless, sexual dimorphism has not been detected in measurements of absolute enamel thickness, nor is sexual dimorphism evident in relative enamel thickness (i.e., enamel thickness scaled to tooth or body size), although few studies have directly tested male and female differences (Macho and Berner, 1993; Smith et al., in press). Gantt et al. (2001) presented data suggesting that human female deciduous molars may possess thicker enamel than male deciduous molars. As noted by

*Table 7.2: Results (2-tailed significance values) of Mann-Whitney tests for sexual dimorphism in 3D measurements.*

| Taxon | Total Coronal Volume | Enamel Volume | Dentine Volume | Total Coronal Surface Area | Total Enamel Surface Area | EDJ Surface Area | Outer Enamal Surface Area | Basal Area | Average Enamel Thickness | Relative Enamel Thickness |
|---|---|---|---|---|---|---|---|---|---|---|
| *Alouatta* | 0.139 | 0.441 | 0.173 | 0.139 | 0.515 | 0.953 | 0.173 | 0.767 | 0.515 | 0.859 |
| *Ateles* | 0.104 | 0.129 | 0.193 | 0.664 | 0.448 | 0.278 | 0.914 | 0.745 | 0.386 | 0.515 |
| *Hylobates* | 0.239 | 0.157 | 0.239 | 0.239 | 0.099 | 0.099 | 0.157 | 0.480 | 0.814 | 0.814 |
| *Symphalangus* | 0.132 | 0.247 | 0.203 | 0.298 | 0.643 | 0.643 | 0.247 | 1.000 | 0.355 | 0.487 |

Grine (2005), however, the treatment of data by Gantt et al. (2001) did not account for the statistical dependence of measurements, effectively exaggerating any actual differences between males and females.

The data collected in the present study show that sexual dimorphism is absent with regard to both average enamel thickness and relative enamel thickness (based on the three-dimensional measurements *aet3d* and *ret3d*; Figures 7.5 and 7.6). Moreover, Mann-Whitney tests (Conover, 1999) demonstrate that there are no significant differences between males in females for any of the three-dimensional measurements (Table 7.2). Thus, in accord with previous studies (e.g., Martin (1983), Shellis et al. (1998), Martin et al. (2003), Grine (2005), Smith et al., (in press)), sexes were combined in all of the analyses and comparisons that follow.

## Correspondence of 2D and 3D Measurements

### *The Utility of Surrogate (2D) Measurements to Describe the (3D) Molar Crown*

The majority of enamel thickness studies published in the last 23 years have relied on mesial ideal planes of section (e.g., Martin, 1985; Grine and Martin, 1988; Andrews and Martin, 1991; Beynon et al., 1998; Macho and Spears, 1999; Dean, 2000; Schwartz, 2000; Grine, 2002; Martin et al., 2003; Dean and Schrenk, 2003; Smith et al., 2003, 2004, 2005; Grine et al., 2005). Martin (1983) suggested that "the ideal measurement of the quantity of enamel on a tooth would be the volume of the tissue," but in light of technological obstacles preventing the non-destructive measurement of enamel volume

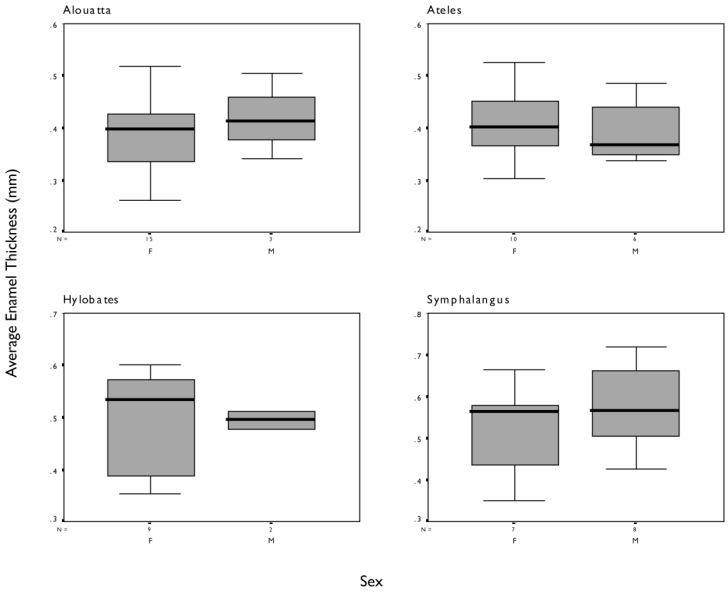


Figure 7.5: Box-plots depicting the three-dimensional average enamel thickness in male and female specimens of each species. There is no significant sexual dimorphism.

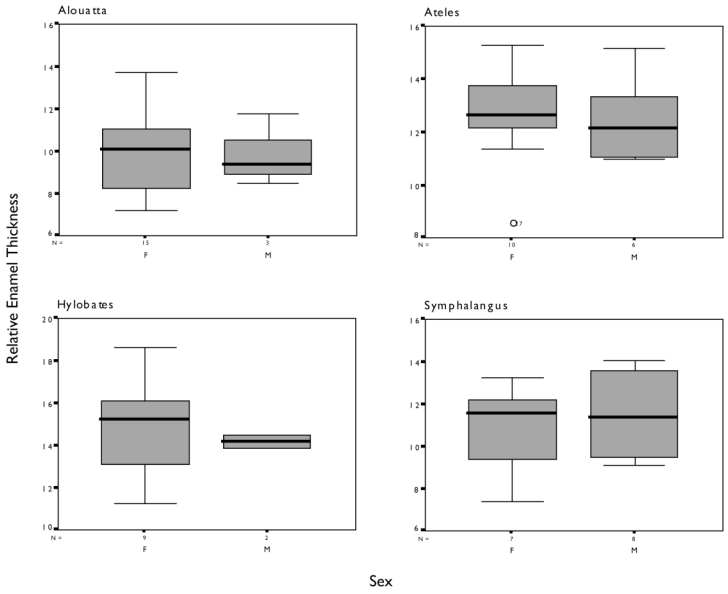


Figure 7.6: Box-plots depicting the three-dimensional relative enamel thickness in male and female specimens of each species. There is no significant sexual dimorphism.

and other aspects of molar morphology at the time of his writing, two-dimensional surrogate measurements in the mesial section plane were devised (also discussed in Chapter 1 of this dissertation). The data collected in the present study facilitates an assessment of whether these surrogate measurements are indeed representative of the structures they are meant to represent. Thus, to examine the relationship between each mesial two-dimensional measurement that is a component of the relative enamel thickness index and its three-dimensional counterpart, a series of linear regression analyses were performed. Pairs of variables tested can be seen in Figure 7.7. The inclusion of the basal area and bi-cervical diameter in this list stems from the recent advocacy of these measurements as scalars in lieu of dentine area by some scholars (e.g., Schwartz, 2000; Grine, 2002).

The three components of relative enamel thickness (enamel area (volume), EDJ length (surface area), and dentine area (volume)) as well as the bi-cervical diameter (basal area) show significant positive regression results, suggesting that the mesial plane of section captures the morphology of the entire crown with some predictability (Figure 7.7). When average enamel thickness index is examined, however, the regression plot appears more scattered than those of the individual measurements, although the regression equation is also significant (Figure 7.8). The relative enamel thickness index regression plot shows an even more scattered distribution, although this regression was also significant (Figure 7.8). It is also clear that the relationship between two- and three-dimensional average enamel thickness and relative enamel thickness follows a different pattern in *Alouatta* than in the other taxa, such that the best-fit line for *Alouatta* has a

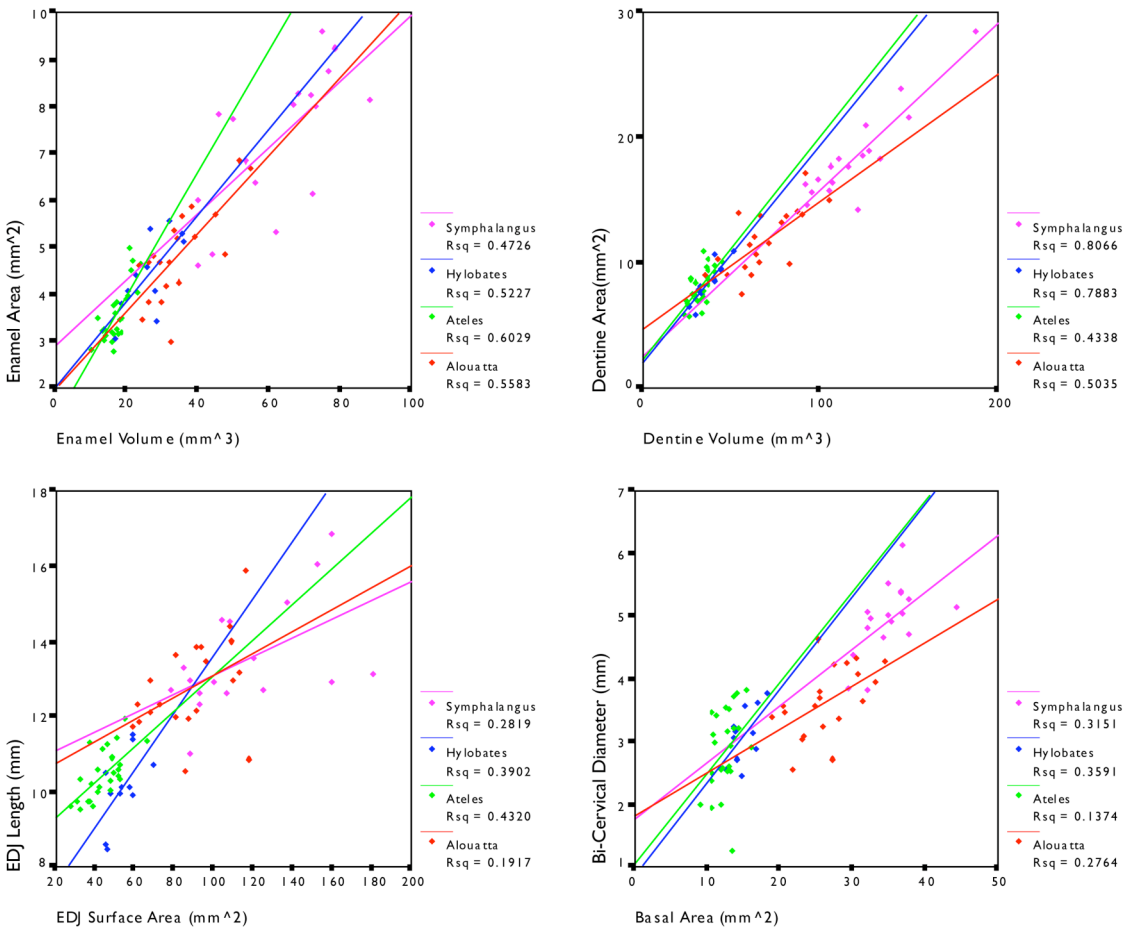


Figure 7.7: Regression plots of the 2D components of the relative enamel thickness index (and the bi-cervical diameter) and their 3D counterparts. R-squared for each genus appears in the figure legends.

slope close to zero in the average enamel thickness regression, and a negative slope in the relative enamel thickness regression.

The former result, that the average and relative enamel thickness indices evince a less organized scatter than the component variables that they summarize, may be explained by the compounding of errors (deviations from the best-fit line) as indices are compiled. Slight deviations from the best-fit line for dentine area and dentine volumefor instance, combined with the deviation from the enamel thickness and enamel volume line, results in the combination of multiple sources of error resulting in greater deviations

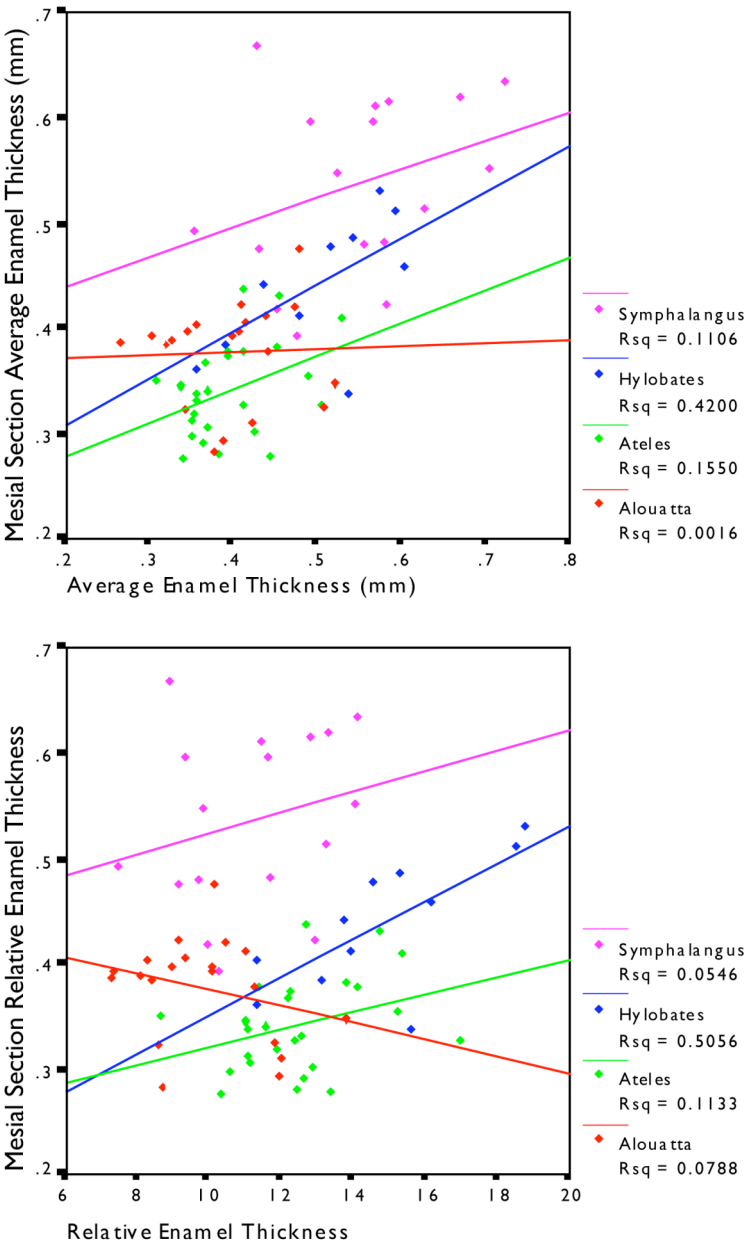


Figure 7.8: Regression plots of 2D and 3D average enamel thickness and relative enamel thickness. R-squared for each genus appears in the figure legends. Note that these plots are much more scattered than those of the component variables of these indices, pictured in Figure 7.7.

from the best-fit lines. Because each of the components shows a positive relationship between the two- and three-dimensional measurements, it follows that each individual molar is not uniform in its relationship to the best-fit line for each variable. That is to say, a single specimen may have a lower than expected enamel volume given the enamel area, and a higher then expected EDJ length given the EDJ surface area, for example. An individual molar's deviations from the best-fit line are not consistent between variables so the combination of deviations is detectable in the widely scattered average and relative enamel thickness plots.

The inconsistency of directional deviations from the best-fit line between two- and three-dimensional measurements is especially manifest in *Alouatta* molars, where the average and relative enamel thickness indices do not show the same positive slope tendency as each of the component variables. This is most likely due to the particularly low $R^2$ value for the enamel-dentine junction regression (also manifest to a lesser extent in *Symphalangus* molars). Because the length (surface area) of the EDJ is the scalar of enamel area (volume) in both enamel thickness indices, this variable may influence the weak correlation in *Alouatta* molars. Inconsistencies between two- and three-dimensional EDJ measurements in *Alouatta* demonstrate that as EDJ surface area becomes greater, EDJ length does not increase at the same rate; it has been documented that the dentine surface of molars of folivorous taxa show more accentuated crests than do frugivorous species' molars, as these crests may act as shearing surfaces when they are exposed through attrition (e.g., Korenhof, 1960; Corruccini, 1987; Shimuzu, 2002). This explanation is particularly appealing because *Symphalangus* molars also show a relatively weak relationship between the EDJ variables, and tend to also have lower

slopes than the primarily frugivorous taxa for the average and relative enamel thickness indices. In sum, the length of the EDJ appears not to capture the more complex crests apparent on the molars of folivores, rendering their two- and three-dimensional enamel thickness index measurements less comparable than those of frugivores, in which the EDJ morphology more closely resembles that of the enamel surface.

The results presented here are in general agreement with those of Kono (2004), who found that average enamel thickness recorded in both two- and three-dimensions do not necessarily convey the same information. Kono reasoned that local variations in enamel thickness are exacerbated in two-dimensional sections (i.e., the mesial ideal plane); moreover, local variations in enamel thickness at locations other than the mesial ideal plane may be missed when only this section is examined. The comparison of two- and three-dimensional average enamel thickness depicted in Figure 7.8 may be explained in part by these local variations in thickness. Additionally, based on the evidence presented above, it is likely that the morphology of the EDJ is also responsible for dimensional differences in average and relative enamel thickness, as this scalar may be variably smooth or complex in different species, and a two-dimensional representation of this structure may not capture its relative complexity. Following the recent conclusion of Kono (2004), and the original supposition of Martin (1983), the data examined here suggest that three-dimensional measurements are less influenced by local variations in thickness and surface area complexity than their two-dimensional counterparts, and are therefore better suited as descriptors of the entire crown. Nonetheless, it is important to note that the most comprehensive analyses of great ape molars (in terms of sample size) in two-dimensions (Smith et al., 2005) and three-dimensions (Kono, 2004) demonstrate

the same overall enamel thickness patterns, such that *Gorilla* molars have thinner enamel than those of *Pan* (but with overlapping ranges), which has slightly thinner enamel than *Pongo* (but with overlapping ranges). Two-dimensional proxies thus have served to capture broad species-level trends in enamel thickness, although three-dimensional measurements are undoubtedly less influenced by local variations in shape and thickness, and should be preferred in future analyses.

*The Best Linear Predictors of Average Enamel Thickness*

Many fossil teeth are broken, worn, or cracked, and therefore cannot be volumetrically analyzed or sectioned in ideal planes in the same way that unworn molars may be studied (e.g., the Ad Dabtiyah maxillary dentition, Andrews and Martin, 1987b; the Shanidar 3 Neandertal maxillary third molar, Olejniczak and Grine, 2005). In these instances, it is useful to know whether there are certain areas of the enamel cap that provide useful proxy measures of total crown enamel thickness. These regions may act as predictors of the entire crown enamel thickness, allowing fragmentary and worn fossils to be included in comparative analyses. In order to identify such regions, a series of forward stepwise regression analyses were performed (Tabachnick and Fidell, 2001).

Stepwise regression (a.k.a. "statistical regression") is a useful method for the identification of the order of importance of independent variables in the prediction of a dependent variable. Independent variables are entered into the regression model one at a time, beginning with the variable that explains the most variance in the dependent variable while controlling for the effects of the other independent variables (i.e., the independent variable with the highest partial correlation coefficient with the dependent

variable). Variables are continually added to the model until the next variable to be added does not contribute to the overall significance of the model. In this way, an ordered list of only those variables that have a significant relationship with the dependent variable is created.

A regression analysis was performed for each of the four species studied, and another analysis was performed using the entire sample. In each case, the dependent variable was average enamel thickness (*aet3d*); the linear measurements of enamel thickness from both the mesial and distal ideal planes (14 total measurements: mesial and distal variables *e1-e7*) were independent variables, seeking to identify the best linear predictor(s) of overall crown average enamel thickness. All analyses were performed using SPSS software (Macintosh v11.0.4, SPSS Science, Inc.).

Results of the stepwise regression performed on the entire sample show that there is a single best predictor of average enamel thickness: the lateral enamel thickness of the disto-buccal cusp (hypoconid). After this variable was entered into the model as the first step, $R^2 = 0.543$, $F\ (1, 71) = 84.500$, and $p < 0.001$. Also adding significance to the entire regression model was the second step, at which point the thickness of the disto-lingual (entoconid) cusp tip was entered. After this step, $R^2 = 0.603$, $F\ (2, 70) = 53.204$, and $p < 0.001$. The change in $R^2$ from step one to step two is only 0.060, but this addition was significant. After these two variables were added to the model, no other variables contributed significantly to the prediction of average enamel thickness. That is to say, when statistically controlling for the correlation of all the independent variables with each other, only the lateral thickness of the disto-buccal cusp and the cusp tip thickness of the disto-lingual cusp are significant predictors of three-dimensional average enamel

thickness. Figure 7.9 shows the relationship between the disto-buccal cusp lateral enamel thickness and average enamel thickness.

When taxa were examined individually, results again point towards measurements of the distal aspect of the molar as significant predictors of average enamel thickness. The stepwise regression of *Alouatta* did not result in any significant predictors of average enamel thickness, so no ordered list of independent variables added to a regression model may be shown. The regression of *Ateles* molars showed that the first step added the thickness of the disto-buccal cusp lateral wall ($R^2 = 0.338$, $F$ (1, 23) = 11.795, and $p = 0.002$). The second and last step of the *Ateles* regression added the thickness of the occlusal wall of the disto-buccal cusp ($R^2 = 0.462$, $F$ (2, 22) = 9.453, and $p = 0.001$). The *Symphalangus* regression involved only one step, adding only the lateral wall thickness of the disto-buccal cusp, and did not result in a particularly low $p$-value, unlike the *Ateles* regressions ($R^2 = 0.258$, $F$ (1, 15) = 5.227, and $p < 0.037$).

The *Hylobates* regressions involved more steps (and therefore more significant predictors of average enamel thickness), but the overall trend of distal aspects of molar morphology predicting the average enamel thickness was evident. The first step of this regression involved the addition of the disto-lingual cusp lateral wall enamel thickness ($R^2 = 0.828$, $F$ (1, 9) = 43.439, and $p < 0.001$). The second step added the enamel thickness of the mid-occlusal basin in the distal ideal plane ($R^2 = 0.965$, $F$ (2, 8) = 137.087, and $p < 0.001$). The third step added the thickness of the occlusal aspect of the disto-lingual cusp ($R^2 = 0.992$, $F$ (3, 7) = 280.100, and $p < 0.001$). The fourth step added the thickness of enamel of the disto-lingual cusp tip ($R^2 = 0.996$, $F$ (4, 6) = 404.630, and $p$

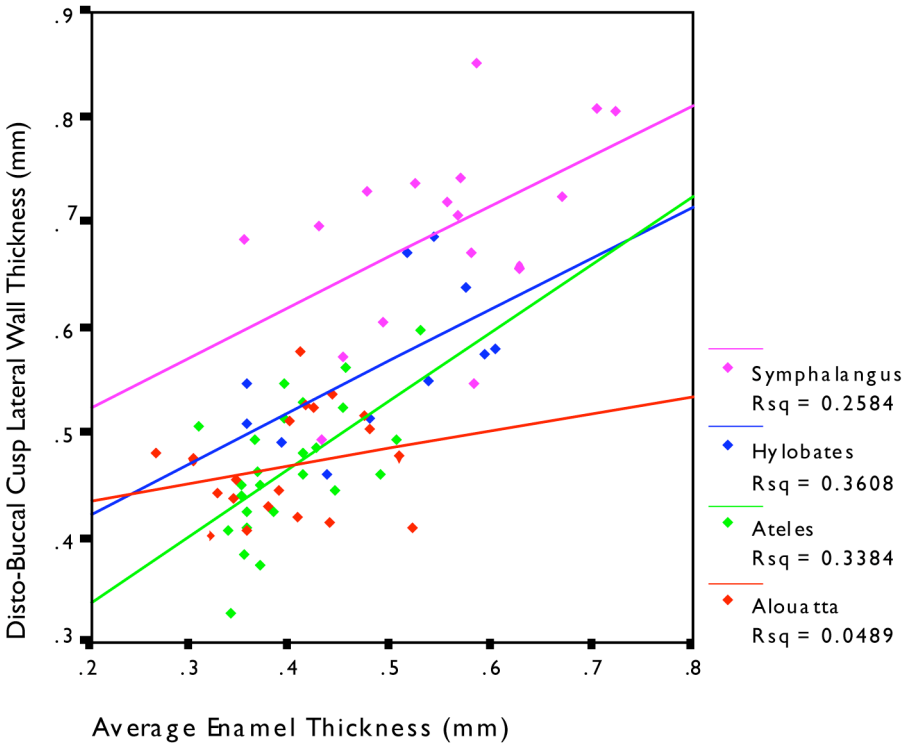


Figure 7.9: Regression plot showing the linear enamel thickness of the disto-buccal cusp lateral wall versus 3D average enamel thickness. In a stepwise regression analysis, this linear measure of enamel thickness was the best predictor of 3D average enamel thickness; other distal linear thickness measurements were also superior to mesial measurements, overall.

< 0.001). The fifth and final step added the lateral wall thickness of the disto-buccal cusp ($R^2 = 0.999$, $F$ (5, 5) = 739.618, and $p < 0.001$).

In sum, stepwise regressions with average enamel thickness as the dependent variable show highly significant results in the primarily frugivorous taxa, and either less significant (*Symphalangus*) or non-significant (*Alouatta*) results in the primarily folivorous taxa. In all cases where significance was achieved, the best predictors of total crown average enamel thickness are located in the distal aspect of the molar. Martin (1983) experimented with sections through molars at multiple locations, including sections coursing through the mesio-distal axis of a molar and some coursing through the

two distal cusps, analogous to the distal ideal plane studied here. Martin (1983, 1985) chose, however, to base his primary analysis on only mesial cusp sections, citing a desire to make as few sections through each tooth as possible, and the relative ease of minimizing the area of enamel relative to the area of dentine in this plane of section. Gantt (1977) also studied mesial cusp sections, and presumably mesial section planes in Martin's study facilitated comparisons between the two datasets. Martin (1983: page 160) notes, "Gantt (1977) sectioned teeth from buccal to lingual through the mesial cusps and I have also concentrated on this plane as it is difficult to produce a reliable section through the distal cusps of lower molars."

In any case, superiority of mesial section linear enamel thickness measurements as proxies of total crown average enamel thickness is not supported by the data presented here, which uniformly show that aspects of distal enamel thickness are better predictors of overall crown average enamel thickness when significance is achieved. It is likely, however, that the specific combination of linear enamel thickness variables that best predict overall crown average enamel thickness is species-specific, and neither Martin (1983) nor Gantt (1977) produced large samples of the species studied here, so a direct comparison is not possible. Moreover, Kono (2004) has recently demonstrated that three-dimensional measurements of average enamel thickness in extant hominoids separate taxa in approximately the same way that mesial section planes do (cf. Smith et al., 2005), suggesting that mesial sections do capture much of the same signal as three-dimensional measurements. Nonetheless, when broken or worn fossil teeth are to be examined, the results presented here suggest that distal cusp linear enamel thickness measurements may

serve as better proxies for total crown average enamel thickness than mesial measurements.

The reason that distal measurements possess a greater predictive signal for average enamel thickness than mesial measurements is unclear. Few studies have explicitly examined mesial and distal sections from the same molars (e.g., Smith et al., 2005), and these planes of section have not been evaluated in light of the known whole crown average enamel thickness. The results of the overall regression point towards the thickness of enamel on both the hypoconid and the entoconid as the most significant predictors of overall crown average thickness, ruling out the possibility that the enamel thickness of one particular cusp is a uniquely good predictor of overall average thickness.

*The Best Linear Predictors of Enamel Volume*

The data presented above show that distal measurements tend to be better predictors of average enamel thickness than mesial measurements. The total volume of enamel on the molar crown, however, may provide a different signal than average enamel thickness. Average enamel thickness is scaled by the length of the EDJ, resulting in the average straight line distance between the EDJ and the outer enamel surface. Enamel volume has no relationship to the thickness of enamel, per se, in that the same volume of enamel could be spread across a larger (or smaller) EDJ, resulting in many possible enamel thicknesses. Because many fossils are broken or worn, and therefore do not lend themselves to the measurement of enamel volume, it is worthwhile to examine whether any particular measurement best predicts total enamel volume. To this end, a stepwise regression analysis was run. This regression was identical to that run above, except the

total enamel volume was used in lieu of the average thickness of enamel as the dependent variable.

A regression analysis was performed for each of the four species studied, and a fourth analysis was performed using the entire sample. In each case, the dependent variable was enamel volume (*evol*); the linear measurements of enamel thickness from both the mesial and distal ideal planes (14 total measurements: mesial and distal variables *e1-e7*) were independent variables. All analyses were performed using SPSS software (Macintosh v11.0.4, SPSS Science, Inc.).

Results of the stepwise regression performed on the entire sample show that there is a single best predictor of average enamel thickness: the occlusal enamel thickness of the disto-lingual cusp (entoconid). After this variable was entered into the model as the first step, $R^2 = 0.646$, $F\ (1, 71) = 132.269$, and $p < 0.001$. Also adding significance to the entire regression model was the second step, at which point the thickness of the mesio-buccal (protoconid) occlusal wall was entered. After this step, $R^2 = 0.705$, $F\ (2, 70) = 86.842$, and $p < 0.001$. The change in $R^2$ from step one to step two is 0.062, and this addition is significant ($p < 0.001$). After these two variables were added to the model, a third step added the thickness of the disto-buccal (hypoconid) lateral wall was entered. After this step, $R^2 = 0.722$, $F\ (3, 69) = 63.246$, and $p < 0.001$. The change in $R^2$ from step two to step three is 0.021, and this addition is significant ($p = 0.024$). No other variables contributed significantly to the prediction of enamel volume. That is to say, when statistically controlling for the correlation of all the independent variables with each other, only the occlusal thickness of the disto-lingual cusp, the occlusal thickness of the

mesio-buccal cusp, and the lateral thickness of the disto-buccal cusp are significant predictors of enamel volume.

When taxa were examined individually, results were not clearly in favor of any single variable best predicting enamel volume. The stepwise regression of *Alouatta* did not result in any significant predictors of enamel volume, so no ordered list of independent variables added to a regression model may be shown. The regression of *Ateles* molars showed that the first step added the thickness of the mesio-lingual cusp lateral wall ($R^2 = 0.372$, $F$ (1, 23) = 15.245, and $p = 0.001$). No other variables were added to the regression model. The *Symphalangus* regression also involved only one step, adding the occlusal wall thickness of the disto-lingual cusp ($R^2 = 0.557$, $F$ (1, 15) = 21.122, and $p < 0.001$). The *Hylobates* regression again involved only one step. This was the addition of the disto-lingual cusp lateral wall enamel thickness to the regression model ($R^2 = 0.617$, $F$ (1, 9) = 17.087, and $p = 0.003$.

In sum, stepwise regressions with enamel volume as the dependent variable show highly significant results when all taxa are combined. The results of the species-specific regressions, however, demonstrate that the variables identified in the overall model as the most significant predictors do not correspond to any one species. That is to say, each species has a different set of best predictors of enamel volume (except the non-significant regression for *Alouatta*) than the overall model. Unlike the results of the stepwise regressions using average enamel thickness as the dependent variable, the significant predictors of enamel volume were not entirely from the distal sections. These results cast doubt as to whether a predictive model of enamel volume based on local linear measurements exists for primates generally, and implies that each species must be treated

separately. Given these results, it is not possible to accurately ascertain the enamel volume of a fossil molar by looking at one or some combination of linear measurements without first knowing the relationships between linear and volumetric variables in that taxon.

*Mesial and Distal Section Measurement Correlation*

The results presented above show that measurements from the distal sections of teeth explain more of the variance in total crown average enamel thickness than measurements from mesial sections. It is relevant, nonetheless, to inquire whether distal and mesial planes of section correlate sufficiently that they may be used interchangeably. In the case of many broken fossil molars, only one of these planes of section is available for measurement. If both planes of section convey the same signal, then such fossil teeth might be added to enamel thickness analyses. To this end, a series of linear regressions were performed testing the mesial-distal relationships of five variables: enamel area, dentine area, enamel-dentine junction length, average enamel thickness, and relative enamel thickness.

Scatter plots of each pair of variables appear in Figures 7.10 and 7.11. In many cases significance was achieved, although the relationship between mesial and distal relative enamel thickness (as well as bi-cervical diameter) was not as strong as the relationships between some of the other variables. The regression of the area of the enamel cap produced an $R^2$ of 0.878 ($F$ (1, 71) = 516.931, $p < 0.001$). For dentine area, $R^2 = 0.842$ ($F$ (1, 71) = 385.684, $p < 0.001$); for enamel-dentine junction length $R^2 = 0.790$ ($F$ (1, 71) = 267.844, $p < 0.001$); for average enamel thickness $R^2 = 0.843$ ($F$ (1,

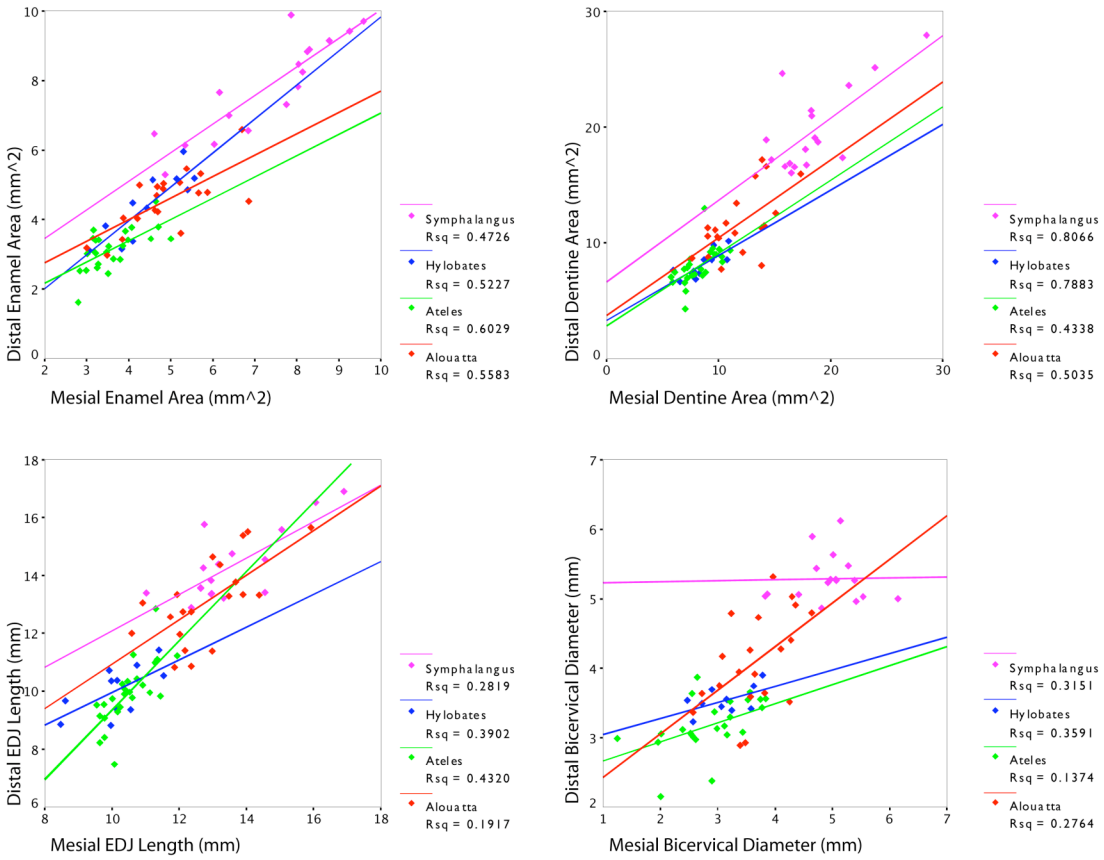


Figure 7.10: Regression plots of the 2D components of the relative enamel thickness index (and the bi-cervical diameter) in mesial and distal planes of section. R-squared for each genus appears in the figure legends.

71) = 387.578, $p < 0.001$); and for relative enamel thickness $R^2 = 0.581$ ($F$ (1, 71) = 100.654, $p < 0.001$).

The relative enamel thickness index fares worse than the other variables in terms of mesial-distal relationships, perhaps for the same reasons outlined above for 2D-3D correspondence (the RET index includes the measurement error of three other variables). Nonetheless, the regressions of the other variables, although significant, do not necessarily imply that one may simply include a distal measurement from a broken fossil

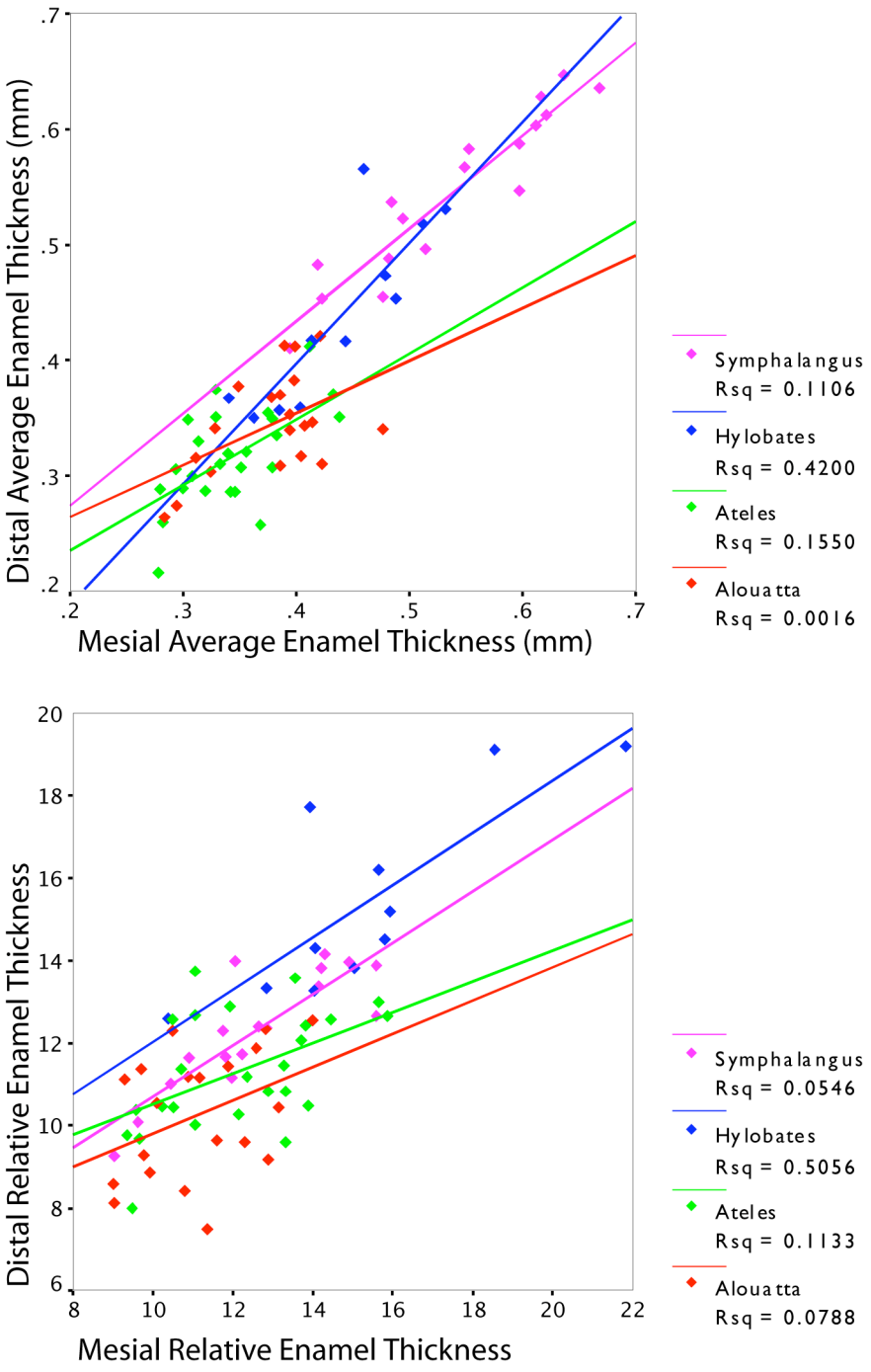


Figure 7.11: Regression plots of 2D and 3D average enamel thickness and relative enamel thickness. R-squared for each genus appears in the figure legends.

in an analysis of mesial sections. In the best case (enamel cap area) only 87.8% of the variance in one plane of section is explained by the other plane of section. This indicates

that at approximately 12% of the variance is unaccounted for. Although variance explained does not directly translate into confidence intervals, a conservative estimate of the confidence band for the prediction of one plane of section's enamel area from another would be ± 12%, which does not bode well for the substitution of one plane for the other.

The bi-cervical diameter, which is occasionally used as a scalar in enamel thickness studies, shows relatively little correspondence between mesial and distal sections with the exception of *Alouatta* molars (Figure 7.10), despite a significant result when the molar samples were combined for analysis. The regression results for this variable produced an $R^2$ of 0.818 ($F$ (1, 71) = 143.803, $p < 0.001$). This result suggests that the breadth of each molar at the locations of the mesial and distal planes are not the same within a taxon, with the exception of *Alouatta* molars which are longer and more narrow than those of the other taxa, and have a similar breadth in both the mesial and distal sections of the tooth. Although bi-cervical diameter is not often used as a scalar (but see Schwartz, 2000; Grine, 2002; Olejniczak & Grine, 2005), this result points towards an explanation of the other regression results presented here. That is, if the mesial and distal sections taken from a molar are not similar in terms of their basic shape (i.e., bi-cervical breadth), then it is unlikely that that they are representing homologous anatomical structures. If this is the case, then mesial and distal sections should not be included interchangeably in the same study, or taken to convey the same information, as noted above.

In sum, mesial and distal planes of section do not convey identical information. The regression results presented above indicate that not enough variance is explained to facilitate using one plane of section in lieu of another, or to compare different section

planes in the same analysis. Because distal measurements are superior at predicting the overall crown volumetric measurements, distal planes are to be preferred when the goal is to predict total crown enamel thickness from a broken specimen.

**Metamerism in Enamel Thickness Measurements**

Previous studies of enamel thickness typically have employed combined samples of molars from different positions, and sometimes from both the maxillary and mandibular tooth rows, such that the (relative) enamel thickness for a given taxon was an average of all the teeth of that taxon in the analysis (e.g., Martin, 1983, 1985; Dumont, 1995; Schwartz, 2000; Martin et al., 2003). Martin (1983) noted that an increase in the thickness of enamel from mesial to distal may exist, although his data did not demonstrate a substantial difference that would warrant separating teeth from different positions in analyses. A recent study by Hlusko (2002; see also Weiss, 1990), however, found that metameric variation (i.e., slight differences in morphology between adjacent, serial anatomical structures) in hominoid molars was detectable, and that it yields useful taxonomic information. When considered in light of masticatory models positing a functional discrimination of molars in different positions relative to the mandibular ramus (reviewed by Kono (2004) and Grine (2005)), it is possible that different molars may have different functional demands, and therefore different enamel thicknesses.

Grine (2002) and Smith et al. (2005) studied enamel thickness in ideal planes of human and extant great ape molars, respectively, testing for differences in enamel thickness between tooth positions (and the measurements that are components of the relative enamel thickness index). The results of Smith et al.'s (2005) study indicate that

substantial (and in some cases statistically significant) differences in enamel thickness occur between molars. Notably, there is an increase in the area of the enamel cap from M1 to M3, which coincides with a decrease in the area of dentine and the length of the enamel-dentine junction (see also Grine, 2002). Average enamel thickness therefore increases from the first to third molar, as does relative enamel thickness. These results indicate that combined samples of molars from different positions should be avoided in future analyses, echoing the conclusions of Macho and Berner (1993) and Grine (2002).

Data describing enamel thickness from a whole-crown, three-dimensional perspective are rare, and only Kono (2004) has examined three-dimensional enamel thickness at different tooth positions. In her study, the first and second molars (both maxillary and mandibular) of *Pan* and *Homo* were compared for differences in average enamel thickness (equivalent to measurement *aet3d* in this study); no significant difference was detected. This lack of significant differences between M1's and M2's stands in contrast to the results of Smith et al. (2005), obtained using planar sections. A possible explanation for Kono's lack of significant differences is her choice of parametric statistical tests (*t*-tests), which assume normality in the distribution of data. Small sample sizes render it likely that the probability theory underlying such a test will be violated (Conover, 1999). The asymptotic relative efficiency (A.R.E.; a comparative measure of the sample size required for reliable results for two different tests; see Noether, 1967) also demonstrates that the Mann-Whitney test is superior to the two-sample *t*-test as the *t*-test's efficiency atrophies rapidly as sample size decreases (Conover, 1999), such that small samples (e.g., Kono, 2004: Table 4) should be avoided when employing the *t*-test.

In light of previous findings suggesting that enamel thickness increases from M1 to M3 in planar sections, and functional models that may explain this metameric variation, one of the aims of the present study is to examine whether this pattern is also present when the whole crown is considered (i.e., aet3d and ret3d). In order to assess whether significant differences exist between molar types, the three-dimensional measurements recorded in this study were subjected to the Jonckheere-Terpstra test for trends. This rank-based (i.e., non-parametric) test is more appropriate for testing directional trends in data than an ANOVA or a Kruskal-Wallace test, which examine differences in the location of the mean of multiple groups without regard to direction (discussed in Smith et al., 2005). Table 7.3 shows the results of the Jonckheere-Terpstra test within each species. Similar to the findings of Kono (2004), no significant mesial-to-distal trend was identified. Figures 7.12-7.17, however, show that directional trends are apparent in certain measurements, despite their lack of significance. Figure 7.12 shows the total crown volume in each species at each molar position. There is a general tendency for the second mandibular molar to be the largest tooth, and the third mandibular molar to be the smallest tooth, although there is substantial overlap in the distributions of these measurements. Figures 7.12-7.14 show the volume of enamel, the volume of dentine, and the surface area of the enamel-dentine junction at each molar position in each taxon. In each species, there is a pattern of increasing mean enamel

*Table 7.3: Results (significance values) of the Jonckheere-Terpstra test for M1 to M3 directional trends in three-dimensional measurements.*

| Taxon | Total Coronal Volume | Enamel Volume | Dentine Volume | EDJ Surface Area | Average Enamel Thickness | Relative Enamel Thickness |
|---|---|---|---|---|---|---|
| *Alouatta* | 0,749 | 0,555 | 0,279 | 0,706 | 0,141 | 0,130 |
| *Ateles* | 0,454 | 0,945 | 0,107 | 0,617 | 0,545 | 0,465 |
| *Hylobates* | 0,641 | 0,966 | 0,431 | 0,381 | 0,217 | 0,229 |
| *Symphalangus* | 0,906 | 0,917 | 0,665 | 0,483 | 0,113 | 0,136 |

volume from M1 to M2, and decreasing mean enamel volume from M2 to M3. This pattern is repeated in the plot depicting dentine volume, with the exception of *Ateles* molars, in which the M1 and M2 show similar dentine volumes, while the M3 mean dentine volume is substantially smaller. The same pattern also describes the surface area of the enamel-dentine junction, although *Ateles* molars in this case show a steady decrease from M1 to M3 rather than a higher mean surface area at M2. Each of these patterns may be explained by tooth size (measured as total crown volume; Figure 7.12), as the volumes (and therefore the surface areas of those volumes) contribute to the total crown volume.

Enamel thickness indices (*aet3d* and *ret3d*), however, demonstrate that the relationships of these tissues and surfaces show a different pattern than simply indicating tooth size (Figures 7.16 and 7.17). Average enamel thickness shows a steady, non-significant increase from M1 to M3 (although the M3 of *Ateles* is has slightly thinner enamel on average than the M2); relative enamel thickness also increases from M1 to M3, but rather than the steady increase seen in average enamel thickness, the M3 tends to have substantially (but not significantly) greater relative enamel thickness (with the exception of *Ateles*, in which the M3 shows only slightly greater relative enamel thickness than the M2). These results are broadly comparable to those of Smith et al.

(2005), who also found a sharp increase in relative enamel thickness at the mandibular third molars in planar sections of extant great apes.

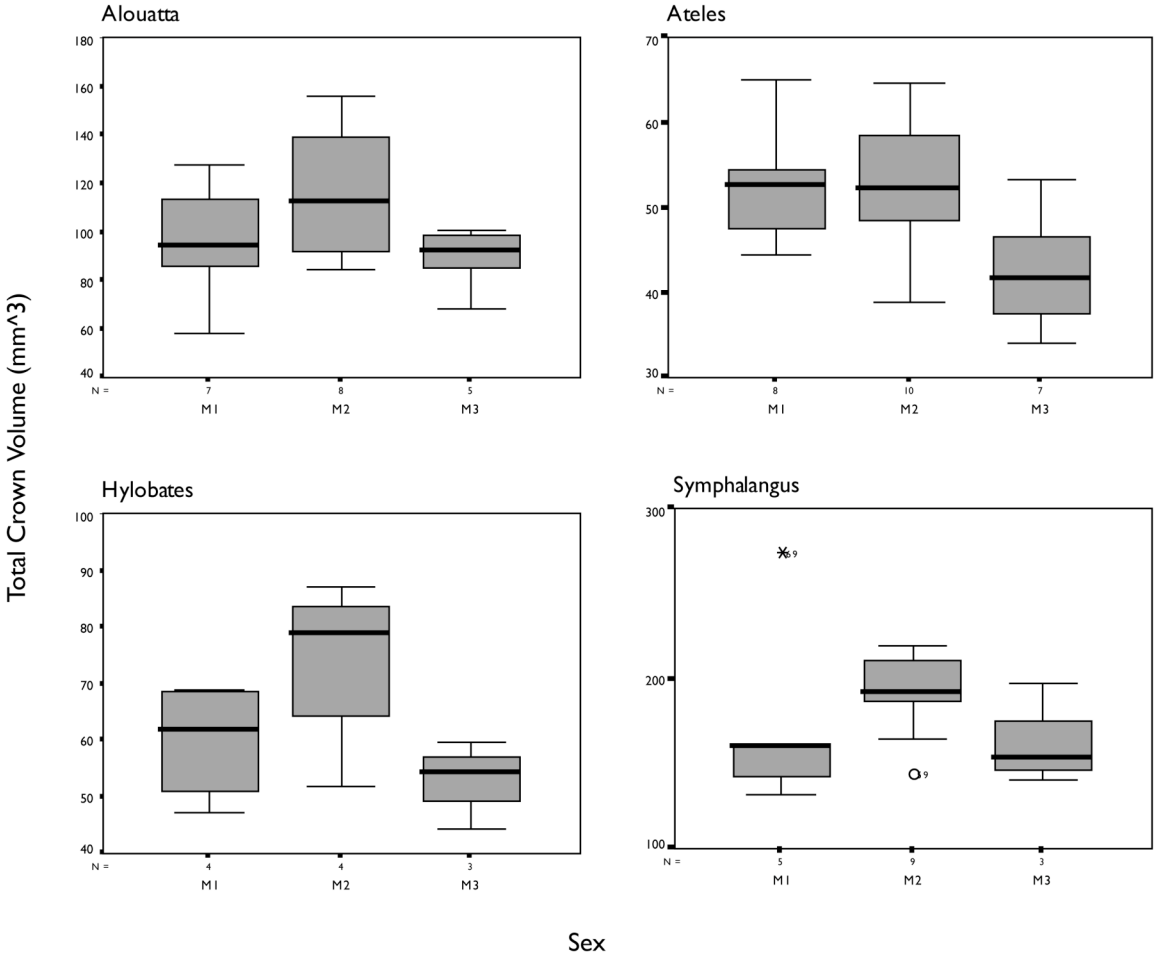


Figure 7.12: Box-plots showing the total crown volume in first, second, and third mandibular molars in each of the four species examined in this study. An asterisk indicates an extreme statistical outlier.

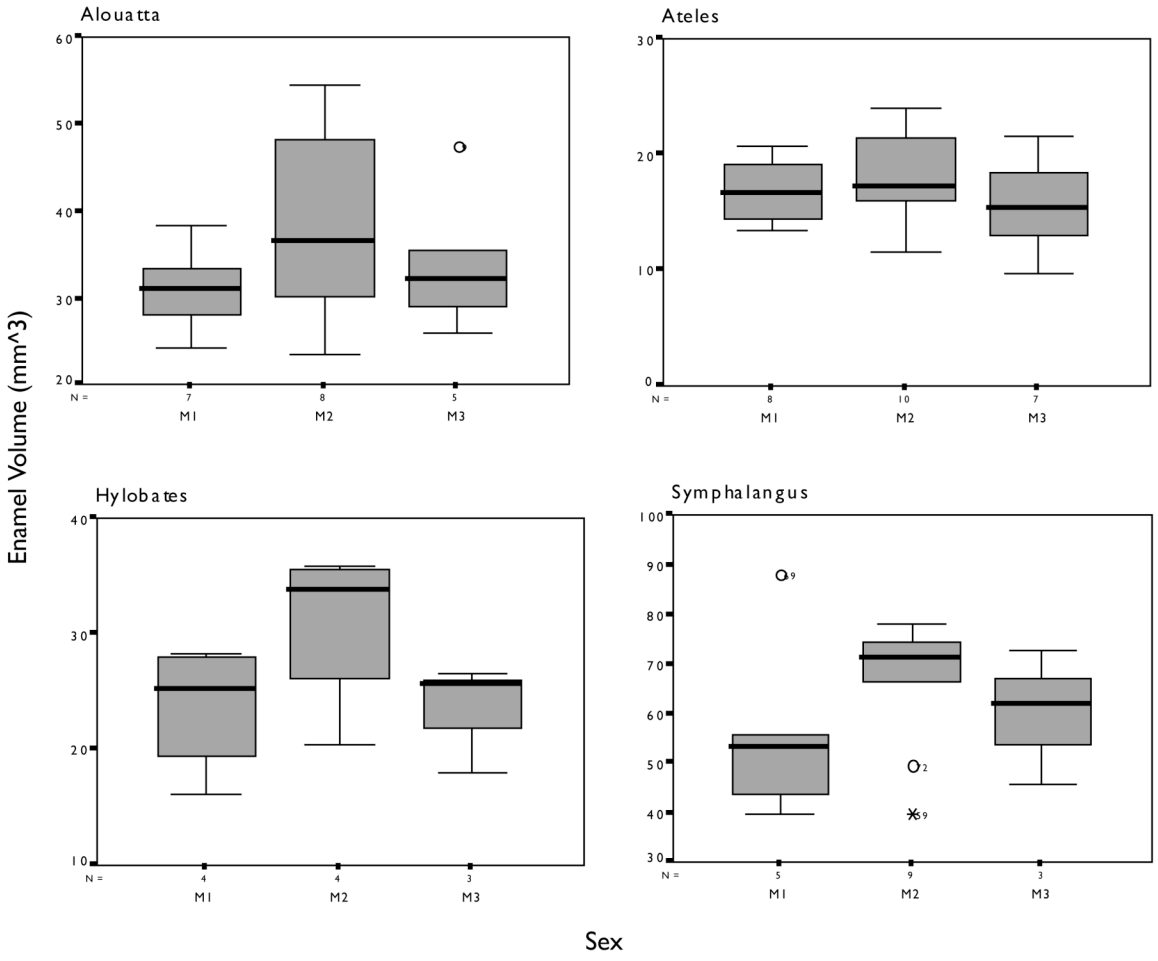


Figure 7.13: Box-plots showing the enamel volume in first, second, and third mandibular molars in each of the four species examined in this study. Circles indicate statistical outliers.

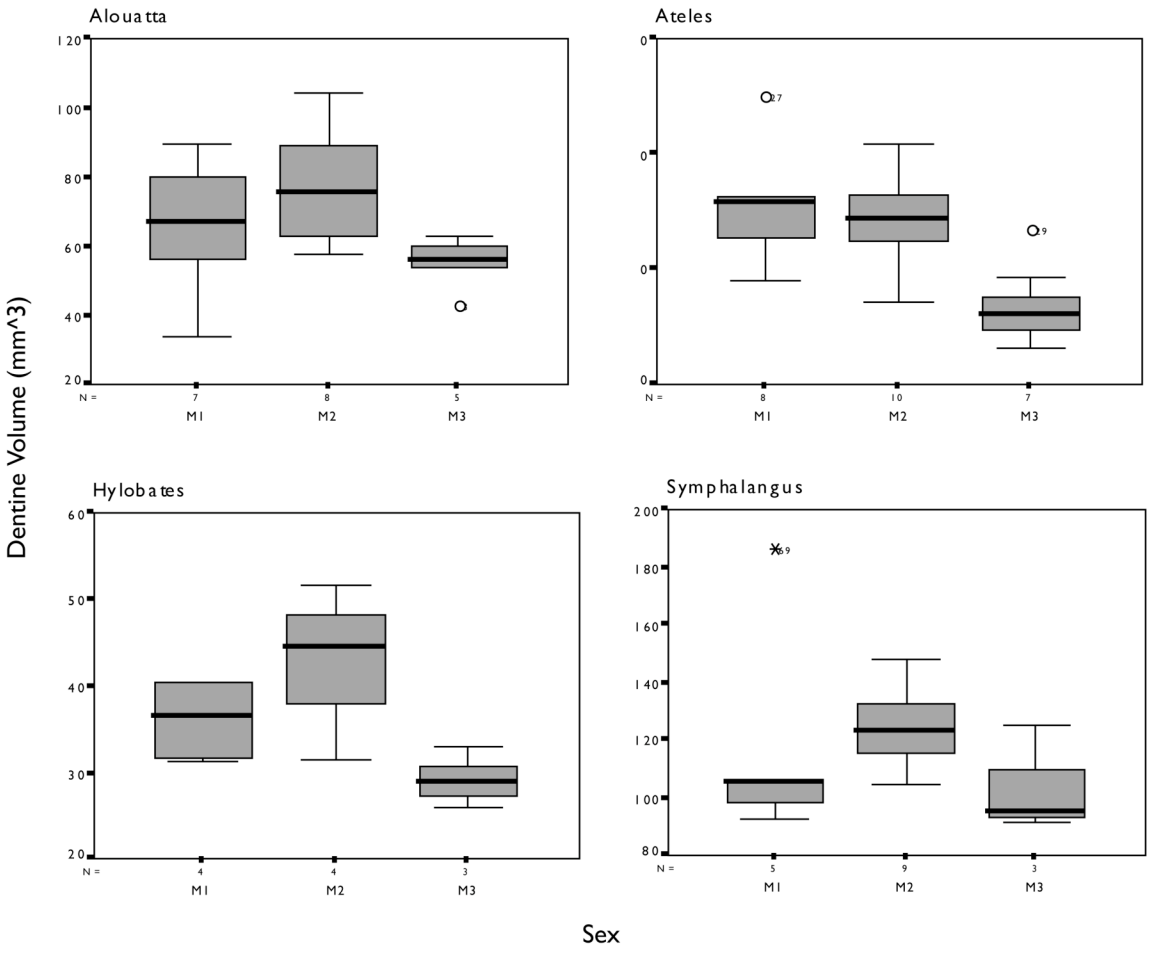


Figure 7.14: Box-plots showing the dentine volume in first, second, and third mandibular molars in each of the four species examined in this study. An asterisk indicates an extreme statistical outlier; circles indicate statistical outliers.

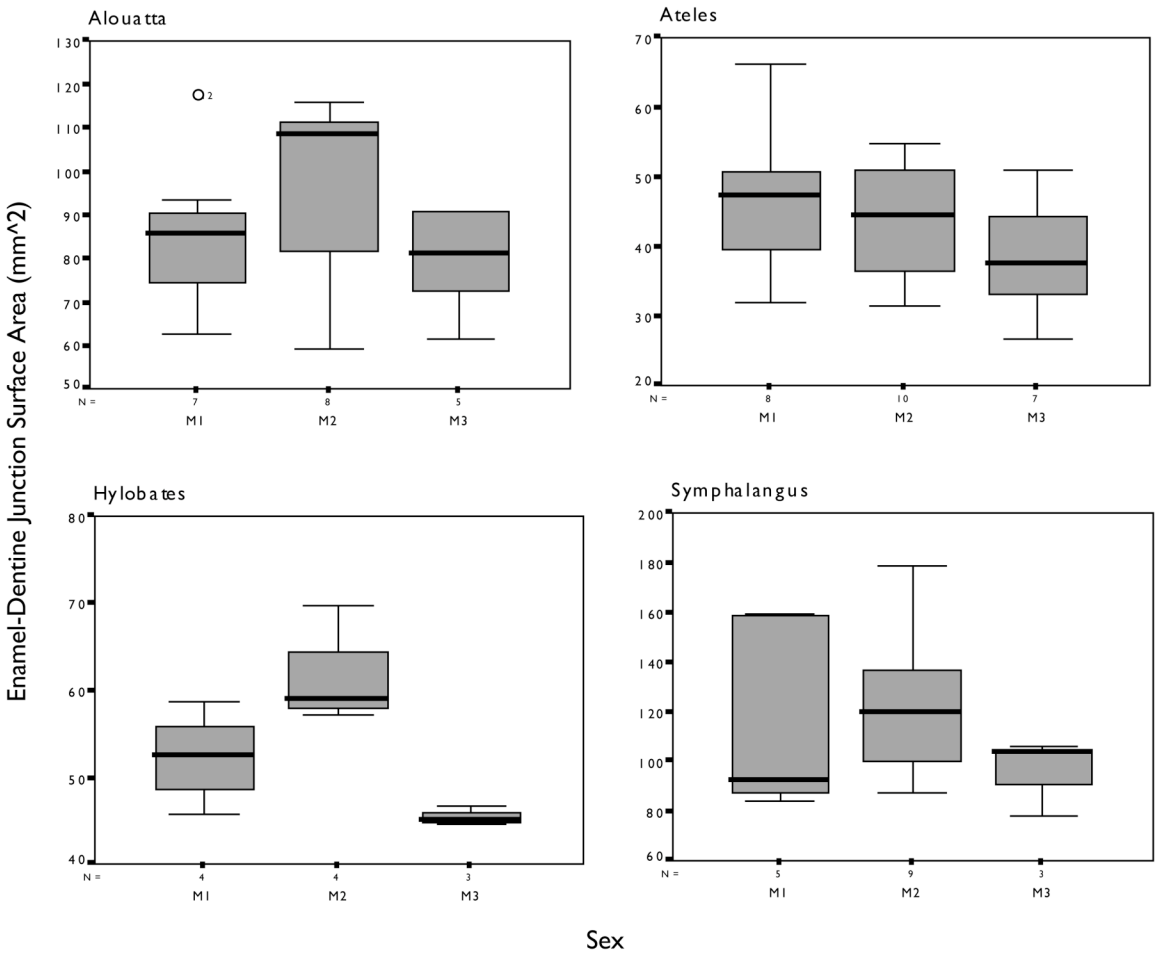


Figure 7.15: Box-plots showing the enamel-dentine junction length in first, second, and third mandibular molars in each of the four species examined in this study. An asterisk indicates an extreme statistical outlier; circles indicate statistical outliers.

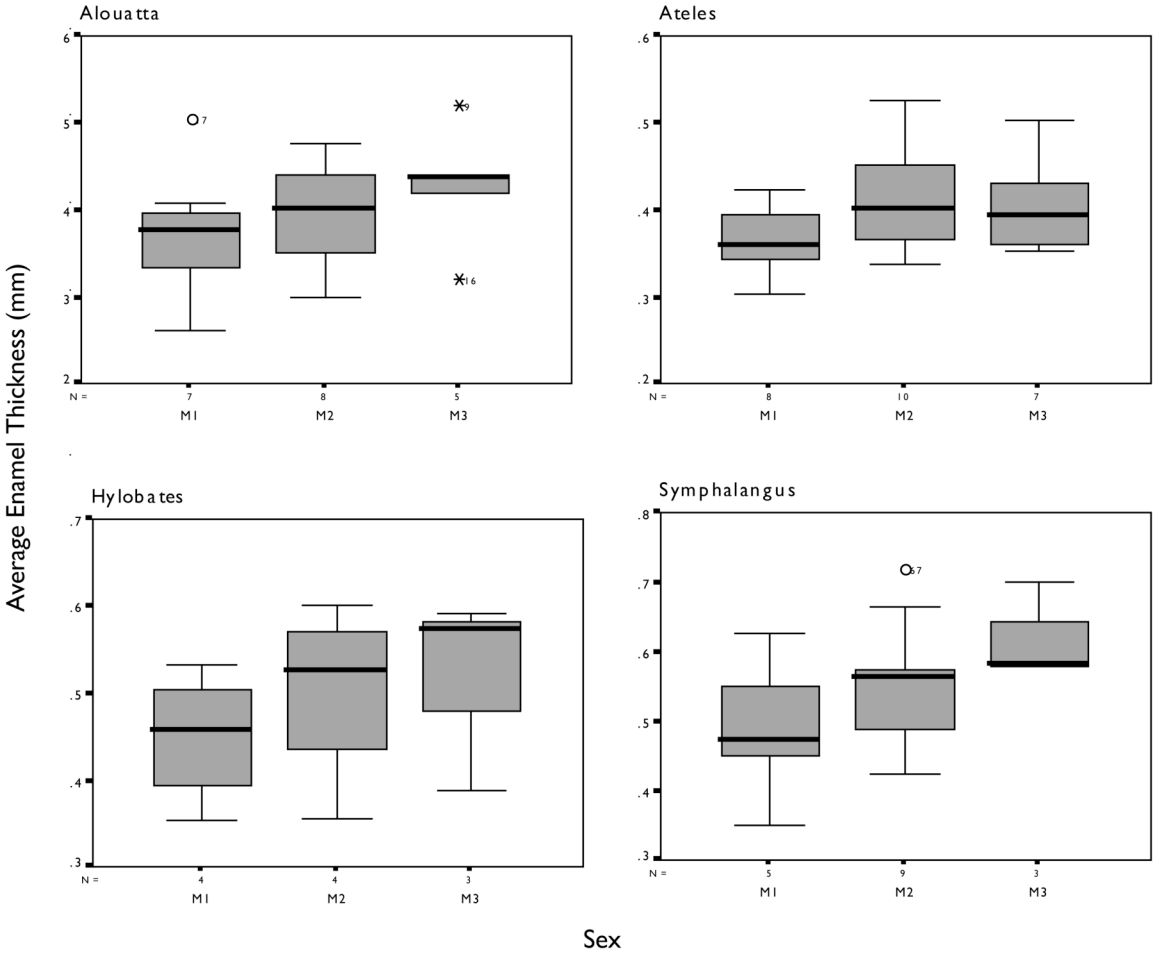


Figure 7.16: Box-plots showing the 3D average enamel thickness in first, second, and third mandibular molars in each of the four species examined in this study. An asterisk indicates an extreme statistical outlier; circles indicate statistical outliers.

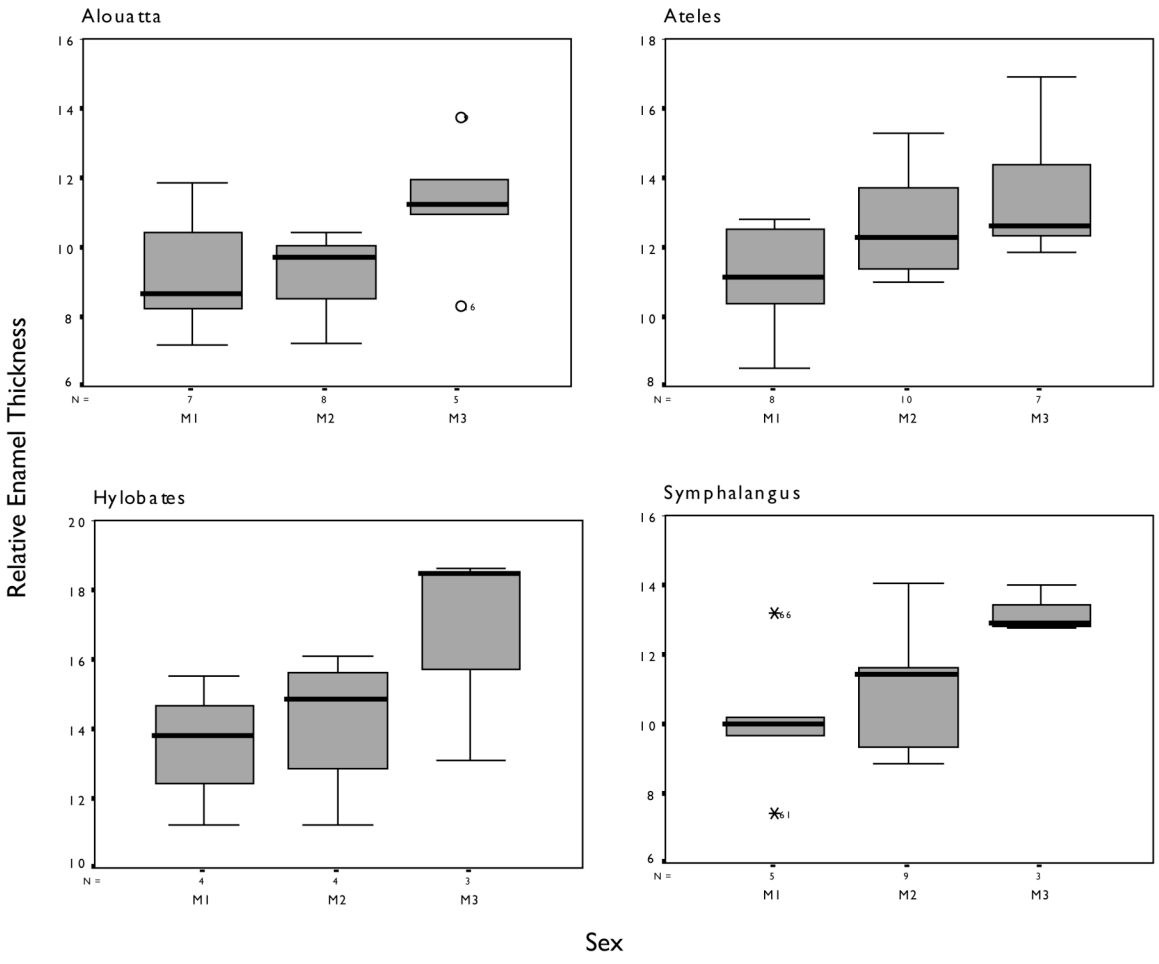


Figure 7.17: Box-plots showing the 3D relative enamel thickness in first, second, and third mandibular molars in each of the four species examined in this study. An asterisk indicates an extreme statistical outlier; circles indicate statistical outliers.

The three-dimensional data presented here corroborate the conclusions (based on planar sections or measurements of enamel exposed by attrition) of Macho and Berner (1993), Grine (2002), Hlusko et al. (2004), and Smith et al. (2005), indicating that average and relative enamel thickness, as well as the components of these indices, follow a pattern of metameric variation that is broadly applicable to each of the taxa examined in these studies. It is likely, therefore, that variance has been exaggerated in previous studies where molars from different positions were pooled; it follows that the position of each molar within an analysis of enamel thickness (or related aspects of molar morphology) should be taken into account, especially when isolated fossil molars are to be compared to samples of extant molars.

It is unclear how an increase in average enamel thickness from M1 to M3 may relate to the functional demands of mastication, as data describing bite force are rare. Spencer (1998) showed that in modern humans the first lower molar (and it's maxillary occlusal counterparts: $P^4$ and $M^1$) is preferentially used for masticating a bolus, although such data for other primates is lacking. When considered in light of enamel thickness gradients in modern humans (e.g., Grine, 2002, 2005), Spencer's data appear to be supported in that the first molar is larger (in terms of cross-sectional area) than the second or third molars. However, average enamel thickness is relatively uniform in human molars (contra *Pan* and *Pongo*, Smith et al., 2005), and it is the size of the dentine core that is larger in the first mandibular molar. Thus, it may be the case that tooth size, rather than enamel thickness, is a better predictor of masticatory stress capacity in a molar. The primates studied here show a different pattern than humans, however, as the average thickness of enamel does increase from M1 to M3 (although not significantly).

Since the attrition of enamel is a key component in determining the functional longevity of a tooth, it may be the case that posterior molars incur higher rates of abrasion than first molars in these taxa, as evidence by their thicker enamel, suggesting perhaps that unlike humans, these taxa preferentially masticate using the M2 and M3. This reasoning is entirely speculative, however, and awaits data regarding the masticatory preferences of non-human primates, as well as data pertaining to the three-dimensional distribution of forces in teeth of different sizes and shapes (e.g., a three-dimensional extrapolation of the study by Macho and Spears (1999)). Moreover, Spencer (1999) demonstrated that "Region II" of the three zones of potential bite points (i.e., three regions of the jaw that may be variably loaded during mastication due to changes in joint and muscle configuration) encompasses approximately the same teeth in all of the genera examined in this study. Thus, despite differences in dental formula (i.e., platyrrhines have one more premolar than catarrhines), the forces of mastication should be distributed over approximately the same region of the molar row in these taxa. This partially precludes differential functional demands at different tooth positions from being the single explanation of differential enamel thickness.

Another (non-functional) reason that second and third molars may have greater enamel thickness than first molars is developmental timing: posterior molars may have longer periods of enamel secretion, or perhaps faster enamel secretion but for the same duration (discussed in Grine, 2005 and Smith et al., 2005). At present, evidence suggests that enamel secretion rates are constant in all three molars (e.g., Smith, 2004), so an increase in the total duration of enamel formation (i.e., a longer crown formation time) may be inferred as the reason that average enamel thickness increases posteriorly along

the molar row. Nonetheless, the ultimate cause of thicker enamel posteriorly must still be explained, and may be related to the functional demands of each tooth. Future studies of the non-human primate masticatory system, particularly finite element models of the dentition and in-vivo studies of the masticatory apparatus, may shed light on this trend.

**Enamel Thickness in Hylobatidae**

Enamel thickness has a long history of study among scholars of hominoid primates, and the majority of the enamel thickness literature has focused on the molars of great apes, humans, and fossil hominoids (e.g., Miller, 1918; Gantt, 1977; Kay, 1981; Martin, 1985; Grine and Martin, 1988; Andrews and Martin, 1991; Beynon et al., 1998; Macho and Spears, 1999; Dean, 2000; Schwartz, 2000; Grine, 2002; Martin et al., 2003; Dean and Schrenk, 2003; Smith et al., 2003, 2004, 2005; Grine et al., 2005). To date, however, enamel thickness measurements in the mesial ideal plane of section have been reported for only two hylobatid molars (Martin, 1983; Shellis et al., 1998). Little attention has been paid to the lesser apes for a number of reasons: the primary focus of early enamel thickness studies, for instance, was on the validity of the genus *Eoanthropus* (i.e., Piltdown Man; Miller, 1918), and later on the taxonomic assignment of *Ramapithecus* (e.g., Simons and Pilbeam, 1972; Kay, 1981). These debates would not directly have been informed by studying the lesser apes. Moreover, fossil hylobatid specimens, or specimens of any taxon that is more closely related to hylobatids than to other extant primates, are unknown (e.g., Fleagle, 1984; but see Hooijer, 1960), rendering the interpretation of their enamel thickness without an easily identifiable evolutionary

context (*contra Pongo* and *Homo*, where studies of enamel thickness in their fossil relatives has informed interpretations of the evolution of these lineages).

In many ways, however, hylobatids are an important primate radiation in which to study enamel thickness. They represent the extant outgroup to great apes and humans, facilitating a more nuanced interpretation of the polarity of enamel thickness in hominoid evolution. Hylobatids are also a large biological radiation by extant hominoid standards, comprised of as many as thirteen species and four genera (Groves, 2001), whereas all other extant hominoids are represented by a single genus with at most two species (although multiple subspecies of each great ape may be identified; Groves, 2001). Hylobatids thus represent an opportunity to study a diverse groups of apes, shedding light on the nature of family-level variation in enamel thickness.

In the text that follows, a taxonomy of Hylobatidae has been adopted that favors the separation of what are commonly recognized as only subgenera of *Hylobates* (e.g., by Groves, 2001), in which the siamang (*Symphalangus syndactylus*) is considered generically distinct from gibbons of the genera *Hylobates*, *Nomascus*, and *Bunopithecus*. This taxonomic choice has recently been validated by genetic evidence (e.g., Hayashi et al., 1995; Zhang, 1997). Hayashi et al. (1995) have also proposed that the date of generic separation within Hylobatidae occurred before the separation of *Pan* and *Homo*, and Hall et al. (1998) reported that genetic differences between hylobatid subgenera are also greater than those between *Homo* and *Pan*, lending support to the recognition of distinct genera. Given that *Symphalangus* is nested among other (sub-) genera (the branching order is debated), the use of distinct generic nomina has been adopted.

Until recently, one of the few uncontested points in studies of enamel thickness was that *Homo* molars have thicker enamel than those of *Pongo*, which have thicker enamel than those of *Pan* or *Gorilla* (e.g., Martin, 1983). The categories *thick* and *thin* are actually part of a broader spectrum of enamel thickness categories developed by Martin (1983) (and later expanded by Martin and Grine (1988)) based on confidence intervals of measurements of ape and human enamel thickness. Martin found four groups of enamel thicknesses that had no overlap: thin enamel (*Pan*, *Gorilla*, and *Hylobates*; relative enamel thickness values between 8.90 and 11.30), intermediate thin enamel (no species in Martin's sample fit this category; relative enamel thickness values between 11.31 and 14.64), intermediate thick enamel (*Pongo*; relative enamel thickness values between 14.65 and 17.24), and thick enamel (*Homo*; relative enamel thickness values between 17.25 and 26.20). A "hyperthick" category was later added to accommodate *Paranthropus* (Grine and Martin, 1988).

Contrary to Martin's original findings, recent evidence suggests that *Pongo* and *Pan* molars are actually both of intermediate enamel thickness, although there is overlap in the range of enamel thickness between *Pan* and *Gorilla*, and between *Pan* and *Pongo* (Shellis et al., 1998; Kono, 2004; Smith et al., 2005). Figure 7.18 illustrates Martin's (1983, 1985) general interpretation of enamel thickness polarity in hominoid evolution. It should be noted that Martin (1983) also used developmental data (e.g., the rate of enamel secretion) in his analysis, and a finer resolution of enamel thickness categories including "intermediate-thin" and "intermediate-thick". This interpretation must also be considered in light of the recent change in interpretation of the thickness of *Pan* molars, as well as the somewhat recent acceptance of *Pan* as the sister taxon to *Homo* (e.g., Ruvolo, 1997).

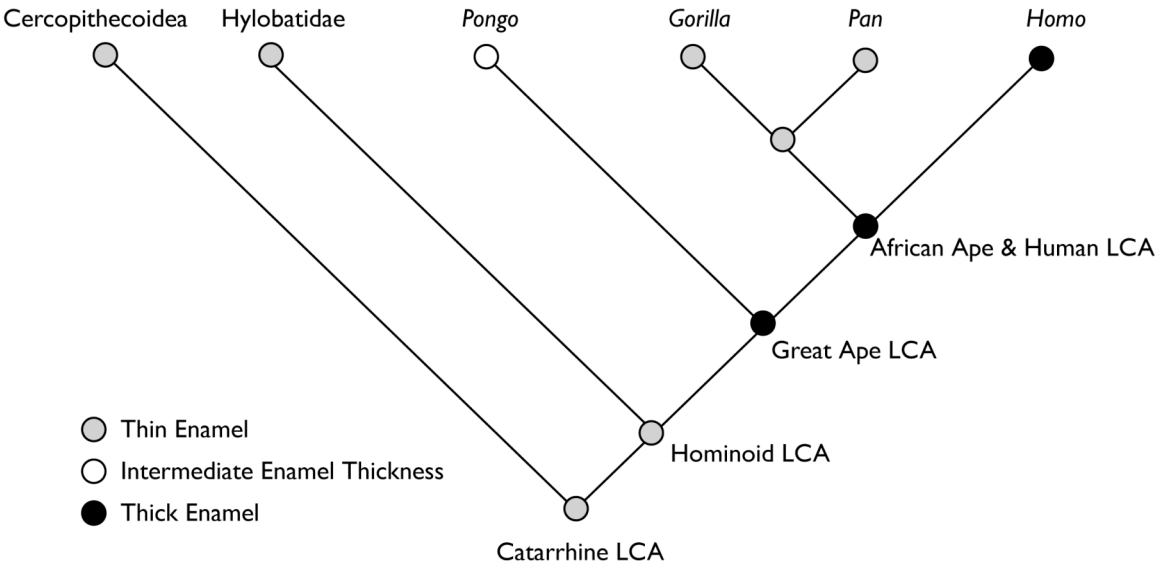


Figure 7.18: Cladistic rendering of Martin's (1983, 1985) interpretation of the polarity of enamel thickness in hominoid evolution.

In this scheme, hylobatids are considered to be thin enameled, as is the last common hominoid ancestor. This interpretation of hylobatid enamel thickness, however, is based on the measurement of a single molar by Martin (1983), and a second molar later measured by Shellis et al. (1998). In neither case was a species attribution possible, so these two molars were considered to represent *Hylobates sp.* (see Martin et al., 2003: Appendix B). These molars evince a relative enamel thickness that is accommodated within the ranges both of *Pan* and *Gorilla*, and hylobatid enamel thickness has since been considered "thin" based on the categories erected by Martin (1983).

A relatively thin enameled hylobatid group fits well within Martin's (1983) interpretation of the last common hominoid ancestor's enamel thickness, which he interpreted to be thin (e.g., Martin, 1983; Andrews and Martin, 1991) based in part on his measurements of the *Hylobates* molar, and also on the accepted notion at that time that cercopithecoid primates were thin-enameled (with the notable exception of *Papio*; Jolly,

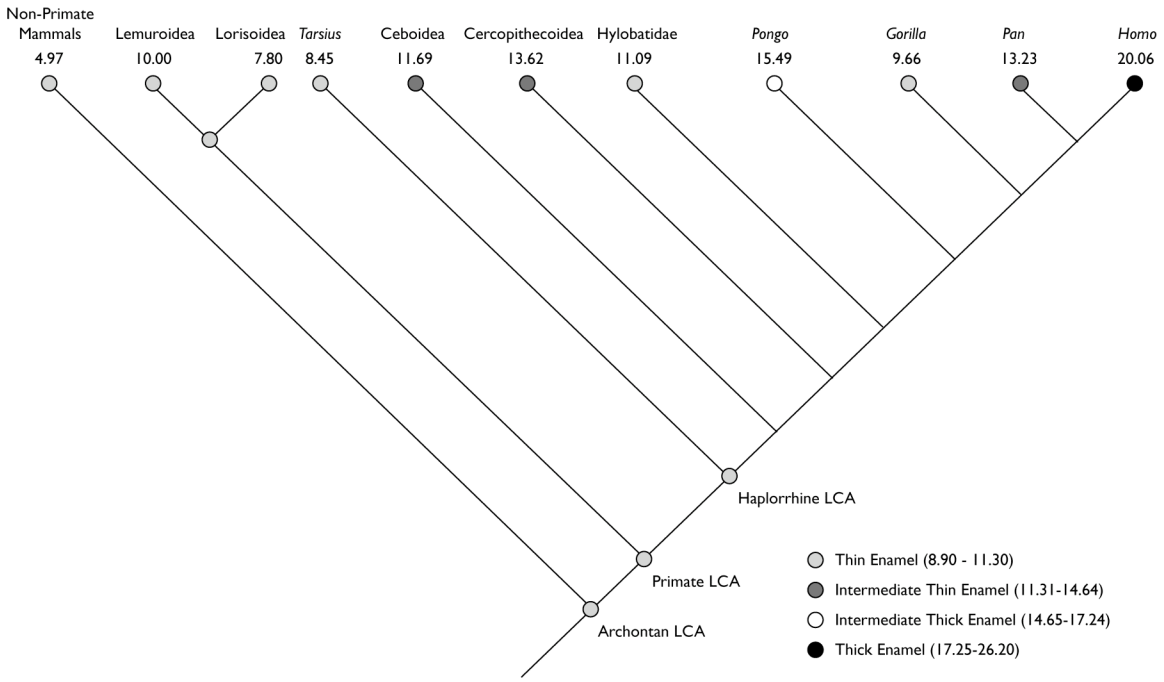


Figure 7.19: Cladistic rendering of Martin's (1983, 1985) interpretation of the polarity of enamel thickness in hominoid evolution in light of some recent changes in cladistic interpretations (the *Pan-Gorilla* clade is replaced by a *Pan-Homo* clade) and enamel thickness studies (cercopithecoids, *Pan*, and *Pongo* appear to have intermediate relative enamel thickness. Data taken from Smith et al. (2005, 2006) and Martin et al. (2003).

1970; see also Gantt, 1977). More recent analyses of taxonomically broad samples of primate molars (Shellis et al., 1998; Martin et al., 2003; Grine et al., 2005), however, have shed light on the cercopithecoid, ceboid, and strepsirrhine enamel thickness conditions, raising doubt as to whether the hominoid last common ancestor indeed had relatively thin molar enamel.

Cercopithecoid primates, for instance, have enamel of "intermediate thick" relative thickness on Martin's scale (Ulhaas et al., 1999; Shimizu, 2002; Grine et al., 2005), ceboid primates have "intermediate thin" enamel (with the exception of *Cebus apella*; Dumont, 1995; Martin et al., 2003), and strepsirrhines (and Chiroptera and Scandentia)

have thin relative enamel thickness (Dumont, 1995; Shellis et al., 1998; Martin et al., 2003). When mapped onto a cladogram (Figure 7.19), it character state of the last common hominoid ancestor is difficult to assess. It may be the case that the last common hominoid ancestor had enamel thickness similar to *Pan* and *Pongo*, in which case *Gorilla* and hylobatids have convergently evolved intermediate thin molar enamel, and *Homo* has evolved relatively thick molar enamel (as do fossil hominins, e.g., Grine and Martin, 1988).

The relatively thin molar enamel of Hylobatidae in the above scenario represents a character reversal. The comparatively large Hylobatidae molar sample studied here, comprised of *Symphalangus syndactylus* and *Hylobates muelleri* molars, serves to examine whether the attribution of relatively thin molar enamel to this primate family is appropriate. The relative enamel thickness index (*ret*) was calculated for each molar in the study in the mesial ideal plane of section for comparison with previously published planar data, and also using three-dimensional measurements (*ret3d*) for comparison with the results of great ape and human measurements by Kono (2004).

The previously reported mean relative enamel thickness in hylobatid molar mesial planes of section (n = 2) is 11.09 (Martin et al., 2003: Appendix B). Results of the data collected in the present study demonstrate that this average is somewhat low; the average relative enamel thickness for *Symphalangus* molars (n = 17) is 12.58, and the average for the *Hylobates* molars (n = 11) is 15.27. The difference between *Symphalangus* and *Hylobates* mean relative enamel thickness is statistically significant (Mann-Whitney *U* statistic = -2.47, $p = 0.14$). The difference between species is also greater than 3%, which is the general level of accuracy observed in the pilot work discussed in previous chapters

(that is to say, measurement error alone does not explain the differences between enamel thickness in these species). Both of these averages fall within in Martin's (1983) "intermediate" enamel thickness categories. The aforegoing discussion of metameric variation, however, indicates that relative enamel thickness should be considered per tooth type. In the case of *Symphalangus* mandibular molars, the average relative enamel thicknesses for each tooth type were as follows: M1 = 10.76, M2 = 13.55, and M3 = 12.69. In the *Hylobates* molars, the relative enamel thickness for each tooth type was: M1 = 13.29, M2 = 14.85, and M3 = 18.47. The previously reported average of 11.09 thus falls closest to the mean M1 relative enamel thickness value of the *Symphalangus* sample, but on the whole, the hylobatid (especially the *Hylobates*) molars have relatively thicker enamel than was expected from previous work. Relative enamel thickness in the *Hylobates* molars is substantially thicker than previously thought, spanning the "intermediate-thick" and "thick" categories of Martin (1983), while the *Symphalangus* molars are contained within the "thin" and "intermediate-thin" categories.

These results demonstrate that there is a species-level difference in hylobatid enamel thickness, and that the entire radiation of Hylobatidae should not be considered a single group in terms of relative enamel thickness. Whether the primarily folivorous *Symphalangus syndactylus* or the more frugivorous *Hylobates muelleri* more accurately represents the enamel thickness condition of the hylobatid common ancestor may be elucidated through the study of other hylobatid species. The evidence presented here based on two species, however, suggest that the last common hylobatid ancestor may be conservatively estimated to have had intermediate molar enamel thickness (the average of the relatively thin enameled *Symphalangus* molars and the relatively more thickly

enameled *Hylobates*). Figure 7.20 depicts a cladogram with this interpretation mapped on, in which *Gorilla* has independently evolved relatively thin molar enamel, and *Homo* has independently evolved thick molar enamel; the hylobatid last common ancestor has the same enamel thickness condition as the last common hominoid ancestor and cercopithecoid primates: intermediate relative enamel thickness. Nonetheless, as is apparent from the cladogram depicted in Figure 7.20, the polarization of enamel thickness in hominoid evolution is difficult given the wide range of conditions seen among extant taxa.

The polarity of enamel thickness in catarrhine evolution has also been studied in fossil taxa. The most relevant fossils to the question of the last common hominoid ancestor belong to genus *Proconsul* and, indirectly, the early cercopithecoid *Victoriapithecus*. *Victoriapithecus* has intermediately thick molar enamel, as do later cercopithecoids, lending support to the intermediate relative enamel thickness of the last common catarrhine and cercopithecoid ancestors (Dean and Leakey, 2003). *Proconsul* molars are more diverse in their relative enamel thickness, and span each of Martin's (1983) original enamel thickness categories from "thin" to "thick" (Andrews and Martin, 1991; Beynon et al., 1998) depending on which species is studied (Smith et al., 2003: Table 2). The homogeniety of the fossils typically grouped into genus *Proconsul* has recently been called into question (Senut et al., 2000); this idea is partially supported by the fact that the range of relative enamel thickness values in *Proconsul* has not been observed in any single extant genus (Martin et al., 2003: Appendix B). Nonetheless, the mean value of relative enamel thickness in genus *Proconsul* is in the intermediate range of Martin's (1983) categories, although it is unclear whether the last common *Proconsul*

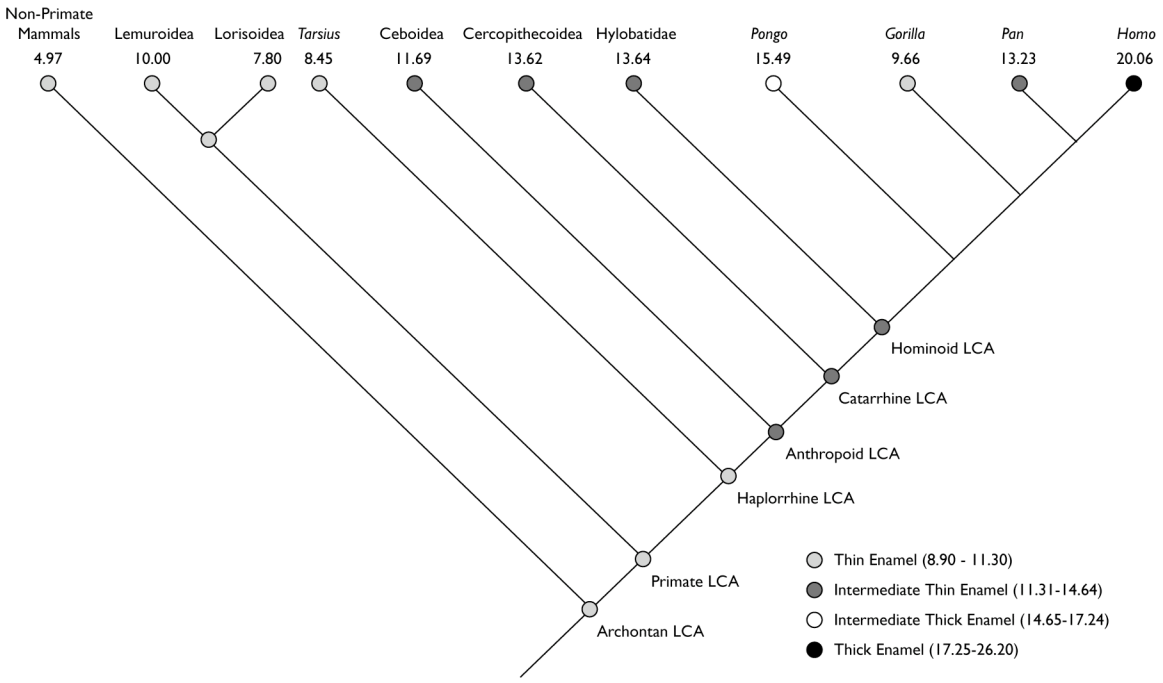


Figure 7.20: Cladistic interpretation of the polarity of enamel thickness in hominoid evolution in light the data presented here showing that hylobatids, on average, have intermediate thin enamel thickness.

ancestor's enamel thickness may be inferred by studying the distribution of this character in the genus' constituent species with so few molars actually measured to date (n = 1 for each of the four *Proconsul* species). In any case, it appears based on the evidence available at present, that the last common hominoid ancestor had "intermediate thin" relative enamel thickness, as do modern cercopithecoids and hylobatids.

Evidence from three-dimensional measurements of relative enamel thickness also support an "intermediate thin" enameled last common ancestor of hominoids. Kono (2004) demonstrated that *Homo* (n = 41; *ret3d* = 20.60) has relatively thicker enamel than *Pan* (n = 22; *ret3d* = 12.30) and *Pongo* (n = 7; *ret3d* = 12.90) when considered in three-dimensions. *Gorilla* relative enamel thickness is thinner still (n = 4; *ret3d* = 9.50). Data presented in this dissertation show that *Symphalangus* (n = 17; *ret3d* = 11.15) has

relatively thin enamel, while *Hylobates* (n = 11; *ret3d* = 14.72) has "intermediate thin" enamel thickness. This species mean difference is statistically significant (Mann-Whitney *U* statistic = -3.175, $p = 0.001$). When considered by tooth type, *Symphalangus* molar relative enamel thickness falls out as follows: M1 = 10.11, M2 = 11.03, and M3 = 13.24. *Hylobates* relative enamel thickness by tooth type is as follows: M1 = 13.62, M2 = 14.30, and M3 = 16.75. The three-dimensional data presented here thus follow the same pattern as the two-dimensional data discussed above, so an "intermediate thin" enameled last common hominoid ancestor is also supported by the three dimensional data.

The implications of an "intermediate thin" common ancestor for hominoids (rather than an explicitly "thin" enameled common ancestor) forces change upon previous ideas about ape dental evolution. The polarity of enamel thickness has previously been interpreted as having changed from thin to thick at the first appearance of great apes in the fossil record (e.g., Martin, 1983; Andrews and Martin, 1987, 1991; Andrews et al., 1987a). In this scenario, *Pongo* and *Homo* have retained the thick-enamel of this last common ancestor (but to varying degrees), while *Pan* and *Gorilla* have reduced enamel thickness. This scenario is indeed parsimonious when *Pan* and *Gorilla* are considered to be sister taxa (to the exclusion of *Homo*) and this scenario also provides a clear Rubicon for the identification of a fossil African ape: it should have thin enamel (e.g., Senut et al.'s (2001) interpretation of the late Miocene genus *Ardipithecus*). The sum of recent evidence, however, makes this scenario less likely, and the interpretation of enamel thickness polarity changes substantially less clear. It appears that a gradient of change exists in primate evolution, beginning with thin enameled archontans, enamel

becoming thicker at the cladistic events yielding anthropoid and catarrhine primates, and ultimately a mélange of thicknesses within the hominoid clade (see also Martin et al., 2003).

Further compounding the difficulty of interpreting enamel thickness in hominoid evolution is the recognition of a *Pan-Homo* clade to the exclusion of *Gorillas*, indicating that thin enamel may have evolved twice from a thick-enameled great ape ancestor, rendering this scenario less parsimonious (e.g., Ruvolo, 1997; Gibbs et al., 2002). Moreover, the recognition that *Pan* has molar enamel that is of intermediate thickness renders a relatively easily identifiable "thin/thick" dichotomy in great apes less likely. Finally, data describing non-hominoid primates and the study presented here describing hylobatid enamel thickness points towards an "intermediate thin" enameled last common hominoid ancestor. With this evidence in mind, it appears that *Gorilla* has reduced relative enamel thickness autapomorphically, *Homo* has increased relative enamel thickness autapomorphically, and hylobatids, *Pongo*, and *Pan* have enamel thickness that is consistent with that of the last common hominoid ancestor (although *Pongo* molar enamel is a bit thicker than either *Pan* or *Hylobates* enamel, on average). In this view of enamel thickness evolution, it is difficult to establish a particular expectation of enamel thickness that may distinguish, for example, a great ape from a lesser ape in the fossil record.

In sum, recent evidence suggests that the evolution of enamel thickness in apes has been more complicated than was previously thought, and neatly defined thresholds of enamel thickness may not be useful for the interpretation of fossil hominoids. Three extant hominoids may be inferred as having enamel of intermediate thickness (*Pan*,

*Pongo*, and the common hylobatid ancestor), and overlapping values of enamel thickness are common between taxa (e.g., between hylobatids, *Pan*, and *Pongo*, all of which overlap with *Gorilla* to some extent in the low end of their ranges, and all of which overlap with *Homo* in the upper end of their ranges); the inter-specific overlap apparent between species complicates the use of enamel thickness in the diagnosis of fossil forms.

**Enamel Thickness in Atelidae**

Ceboid primates have recently been a focus of enamel thickness measurements, due in part to an interest in the identification of molar morphology associated with sclerocarpic foraging in pitheciin primates (Martin et al., 2003). Three studies have presented relative enamel thickness measurements in the mesial ideal section in ceboids (Dumont, 1995; Shellis et al., 1998; Martin et al., 2003), and no single taxon has been represented by more than 5 teeth in any of these studies. Nonetheless, a taxonomically broad range of species from each of the major ceboid radiations has been examined, and with the exceptions of the relatively thick enameled *Cebus apella* and *Cebus capucinus*, ceboids are all characterized by either thin enamel or intermediate thin enamel based on Martin's (1983) categories. It has been inferred that the ancestral ceboid condition was one of thin molar enamel (Martin et al., 2003). What has been clouded by small sample sizes thus is not the overall relative enamel thickness of ceboids; species-level variance, however, is difficult to determine, and it is unclear whether all ceboids have similarly thin enamel, or whether the same patterns seen in hominoid primates (e.g., thinner enamel in primarily folivorous species, differences in enamel thickness in closely related species) may be detected within the ceboids.

To this end, the relatively large samples of mandibular molars of *Alouatta seniculus* and *Ateles geoffroyi* studied here were employed to collect two- and three-dimensional relative enamel thickness measurements (*ret* and *ret3d*). The overall species mean two-dimensional relative enamel thickness for *Alouatta seniculus* in the present study is 11.13, which is similar to the value of 10.88 reported for four molars of *Alouatta villosa* by Shellis et al. (1998). The individual molar positions of *Alouatta seniculus* in the present study yielded relative enamel thickness values as follows: M1 = 10.35, M2 = 11.77, and M3 = 11.20. Although *Alouatta* species are more folivorous than other atelid taxa, and are therefore expected to have thinner enamel than the other atelid species (based on the theoretical grounds established by Ulhaas et al., 1999; Shimizu, 2002), the mean of published values for *Ateles* molar relative enamel thickness is 9.73 (based on 4 *Ateles paniscus* molars and 1 *Ateles sp.* molar; Shellis et al., 1998; Martin et al., 2003), indicating that *Ateles* may actually have relatively thinner enamel than *Alouatta*.

Data from the current study, however, show that *Ateles geoffroyi* molars have a mean relative enamel thickness index of 12.13, which is slightly higher than the mean relative enamel thickness of the *Alouatta* molars, although this difference is not significant (Mann-Whitney $U$ statistic = -1.759, $p = 0.079$). The difference between species is, however, greater than 3%, which is the general level of accuracy observed in the pilot work discussed in previous chapters (that is to say, measurement error alone does not explain the differences between enamel thickness in these species). When examined per tooth type, the *Ateles geoffroyi* molars have the following relative enamel thicknesses: M1 = 11.02, M2 = 12.17, and M3 = 13.31. There exists considerable overlap between the first, second, and third molar relative enamel thickness of *Alouatta*

*seniculus* and the first and second molar relative enamel thickness of *Ateles geoffroyi* (Figure 7.21). The difference in species mean relative enamel thickness is not as pronounced as in the hylobatid comparisons discussed above (where the species were significantly different in terms of mean relative enamel thickness). The data presented here suggest that ceboid primate species may be less distinct from one another in relative enamel thickness as it relates to dietary proclivity than the hylobatid species.

In contrast, when three-dimensional data are considered, a distinction becomes more evident. The mean three-dimensional relative enamel thickness index for *Alouatta* is 9.81, and that of *Ateles* is 12.47. Using this three-dimensional data, the species are statistically significantly different (Mann-Whitney $U$ statistic = -4.157, $p < 0.001$; see also Figure 7.21). In the above discussion of the relationship between two- and three-dimensional measurements, it was clear that the *Alouatta* molars do not have a significant relationship between the mesial plane of section and the whole-crown measurements. This discrepancy may be responsible for the lack of significance in the comparison of *Alouatta* and *Ateles* molars based on the two-dimensional plane of section, while the three-dimensional data show significant differences. While mesial planes of section do a reasonably good job of predicting overall crown measurements, it is clear that *Alouatta*, and possibly other taxa that have not yet been studied, do not evince a clear relationship between the section plane and the overall crown. It is preferable to use overall crown measurements rather than individual sections, and for this reason the greater discrepancy between *Alouatta* and *Ateles* shown in the overall crown measurements is taken to represent a better approximation of the actual difference in relative enamel thickness between these species. In sum, the closely related folivore-frugivore dichotomy in

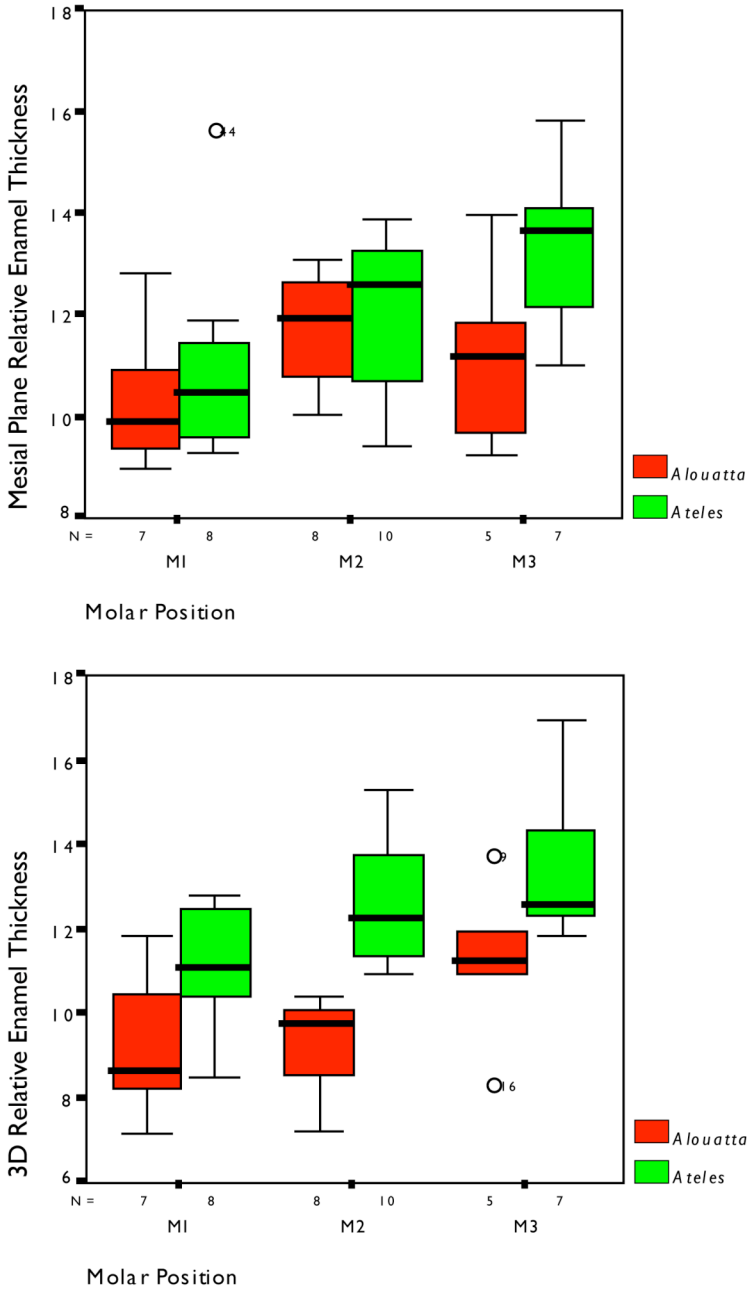


Figure 7.21: Box-plots depicting the ranges of enamel thickness in the mesial plane of section and of the entire 3D model in the two ceboid taxa. There is considerably more overlap in the 2D section data than in the 3D data. Circles are statistical outliers.

relative enamel thickness appears to apply to ceboids as well as hominoids, and closely related ceboid taxa may be distinguished from one another using relative enamel thickness.

The results of Atelidae relative enamel thickness measurements suggest that the range of previously published ceboid enamel thickness measurements based on small samples is accurate. Ceboid relative enamel thickness appears to be thin or of intermediate "thinness", lending support the interpretation of enamel thickness polarity discussed above in reference to the hylobatid sample. Moreover, ceboid relative enamel thickness is thicker than that of strepsirrhines, scandentians, and chiropterans (Martin et al., 2003), so the term "thin enamel" as it applies to ceboids must be couched in relative terms. The "thin" enamel of ceboids is thicker than the "thin" enamel of strepsirrhines, which is in turn thicker than the "thin" enamel of non-primate mammals.

**Functional Signals: Enamel Thickness Patterning and The Potential of Multivariate Analyses**

Martin (1983, 1985) demonstrated that the highly frugivorous *Pan troglodytes* and the relatively folivorous *Gorilla gorilla* have overlapping ranges of relatively thin enamel, suggesting that comparing folivores and frugivores represents a comparison of similar enamel thicknesses, and that the patterning of enamel thickness and overall crown morphology must be examined to separate these dietary types (the difference in thickness between *Pan* and *Gorilla* now appears to be greater than Martin (1983) had reported (Smith et al., 2005)). Other evidence suggesting that folivores have thinner enamel than closely related frugivores has been reported by Kay (1981) in several anthropoid taxa,

and by Ulhaas et al. (1999) and Shimizu (2002), who found that colobines tend to have relatively thinner enamel than cercopithecines. Schwartz (2000) also demonstrated that differences exist between *Pan* and *Gorilla* in terms of the distribution of the thickness of their molar enamel in cross-section. Thus, it was predicted in the present study that among closely related species dyads both the patterning of enamel thickness and the relative thickness of enamel would allow for discrimination of folivores from frugivores.

Differences in mean relative enamel thickness between the two closely related species dyads have been described above. When a whole crown perspective is taken, the primarily folivorous taxa have significantly thinner enamel than the primarily frugivorous taxa. A functional explanation for thinner enamel in folivores has been given by Shimizu (2002), who suggested that the early exposure of dentine in folivorous taxa provides shearing surfaces suitable for the mastication of leaves. Moreover, Shimizu (2002) suggested that folivores have more uniform enamel thickness at various locations on the enamel crown than frugivores. Frugivores may have enamel that is thicker in areas where crushing and grinding stresses are strongest (Macho and Spears, 1999), while folivorous molars lack such local stress distribution adaptations. Schwartz (2000: Figure 5) presented evidence that *Gorilla* molars have a more uniform distribution of enamel than *Pan*, lending some support to this idea.

If differences in the patterning of enamel thickness represent a functional signal, then the two distantly related folivores in the present study should have patterns of enamel distribution that are more similar to each other than they are to the more closely related species, and this should also be true of the frugivores. To explore variation in the patterning of enamel thickness, the seven linear enamel thickness measurements (Figure

7.1) in the mesial and distal ideal planes of section were plotted, and the pattern was inspected.

Figure 7.22 depicts the mean pattern of enamel thickness from the buccal to the lingual side of mesial and distal ideal planes of section in each taxon. In each case, the buccal lateral wall linear enamel thickness (*e1*) is thicker than the lingual lateral wall linear enamel thickness (*e7*). This discrepancy between the mesial and lingual lateral wall cusp thicknesses is in accord with functional models of enamel thickness distribution, which suggest that the lateral wall of the buccal cusp of lower molars must endure the application of higher forces during mastication (Spears and Macho, 1998; Macho and Spears, 1999). Another apparent trend in these plots is the presence of thicker enamel in the mid-occlusal basin (*e4*) in the mesial sections, and thinner enamel in the mid-occlusal basin in distal sections. This mid-occlusal thickening is due to the presence of an intercuspal ridge of enamel connecting the protoconid to the metaconid, and no such ridge is apparent connecting the distal cusps.

It is notable that in neither the mesial nor the distal sections is there a pattern demonstrating that the folivorous taxon within each species dyad has a more uniform distribution of linear enamel thickness (cf. Schwartz, 2000: Figure 5). With the exception of Schwartz's (2000) plot depicting the even distribution of enamel across the molar crown, and the work of Macho and Spears (1999; Spears and Macho, 1998), previous comparisons of total crown enamel thickness distribution have come largely from studies of cercopithecoid primates (Ulhaas et al., 1999; Shimizu, 2002). The unique bilophodont condition of cercopithecoid molars may impact their distribution of enamel, as their taller interconnected cusps may be worn in order to expose long crests of dentine more

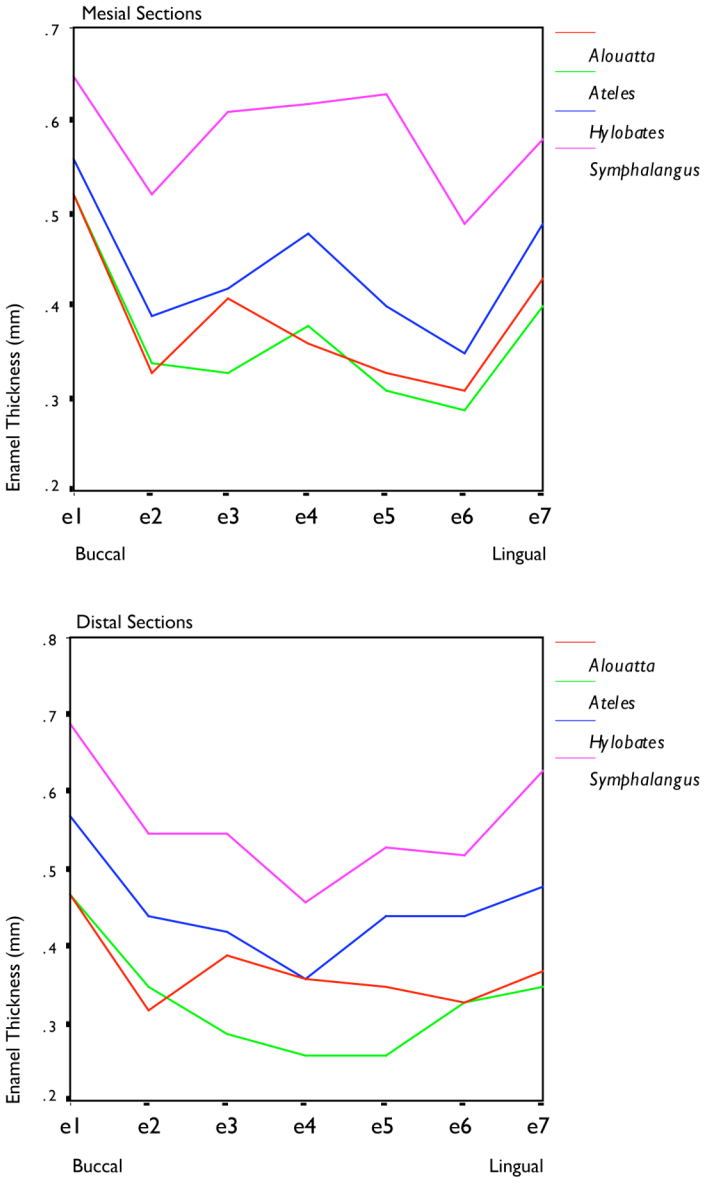


Figure 7.22: The mean linear thickness of enamel in the seven measurements of the mesial and distal ideal planes of section. The folivorous taxa do not show the predicted pattern of more uniform enamel thickness across the molar crown.

effectively than the bunodont cusps typical of hominoids and ceboids, essentially creating a continuous ring of dentine at the internal periphery of the occlusal basin (Shimizu, 2002). *Gorilla* molars also have particularly tall cusps, perhaps emulating the cercopithecoid condition in which long ridges of dentine may be exposed, thereby explaining the pattern described by Schwartz (2000). In any case, it appears that while relative enamel thickness of the entire crown separates folivores from closely related frugivores in the species dyads examined in the present study, the specific pattern of enamel thickness distribution is not effective at separating dietary groups, and is perhaps more effective at separating colobine from cercopithine primates because of their unique bilophodont condition.

Up to this point in the presentation of enamel thickness data for the taxa examined in this study, it is clear that the primarily folivorous taxon in each species dyad has relatively thinner enamel than its primarily frugivorous counterpart. It is also apparent that each hylobatid species has relatively thicker enamel than its ceboid dietary analogue (*Symphalangus ret3d* = 11.15, and *Alouatta ret3d* = 9.81; *Hylobates ret3d* = 14.72, and *Ateles ret3d* = 12.47). When combined with previously published values (e.g., Martin et al., 2003), ceboids (when considered as a single group) have relatively thinner enamel than hominoids (also when considered as a single group). This may be interpreted by some degree as a phylogenetic constraint stemming from an inferred thin-enameled ceboid ancestor, and an inferred intermediate-thickness enameled hominoid ancestor.

The influence of dietary proclivity and phylogenetic constraint on relative enamel thickness thus remains unresolved. The research question be phrased as follows: when the phylogenetic (i.e., superfamilial) group to which each species belongs is taken into

account (i.e., held constant statistically), do primary folivores have relatively thinner enamel than primary frugivores? Another way to ask this question is: because they both incorporate substantial amounts of leaves in their diets, would the molars of *Symphalangus* and *Alouatta* have the same relative enamel thickness were it not for phylogenetic constraint (i.e., *Symphalangus* molars have relatively thicker enamel than *Alouatta* molars simply because they inherited thicker enamel from the last common hominoid ancestor)? The same question may be asked of the primarily frugivorous taxa. It should be mentioned at this point that relative enamel thickness is an index that attempts to remove the confounding effects of body and tooth size, and it appears to be adept at doing so (e.g., Shellis et al., 1998: regression statistics therein); thus, the generally larger size of hominoids versus ceboids is not likely to influence differences in their relative enamel thickness.

In order to test the null hypothesis that primary frugivores (folivores) have equal relative enamel thickness when their superfamilial affiliation is statistically controlled, multiple statistical techniques may be employed (e.g., analysis of covariance (ANCOVA) yielding adjusted means, phylogenetic independent contrasts (PIC)). Unfortunately, the samples in the present study do not lend themselves to this type of rigorous analysis. ANCOVA, for instance, is a particularly difficult test in terms its underlying assumptions (e.g., data must be normally distributed, variance should be homogenous, and ideally covariates should be at least of a nominal scale; Sokal and Rohlf, 1995; Tabachnick and Fidell, 2001). The relative enamel thickness data (*ret3d*) presented here within each taxon are normally distributed when assessed using one-sample Kolmogorov-Smirnov tests. The null hypothesis was that the sample is normally distributed (*Alouatta*: $Z =$

0.474, $p = 0.978$; *Ateles*: $Z = 0.698$, $p = 0.715$; *Hylobates*: $Z = 0.392$, $p = 0.998$; *Symphalangus*: $Z = 0.604$, $p = 0.859$). The variance in *ret3d* is also homogenous among groups (per Levine's test for homogeneity of variances; $F = 0.881$, $p = 0.455$), but the covariate in this analysis (the superfamilial affiliation) is dichotomous (ceboid or hominoid), and therefore not linearly associated with *ret3d*. This violates a primary assumption of ANCOVA, and therefore prevents statistical software from producing adjusted means (based on an ANCOVA run using these data, performed with SPSS and STATA software).

Phylogenetic independent contrast (PIC) analysis is another approach by which to examine differences between groups while holding constant their phylogenetic relatedness (e.g., Harvey and Pagel, 1991). This technique incorporates the relative phylogenetic distance between taxa, and adjusts the variable of interest accordingly. Ideally, however, the sample of taxa would be much greater than the four species examined here (e.g., Seibel and Carlini, 2001). Moreover, several of the assumptions of Felsenstein (1985) are not met in the dataset produced in this study. An explicit multivariate comparison of primate relative enamel thickness and other dental characters for the purpose of discriminating functional from phylogenetic influences must therefore await the three-dimensional analysis of the molars of many more taxa, and perhaps dietary data that is more than simple dichotomous categories (e.g., the actual percentage of leaves consumed in the overall diet of each species). The latter point is especially important in light of recent studies demonstrating that species commonly considered to be folivorous actually incorporate large amounts of fruit into their diets (e.g., Doran et al., 2002).

In lieu of an explicit comparison, one strategy by which to infer metric traits associated with diet is an exploratory factor analysis (specifically, a principal components analysis). In this case, all of the variables collected in this study may be simultaneously examined, and their latent roots and vectors (i.e., eigenroots and eigenvectors) determined. A principal components analysis also produces a set of coefficients that describe the data in such a way that that the relationship of each variable to each other variable is accounted for, essentially producing new, smaller set of variables that are completely independent of one another and are comprised of combinations of the original variables (i.e., principal component scores). The principal component scores may then be plotted, the species of each point in the plot noted, and the relationships of the species to each other in terms of dental traits may be thus observed. If the plots produced show that certain principal components align the folivores with one another to the exclusion of the folivores, the variables constituting that principal component may be hypothesized to be characters associated with folivory.

An exploratory factor analysis was performed on the entire database collected for the biological experiments described in this chapter (68 metric variables), using principal components extraction and varimax rotation of the resultant component scores in SPSS software (v11.0.4 for the Macintosh, SPSS Science, Inc.). Eight principle components were produced from the original 68 variables, explaining 87.32% of the variation (Table 7.4; the threshold for component significance was an eigenvalue of 1.0 or above). The rotated component matrix is displayed in Table 7.5, which shows the score of each variable on only the component on which its score was highest. The first component is constructed of those variables that account for the size of a tooth (e.g., basal area, total

*Table 7.4: Variance explained by the components extraced in the PCA.*

| | Initial Eigenvalues | | | Extraction Sums of Squared Loadings | | | Rotation Sums of Squared Loadings | | |
|---|---|---|---|---|---|---|---|---|---|
| Component | Total | % of Variance | Cumulative % | Total | % of Variance | Cumulative % | Total | % of Variance | Cumulative % |
| 1 | 38.82 | 57.09 | 57.09 | 38.82 | 57.09 | 57.09 | 25.90 | 38.08 | 38.08 |
| 2 | 10.99 | 16.15 | 73.24 | 10.99 | 16.15 | 73.24 | 21.54 | 31.67 | 69.75 |
| 3 | 2.21 | 3.25 | 76.50 | 2.21 | 3.25 | 76.50 | 2.77 | 4.07 | 73.82 |
| 4 | 2.03 | 2.98 | 79.48 | 2.03 | 2.98 | 79.48 | 2.05 | 3.02 | 76.84 |
| 5 | 1.59 | 2.34 | 81.82 | 1.59 | 2.34 | 81.82 | 2.00 | 2.95 | 79.78 |
| 6 | 1.37 | 2.02 | 83.84 | 1.37 | 2.02 | 83.84 | 1.88 | 2.76 | 82.55 |
| 7 | 1.22 | 1.80 | 85.63 | 1.22 | 1.80 | 85.63 | 1.87 | 2.75 | 85.30 |
| 8 | 1.15 | 1.68 | 87.32 | 1.15 | 1.68 | 87.32 | 1.37 | 2.02 | 87.32 |

*Table 7.5: Rotated component matrix from the PCA, showing the component with the highest score for each variable.*

| | Component | | | | | | | |
|---|---|---|---|---|---|---|---|---|
| Variable | 1 | 2 | 3 | 4 | 5 | 6 | 7 | 8 |
| Protoconid Metaconid Distance (mm) | 0.59 | | | | | | | |
| Mesial Section Bicervical Diameter (mm) | 0.62 | | | | | | | |
| Distal Section Total Area (mm^2) | 0.65 | | | | | | | |
| Distal Section Dentine Area (mm^2) | 0.67 | | | | | | | |
| Protoconid Metaconid Dentine Distance (mm) | 0.69 | | | | | | | |
| Enamel Volume (mm^3) | 0.70 | | | | | | | |
| Distal Section Bicervical Diameter (mm) | 0.71 | | | | | | | |
| Mesial Section Total Area (mm^2) | 0.71 | | | | | | | |
| Mesial Section Dentine Area (mm^2) | 0.73 | | | | | | | |
| Total Coronal Volume (mm^3) | 0.75 | | | | | | | |
| Protoconid Metaconid Pulp Distance (mm) | 0.76 | | | | | | | |
| Dentine Volume (mm^3) | 0.76 | | | | | | | |
| Hypoconid Entoconid Distance (mm) | 0.80 | | | | | | | |
| EDJ Surface Area (mm^2) | 0.80 | | | | | | | |
| Hypoconid Entoconid Dentine Distance (mm) | 0.83 | | | | | | | |
| Hypoconid Entoconid Pulp Distance (mm) | 0.83 | | | | | | | |
| Outer Enamal Surface Area (mm^2) | 0.84 | | | | | | | |
| Metaconid Entoconid Distance (mm) | 0.84 | | | | | | | |
| Total Coronal Surface Area (mm^2) | 0.85 | | | | | | | |
| Mesial Section EDJ Length (mm) | 0.85 | | | | | | | |
| Total Enamel Surface Area (mm^2) | 0.85 | | | | | | | |
| Distal Section EDJ Length (mm) | 0.85 | | | | | | | |
| Basal Area (mm^2) | 0.86 | | | | | | | |
| Metaconid Entoconid Dentine Distance (mm) | 0.86 | | | | | | | |
| Protoconid Entoconid Distance (mm) | 0.86 | | | | | | | |
| Metaconid Hypoconid Distance (mm) | 0.88 | | | | | | | |
| Protoconid Entoconid Dentine Distance (mm) | 0.89 | | | | | | | |
| Metaconid Hypoconid Dentine Distance (mm) | 0.89 | | | | | | | |
| Protoconid Hypoconid Distance (mm) | 0.91 | | | | | | | |
| Protoconid Hypoconid Dentine Distance (mm) | 0.93 | | | | | | | |
| Protoconid Hypoconid Pulp Distance (mm) | 0.95 | | | | | | | |
| Metaconid Hypoconid Pulp Distance (mm) | 0.95 | | | | | | | |
| Metaconid Entoconid Pulp Distance (mm) | 0.95 | | | | | | | |
| Protoconid Entoconid Pulp Distance (mm) | 0.96 | | | | | | | |
| Distal Mid-Occlusal Basin (mm) | | 0.56 | | | | | | |
| Entoconid Dentine Thickness (mm) | | 0.58 | | | | | | |
| Distal Relative Enamel Thickness | | 0.62 | | | | | | |
| Mesial Relative Enamel Thickness | | 0.63 | | | | | | |
| Average Enamel Thickness (mm) | | 0.70 | | | | | | |
| Protoconid Enamel Thickness (mm) | | 0.70 | | | | | | |
| DB Cusp Occlusal Thickness (mm) | | 0.72 | | | | | | |
| MB Cusp Occlusal Thickness (mm) | | 0.72 | | | | | | |
| MB Cusp Lateral Thickness (mm) | | 0.72 | | | | | | |
| Mesial Section Enamel Area (mm^2) | | 0.74 | | | | | | |
| DL Cusp Occlusal Thickness (mm) | | 0.75 | | | | | | |
| Mesial Mid-Occlusal Basin (mm) | | 0.75 | | | | | | |
| Metaconid Enamel Thickness (mm) | | 0.76 | | | | | | |
| Entoconid Enamel Thickness (mm) | | 0.76 | | | | | | |
| Distal Section Enamel Area (mm^2) | | 0.77 | | | | | | |
| DL Cusp Lateral Thickness (mm) | | 0.77 | | | | | | |
| Hypoconid Enamel Thickness (mm) | | 0.81 | | | | | | |
| DB Cusp Lateral Thickness (mm) | | 0.82 | | | | | | |
| MB Cusp Tip Thickness (mm) | | 0.82 | | | | | | |
| ML Cusp Lateral Thickness (mm) | | 0.83 | | | | | | |
| DB Cusp Tip Thickness (mm) | | 0.83 | | | | | | |
| ML Cusp Occlusal Thickness (mm) | | 0.83 | | | | | | |
| ML Cusp Tip Thickness (mm) | | 0.85 | | | | | | |
| DL Cusp Tip Thickness (mm) | | 0.85 | | | | | | |
| Mesial Average Enamel Thickness (mm) | | 0.89 | | | | | | |
| Distal Average Enamel Thickness (mm) | | 0.89 | | | | | | |
| Hypoconid Dentine Thickness (mm) | | | 0.66 | | | | | |
| Metaconid Dentine Thickness (mm) | | | 0.69 | | | | | |
| Entoconid Angle (degrees) | | | | 0.82 | | | | |
| Hypoconid Angle (degrees) | | | | | | | -0.84 | |
| Protoconid Dentine Thickness (mm) | | | | | -0.37 | | | |
| Protoconid Angle (degrees) | | | | | -0.93 | | | |
| Metaconid Angle (degrees) | | | | | 0.57 | | | |
| Relative Enamel Thickness (3D) | | | | | | | | 0.63 |

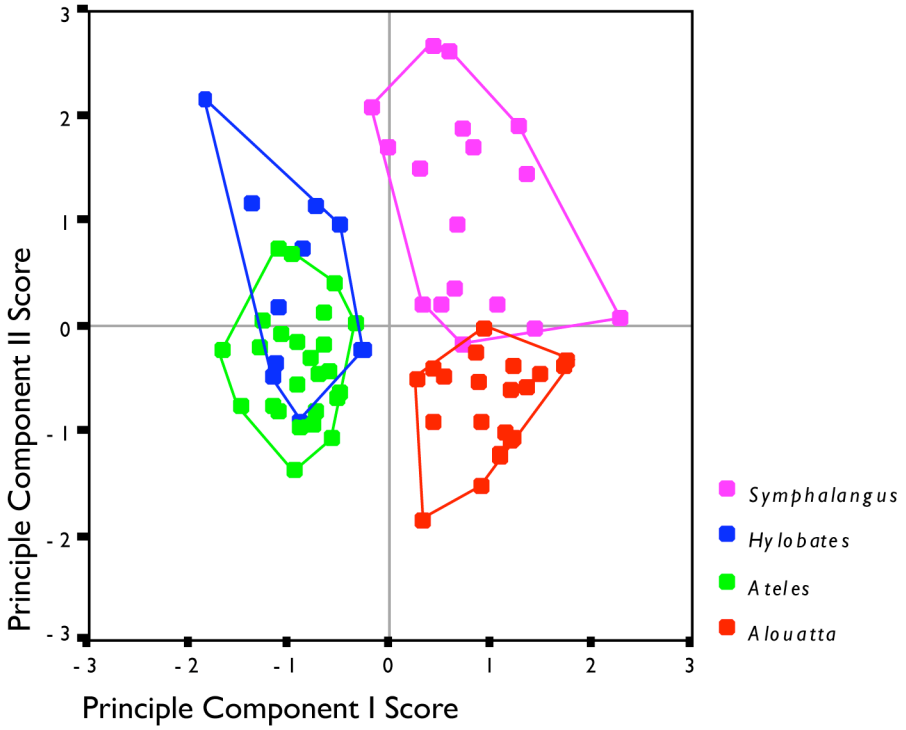


Figure 7.23: Scatter-plot showing the first two principle components based on an exploratory factor analysis of 68 variables. Component one separates the species based on size, and is no classificatory value. The second principle component separates ceboids from hominoids. None of the 8 significant components separated taxa based on dietary proclivity.

crown volume), which is expected in a principle components analysis. This component therefore separates taxa based on tooth size (Figure 7.23), and is of no use in the phylogenetic or dietary separation of taxa. Because the folivorous taxon in each group is larger than the frugivorous taxon, this principle component only appears to be separating dietary groups.The second principle component appears to be of some phylogenetic value, as the species are separated into hylobatids (above zero) and atelids (below zero), although there is substantial overlap between *Ateles* and *Hylobates*. This component has an element of relative enamel thickness, as it describes both the mesial and distal section relative enamel thickness index (Table 7.5), and also the average enamel thickness (in the

mesial and distal planes, as well as the total crown average enamel thickness). The remaining variables described by the second principle component, however, consist primarily of linear enamel thickness measurements at specific cusp locations in the mesial and distal planes. Thus, while the pattern of enamel thickness in a specific plane of section appears not to distinguish folivores from frugivores (see discussion above), the combination of all of these linear measurements in both the mesial and distal planes (as well as cusp thickness as measured in three-dimensions by way of computing the distance between Cartesian landmarks) does appear to distinguish hylobatids from atelids, suggesting that enamel thickness patterning may actually have some taxonomic value when considered in multiple planes of section. Visual inspection of the remaining principle components showed that taxa were completely overlapping, and overlapping in each quadrant of the plot in many cases. Thus, only the first two principle components, explaining 73.24% of the total variance, seem to have value for the discrimination of groups.

Importantly, no principle component, and therefore no independent set of variables among those collected for this study, caused folivores to be grouped separately from frugivores. This includes the distribution of enamel thickness, which does not evince a specific dietary pattern in two-dimensional sections (see discussion above), as well as the three-dimensional pattern of linear enamel thickness from multiple sections and computed by Cartesian coordinates (which appears to group the taxa by superfamily rather than by dietary type; Figure 7.21).

Nonetheless, the data presented here do point towards thicker enamel in frugivores compared to folivores, and generally thicker enamel in the hominoids

compared to the ceboids. A hypothesis for future analyses with more taxa is that these patterns will hold true as more taxa are studied, and that folivore-frugivore differences are essentially equal when superfamilial affiliation is taken into account. Another future experiment may take into account hard-object feeders (e.g., *Cebus apella*, *Lophocebus albigena*), allowing the influence of hard and brittle foodstuffs on enamel thickness in different superfamilies to be assessed.

**Occlusal and Dentine Polygons**

Bailey (2004) recently demonstrated the utility of occlusal polygons in discriminating two closely related taxa (Neandertals and anatomically modern humans; the later group was comprised of both Pleistocene fossils and contemporary (i.e., "present-day") humans). The occlusal polygon is defined by the angles connecting the enamel cusp tips. When the cusp tips of a molar are connected by lines drawn on an occlusal image, a rhomboid is formed, the angles of which may be measured. Bailey took angle measurements on occlusal photographs in her analysis, and reported that three-dimensional measurements (using a point digitizer) resulted in data that were only 4% different than their two-dimensional counterparts (Bailey, 2004, 2002). Nonetheless, whether the height differences apparent in cusps that are not apparent in photographs (particularly the shorter entoconid in the taxa studied in this dissertation; see Chapter 6) impact the utility of occlusal polygons in taxonomic discrimination remains unstudied in non-hominin taxa.

In addition to occlusal polygons, several authors have also noted that the enamel-dentine junction (EDJ) may yield shape information that is different than that culled from

the outer enamel surface. Taxonomically broad studies of the enamel-dentine junction shape of maxillary molars in a broad sample of anthropoid primates have revealed that this aspect of morphology discriminates taxa well at several taxonomic levels (Olejniczak et al., 2003, in press). Nonetheless, all of the shape data collected in the studies by Olejniczak et al. came from maxillary molars. A recent study by Smith et al. (in press) compared data from both the maxillary and mandibular molars of modern humans, and found that the morphology of molars from each jaw is different enough to preclude making direct comparisons. Because the data collected in this dissertation are exclusively from mandibular molars, a comparative context based in previous literature is wanting, and another method of analyzing the shape of the EDJ was sought.

While the shape of the EDJ has been studied in relative detail, comparisons between the EDJ and the enamel surface of molars are lacking (but see Kraus, 1952). Kraus (1952) found that the EDJ predicts gross anatomical features of the enamel surface (e.g., the number of cusps). Kraus also noted, however, that the locations of the dentine horns are not directly inferior to the enamel cusp tips (they tend to lie distally to the cusp tips, but their position relative to the cusp tip is variable). Thus, the shape of the polygon based on the dentine horn tips (hereafter called the "dentine polygon") may be slightly different than that found using the outer enamel surface (the "occlusal polygon"). It is expected that these two polygons will not differ substantially, but it is important to measure the relative efficacy of each at discriminating taxa because even slightly worn enamel may alter the apparent location of enamel cusp tips, so EDJ polygons may be better suited for measurement in worn fossil specimens. To this end, it is important to measure whether the dentine polygon discriminates as well as the occlusal polygon so

that it may be used in cases where worn teeth are involved, thereby expanding the possible sample of fossil teeth that may be studied using this character. The Cartesian coordinates of enamel cusp tips and dentine horn tips were recorded in this study, and the polygons formed by both sets of points were calculated for each tooth in order to examine the effectiveness of these shapes at taxonomic discrimination, as well as to ascertain whether the dentine horn tips provide a different signal than the enamel cusp tips.

Kruskal-Wallace statistics were used to test for group differences in occlusal angles and, in a separate analysis, dentine horn angles; in each case, all four species were included in the analyses. When significant differences were found, the post-hoc comparisons suggested by Conover (1999) were employed to determine which groups were significantly different.

Results of the Kruskal-Wallace tests are reported in Table 7.6. Significant inter-species differences (at the alpha = 0.05 level) were achieved in every comparison except those involving the protoconid (both occlusal and dentine). Post hoc tests reveal, however, that species differences are not consistent at each cuspal angle (Table 7.7). The entoconid angle of both the dentine and the occlusal polygon is significantly different between *Symphalangus* and every other species (the *Symphalangus* entoconid angle is larger than that of the other taxa), for instance, while *Alouatta* is significantly different from each other taxon in terms of the metaconid angle (which is smaller in *Alouatta* than the other taxa). Overall, there were few differences in the significance of angles between the occlusal and dentine polygons, as was expected (Table 7.7), suggesting that these polygons measure the same morphology and that the dentine polygon is interchangeable with the occlusal polygon when worn teeth are to be included in analyses.

Following Bailey (2004), a principle components analysis was performed to examine the variation within the sample, and to readily plot the differences in polygon shape that describe each species. This analysis was run using varimax rotation, and produced three principle components accounting for 87.03% of the variance. The first two components are plotted in Figure 7.24, and the rotated component matrix is given in Table 7.8. As can be seen in the rotated component matrix, the occlusal and dentine polygons are nearly identically loaded on each of the components, suggesting (as above) that they are measuring the same morphology. Unlike the results of Bailey (2004), however, the plot of principle components one and two that shows that the distribution of data does not discriminate species effectively based on these characters (Figure 7.24). *Symphalangus* and *Ateles* show the least overlap on the second principle component, indicating that *Symphalangus* molars have the widest entoconid angles and *Ateles* has the narrowest (concurring with the Kruskal-Wallace analysis, above); the other two species show considerable overlap on the second principle component, and the first component shows a classic "shotgun" pattern where all of the species are nearly entirely overlapping. In sum, the angles of the occlusal and dentine polygons appear to convey the same morphological information, as was expected, but these polygons do not effectively discriminate the species.

The shape of the EDJ in terms of the dentine polygon (i.e., the relative locations of the dentine horns) does not discriminate taxa as well as the shape of the EDJ as measured in maxillary molar mesial ideal planes of section. Future analyses of EDJ morphology may attempt to replicate the relatively high discriminatory power found when maxillary molar mesial ideal planes are measured; until a larger comparative

| *Table 7.6: Kruskal Wallace Results for Polygon Angles.* | | | | | |
|---|---|---|---|---|---|
| | | Protoconid | Metaconid | Hypoconid | Entoconid |
| Enamel Polygon | Chi-Square | 4.993 | 9.268 | 10.983 | 18.727 |
| | d.f. | 3 | 3 | 3 | 3 |
| | Significance | 0.172 | 0.026 | 0.012 | 0 |
| Dentine Polygon | Chi-Square | 3.817 | 9.933 | 15.979 | 14.978 |
| | d.f. | 3 | 3 | 3 | 3 |
| | Significance | 0.282 | 0.019 | 0.001 | 0.002 |

| *Table 7.7: Significant inter-group differences from Kruskal-Wallace Tests.* | | | |
|---|---|---|---|
| Taxa Compared | Metaconid | Hypoconid | Entoconid |
| | Enamel | Enamel | Enamel |
| *Symphalangus - Alouatta* | Sig. | Sig. | Sig. |
| *Symphalangus - Hylobates* | | Sig. | Sig. |
| *Symphalangus - Ateles* | | Sig. | Sig. |
| *Alouatta - Hylobates* | Sig. | | |
| *Alouatta - Ateles* | Sig. | | |
| *Hylobates - Ateles* | | | |
| | Dentine | Dentine | Dentine |
| *Symphalangus - Alouatta* | Sig. | Sig. | Sig. |
| *Symphalangus - Hylobates* | | | Sig. |
| *Symphalangus - Ateles* | | Sig. | Sig. |
| *Alouatta - Hylobates* | Sig. | Sig. | |
| *Alouatta - Ateles* | Sig. | | |
| *Hylobates - Ateles* | | Sig. | |

context is established for mandibular molars (including perhaps landmarks and morphological features that are not apparent in ideal sections), however, the taxonomic utility of this morphology in the lower post-canine dentition cannot be assessed.

## Conclusions

The analyses presented in this chapter have, in part, validated previous two-dimensional studies; they have also shed light on aspects of molar morphology and the evolution of enamel thickness that previous analyses have not been able to explore. The absence of sexual dimorphism apparent in the three-dimensional measurements of the sample studied here is in accord with previous two-dimensional studies, which demonstrated that sexual dimorphism is absent from both average and relative enamel

*Table 7.8: Rotated component matrix from the PCA of angles.*

| | Component | | |
|---|---|---|---|
| Variable | 1 | 2 | 3 |
| Protoconid Enamel Angle | 0.58 | -0.12 | -0.68 |
| Metaconid Enamel Angle | -0.83 | 0.44 | -0.18 |
| Hypoconid Enamel Angle | -0.11 | -0.86 | 0.31 |
| Entoconid Enamel Angle | 0.55 | 0.53 | 0.57 |
| Protoconid Dentine Angle | 0.68 | -0.10 | -0.61 |
| Metaconid Dentine Angle | -0.89 | 0.33 | -0.18 |
| Hypoconid Dentine Angle | -0.08 | -0.82 | 0.37 |
| Entoconid Dentine Angle | 0.58 | 0.61 | 0.43 |

thickness in primates. The lack of sexual dimorphism in three-dimensional data implies that combined sex samples may be utilized in future analyses, thereby increasing sample sizes.

Metameric variation in the molar row was also roughly equivalent to previous two-dimensional studies. Unlike the combined samples that are possible when sex is considered, results of the metameric variation experiment indicate that each tooth position should be analyzed separately as the patterning of dental tissues is not consistent within the tooth row (echoing the findings of Smith et al., 2005). At present, necessary non-human primate bite force data are lacking, precluding a rigorous analysis of whether the trends of increasing average and relative enamel thickness are related to the functional demands of mastication.

The sample of Atelidae molars studied here demonstrated that previous interpretations of ceboid relative enamel thickness based on small samples have accurately characterized this group as having relatively thin enamel. When considered in light of intermediate-thickness cercopithecoids and hylobatids, and recent evidence indicating that *Pan* and *Pongo* have substantially overlapping enamel thickness ranges, Martin's (1983, 1985) interpretation of the polarity of enamel thickness may be reconsidered in light of a taxonomically more broad sample. The current evidence

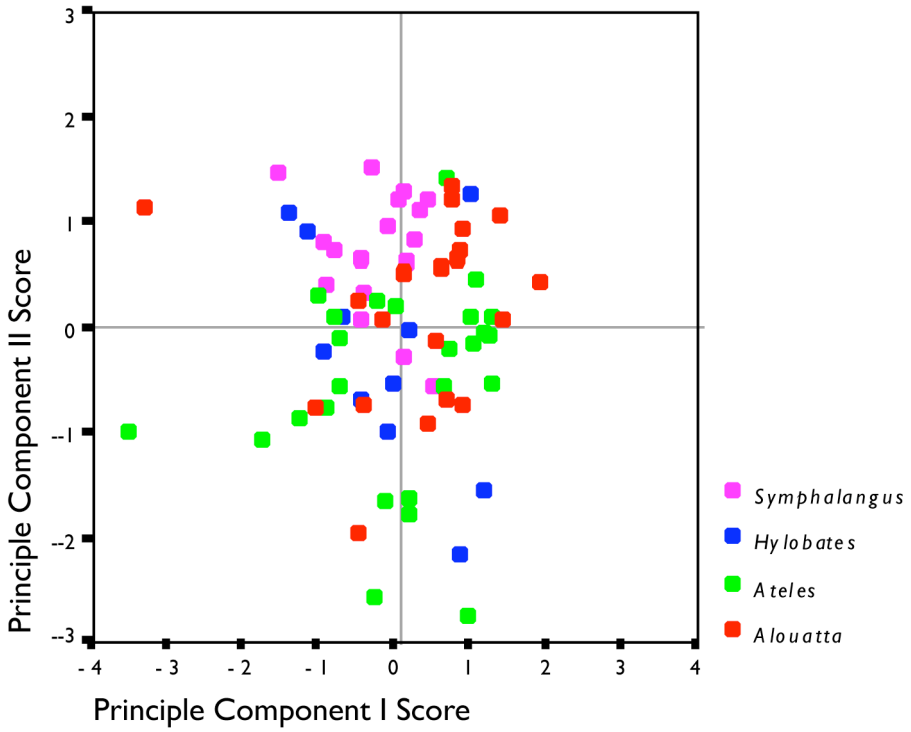


Figure 7.24: Scatter-plot showing the first two principle components of the analysis involving angle variables from occlusal polygons. Neither of the components effectively separates taxa.

suggests that enamel thickness is more difficult to interpret than was previously thought, and that the last common hominoid ancestor may have had enamel of intermediate thickness. Because *Pan*, *Pongo*, and hylobatids also have enamel of intermediate thickness, the notion that a fossil great ape may be identified by its thick molar enamel is unlikely. Unlike cercopithecoids and ceboids, extant apes are represented by a large range of relative enamel thicknesses, with *Gorilla* at the thin end of the range and *Homo* at the thick end of the range. Certainty about the polarity of enamel thickness changes in the fossil record, and whether there is indeed an enamel thickness Rubicon that clearly identifies great apes in the fossil record, must await the analysis of more hominoid taxa

from the early Miocene than the four *Proconsul* molars measured to date  An analysis of basal catarrhine primates (e.g., *Aegyptopithecus*) may also shed light on the polarity of this character.  With the advent of the nondestructive microtomographic techniques described in this dissertation and by Kono (2004) and Tafforeau (2004), it is hoped that a myriad of valuable fossil specimens may become available for analysis.

Functional signals in the patterning of enamel thickness were expected based on the cercopithecoid data provided by Ulhaas et al. (1999) and Shimizu (2002), such that folivorous taxa were expected to have a more uniform enamel thickness across their tooth crown.  This pattern was not evident in the sample studied here, which showed no detectable difference in the patterning of enamel thickness between folivores and frugivores.  In light of the taxonomic constituency of the data collected for this dissertation, complex multivariate analyses aimed at parsing functional from phylogenetic signals were not possible (i.e., phylogenetic independent contrasts), and an exploratory factor analysis using principle component extraction identified no functional groups based on independent components.  Nonetheless, in both of the species dyads, the folivore had significantly thinner enamel than the frugivore when three-dimensional variables were examined, verifying the original functional prediction outlined in Chapter 1.  Future studies should include a more broad range of taxa with different dietary proclivities in order to explore this question directly.

Finally, a comparison of the EDJ shape and the outer enamel surface shape by means of occlusal polygon analysis (sensu Bailey, 2004) demonstrated that the locations of dentine horn tips are predictive of the locations of enamel cusps.  “Occlusal” polygons may therefore be recorded from the dentine horn tips when such data are sought in worn

specimens, thereby increasing the sample size available for many fossil taxa. In contrast to Bailey's (2002, 2004) results, however, the occlusal and dentine polygons recorded in this study did not separate closely related taxa. Principle components analysis revealed that, in lieu of a specific polygon shape describing each taxon, the four species examined here have similar polygon shapes.

In conclusion, it may be stated that the biological analyses conducted in this chapter have demonstrated not only a particular set of results, but also that the methods described in the first six chapters of this dissertation may be applied to these and other biological questions. Because of the non-destructive nature of the techniques employed, future analyses may have larger samples of extant primate molars from museum collections, and also valuable fossil specimens that may not be physically sectioned. The inclusion of large samples and fossil molars in study samples will facilitate the extension of the analyses presented here, and the development of new analyses, into areas of research that have previously been difficult to investigate (e.g., EDJ morphology).

# CHAPTER 8: CONCLUSIONS AND FUTURE DIRECTIONS

Beginning with Miller's (1918) analysis of the Piltdown jaw, molar enamel thickness has played an important role in the diagnosis and taxonomic discrimination of fossil hominoid primates, and has also been central to theories of dental adaptation to diet. Miller's (1918) quantification of enamel thickness in the Piltdown jaw was based on the roentgenographic technology of his day (Figure 8.1), and he concluded that thick molar enamel is found not only in genus *Homo*, but also in non-human hominoids. Miller's work thus represents the first among 90 years of technological advancements applied to the assessment of hominoid molar enamel thickness for the purposes of taxonomic and functional interpretation.

Many of these technological advancements have disappointed. Standard X-Rays (Grine, 2001), medical CT (Grine et al., 1991), TerraHz imaging (personal trials of TerraHz equipment), and ultrasound imaging (Feeney, 2005) have all been demonstrated to be inaccurate or lacking resolution with reference to enamel thickness measurements. In the last five years, however, an accurate technique has emerged (micro-computed tomography), and has been thoroughly investigated by two authors before the writing of this thesis (Kono, 2004; Tafforeau, 2004). The dissertation presented here has attempted foremost to rigorously determine the accuracy of laboratory mCT for enamel thickness analyses, as Tafforeau has done for synchrotron mCT, and also to use this technology to make inferences about dental evolution in primates, as Kono has done.

The results presented in this dissertation have specifically shown that measurements are accurate using laboratory mCT when slice thickness and image resolution are carefully chosen. Moreover, multiple mCT systems, including synchrotron mCT, are approximately equally reliable given the same settings. The consequence of

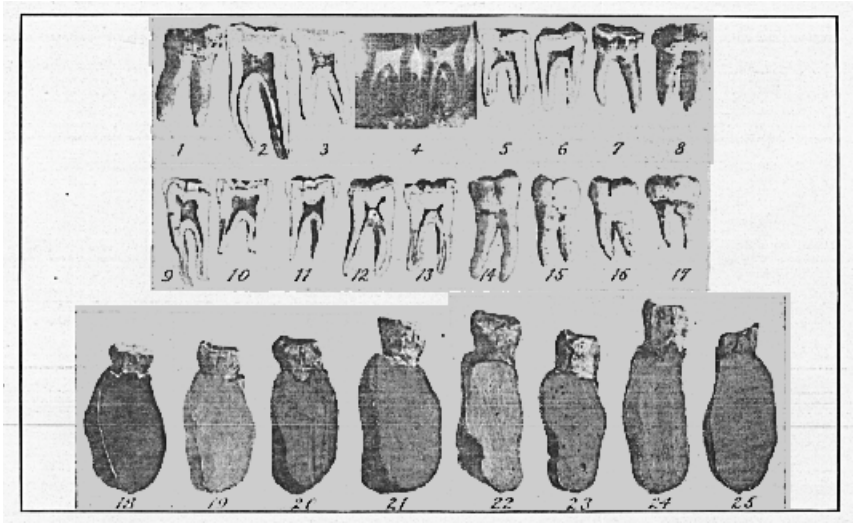

Figure 8.1: Miller's (1918) plate showing an X-ray image of the Piltdown molars (#4) surrounded by sections of *Pan* molars (#5-#8), *Pongo* molars (#1-#3), and *Homo* molars (#9-#17).

multiple accurate systems for the measurement of mCT is that many researchers may produce data of equal quality, and so-called "meta-analyses" combining data from multiple sources may be performed without an added element of inter-observer error.

Nonetheless, the specific means by which data are handled by different researchers after mCT scanning must be treated with caution. The filtering protocol advocated in Chapter 5 of this dissertation has been tested, and works well on extant material and some recent fossils, but is not a perfect solution. Teeth that have undergone severe diagenetic re-mineralization, for instance, may require another filtering process, or may require manual segmentation. An important focus for future research is thus to identify the ideal segmentation routines and filtering protocols for teeth of varying quality in order to ease the process of tissue segmentation without negatively impacting the accuracy if the image stack's representation of the tooth.

Beyond the technical aspects of mCT and image handling, the research presented here has also shed light on the degree to which previous studies have been impacted by

obliquity that may be introduced in the process of manually sectioning teeth. Although obliquity may severely impact measurements when the ideal plane of section is missed or is coursed at an angle that is not parallel to the cervix, it appears that the concerns of previous scholars (e.g., Martin, 1983; Smith et al., 2003), while warranted, have not caused their analyses to be substantially different than if they had found ideal planes using mCT. Evidence presented in Chapters 3 and 6 showed that ideal planes generated by mCT are very similar to physically produced sections, indicating that the manual sectioning process, when carefully performed, produces reliable planes from which to record measurements. Nonetheless, manually produced datasets should be treated as having values that are floating between two confidence intervals, as the degree of obliquity in previously produced sections is impossible to measure with certainty. Moreover, it is recommended that scholars wishing to produce manual sections (e.g., for developmental studies) first record mCT scans of the teeth, and use landmarks from the virtual models to guide the sectioning process.

The biological analyses conducted in Chapter 7 showed that previous interpretations of the polarity of enamel thickness may need to be revised, given the recent results of Shellis et al. (1998), Kono (2004), and Smith et al. (2005), who demonstrated that *Pan* and *Pongo* have substantially overlapping relative enamel thickness ranges. Data from this dissertation lend support to the idea that the last common hominoid ancestor had intermediate enamel thickness (rather than thin enamel, as has been proposed). When combined with the evidence that *Pan* and *Pongo* relative enamel thickness is quite similar, the polarity of enamel thickness in hominoid evolution becomes difficult to interpret. The specific threshold that has been suggested in the past,

namely that great apes are thick enameled and descended from a thin enameled ancestor, is not supported by the weight of current evidence. Because many apes have relative enamel thickness that is intermediate, the specific character state changes cannot be deduced from the available fossil evidence. Echoing the sentiments of Korenhof (1960), it is best to examine many dental characters simultaneously in order to infer temporal evolutionary patterns.

With this in mind, it is recommended that future analyses concentrate on the thickness, shape, and development of the enamel component of the molar crown simultaneously, as has recently been done by Smith et al. (2006). In this way, the growth and structure of enamel may be studied as a process as well as the result of that process, shedding more light on the evolution of the enamel character complex than either approach could yield alone (this was also the strategy employed by Martin (1983), who studied both the development and the thickness of hominoid molars).

Finally, there is a discrepancy between two- and three-dimensional studies in terms of the ability to access developmental data. Two-dimensional section planes have the distinct advantage that microscopy techniques may be employed to extract developmental data in the same specimens as data regarding overall tissue quantities (e.g., Martin, 1983, Smith, 2004). The morphology of the enamel cap of a tooth is only part of the wealth of biological information available; teeth are perhaps the best anatomical structure in terms of their preservation of developmental processes, and future techniques aimed at non-destructive three-dimensional analyses should strive to also cull such developmental data, nondestructively. In this way, development and morphology

may be studied at once, providing a more comprehensive view of both dental evolution, and the evolution of primates generally.

**Bibliography**

Andrews, P. & Martin, L. (1987a). Cladistic relationships of extant and fossil hominoids. J. Hum. Evol. 16, 101-118.

Andrews, P. & Martin, L. (1987b). The phyletic position of the Ad Dabtiyah hominoid. Bull. Br. Mus. Nat. Hist. (Geol.) 41, 383-393.

Andrews, P. & Martin, L. (1991). Hominoid dietary evolution. Philos. Trans. R. Soc. Lond. Ser. B-Biol. Sci. 334, 199-209.

Asfaw, B., White, T., Lovejoy, O., Latimer, B., Simpson, S. & Suwa, G. (1999). *Australopithecus garhi*: A new species of early hominid from Ethiopia. Science 284, 629-635.

Avishai, G., Müller, R., Gabet, Y., Bab, I., Zilberman, U., & Smith, P. (2004). New approach to quantifying developmental variation in the dentition using serial microtomographic imaging. Microsc. Res. Tech. 65, 263-269.

Bailey, S. E. (2002). Neandertal Dental Morphology: Implications for Modern Human Origins. Ph.D. Dissertation, Arizona State University.

Bailey, S. E. (2004). A morphometric analysis of maxillary molar crowns of Middle-Late Pleistocene hominins. J. Hum. Evol. 47, 183-198.

Balto, K., Müller, R., Carrington, D. C., Dobeck, J., & Stachenko, P. (2000). Quantification of periapical bone destruction in mice by micro-computed tomography. J. Dent. Res. 79, 35-40.

Begun, D. R. & Kordos, L. (1993). Revision of *Dryopithecus brancoi* Schlosser, 1901 based on the fossil hominoid material from Rudabanya. J. Hum. Evol. 25, 271-285.

Begun, D., Ward, C. V. & Rose, M. D. (1997). Events in hominoid evolution. In (Begun, D., Ward, C. V. & Rose, M. D., Eds) *Function, Phylogeny, and Fossils: Miocene Hominoid Evolution and Adaptation*, pp. 389-415. New York: Plenum Press.

Beynon, A. D., Dean, M. C., Leakey, M. G., Reid, D. J. & Walker, A. (1998). Comparative dental development and microstructure of *Proconsul* teeth from Rusinga Island, Kenya. J. Hum. Evol. 35, 163-209.

Beynon, A. D. & Wood, B. A. (1986). Variations in enamel thickness and structure in East-African hominids. Am. J. Phys. Anthropol. 70, 177-193.

Bookstein, F. L. (1991). *Morphometric tools for landmark data: geometry and biology*. Cambridge [England]: Cambridge University Press.

Brunet, M., Beauvilain, A., Coppens, Y., Heintz, E., Moutaye, A. H. E. & Pilbeam, D. (1995). The first australopithecine 2,500 kilometers west of the Rift-Valley (Chad). Nature 378, 273-275.

Brunet, M., Guy, F., Pilbeam, D., Mackaye, H. T., Likius, A., Ahounta, D., Beauvilain, A., Blondel, C., Bocherens, H., Boisserie, J. R., De Bonis, L., Coppens, Y., Dejax, J., Denys, C., Duringer, P., Eisenmann, V. R., Fanone, G., Fronty, P., Geraads, D., Lehmann, T., Lihoreau, F., Louchart, A., Mahamat, A., Merceron, G., Mouchelin, G., Otero, O., Campomanes, P. P., De Leon, M. P., Rage, J. C., Sapanet, M., Schuster, M., Sudre, J., Tassy, P., Valentin, X., Vignaud, P., Viriot, L., Zazzo, A. & Zollikofer, C. (2002). A new hominid from the Upper Miocene of Chad, central Africa. Nature 418, 145-151.

Bush, E.C., Simons, E. L., & Allman, J. M. (2004). High-resolution computed tomography study of the cranium of a fossil anthropoid primate, *Parapithecus grangeri*: new insights into the evolutionary history of primate sensory systems. Anat. Rec. A. 281A, 1083–1087.

Castleman, K. R. (1996). *Digital Image Processing*. Prentice Hall: Upper Saddle River, NJ.

Chaimanee, Y., Jolly, D., Benammi, M., Tafforeau, P., Duzer, D., Moussa, I. & Jaeger, J. J. (2003). A Middle Miocene hominoid from Thailand and orangutan origins. Nature 422, 61-65.

Chapman, C. A., Chapman, L. J. (1991). The foraging itinerary of spider monkeys: when to eat leaves? *Folia Primatologica*. 56, 162-166.

Conover, W. J. (1999). *Practical Nonparametric Statistics*. Wiley: New York.

Conroy, G. C., Pickford, M., Senut, B., Vancouvering, J. & Mein, P. (1992). *Otavipithecus namibiensis*, 1st Miocene hominoid from southern Africa. Nature 356, 144-148.

Conroy, G. C., Lichtman, J. W. & Martin, L. B. (1995). Brief communication - some observations on enamel thickness and enamel prism packing in the Miocene hominoid *Otavipithecus namibiensis*. Am. J. Phys. Anthropol. 98, 595-600.

Cooper, D. M. L., Matyas, J. R., Katzenberg, M. A., & Hallgrimsson ,B. (2004). Comparison of microcomputed tomographic and microradiographic measurements of cortical bone porosity. Calcif. Tiss. Int. 74, 437–447.

Corruccini, R. S. (1987). The dentinoenamel junction in primates. Int J Primatol 8, 99-114.

Crawley, D., Longbottom, C., Wallace, V. P., Cole, B., Arnone, D. & Pepper, M. (2003). Three-dimensional terahertz pulse imaging of dental tissue. J. Biomed. Opt. 8, 303-307.

Dauphin, Y. (1987). Some results on the dental enamel structure in fossil and recent reptiles. CR Acad Sci II 305, 1217–1219.

Dean, M. C. (2000). Progress in understanding hominoid dental development. J. Anat. 197, 77-101.

Dean, M. C., & Leakey, M. G. (2003). Enamel and dentine development and the life history profile of *Victoriapithecus macinnesi* from Maboko Island, Kenya. Annals of Anatomy-Anatomischer Anzeiger 186, 405-412.

Dean, M. C. & Schrenk, F. (2003). Enamel thickness and development in a third permanent molar of *Gigantopithecus blacki*. J. Hum. Evol. 45, 381-387.

Doran, D. M., McNeilage, A., Greer, D., Bocian, C., Mehlman, P., Shah, N. (2002). Western lowland gorilla diet and resource availability: new evidence, cross-site comparisons, and reflections on indirect sampling methods. Am. J. Primatol. 58, 91-116.

Dumont, E. R. (1995). Enamel thickness and dietary adaptation among extant primates and chiropterans. J. Mammal. 76, 1127-1136.

Durand, E. P., & Rüegsegger, P. (1991). Cancellous bone structure: analysis of high-resolution CT images with run-length method. J. Comp. Assist. Tomogr. 15, 133–139.

Fajardo, R. J., Ryan, T. M., & Kappelman, J. (2002). Assessing the accuracy of high-resolution X-ray computed tomography of primate trabecular bone by comparison with histological sections. Am. J. Phys. Anthropol. 118, 1–10.

Feeney, R. N. M. (2005). An investigation of ultrasound methods for the assessment of sex and age from intact human teeth. Dent. Anthropol. 18, 2-11.

Felsenstein, J. (1985). Phylogenies and the comparative method. Am. Natural. 1, 1-15.

Fleagle, J. G. (1984). Are there any fossil gibbons? In (Preuschoft, H., Chivers, D. J., Brockelman, W. Y., & Creel, N., Eds.) *The Lesser Apes: Evolutionary and Behavioral Biology*, pp. 431-447. Edinburgh: Edinburgh University Press.

Fleagle, J. G. (1999). *Primate Adaptation and Evolution*. Academic Press: New York.

Gantt, D. G. (1977). Enamel of Primate Teeth: its Structure with Reference to Functional and Phyletic implications. Ph.D. Dissertation, Washington University, St. Louis.

Gantt, D. G. (1982). Neogene hominoid evolution: a tooth's inside view. In (Kurten, B., Ed) *Teeth: Form, Function, and Evolution*, pp. 93-108. New York: Columbia University Press.

Gantt, D. G., Harris, E. F., Rafter J. A., & Rahn, J. K. (2001). Distribution of enamel thickness in human deciduous teeth. In (Brook, A., Ed) *Dental Morphology 2001*, pp. 167-190. Sheffield Academic Press: Sheffield, UK.

Gantt, D. G., Kappleman, J., Ketcham, R. A., Alder, M. E. & Deahl, T. H. (2003). 3D approach to interpret enamel thickness and volume. Am. J. Phys. Anthropol. Supp. 41, 99.

Gibbs, S., Collard, M., Wood, B. (2002). Soft-tissue anatomy of the extant hominoids: a review and phylogenetic analysis. J. Anat. 200, 3-49.

Gittins, S. P., & Raemaekers, J. J. (1980). Siamang, lar, and agile gibbons. In (Chivers, D. J., Ed) *Malayan forest primates: Ten year's study in tropical rain forest*. Plenum Press: New York, NY.

Grine, F. E. (1991). Computed tomography and the measurement of enamel thickness in extant hominoids: implications for its paleontological application. Palaeont. afr. 28, 61-69.

Grine FE. (2000). Middle Stone Age human fossils from Die Kelders Cave 1, Western Cape Province, South Africa. J. Hum. Evol. 38, 129-145.

Grine, F. E. (2002). Scaling of tooth enamel thickness, and molar crown size reduction in modern humans. S. Afr. J. Sci. 98, 503-509.

Grine, F. E. (2004). Geographic variation in tooth enamel thickness does not support Neandertal involvement in the ancestry of modern Europeans. S. Afr. J. Sci. 100, 389–394.

Grine, F. E. (2005). Enamel thickness of deciduous and permanent molars in modern *Homo sapiens*. Am. J. Phys. Anthropol. 126, 14-31.

Grine, F. E. & Martin, L. (1988). Enamel thickness and development in *Australopithecus* and *Paranthropus*. In (Grine, F. E., Ed) *Evolutionary History of the "Robust" Australopithecines*, pp. 3-42. Aldine de Gruyter: New York, NY.

Grine, F. F., Spencer, M. A., Demes, B., Smith, H. F., Strait, D. S., Constant, D. A. (2005). Molar enamel thickness in the chacma baboon, *Papio ursinus* (Kerr, 1792). Am. J. Phys. Anthropol. 128, 812-822.

Grine, F. E., Stevens, N. J. & Jungers, W. L. (2001). An evaluation of dental radiograph accuracy in the measurement of enamel thickness. Arch. Oral Biol. 46, 1117-1125.

Grine, F. E., Spencer, M. A., Demes, A. B., Smith, H. F., Strait, D. S., Constant, & D. A. (2005). Molar enamel thickness in the Chacma baboon, *Papio ursinus*. Am. J. Phys. Anthropol. 128, 812–822.

Groves, C. P. (2001). *Primate Taxonomy*. Smithsonian Institution Press: Washington, DC.

Haile-Selassie, Y. (2001). Late Miocene hominids from the Middle Awash, Ethiopia. Nature 412, 178-181.

Hall, L. M., Jones, D. S., Wood, B. A. (1998). Evolution of gibbon subgenera inferred from Cytochrome *b* DNA sequence data. Mol. Phyl. Evol. 39, 281-286.

Harvey, P. H., & Pagel, M. D. (1991). *The Comparative Method in Evolutionary Biology*. Oxford University Press: Oxford.

Hayashi, S., Hayasaka, K., Takenaka, O., & Horai, S. (1995). Molecular phylogeny of gibbons inferred from mitochondrial DNA sequences: preliminary report. J. Molec. Evol. 41, 359-365.

Heizmann, E. P. J. & Begun, D. R. (2001). The oldest Eurasian hominoid. J. Hum. Evol. 41, 463-481.

Hendee W.R., & Ritenour ER. 2002. *Medical Imaging Physics*. Wiley-Liss: New York, NY.

Hildebrand, T., Laib, A., Müller, R., Dequekker, J., & Rüegsegger, P. (1999). Direct three-dimensional morphometric analysis of human cancellous bone: microstructural data from spine, femur, iliac crest, and calcaneus. J. Bone. Miner. Res. 14, 1167–1174.

Hlusko, L. J. (2002). Identifying metameric variation in extant hominoid and fossil hominid mandibular molars. Am. J. Phys. Anthropol. 118, 86-97.

Hlusko, L. J., Suwa, G., Kono, R. T., Mahaney, M. C. (2004). Genetics and the evolution of primate enamel thickness: a baboon model. Am. J. Phys. Anthropol. 124, 223-233.

Jähne B. 1997. *Digital Image Processing: Concepts, Algorithms, and Scientific Applications*. Springer: Berlin.

Jolly, C. J. (1970). Seed-eaters: a new model of hominid differentiation based on a

baboon analogy. Man 5, 5-26.

Kay, R. F. (1981). The nut-crackers - a new theory of the adaptations of the Ramapithecinae. Am. J. Phys. Anthropol. 55, 141-151.

Kono, R. (2004). Molar enamel thickness and distribution patterns in extant great apes and humans: new insights based on a 3-dimensional whole crown perspective. Anthropol. Sci. 112, 121-146.

Korenhof, C. A. W. (1961). The enamel-dentine border: a new morphological factor in the study of the (human) molar pattern. Proceedings of the Koninklijke Nederlands 64B, 639-664.

Kraus, B. S. (1952). Morphologic relationships between enamel and dentine surfaces of lower first molar teeth. J. Dent. Res. 31, 248-256.

Kuhn, J. L., Goldstein, S. A., Feldkamp, L.A., Goulet, R.W., & Jesion, G. (1990). Evaluation of a microcomputed tomography system to study trabecular bone structure. J. Orthoped. Res. 8, 833–842.

Leakey, M. G., Ungar, P. S. & Walker, A. (1995). A new genus of large primate from the Late Oligocene of Lothidok, Turkana District, Kenya. J. Hum. Evol. 28, 519-531.

Leakey, M. G., Spoor, F., Brown, F. H., Gathogo, P. N., Kiarie, C., Leakey, L. N. & McDougall, I. (2001). New hominin genus from eastern Africa shows diverse middle Pliocene lineages. Nature 410, 433-440.

Leighton, D. R. (1987). Gibbons: territoriality and monogamy. In (Smuts, B. B., Cheney, D. L., Seyfarth, R. M., Wrangham, R. W., Struhsaker, T. T., Eds) *Primate Societies*. University of Chicago Press: Chicago, IL.

Macho, G. A. & Berner, M. E. (1993). Enamel thickness of human maxillary molars reconsidered. Am. J. Phys. Anthropol. 92, 189-200.

Macho, G. A. & Spears, I. R. (1999). Effects of loading on the biochemical behavior of molars of Homo, Pan, and Pongo. Am. J. Phys. Anthropol. 109, 211-227.

Macho, G. A. & Thackeray, J. F. (1992). Computed-tomography and enamel thickness of maxillary molars of Plio-pleistocene hominids from Sterkfontein, Swartkrans, and Kromdraai (South-Africa) - an exploratory study. Am. J. Phys. Anthropol. 89, 133-143.

Martin, L. B. (1983). Relationships of the Later Miocene Hominoidea. Ph.D. Dissertation, University College London.

Martin LB. 1985. Significance of enamel thickness in hominoid evolution. Nature

314:260-263.

Martin, L. B. & Andrews, P. (1984). The phyletic position of *Graecopithecus freybergi* Koenigswald. Cour. Forsch. Inst. Senkenberg 69, 25-40.

Martin LB, Olejniczak AJ, & Maas MC. 2003. Enamel thickness and microstructure in pitheciin primates, with comments on dietary adaptations of the middle Miocene hominoid *Kenyapithecus*. J. Hum. Evol. 45, 351-367.

McErlain, D. D., Chhem, R. K., Bohay, R. N., & Holdsworth, D. W. (2004). Microcomputed tomography of a 500-year-old tooth: technical note. J. Assoc. Canad. Radiol. 55, 242–245.

Mezava S, Kawato T, Yoshida K, Molnar, S., Hildebolt, C., Molnar, I. M., Radovcic, J. & Gravier, M. (1993). Hominid enamel thickness.1. the Krapina Neandertals. Am. J. Phys. Anthropol. 92, 131-138.

Miller, G. S. (1918). The Piltdown jaw. Am. J. Phys. Anthropol. 1, 25-52.

Morgan, C. L. (1983). *Basic Principles of Computed Tomography*. Baltimore, MD: University Park Press.

Müller R., Hahn, M., Vogel, M., Delling, G., & Rüegsegger, P. (1996). Morphometric analysis of noninvasively assessed bone biopsies: comparison of high-resolution computed tomography and histologic sections. Bone 18, 215–220.

Müller, R., van Campenhout, H., Van Damme, B., Van der Perre, G., Dequeker, J., Hildebrand, T., & Rüegsegger, P. (1998). Morphometric analysis of human bone biopsies: a quantitative structural comparison of histological sections and micro-computed tomography. Bone 23, 59–66.

Nagatoshi, K. (1990). Molar enamel thickness in European Miocene and extant Hominoidea. Int J Primatol 11, 283-295.

Neville, M. K., Glander, K. E., Braza, F., & Rylands, A. B. (1998). The howling monkeys, genus *Alouatta*. In (Mittermeier, R. A., Coimbra-Filho, A., & da Fonseca, G. A. B., Eds) *Ecology and behavior of neotropical primates*. World Wildlife Fund: Washington, DC.

Noether, G. E. (1967). Wilcoxon confidence intervals for location parameters in the discrete case. J. Am. Stat. Assoc. 62, 184-188.

Olejniczak, A. J. (2005) Mesio-distal and angular obliquity in the study of dental sections. Am. J. Phys. Anthropol, Supp. 41:140-141.

Olejniczak, A. J., & Grine, F. E. (2005). High-resolution measurement of Neanderthal

tooth enamel thickness by micro-focal computed tomography. S. Afr. J. Sci. 101, 219-220.

Olejniczak, A. J., & Grine, F. E. (2006). Assessment of the accuracy of dental enamel thickness measurements using microfocal X-ray computed tomography. Anat. Rec. A. 288, 263-275.

Olejniczak AJ, Martin LB, & Ulhaas L. (2004). Quantification of dentine shape in anthropoid primates. Annals of Anatomy-Anatomischer Anzeiger 186, 479-485.

Olejniczak, A. J., Gilbert, C. C., Grine, F. E., Martin, L. B., Smith, T. M. & Ulhaas, L. (in review) Enamel-dentine junction morphology as a taxonomic discriminator in anthropoid primates. J. Hum. Evol.

Olejniczak, A. J., Smith, T. M., Tafforeau, P., Temming, H., & Hublin, J-J. (2006). A comparison of microtomographic systems for the analysis of dental tissues. Am. J. Phys. Anthropol. Supp. 42, 140-141.

Olejniczak, A. J., Grine, F. E., & Martin, L. B. (in press). Micro-computed tomography of primate molars: methodological aspects of three-dimensional data collection. In (Bailey, S. & Hublin, J-J., Eds.) *Dental Perspectives on Human Evolution: State of the Art Research in Dental Paleoanthropology*.

Peters, O.A., Laib, A., Rüegsegger, P., Barbakow, F. (2000). Three-dimensional analysis of root canal geometry by high-resolution computed tomography. J. Dent. Res. 79, 1405–1409.

Pickford, M. & Ishida, H. (1998). Interpretation of *Samburupithecus*, an Upper Miocene hominoid from Kenya. Comptes Rendus Acad. Sci. Ser II-A 326, 299-306.

Pitas I. 1993. *Digital Image Processing Algorithms*. Prentice Hall International: Hemel Hempsted, UK.

Rangayyan, R. M. (2005). *Biomedical Image Analysis*. Boca Raton, FL: CRC Press.

Rhodes, J. S., Pitt-Ford, T. R., Lynch, J. A., Liepins, P. J., & Curtis, R. V. (1999). Micro-computed tomography: a new tool for experimental endodontology. Int. Endodont. J. 32, 165–170.

Rosset, A., Spadola, L. & Ratib, O. (2004). OsiriX: an open-source software for navigating in multidimensional DICOM images. Journal of Digital Imaging 17, 205-216.

Ruvolo M. (1997). Molecular phylogeny of the hominoids: influences from multiple independent DNA sequence data sets. Mol. Biol. Evol. 14, 248-265.

Sakai, T., Sasaki, I. & Hanamura, H. (1965). A morphological study of enamel-dentin border on the Japanese dentition: I. maxillary median incisor. J. Anthropol. Soc. Nip. 73, 91-109.

Sakai, T. & Hanamura, H. (1971). A morphological study of enamel-dentin border on the Japanese dentition: V. maxillary molar. J. Anthropol. Soc. Nip. 79, 297-322.

Sakai, T. & Hanamura, H. (1973a). A morphological study of enamel-dentin border on the Japanese dentition: VI. mandibular molar. J. Anthropol. Soc. Nip. 81, 25-45.

Sakai, T. & Hanamura, H. (1973b). A morphological study of enamel-dentin border on the Japanese dentition: VII general conclusion. J. Anthropol. Soc. Nip. 81, 87-102.

Sato, I., Shimada, K., Handal, J. C., Lance, V., & Gasser, R. F. (1988). Morphology of the American alligator (*Alligator mississipiensis*) tooth: I, the fine-structure and analysis of the enamel. Am. Zool. 28, A78.

Schwartz, G. T. (1997). Taxonomic and functional aspects of enamel cap structure in South African Plio-Pleistocene hominids: a high-resolution computed tomographic study. Ph.D. Dissertation, Washington University.

Schwartz GT. (2000). Taxonomic and functional aspects of the patterning of enamel thickness distribution in extant large-bodied hominoids. Am. J. Phys. Anthropol. 111, 221-244.

Schwartz, G. T., Thackeray, J. F., Reid, C. & van Reenan, J. F. (1998). Enamel thickness and the topography of the enamel-dentine junction in South African Plio-Pleistocene hominids with special reference to the Carabelli trait. J. Hum. Evol. 35, 523-542.

Seibel, B. A., & Carlini, D. B. (2001). Metabolism of pelagic cephalopods as a function of habitat depth: a reanalysis using phylogenetically independent contrasts. Biol. Bull. 1, 1-5.

Senut, B., Pickford, M., Gommery, D., Mein, P., Cheboi, K. & Coppens, Y. (2001). First hominid from the Miocene (Lukeino Formation, Kenya). Comptes Rendus Acad. Sci. Ser II-A 332, 137-144.

Senut, B., Pichford, M., Gommery, D. & Kunimatsu, Y. (2000). A new genus of early Miocene hominoid from East Africa: *Ugandapithecus major* (Le Gros Clark & Leakey, 1950). Compte Rendus Acad. Sci. Ser II-A 331, 227-233.

Shellis RP, Beynon AD, Reid DJ, & Hiiemae KM. (1998). Variations in molar enamel thickness among primates. J. Hum. Evol. 35, 507-522.

Shimizu, D. (2002). Functional implications of enamel thickness in the lower molars of red colobus (*Procolobus badius*) and Japanese macaque (*Macaca fuscata*). J. Hum. Evol. 43, 605-620.

Simons, E. L., & Pilbeam, D. (1972). Hominoid paleoprimatology. In (Tuttle, R., Ed.) *The Functional and Evolutionary Biology of Primates*. Aldine: Chicago.

Smith, R. J., Jungers, W. L. (1997). Body mass in comparative primatology. J. Hum. Evol. 32, 523-559.

Smith, T. M., Martin, L. B. & Leakey, M. G. (2003). Enamel thickness, microstructure and development in *Afropithecus turkanensis*. J. Hum. Evol. 44, 283-306.

Smith, T. M., Martin, L. B., Reid, D. J., De Bonis, L. & Koufos, G. (2004). An examination of dental development in *Graecopithecus freybergi* (=*Ouranopithecus macedoniensis*). J. Hum. Evol. 46, 551-577.

Smith, T. M., Olejniczak, A. J., Martin, L. B. & Reid, D. J. (2005). Variation in hominoid molar enamel thickness. J. Hum. Evol. 48, 575-592.

Smith, T. M., Olejniczak, A. J., Tafforeau, P., Grine, F. E. & Hublin, J.-J. (2006) High resolution microtomography of Middle Stone Age human molars from South Africa. Am. J. Phys. Anthropol. Sup. 42 167.

Smith, T. M., Olejniczak, A. J., Reid, D. J., Ferrell, R. J., & Hublin, J-J. (in press). Modern human molar enamel thikcnes and enamel-dentine junction shape. Arch. Oral. Bio.

Sokal, R. R., & Rohlf F. J. (1995). *Biometry: the Principles and Practice of Statistics in Biological Research*. W. H. Freeman: New York.

Spears, I. R. & Crompton, R. H. (1996). The mechanical significance of the occlusal geometry of great ape molars in food breakdown. J. Hum. Evol. 31, 517-535.

Spears, I. R. & Macho, G. A. (1998). Biomechanical behaviour of modern human molars: implications for interpreting the fossil record. Am. J. Phys. Anthropol. 106, 467-482.

Spencer, M. A. (1998). Force production in the primate masticatory system: electromyographic tests of biomechanical hypotheses. J. Hum. Evol. 34. 25-34.

Spencer, M. A. (1999). Constraints on masticatory system evolution in anthropoid primates. Am. J. Phys. Anthropol. 108, 483-506.

Spoor, C. F., Zonneveld, F. W. & Macho, G. A. (1993). Linear measurements of cortical bone and dental enamel by computed-tomography - applications and problems. Am. J. Phys. Anthropol. 91, 469-484.

Suwa, G., & Kono, R. (2005). A micro-CT based study of linear enamel thickness in the mesial cusp section of human molars: reevaluation of methodology and assessment of within-tooth, serial, and individual variation. Anthropol. Sci. 113, 273-289.

Swindler, D. R. (2005). *Primate Dentition: an Introduction to the Teeth of Non-human Primates*. Cambridge University Press: Cambridge.

Tabachnick, B. G., & Fidell, L. S. (2000). *Using multivariate statistics*. Allyn and Bacon: Boston.

Tafforeau, P. (2004). Aspects phylogénétiques et fonctionnels de la microstructure de l'émail dentaire et de la structure tridimensionnelle des molaires chez les primates fossiles et ctuels: apports de la microtomographie à rayonnement X synchrotron. Ph.D. Dissertation, Université de Montpellier II.

Tafforeau, P., Boistel. R,, Boller. E,, Bravin, A., Brunet, M., Chaimanee, Y., Cloetens, P., Feist, M., Hoszowska, J., Jaeger, J-J., Kay, R.F., Lazzari, V., Marivaux, L., Nel, A., Nemoz, C., Thibault, X., Vignaud, P., Zabler, S. (2006). Applications of X-Ray synchrotron microtomography for non-destructive 3D studies of paleontological specimens. Appl. Phys. A 83, 195-202.

Ulhaas, L., Henke, W., & Rothe, H. (1999). Variation in molar enamel thickness in genera *Cercopithecus* and *Colobus*. Anthropologie 37, 265-271.

von Stechow, D., Balto, K., Stashenko, P., & Müller, R. (2003). Three-dimensional quantitation of periradicular bone destruction by micro-computed tomography. J. Endodont. 29, 252–256.

Weiss, K.M. (1990). Duplication with variation: metameric logic in evolution from genes to morphology. Yrbk. Phys. Anthropol. 33, 1-23.

Welch, T.A. (1984). A technique for high performance data compression. IEEE Computer 17, 8-19.

White, T.D, Suwa, G., & Asfaw, B. 1994. AustralopithecusWalker, A., Teaford, M. F., Martin, L. & Andrews, P. (1993). A new species of *Proconsul* from the Early Miocene of Rusinga and Mfangano Islands, Kenya. J. Hum. Evol. 25, 43-56.

White, T. D., Suwa, G. & Asfaw, B. (1994). *Australopithecus ramidus*, a new species of early hominid from Aramis, Ethiopia. Nature 371, 306-312.

White, T. D., Suwa, G. & Asfaw, B. (1995). *Australopithecus ramidus*, a new species of early hominid from Aramis, Ethiopia (Vol 371, Pg 306, 1994). Nature 375, 88-88.

Yang, Z. (1991). Ultrasound surface imaging and the measurement of tooth enamel thickness. Ph.D. Dissertation, University of Manchester, UK.

Zhang, Y. (1997). Mitochondrial DNA sequence evolution and phylogenetic relationships of gibbons. Acta Genetica Sinica 24, 231-237.

## Appendix A: Median filter implementation in the Objective-C language

```
//  MEDIANFILTER.M
//  Created by Anthony J. Olejniczak on Sun Sep 11 2005.

#import "MedianFilter.h"
@implementation MedianFilter
- (NSImage *) medFilter: (NSImage *) srcImage
{
     // Variable declarations:
     // Memory management pool
     NSAutoreleasePool *pool = [[NSAutoreleasePool alloc] init];
     // Bitmap representation of the image passed to the method
     NSBitmapImageRep *srcImageRep = srcImageRep = [NSBitmapImageRep imageRepWithData:
     [srcImage TIFFRepresentation]];
     // Width of the image in pixels
     int w = [srcImageRep pixelsWide];
     // Height of the image in pixels
     int h = [srcImageRep pixelsHigh];
     // A new image to store the results of the median filtration
     NSImage *destImage = [[NSImage alloc] initWithSize:NSMakeSize(w,h)];
     // Integer counter variables represeting the coordinates of the pixels in question
     int x, y;
     // A holder for the number of bytes in each row (this method assumes 8-bit images)
     int bytesPerRowHolder = w * 8 * 1 / 8;
     // Bitmap representation of the newly established, filtered image
     NSBitmapImageRep *destImageRep = [[[NSBitmapImageRep alloc]
            initWithBitmapDataPlanes:NULL pixelsWide:w pixelsHigh:h bitsPerSample:8
            samplesPerPixel:1 hasAlpha:NO isPlanar:NO
            colorSpaceName:NSCalibratedWhiteColorSpace bytesPerRow:bytesPerRowHolder
            bitsPerPixel:8] autorelease];
     // Pixel value from the source image
     unsigned char *srcData = [srcImageRep bitmapData];
     // Pixel value in the destination image
     unsigned char *destData = [destImageRep bitmapData];
     // Pointer variables
     unsigned char *p, *p2;
     // Number of bits per pixel / 8 (= 1)
     int n = [srcImageRep bitsPerPixel] / 8;
     // Variables that hold the "neighborhood" of pixels
     unsigned char *x1, *x2, *x3, *x4, *x5, *x6, *x7, *x8;

     // The filter process:
     for ( y = 0; y < h; y++)
     {
          for ( x = 0; x < w; x++)
          {
          // Do not perform the filter on the borders of the image
               if ((y != 0) && (y != h) && (x != 0) && (x != w))
               {
                    NSMutableArray *neighborhoodPixels = [NSMutableArray
                    arrayWithCapacity: 1];
                    p = srcData + n * ( y * w + x );
                    x1 = srcData + n * ( (y - 1) * w + (x - 1));
                    x2 = srcData + n * ( (y - 1) * w + x);
                    x3 = srcData + n * ( (y - 1) * w + (x + 1));
                    x4 = srcData + n * ( y * w + (x - 1));
                    x5 = srcData + n * ( y * w + (x + 1));
                    x6 = srcData + n * ( (y - 1) * w + (x - 1));
                    x7 = srcData + n * ( (y - 1) * w + x);
                    x8 = srcData + n * ( (y - 1) * w + (x + 1));
                    [neighborhoodPixels addObject: [NSNumber numberWithInt: *x1]];
```

```
                    [neighborhoodPixels addObject: [NSNumber numberWithInt: *x2]];
                    [neighborhoodPixels addObject: [NSNumber numberWithInt: *x3]];
                    [neighborhoodPixels addObject: [NSNumber numberWithInt: *x4]];
                    [neighborhoodPixels addObject: [NSNumber numberWithInt: *x5]];
                    [neighborhoodPixels addObject: [NSNumber numberWithInt: *x6]];
                    [neighborhoodPixels addObject: [NSNumber numberWithInt: *x7]];
                    [neighborhoodPixels addObject: [NSNumber numberWithInt: *x8]];
                    [neighborhoodPixels addObject: [NSNumber numberWithInt: *p]];

                    // Bubble sort the array of pixel values
                    int temp, c, d;
                    for (c = 0; c < 8; c++)
                    {
                         for (d = 0; d < (8-c); d++)
                         {
                              if ([[neighborhoodPixels objectAtIndex: d] intValue] <
                                   [[neighborhoodPixels objectAtIndex: d+1] intValue])
                              {
                                   temp = [[neighborhoodPixels objectAtIndex: d]
                                   intValue];
                                   [neighborhoodPixels insertObject: [NSNumber
                                   numberWithInt: [[neighborhoodPixels objectAtIndex:
                                   d+1] intValue]] atIndex: d];
                                   [neighborhoodPixels removeObjectAtIndex: d+1];
                                   [neighborhoodPixels insertObject: [NSNumber
                                   numberWithInt: temp] atIndex: d+1];
                              }
                         }
                    }
                    // Assign the 4th pixel value (= the median pixel value) to the pixel
                    in the destination image
                    p2 = destData + y * w + x;
                    *p2 = (unsigned char) [[neighborhoodPixels objectAtIndex: 4]
                    intValue];
               }
          }
     }

     //Return the new image
     [destImage addRepresentation: destImageRep];
     [pool release];
     return destImage;
}
@end
```

## Appendix B: A Neighborhood-Based Noise Removal Algorithm in Objective-C

```
//  CleanNoise.m
//  Created by Anthony on 16/09/2005.

#import "CleanNoise.h"
@implementation CleanNoise

- (NSImage *) cleanNoise : (NSImage *) srcImage
{
     // Variable declaration:
     NSBitmapImageRep *srcImageRep = srcImageRep = [NSBitmapImageRep imageRepWithData:
     [srcImage TIFFRepresentation]];
     int w = [srcImageRep pixelsWide];
     int h = [srcImageRep pixelsHigh];
     NSImage *destImage = [[NSImage alloc] initWithSize:NSMakeSize(w,h)];
     int x, y;
     int bytesPerRowHolder = w * 8 * 1 / 8;
     NSBitmapImageRep *destImageRep = [[[NSBitmapImageRep alloc]
                                   initWithBitmapDataPlanes:NULL
                                   pixelsWide:w
                                   pixelsHigh:h
                                   bitsPerSample:8
                                   samplesPerPixel:1
                                   hasAlpha:NO
                                   isPlanar:NO
                                   colorSpaceName:NSCalibratedWhiteColorSpace
                                   bytesPerRow:bytesPerRowHolder
                                   bitsPerPixel:8] autorelease];
     unsigned char *srcData = [srcImageRep bitmapData];
     unsigned char *destData = [destImageRep bitmapData];
     unsigned char *p, *p2, *northP, *southP, *eastP, *westP;
     int n = [srcImageRep bitsPerPixel] / 8;
     int north, south, east, west;
     int northeast, northwest, southeast, southwest;
     int c;

     // Method implementation section: (this section assumes a neighborhood spanning 10
     // pixels in any direction - change the number ten in the code below to change
     // the size of the neighborhood.
     for ( y = 0; y < h; y++)
     {
          for ( x = 0; x < w; x++)
          {
               // Do not perform the filter on the borders of the image
               if ((y > 10) && (y < h-10) && (x > 10) && (x < w-10))
               {
                    p = srcData + n * ( y * w + x );
                    if ((int) *p == 0)
                    {
                         north = 0; south = 0; east = 0; west = 0;
                         northeast = 0; northwest = 0; southeast = 0; southwest = 0;
                         for (c = 1; c < 10; c++)
                         {
                              northP = srcData + n * ( (y+c) * w + x );
                              southP = srcData + n * ( (y-c) * w + x );
                              eastP = srcData + n * ( y * w + (x+c) );
                              westP = srcData + n * ( y * w + (x-c) );
                              if (((int) *northP) > 0) {north =1;}
                              if (((int) *southP) > 0) {south =1;}
                              if (((int) *eastP) > 0) {east =1;}
                              if (((int) *westP) > 0) {west =1;}
```

```
                    }
                    if ((north == 1) && (south == 1) && (east == 1) && (west == 1))
                    {
                        p2 = destData + y * w + x;
                        *p2 = (unsigned char) 250;
                    }
                    else
                    {
                        p2 = destData + y * w + x;
                        *p2 = (unsigned char) 0;
                    }
                }
                else
                {
                    p2 = destData + y * w + x;
                    *p2 = (unsigned char) 250;
                }
            }
            else
            {
                p2 = destData + y * w + x;
                *p2 = (unsigned char) 0;
            }
        }
    }
    // The function now returns the new image
    [destImage addRepresentation: destImageRep];
    return destImage;
}

@end
```

## Appendix C: SPSS Syntax for Calculated Measurements

```
* The following commands calculate the average and relative
enamel thickness of mesial and distal ideal planes of section.

COMPUTE mesb = mestota - mesc .
EXECUTE .

COMPUTE distb = disttota - distc .
EXECUTE .

COMPUTE mesaet = mesc / mese .
EXECUTE .

COMPUTE distaet = distc / diste .
EXECUTE .

COMPUTE mesret = (mesaet/(mesb**0.5))*100 .
EXECUTE .

COMPUTE distret = (distaet/(distb**0.5))*100 .
EXECUTE .


* The following commands calculate the average and relative
enamel thickness of three-dimensional measurements.

COMPUTE dvol = totvol - evol .
EXECUTE .

COMPUTE oessa = totsa - basarea .
EXECUTE .

COMPUTE edjsa = totesa - oessa .
EXECUTE .

COMPUTE aet3d = evol / edjsa .
EXECUTE .

COMPUTE ret3d = 100 * ( aet3d / ( dvol ** ( 1 / 3 ) ) ) .
EXECUTE .


* The following lines calculate the intercuspal distances (the
distances between enamel cup tips).

* Protoconid - Metaconid intercuspal distance.
COMPUTE prmt_ed = ( ((cartprex-cartmtex)**2) + ((cartprey-
cartmtey)**2) + ((cartprez-cartmtez)**2) )**0.5 .
EXECUTE .
* Protoconid - Hypoconid intercuspal distance.
COMPUTE prhp_ed = ( ((cartprex-carthpex)**2) + ((cartprey-
carthpey)**2) + ((cartprez-carthpez)**2) )**0.5 .
EXECUTE .
* Protoconid - Entoconid intercuspal distance.
COMPUTE pren_ed = ( ((cartprex-cartenex)**2) + ((cartprey-
carteney)**2) + ((cartprez-cartenez)**2) )**0.5 .
EXECUTE .
* Metaconid - Hypoconid intercuspal distance.
```

```
COMPUTE mthp_ed = ( ((cartmtex-carthpex)**2) + ((cartmtey-
carthpey)**2) + ((cartmtez-carthpez)**2) )**0.5 .
EXECUTE .
* Metaconid - Entoconid intercuspal distance.
COMPUTE mten_ed = ( ((cartmtex-cartenex)**2) + ((cartmtey-
carteney)**2) + ((cartmtez-cartenez)**2) )**0.5 .
EXECUTE .
* Hppoconid - Entoconid intercuspal distance.
COMPUTE hpen_ed = ( ((carthpex-cartenex)**2) + ((carthpey-
carteney)**2) + ((carthpez-cartenez)**2) )**0.5 .
EXECUTE .

* The following commands calculate the inter-dentine horn
distances (the distances between dentine horns).

* Protoconid - Metaconid intercuspal distance.
COMPUTE prmt_dd = ( ((cartprdx-cartmtdx)**2) + ((cartprdy-
cartmtdy)**2) + ((cartprdz-cartmtdz)**2) )**0.5 .
EXECUTE .
* Protoconid - Hppoconid inter-dentine horn distance.
COMPUTE prhp_dd = ( ((cartprdx-carthpdx)**2) + ((cartprdy-
carthpdy)**2) + ((cartprdz-carthpdz)**2) )**0.5 .
EXECUTE .
* Protoconid - Entoconid inter-dentine horn distance.
COMPUTE pren_dd = ( ((cartprdx-cartendx)**2) + ((cartprdy-
cartendy)**2) + ((cartprdz-cartendz)**2) )**0.5 .
EXECUTE .
* Metaconid - Hppoconid inter-dentine horn distance.
COMPUTE mthp_dd = ( ((cartmtdx-carthpdx)**2) + ((cartmtdy-
carthpdy)**2) + ((cartmtdz-carthpdz)**2) )**0.5 .
EXECUTE .
* Metaconid - Entoconid inter-dentine horn distance.
COMPUTE mten_dd = ( ((cartmtdx-cartendx)**2) + ((cartmtdy-
cartendy)**2) + ((cartmtdz-cartendz)**2) )**0.5 .
EXECUTE .
* Hppoconid - Entoconid inter-dentine horn distance.
COMPUTE hpen_dd = ( ((carthpdx-cartendx)**2) + ((carthpdy-
cartendy)**2) + ((carthpdz-cartendz)**2) )**0.5 .
EXECUTE .

* The following commands calculate the inter-pulp horn distances
(the distances between pulp horns).

COMPUTE prmt_pd = ( ((cartprpx-cartmtpx)**2) + ((cartprpy-
cartmtpy)**2) + ((cartprpz-cartmtpz)**2) )**0.5 .
EXECUTE .
* Protoconid - Hppoconid interpulp horn distance.
COMPUTE prhp_pd = ( ((cartprpx-carthppx)**2) + ((cartprpy-
carthppy)**2) + ((cartprpz-carthppz)**2) )**0.5 .
EXECUTE .
* Protoconid - Entoconid interpulp horn distance.
COMPUTE pren_pd = ( ((cartprpx-cartenpx)**2) + ((cartprpy-
cartenpy)**2) + ((cartprpz-cartenpz)**2) )**0.5 .
EXECUTE .
* Metaconid - Hppoconid interpulp horn distance.
COMPUTE mthp_pd = ( ((cartmtpx-carthppx)**2) + ((cartmtpy-
carthppy)**2) + ((cartmtpz-carthppz)**2) )**0.5 .
EXECUTE .
```

```
* Metaconid - Entoconid interpulp horn distance.
COMPUTE mten_pd = ( ((cartmtpx-cartenpx)**2) + ((cartmtpy-
cartenpy)**2) + ((cartmtpz-cartenpz)**2) )**0.5 .
EXECUTE .
* Hppoconid - Entoconid interpulp horn distance.
COMPUTE hpen_pd = ( ((carthppx-cartenpx)**2) + ((carthppy-
cartenpy)**2) + ((carthppz-cartenpz)**2) )**0.5 .
EXECUTE .


* The following commands calculate the enamel and dentine
thicknesses of each cusp based on the locations of Cartesian
coordinates.

COMPUTE prethick = ( ((cartprex-cartprdx)**2) + ((cartprey-
cartprdy)**2) + ((cartprez-cartprdz)**2) )**0.5 .
EXECUTE .

COMPUTE mtethick = ( ((cartmtex-cartmtdx)**2) + ((cartmtey-
cartmtdy)**2) + ((cartmtez-cartmtdz)**2) )**0.5 .
EXECUTE .

COMPUTE hpethick = ( ((carthpex-carthpdx)**2) + ((carthpey-
carthpdy)**2) + ((carthpez-carthpdz)**2) )**0.5 .
EXECUTE .

COMPUTE enethick = ( ((cartenex-cartendx)**2) + ((carteney-
cartendy)**2) + ((cartenez-cartendz)**2) )**0.5 .
EXECUTE .

COMPUTE prdthick = ( ((cartprpx-cartprdx)**2) + ((cartprpy-
cartprdy)**2) + ((cartprpz-cartprdz)**2) )**0.5 .
EXECUTE .

COMPUTE mtdthick = ( ((cartmtpx-cartmtdx)**2) + ((cartmtpy-
cartmtdy)**2) + ((cartmtpz-cartmtdz)**2) )**0.5 .
EXECUTE .

COMPUTE hpdthick = ( ((carthppx-carthpdx)**2) + ((carthppy-
carthpdy)**2) + ((carthppz-carthpdz)**2) )**0.5 .
EXECUTE .

COMPUTE endthick = ( ((cartenpx-cartendx)**2) + ((cartenpy-
cartendy)**2) + ((cartenpz-cartendz)**2) )**0.5 .
EXECUTE .


* The following commands calculate the intercuspal angles.

* Angle = arcsine[(adjacent_side1^2 + adjacent_side2^2 -
opposite_side^2) / (2*adjacent_side1*adjacent_side2)] +
[arsine(1)].

* This result is in radians; multiply by [180/pi] to convert to
degrees.

* protoconid enamel angle calculation.
```

```
COMPUTE prang_e = ( ( arsin ( ( prmt_ed**2 + prhp_ed**2 -
mthp_ed**2 ) / ( 2*prmt_ed*prhp_ed ) ) + arsine( 1 ) ) * (
180/3.14159 ) ) .
EXECUTE .

* metaconid enamel angle calculation.
COMPUTE mtang_e = ( ( arsin ( ( prmt_ed**2 + mten_ed**2 - pren_ed
**2) / ( 2*prmt_ed*mten_ed ) ) + arsine( 1 ) ) * ( 180/3.14159 )
) .
EXECUTE .

* hypoconid enamel angle calculation.
COMPUTE hpang_e = ( ( arsin ( ( prhp_ed**2 + hpen_ed**2 - pren_ed
**2) / ( 2*prhp_ed*hpen_ed ) ) + arsine( 1 ) ) * ( 180/3.14159 )
) .
EXECUTE .

* entoconid enamel angle calculation.
COMPUTE enang_e = ( ( arsin ( ( mten_ed**2 + hpen_ed**2 - mthp_ed
**2) / ( 2*mten_ed*hpen_ed ) ) + arsine( 1 ) ) * ( 180/3.14159 )
) .
EXECUTE .

* protoconid enamel angle calculation.
COMPUTE prang_d = ( ( arsin ( ( prmt_dd**2 + prhp_dd**2 -
mthp_dd**2 ) / ( 2*prmt_dd*prhp_dd ) ) + arsine( 1 ) ) * (
180/3.14159 ) ) .
EXECUTE .

* metaconid enamel angle calculation.
COMPUTE mtang_d = ( ( arsin ( ( prmt_dd**2 + mten_dd**2 - pren_dd
**2) / ( 2*prmt_dd*mten_dd ) ) + arsine( 1 ) ) * ( 180/3.14159 )
) .
EXECUTE .

* hypoconid enamel angle calculation.
COMPUTE hpang_d = ( ( arsin ( ( prhp_dd**2 + hpen_dd**2 - pren_dd
**2) / ( 2*prhp_dd*hpen_dd ) ) + arsine( 1 ) ) * ( 180/3.14159 )
) .
EXECUTE .

* entoconid enamel angle calculation.
COMPUTE enang_d = ( ( arsin ( ( mten_dd**2 + hpen_dd**2 - mthp_dd
**2) / ( 2*mten_dd*hpen_dd ) ) + arsine( 1 ) ) * ( 180/3.14159 )
) .
EXECUTE .
```

# Appendix D: Two-Dimensional Mesial Plane Measurements

| AMNH Cat. # | Tooth | Sex | Genus | Species | TOTA | C | B | E | BICD | E1 | E2 | E3 | E4 | E5 | E6 | E7 | AET | RET |
|---|---|---|---|---|---|---|---|---|---|---|---|---|---|---|---|---|---|---|
| 33074 | 1 | F | *Alouatta* | *sp.* | 12.50 | 3.48 | 9.02 | 11.85 | 3.39 | .36 | .18 | .28 | .15 | .16 | .12 | .25 | .29 | 9.78 |
| 129415 | 1 | M | *Alouatta* | *seniculus* | 14.51 | 3.86 | 10.64 | 11.93 | 3.56 | .40 | .26 | .36 | .32 | .29 | .27 | .39 | .32 | 9.93 |
| 73553 | 1 | F | *Alouatta* | *seniculus* | 18.47 | 4.68 | 13.80 | 12.01 | 4.64 | .38 | .35 | .36 | .44 | .31 | .28 | .32 | .39 | 10.49 |
| 73548 | 1 | F | *Alouatta* | *seniculus* | 19.72 | 5.87 | 13.85 | 13.89 | 3.96 | .67 | .60 | .38 | .37 | .24 | .30 | .49 | .42 | 11.35 |
| 239857 | 1 | F | *Alouatta* | *seniculus* | 13.17 | 4.20 | 8.97 | 10.89 | 3.24 | .46 | .27 | .39 | .48 | .40 | .53 | .47 | .39 | 12.89 |
| 32145 | 1 | M | *Alouatta* | *seniculus* | 17.50 | 4.25 | 13.25 | 12.99 | 3.70 | .51 | .26 | .40 | .29 | .38 | .20 | .40 | .33 | 9.00 |
| 23347 | 1 | U | *Alouatta* | *seniculus* | 12.88 | 3.00 | 9.88 | 10.58 | 3.37 | .51 | .23 | .31 | .30 | .30 | .17 | .31 | .28 | 9.02 |
| 33074 | 2 | F | *Alouatta* | *sp.* | 13.62 | 4.62 | 9.00 | 11.73 | 2.57 | .61 | .35 | .50 | .34 | .26 | .21 | .35 | .39 | 13.13 |
| 94139 | 2 | F | *Alouatta* | *seniculus* | 14.81 | 4.81 | 10.00 | 12.11 | 3.08 | .48 | .30 | .42 | .40 | .33 | .38 | .53 | .40 | 12.57 |
| 73553 | 2 | F | *Alouatta* | *seniculus* | 19.03 | 5.23 | 13.80 | 12.96 | 4.25 | .55 | .40 | .39 | .33 | .32 | .25 | .38 | .40 | 10.87 |
| 73548 | 2 | F | *Alouatta* | *seniculus* | 24.00 | 6.69 | 17.30 | 15.92 | 4.30 | .63 | .28 | .36 | .39 | .36 | .40 | .45 | .42 | 10.10 |
| 239857 | 2 | F | *Alouatta* | *seniculus* | 15.03 | 5.37 | 9.66 | 13.48 | 2.72 | .64 | .36 | .48 | .42 | .42 | .32 | .52 | .40 | 12.82 |
| 33063 | 2 | F | *Alouatta* | *seniculus* | 16.79 | 5.21 | 11.58 | 13.21 | 4.36 | .54 | .39 | .50 | .46 | .41 | .29 | .54 | .39 | 11.58 |
| 32145 | 2 | M | *Alouatta* | *seniculus* | 19.93 | 5.70 | 14.22 | 14.03 | 4.27 | .53 | .30 | .46 | .37 | .40 | .34 | .47 | .41 | 10.78 |
| 23347 | 2 | U | *Alouatta* | *seniculus* | 21.92 | 6.85 | 15.06 | 14.38 | 3.64 | .55 | .34 | .58 | .51 | .40 | .33 | .55 | .48 | 12.28 |
| 33074 | 3 | F | *Alouatta* | *sp.* | 14.08 | 3.84 | 10.24 | 12.35 | 3.48 | .54 | .32 | .30 | .31 | .24 | .35 | .38 | .31 | 9.71 |
| 94139 | 3 | F | *Alouatta* | *seniculus* | 16.12 | 4.67 | 11.46 | 12.35 | 3.57 | .47 | .54 | .37 | .45 | .27 | .40 | .35 | .38 | 11.17 |
| 73553 | 3 | F | *Alouatta* | *seniculus* | 18.87 | 4.83 | 14.04 | 13.90 | 4.09 | .49 | .21 | .48 | .32 | .27 | .25 | .44 | .35 | 9.28 |
| 239857 | 3 | F | *Alouatta* | *seniculus* | 17.77 | 5.66 | 12.12 | 13.68 | 3.82 | .49 | .38 | .45 | .32 | .42 | .41 | .50 | .41 | 11.88 |
| 33063 | 3 | F | *Alouatta* | *seniculus* | 12.30 | 4.69 | 7.61 | 12.17 | 3.03 | .54 | .29 | .40 | .31 | .43 | .35 | .52 | .39 | 13.98 |
| 123282 | 1 | U | *Ateles* | *geoffroyi* | 9.77 | 2.79 | 6.98 | 10.06 | 2.89 | .46 | .32 | .28 | .18 | .27 | .24 | .26 | .28 | 10.52 |
| 176649 | 1 | U | *Ateles* | *geoffroyi* | 13.49 | 3.17 | 10.32 | 10.31 | 3.77 | .47 | .19 | .38 | .34 | .38 | .18 | .39 | .31 | 9.58 |
| 172171 | 1 | F | *Ateles* | *geoffroyi* | 14.05 | 3.98 | 10.07 | 11.35 | 3.22 | .53 | .36 | .31 | .39 | .34 | .27 | .38 | .35 | 11.05 |
| 14484 | 1 | F | *Ateles* | *geoffroyi* | 11.54 | 3.15 | 8.39 | 10.36 | 2.98 | .51 | .38 | .30 | .23 | .20 | .23 | .35 | .30 | 10.49 |
| 172170 | 1 | U | *Ateles* | *geoffroyi* | 13.47 | 3.21 | 10.26 | 10.73 | 3.83 | .50 | .27 | .23 | .40 | .19 | .16 | .40 | .30 | 9.34 |
| 123283 | 1 | M | *Ateles* | *geoffroyi* | 9.94 | 3.02 | 6.92 | 9.64 | 2.61 | .39 | .34 | .27 | .28 | .30 | .27 | .45 | .31 | 11.90 |
| 29844 | 1 | M | *Ateles* | *geoffroyi* | 11.48 | 2.98 | 8.50 | 10.60 | 3.16 | .43 | .34 | .39 | .43 | .37 | .22 | .34 | .28 | 9.66 |
| 11074 | 1 | F | *Ateles* | *sp.* | 12.80 | 5.00 | 7.80 | 11.44 | 2.55 | .61 | .33 | .36 | .37 | .33 | .34 | .44 | .44 | 15.65 |
| 123282 | 2 | U | *Ateles* | *geoffroyi* | 9.84 | 3.80 | 6.05 | 11.12 | 2.01 | .70 | .30 | .25 | .26 | .20 | .26 | .37 | .34 | 13.88 |
| 176649 | 2 | U | *Ateles* | *geoffroyi* | 12.72 | 3.29 | 9.44 | 10.00 | 3.56 | .58 | .43 | .39 | .48 | .31 | .27 | .42 | .33 | 10.69 |
| 172171 | 2 | F | *Ateles* | *geoffroyi* | 14.27 | 4.52 | 9.75 | 11.94 | 3.53 | .58 | .43 | .33 | .38 | .33 | .33 | .57 | .38 | 12.13 |
| 14484 | 2 | F | *Ateles* | *geoffroyi* | 11.12 | 3.51 | 7.61 | 9.54 | 3.43 | .52 | .23 | .34 | .32 | .32 | .27 | .34 | .37 | 13.32 |
| 172170 | 2 | U | *Ateles* | *geoffroyi* | 14.52 | 3.52 | 11.01 | 10.38 | 3.74 | .51 | .34 | .33 | .52 | .38 | .35 | .46 | .34 | 10.22 |
| 17220 | 2 | M | *Ateles* | *geoffroyi* | 11.87 | 3.16 | 8.71 | 11.30 | 2.63 | .40 | .38 | .34 | .25 | .40 | .28 | .29 | .28 | 9.47 |
| 17222 | 2 | F | *Ateles* | *geoffroyi* | 13.86 | 4.64 | 9.22 | 11.28 | 2.94 | .52 | .33 | .27 | .52 | .36 | .36 | .49 | .41 | 13.54 |
| 123283 | 2 | M | *Ateles* | *geoffroyi* | 10.62 | 3.47 | 7.16 | 9.77 | 2.57 | .43 | .33 | .31 | .42 | .29 | .28 | .48 | .35 | 13.27 |
| 29844 | 2 | M | *Ateles* | *geoffroyi* | 10.80 | 3.63 | 7.17 | 10.52 | 2.55 | .59 | .34 | .40 | .45 | .41 | .32 | .39 | .35 | 12.89 |
| 11074 | 2 | F | *Ateles* | *sp.* | 13.68 | 4.06 | 9.61 | 10.62 | 3.22 | .60 | .37 | .42 | .46 | .39 | .36 | .41 | .38 | 12.33 |
| 123282 | 3 | U | *Ateles* | *geoffroyi* | 9.14 | 3.25 | 5.89 | 9.77 | 2.00 | .46 | .30 | .29 | .27 | .23 | .24 | .31 | .33 | 13.69 |
| 176649 | 3 | U | *Ateles* | *geoffroyi* | 12.02 | 3.21 | 8.81 | 9.77 | 3.12 | .51 | .38 | .30 | .34 | .32 | .32 | .42 | .33 | 11.05 |
| 172171 | 3 | F | *Ateles* | *geoffroyi* | 11.29 | 3.92 | 7.37 | 10.45 | 1.96 | .61 | .31 | .35 | .36 | .26 | .42 | .49 | .37 | 13.80 |
| 14484 | 3 | F | *Ateles* | *geoffroyi* | 9.88 | 2.83 | 7.05 | 9.64 | 3.48 | .49 | .41 | .28 | .80 | .20 | .29 | .31 | .29 | 11.05 |
| 172170 | 3 | U | *Ateles* | *geoffroyi* | 10.72 | 3.85 | 6.88 | 10.16 | 2.38 | .61 | .38 | .38 | .27 | .26 | .30 | .40 | .38 | 14.43 |
| 17220 | 3 | M | *Ateles* | *geoffroyi* | 9.03 | 3.27 | 5.76 | 10.24 | 1.25 | .42 | .39 | .19 | .21 | .37 | .27 | .37 | .32 | 13.31 |
| 17222 | 3 | F | *Ateles* | *geoffroyi* | 12.12 | 4.71 | 7.41 | 10.90 | 2.52 | .59 | .45 | .49 | .68 | .38 | .40 | .43 | .43 | 15.86 |
| 106781 | 1 | F | *Hylobates* | *muelleri* | 14.18 | 3.45 | 10.73 | 10.15 | 3.62 | .57 | .46 | .31 | .35 | .43 | .21 | .43 | .34 | 10.37 |
| 103725 | 1 | F | *Hylobates* | *muelleri* | 12.16 | 4.42 | 7.74 | 9.98 | 2.72 | .51 | .36 | .43 | .64 | .42 | .46 | .56 | .44 | 15.92 |
| 103726 | 1 | M | *Hylobates* | *muelleri* | 12.73 | 4.09 | 8.64 | 9.92 | 2.47 | .65 | .33 | .36 | .48 | .30 | .15 | .49 | .41 | 14.04 |
| 106328 | 1 | F | *Hylobates* | *muelleri* | 10.99 | 3.06 | 7.93 | 8.47 | 3.24 | .48 | .28 | .28 | .24 | .29 | .20 | .35 | .36 | 12.84 |
| 106781 | 2 | F | *Hylobates* | *muelleri* | 16.18 | 5.29 | 10.89 | 11.53 | 3.78 | .73 | .41 | .52 | .56 | .54 | .48 | .52 | .46 | 13.91 |
| 103725 | 2 | F | *Hylobates* | *muelleri* | 15.08 | 5.56 | 9.53 | 11.39 | 3.15 | .56 | .54 | .57 | .69 | .50 | .27 | .52 | .49 | 15.80 |
| 103726 | 2 | M | *Hylobates* | *muelleri* | 14.51 | 5.14 | 9.37 | 10.74 | 2.89 | .61 | .44 | .36 | .38 | .40 | .51 | .55 | .48 | 15.64 |
| 106328 | 2 | F | *Hylobates* | *muelleri* | 12.34 | 4.09 | 8.25 | 10.14 | 3.58 | .53 | .30 | .37 | .44 | .38 | .26 | .51 | .40 | 14.04 |
| 106781 | 3 | F | *Hylobates* | *muelleri* | 13.00 | 5.40 | 7.61 | 10.55 | 3.16 | .43 | .38 | .58 | .58 | .36 | .46 | .55 | .51 | 18.54 |
| 103725 | 3 | F | *Hylobates* | *muelleri* | 10.49 | 4.57 | 5.92 | 8.61 | 2.57 | .68 | .57 | .47 | .46 | .48 | .55 | .53 | .53 | 21.83 |
| 106328 | 3 | F | *Hylobates* | *muelleri* | 10.37 | 3.83 | 6.55 | 9.96 | 3.06 | .44 | .28 | .43 | .43 | .36 | .30 | .45 | .38 | 15.03 |
| 102722 | 1 | F | *Symphalangus* | *syndactylus* | 24.10 | 6.39 | 17.71 | 12.93 | 4.81 | .55 | .44 | .53 | .58 | .53 | .36 | .59 | .49 | 11.73 |
| 102191 | 1 | F | *Symphalangus* | *syndactylus* | 19.30 | 4.60 | 14.69 | 11.01 | 4.97 | .61 | .32 | .40 | .53 | .42 | .30 | .47 | .42 | 10.90 |
| 102193 | 1 | M | *Symphalangus* | *syndactylus* | 23.34 | 6.84 | 16.50 | 13.31 | 4.41 | .65 | .44 | .59 | .49 | .51 | .32 | .45 | .51 | 12.65 |
| 100048 | 1 | M | *Symphalangus* | *syndactylus* | 36.63 | 8.13 | 28.50 | 16.90 | 5.14 | .57 | .46 | .53 | .51 | .54 | .42 | .52 | .48 | 9.02 |
| 201316 | 1 | U | *Symphalangus* | *syndactylus* | 21.64 | 4.87 | 16.77 | 12.35 | 5.06 | .55 | .46 | .33 | .66 | .43 | .39 | .45 | .39 | 9.62 |
| 102724 | 2 | M | *Symphalangus* | *syndactylus* | 33.51 | 9.59 | 23.93 | 16.05 | 5.27 | .69 | .45 | .76 | .72 | .74 | .58 | .64 | .60 | 12.21 |
| 102729 | 2 | M | *Symphalangus* | *syndactylus* | 29.81 | 8.25 | 21.57 | 15.04 | 5.01 | .63 | .48 | .87 | .57 | .60 | .44 | .57 | .55 | 11.81 |
| 102189 | 2 | M | *Symphalangus* | *syndactylus* | 21.89 | 6.02 | 15.86 | 12.64 | 3.86 | .67 | .38 | .53 | .51 | .37 | .48 | .49 | .48 | 11.96 |
| 102722 | 2 | F | *Symphalangus* | *syndactylus* | 27.08 | 8.77 | 18.31 | 13.15 | 4.72 | .75 | .80 | .80 | .74 | .75 | .64 | .71 | .67 | 15.59 |
| 106582 | 2 | F | *Symphalangus* | *syndactylus* | 20.38 | 6.15 | 14.23 | 12.71 | 5.53 | .69 | .56 | .93 | .76 | .81 | .68 | .58 | .48 | 12.83 |
| 102191 | 2 | F | *Symphalangus* | *syndactylus* | 26.90 | 8.03 | 18.86 | 12.94 | 4.92 | .68 | .54 | .78 | .78 | .77 | .52 | .61 | .62 | 14.30 |
| 102193 | 2 | M | *Symphalangus* | *syndactylus* | 27.46 | 9.24 | 18.22 | 14.54 | 5.05 | .73 | .71 | .71 | .77 | .87 | .54 | .85 | .64 | 14.89 |
| 201316 | 2 | U | *Symphalangus* | *syndactylus* | 26.87 | 8.30 | 18.57 | 13.57 | 5.41 | .73 | .63 | .57 | .61 | .78 | .58 | .61 | .61 | 14.19 |
| 102197 | 2 | F | *Symphalangus* | *syndactylus* | 25.57 | 7.74 | 17.83 | 12.96 | 5.38 | .60 | .63 | .59 | .64 | .75 | .51 | .66 | .60 | 14.15 |
| 102189 | 3 | M | *Symphalangus* | *syndactylus* | 21.67 | 5.34 | 16.34 | 12.64 | 3.83 | .65 | .36 | .40 | .53 | .43 | .38 | .49 | .42 | 10.45 |
| 102193 | 3 | M | *Symphalangus* | *syndactylus* | 29.02 | 8.03 | 21.00 | 14.55 | 6.14 | .67 | .65 | .59 | .54 | .67 | .67 | .59 | .55 | 12.04 |
| 102197 | 3 | F | *Symphalangus* | *syndactylus* | 23.50 | 7.85 | 15.66 | 12.74 | 4.64 | .65 | .57 | .54 | .61 | .77 | .53 | .65 | .62 | 15.58 |

# Appendix E: Two-Dimensional Distal Plane Measurements

| AMNH Cat. # | Tooth | Sex | Genus | Species | TOTA | C | B | E | BICD | E1 | E2 | E3 | E4 | E5 | E6 | E7 | AET | RET |
|---|---|---|---|---|---|---|---|---|---|---|---|---|---|---|---|---|---|---|
| 33074 | 1 | F | *Alouatta* | *sp.* | 11.70 | 2.97 | 8.73 | 10.82 | 2.89 | .45 | .23 | .37 | .26 | .31 | .26 | .38 | .27 | 9.27 |
| 129415 | 1 | M | *Alouatta* | *seniculus* | 15.76 | 4.04 | 11.72 | 13.34 | 4.26 | .44 | .37 | .31 | .31 | .36 | .36 | .28 | .30 | 8.85 |
| 73553 | 1 | F | *Alouatta* | *seniculus* | 16.22 | 4.93 | 11.29 | 11.95 | 4.80 | .44 | .33 | .36 | .35 | .28 | .35 | .38 | .41 | 12.28 |
| 73548 | 1 | F | *Alouatta* | *seniculus* | 21.94 | 4.76 | 17.18 | 15.37 | 5.31 | .58 | .21 | .43 | .71 | .31 | .30 | .34 | .31 | 7.47 |
| 239857 | 1 | F | *Alouatta* | *seniculus* | 15.34 | 4.03 | 11.31 | 13.06 | 4.79 | .48 | .30 | .32 | .23 | .38 | .24 | .35 | .31 | 9.17 |
| 32145 | 1 | M | *Alouatta* | *seniculus* | 20.73 | 4.98 | 15.75 | 14.64 | 4.73 | .48 | .25 | .45 | .42 | .40 | .30 | .35 | .34 | 8.58 |
| 23347 | 1 | U | *Alouatta* | *seniculus* | 13.71 | 3.16 | 10.54 | 11.99 | 3.95 | .43 | .24 | .30 | .33 | .30 | .24 | .25 | .26 | 8.13 |
| 33074 | 2 | F | *Alouatta* | *sp.* | 14.85 | 4.26 | 10.59 | 12.57 | 3.36 | .51 | .35 | .40 | .31 | .30 | .38 | .37 | .34 | 10.42 |
| 94139 | 2 | F | *Alouatta* | *seniculus* | 15.27 | 4.87 | 10.40 | 12.74 | 4.17 | .42 | .32 | .38 | .30 | .28 | .43 | .36 | .38 | 11.87 |
| 73553 | 2 | F | *Alouatta* | *seniculus* | 11.64 | 3.61 | 8.03 | 11.39 | 3.51 | .41 | .21 | .34 | .27 | .32 | .36 | .33 | .32 | 11.18 |
| 73548 | 2 | F | *Alouatta* | *seniculus* | 22.51 | 6.58 | 15.92 | 15.66 | 5.03 | .52 | .39 | .45 | .42 | .41 | .32 | .39 | .42 | 10.53 |
| 239857 | 2 | F | *Alouatta* | *seniculus* | 16.58 | 5.46 | 11.12 | 13.28 | 3.63 | .46 | .38 | .40 | .40 | .38 | .39 | .51 | .41 | 12.33 |
| 33063 | 2 | F | *Alouatta* | *seniculus* | 18.48 | 5.06 | 13.42 | 14.36 | 4.91 | .48 | .25 | .46 | .32 | .43 | .31 | .31 | .35 | 9.62 |
| 32145 | 2 | M | *Alouatta* | *seniculus* | 21.90 | 5.31 | 16.59 | 15.50 | 4.40 | .53 | .36 | .38 | .36 | .35 | .38 | .42 | .34 | 8.41 |
| 23347 | 2 | U | *Alouatta* | *seniculus* | 17.06 | 4.52 | 12.54 | 13.31 | 3.91 | .50 | .29 | .42 | .30 | .36 | .40 | .35 | .34 | 9.59 |
| 33074 | 3 | F | *Alouatta* | *sp.* | 11.12 | 3.42 | 7.70 | 10.87 | 2.93 | .52 | .24 | .28 | .31 | .23 | .22 | .32 | .32 | 11.36 |
| 94139 | 3 | F | *Alouatta* | *seniculus* | 15.51 | 4.68 | 10.83 | 12.74 | 3.59 | .54 | .40 | .45 | .53 | .42 | .27 | .45 | .37 | 11.17 |
| 73553 | 3 | F | *Alouatta* | *seniculus* | 16.52 | 5.03 | 11.49 | 13.34 | 4.27 | .41 | .39 | .47 | .46 | .37 | .48 | .42 | .38 | 11.12 |
| 239857 | 3 | F | *Alouatta* | *seniculus* | 13.90 | 4.76 | 9.14 | 13.78 | 3.64 | .42 | .46 | .26 | .32 | .40 | .36 | .39 | .35 | 11.43 |
| 33063 | 3 | F | *Alouatta* | *seniculus* | 12.88 | 4.21 | 8.67 | 11.40 | 3.75 | .40 | .48 | .56 | .35 | .42 | .30 | .36 | .37 | 12.55 |
| 123282 | 1 | U | *Ateles* | *geoffroyi* | 5.90 | 1.61 | 4.29 | 7.47 | 2.37 | .33 | .27 | .19 | .21 | .22 | .30 | .33 | .22 | 10.41 |
| 176649 | 1 | U | *Ateles* | *geoffroyi* | 11.43 | 3.07 | 8.36 | 10.24 | 3.43 | .45 | .38 | .31 | .29 | .21 | .26 | .41 | .30 | 10.36 |
| 172171 | 1 | F | *Ateles* | *geoffroyi* | 12.82 | 3.41 | 9.42 | 11.09 | 3.52 | .51 | .38 | .21 | .16 | .27 | .34 | .36 | .31 | 10.01 |
| 14484 | 1 | F | *Ateles* | *geoffroyi* | 11.14 | 3.45 | 7.69 | 9.90 | 3.13 | .49 | .45 | .21 | .25 | .24 | .35 | .40 | .35 | 12.56 |
| 172170 | 1 | U | *Ateles* | *geoffroyi* | 11.80 | 3.02 | 8.78 | 10.44 | 3.55 | .45 | .39 | .27 | .16 | .25 | .30 | .28 | .29 | 9.75 |
| 123283 | 1 | M | *Ateles* | *geoffroyi* | 9.57 | 3.01 | 6.56 | 9.14 | 2.97 | .44 | .25 | .28 | .26 | .28 | .21 | .34 | .33 | 12.86 |
| 29844 | 1 | M | *Ateles* | *geoffroyi* | 9.70 | 2.53 | 7.18 | 9.76 | 3.04 | .43 | .28 | .26 | .15 | .25 | .28 | .30 | .26 | 9.67 |
| 11074 | 1 | F | *Ateles* | *sp.* | 10.72 | 3.44 | 7.29 | 9.82 | 3.63 | .46 | .46 | .37 | .34 | .36 | .32 | .33 | .35 | 12.97 |
| 123282 | 2 | U | *Ateles* | *geoffroyi* | 10.30 | 2.84 | 7.46 | 9.94 | 3.06 | .38 | .33 | .28 | .25 | .22 | .24 | .36 | .29 | 10.47 |
| 176649 | 2 | U | *Ateles* | *geoffroyi* | 12.92 | 3.41 | 9.51 | 9.72 | 3.65 | .53 | .42 | .33 | .29 | .28 | .50 | .34 | .35 | 11.37 |
| 172171 | 2 | F | *Ateles* | *geoffroyi* | 12.39 | 3.44 | 8.95 | 11.21 | 3.54 | .55 | .33 | .28 | .25 | .21 | .32 | .34 | .31 | 10.25 |
| 14484 | 2 | F | *Ateles* | *geoffroyi* | 9.62 | 2.44 | 7.18 | 9.52 | 3.08 | .47 | .34 | .23 | .15 | .13 | .31 | .33 | .26 | 9.58 |
| 172170 | 2 | U | *Ateles* | *geoffroyi* | 12.53 | 3.21 | 9.32 | 10.06 | 3.54 | .43 | .32 | .38 | .47 | .33 | .31 | .38 | .32 | 10.45 |
| 17220 | 2 | M | *Ateles* | *geoffroyi* | 16.67 | 3.70 | 12.98 | 12.84 | 3.87 | .45 | .36 | .35 | .22 | .20 | .34 | .37 | .29 | 7.99 |
| 17222 | 2 | F | *Ateles* | *geoffroyi* | 13.71 | 4.52 | 9.19 | 10.99 | 3.37 | .60 | .43 | .41 | .32 | .24 | .46 | .39 | .41 | 13.57 |
| 123283 | 2 | M | *Ateles* | *geoffroyi* | 10.89 | 3.05 | 7.83 | 9.54 | 3.00 | .46 | .30 | .29 | .27 | .30 | .27 | .30 | .32 | 11.44 |
| 29844 | 2 | M | *Ateles* | *geoffroyi* | 9.82 | 2.85 | 6.97 | 9.97 | 3.04 | .41 | .29 | .29 | .32 | .29 | .40 | .39 | .29 | 10.82 |
| 11074 | 2 | F | *Ateles* | *sp.* | 12.72 | 3.77 | 8.96 | 11.25 | 3.30 | .53 | .31 | .26 | .36 | .29 | .34 | .33 | .33 | 11.18 |
| 123282 | 3 | U | *Ateles* | *geoffroyi* | 9.22 | 2.61 | 6.61 | 8.41 | 2.15 | .41 | .33 | .25 | .38 | .26 | .25 | .33 | .31 | 12.05 |
| 176649 | 3 | U | *Ateles* | *geoffroyi* | 10.82 | 3.39 | 7.43 | 9.07 | 3.16 | .49 | .30 | .37 | .33 | .35 | .38 | .43 | .37 | 13.73 |
| 172171 | 3 | F | *Ateles* | *geoffroyi* | 11.79 | 3.66 | 8.13 | 10.33 | 2.94 | .52 | .44 | .30 | .27 | .32 | .49 | .36 | .35 | 12.42 |
| 14484 | 3 | F | *Ateles* | *geoffroyi* | 8.32 | 2.51 | 5.81 | 8.23 | 2.93 | .49 | .38 | .23 | .19 | .21 | .30 | .30 | .31 | 12.67 |
| 172170 | 3 | U | *Ateles* | *geoffroyi* | 10.93 | 3.23 | 7.70 | 9.27 | 3.12 | .48 | .33 | .42 | .25 | .33 | .36 | .38 | .35 | 12.56 |
| 17220 | 3 | M | *Ateles* | *geoffroyi* | 9.75 | 2.71 | 7.04 | 9.44 | 2.99 | .39 | .27 | .19 | .11 | .21 | .30 | .33 | .29 | 10.82 |
| 17222 | 3 | F | *Ateles* | *geoffroyi* | 12.35 | 3.78 | 8.57 | 10.22 | 3.06 | .56 | .29 | .36 | .29 | .31 | .34 | .34 | .37 | 12.64 |
| 106781 | 1 | F | *Hylobates* | *muelleri* | 12.32 | 3.81 | 8.52 | 10.37 | 3.74 | .55 | .52 | .33 | .34 | .40 | .33 | .57 | .37 | 12.57 |
| 103725 | 1 | F | *Hylobates* | *muelleri* | 11.85 | 4.32 | 7.53 | 10.37 | 3.49 | .46 | .42 | .47 | .29 | .43 | .51 | .43 | .42 | 15.17 |
| 103726 | 1 | M | *Hylobates* | *muelleri* | 12.97 | 4.47 | 8.50 | 10.73 | 3.53 | .51 | .35 | .39 | .34 | .40 | .39 | .49 | .42 | 14.29 |
| 106328 | 1 | F | *Hylobates* | *muelleri* | 9.97 | 3.09 | 6.88 | 8.85 | 3.39 | .55 | .34 | .31 | .26 | .28 | .26 | .42 | .35 | 13.31 |
| 106781 | 2 | F | *Hylobates* | *muelleri* | 16.09 | 5.95 | 10.15 | 10.53 | 3.90 | .58 | .52 | .51 | .46 | .50 | .53 | .55 | .56 | 17.72 |
| 103725 | 2 | F | *Hylobates* | *muelleri* | 14.92 | 5.17 | 9.75 | 11.41 | 3.55 | .69 | .53 | .45 | .34 | .50 | .55 | .55 | .45 | 14.50 |
| 103726 | 2 | M | *Hylobates* | *muelleri* | 13.67 | 5.15 | 8.52 | 10.90 | 3.69 | .67 | .47 | .51 | .40 | .43 | .40 | .51 | .47 | 16.19 |
| 106328 | 2 | F | *Hylobates* | *muelleri* | 10.69 | 3.36 | 7.34 | 9.35 | 3.41 | .51 | .33 | .37 | .30 | .33 | .41 | .38 | .36 | 13.25 |
| 106781 | 3 | F | *Hylobates* | *muelleri* | 12.19 | 4.85 | 7.34 | 9.36 | 3.54 | .58 | .50 | .26 | .46 | .55 | .55 | .52 | .52 | 19.11 |
| 103725 | 3 | F | *Hylobates* | *muelleri* | 12.76 | 5.12 | 7.64 | 9.66 | 3.22 | .64 | .64 | .52 | .42 | .53 | .66 | .53 | .53 | 19.18 |
| 106328 | 3 | F | *Hylobates* | *muelleri* | 9.77 | 3.14 | 6.63 | 8.81 | 3.44 | .49 | .24 | .47 | .35 | .48 | .31 | .37 | .36 | 13.82 |
| 102722 | 1 | F | *Symphalangus* | *syndactylus* | 25.06 | 6.98 | 18.08 | 13.36 | 4.86 | .68 | .60 | .51 | .41 | .57 | .42 | .68 | .52 | 12.28 |
| 102191 | 1 | F | *Symphalangus* | *syndactylus* | 23.65 | 6.46 | 17.19 | 13.39 | 5.27 | .57 | .33 | .43 | .53 | .45 | .36 | .61 | .48 | 11.63 |
| 102193 | 1 | M | *Symphalangus* | *syndactylus* | 22.56 | 6.55 | 16.01 | 13.20 | 5.06 | .66 | .28 | .45 | .35 | .45 | .47 | .58 | .50 | 12.39 |
| 100048 | 1 | M | *Symphalangus* | *syndactylus* | 36.11 | 8.24 | 27.87 | 16.88 | 6.12 | .72 | .47 | .52 | .38 | .62 | .46 | .57 | .49 | 9.24 |
| 201316 | 1 | U | *Symphalangus* | *syndactylus* | 21.82 | 5.28 | 16.54 | 12.89 | 5.26 | .73 | .34 | .43 | .39 | .37 | .38 | .58 | .41 | 10.07 |
| 102724 | 2 | M | *Symphalangus* | *syndactylus* | 34.81 | 9.70 | 25.12 | 16.51 | 5.47 | .61 | .62 | .59 | .56 | .55 | .55 | .76 | .59 | 11.72 |
| 102729 | 2 | M | *Symphalangus* | *syndactylus* | 32.40 | 8.82 | 23.58 | 15.57 | 5.63 | .74 | .45 | .57 | .42 | .56 | .64 | .62 | .57 | 11.67 |
| 102189 | 2 | M | *Symphalangus* | *syndactylus* | 22.74 | 6.16 | 16.58 | 13.57 | 5.06 | .49 | .48 | .39 | .36 | .35 | .42 | .45 | .45 | 11.15 |
| 102722 | 2 | F | *Symphalangus* | *syndactylus* | 30.08 | 9.13 | 20.94 | 14.38 | 5.43 | .70 | .66 | .74 | .49 | .68 | .64 | .61 | .64 | 13.88 |
| 106582 | 2 | F | *Symphalangus* | *syndactylus* | 26.51 | 7.65 | 18.87 | 14.26 | 5.03 | .67 | .54 | .74 | .46 | .58 | .48 | .66 | .54 | 12.35 |
| 102191 | 2 | F | *Symphalangus* | *syndactylus* | 27.17 | 8.46 | 18.71 | 13.82 | 5.23 | .73 | .62 | .54 | .64 | .67 | .45 | .67 | .61 | 14.14 |
| 102193 | 2 | M | *Symphalangus* | *syndactylus* | 30.80 | 9.40 | 21.40 | 14.54 | 5.27 | .81 | .70 | .63 | .58 | .77 | .70 | .68 | .65 | 13.97 |
| 201316 | 2 | U | *Symphalangus* | *syndactylus* | 27.94 | 8.88 | 19.06 | 14.73 | 4.96 | .74 | .58 | .64 | .53 | .65 | .61 | .66 | .60 | 13.81 |
| 102197 | 2 | F | *Symphalangus* | *syndactylus* | 24.01 | 7.30 | 16.71 | 13.37 | 5.26 | .71 | .76 | .46 | .24 | .38 | .55 | .58 | .55 | 13.36 |
| 102189 | 3 | M | *Symphalangus* | *syndactylus* | 23.00 | 6.13 | 16.87 | 13.56 | 5.04 | .55 | .35 | .42 | .36 | .37 | .44 | .58 | .45 | 11.02 |
| 102193 | 3 | M | *Symphalangus* | *syndactylus* | 25.15 | 7.81 | 17.34 | 13.41 | 5.00 | .81 | .72 | .59 | .53 | .56 | .62 | .60 | .58 | 13.99 |
| 102197 | 3 | F | *Symphalangus* | *syndactylus* | 34.49 | 9.89 | 24.60 | 15.75 | 5.89 | .85 | .81 | .69 | .54 | .49 | .59 | .82 | .63 | 12.65 |

# Appendix F: Three-Dimensional Measurements

| AMNH Cat. # | Tooth | Sex | Genus | Species | TOTVOL | EVOL | DVOL | TOTSA | TOTESA | EDJSA | OESSA | BASAREA | AET3D | RET3D |
|---|---|---|---|---|---|---|---|---|---|---|---|---|---|---|
| 33074 | 1 | F | *Alouatta* | *sp.* | 58.66 | 24.30 | 34.36 | 103.08 | 146.92 | 62.80 | 84.12 | 18.96 | .39 | 11.90 |
| 129415 | 1 | M | *Alouatta* | *seniculus* | 94.06 | 29.88 | 64.18 | 142.47 | 205.14 | 87.43 | 117.71 | 24.76 | .34 | 8.54 |
| 73553 | 1 | F | *Alouatta* | *seniculus* | 93.47 | 26.42 | 67.05 | 139.46 | 195.00 | 80.68 | 114.32 | 25.15 | .33 | 8.06 |
| 73548 | 1 | F | *Alouatta* | *seniculus* | 128.15 | 38.39 | 89.76 | 170.45 | 231.20 | 93.80 | 137.41 | 33.04 | .41 | 9.14 |
| 239857 | 1 | F | *Alouatta* | *seniculus* | 79.38 | 31.07 | 48.31 | 130.87 | 222.85 | 117.91 | 104.93 | 25.94 | .26 | 7.23 |
| 32145 | 1 | M | *Alouatta* | *seniculus* | 113.19 | 34.56 | 78.62 | 175.38 | 218.16 | 68.30 | 149.86 | 25.52 | .51 | 11.81 |
| 23347 | 1 | U | *Alouatta* | *seniculus* | 114.86 | 32.34 | 82.52 | 156.71 | 214.31 | 85.75 | 128.57 | 28.15 | .38 | 8.66 |
| 33074 | 2 | F | *Alouatta* | *sp.* | 84.68 | 23.65 | 61.04 | 129.96 | 167.80 | 59.53 | 108.28 | 21.68 | .40 | 10.09 |
| 94139 | 2 | F | *Alouatta* | *seniculus* | 93.15 | 27.66 | 65.48 | 133.92 | 178.70 | 67.99 | 110.72 | 23.20 | .41 | 10.09 |
| 73553 | 2 | F | *Alouatta* | *seniculus* | 119.97 | 39.14 | 80.83 | 169.13 | 251.56 | 109.91 | 141.65 | 27.48 | .36 | 8.24 |
| 73548 | 2 | F | *Alouatta* | *seniculus* | 146.04 | 54.75 | 91.29 | 208.49 | 290.24 | 116.20 | 174.04 | 34.45 | .47 | 10.46 |
| 239857 | 2 | F | *Alouatta* | *seniculus* | 90.90 | 33.15 | 57.75 | 150.95 | 219.73 | 95.90 | 123.83 | 27.12 | .35 | 8.94 |
| 33063 | 2 | F | *Alouatta* | *seniculus* | 104.88 | 34.06 | 70.82 | 156.29 | 239.03 | 113.14 | 125.89 | 30.40 | .30 | 7.28 |
| 32145 | 2 | M | *Alouatta* | *seniculus* | 132.28 | 45.02 | 87.26 | 184.80 | 264.22 | 108.63 | 155.59 | 29.21 | .41 | 9.34 |
| 23347 | 2 | U | *Alouatta* | *seniculus* | 156.56 | 51.61 | 104.95 | 209.11 | 286.12 | 108.31 | 177.80 | 31.30 | .48 | 10.10 |
| 33074 | 3 | F | *Alouatta* | *sp.* | 69.09 | 26.07 | 43.02 | 118.85 | 160.17 | 61.96 | 98.21 | 20.65 | .42 | 12.01 |
| 94139 | 3 | F | *Alouatta* | *seniculus* | 92.15 | 32.03 | 60.12 | 137.98 | 190.25 | 72.65 | 117.60 | 20.39 | .44 | 11.25 |
| 73553 | 3 | F | *Alouatta* | *seniculus* | 101.41 | 47.48 | 53.93 | 160.75 | 221.28 | 91.25 | 130.03 | 30.72 | .52 | 13.77 |
| 239857 | 3 | F | *Alouatta* | *seniculus* | 98.96 | 35.51 | 63.45 | 181.04 | 236.70 | 81.03 | 155.67 | 25.37 | .44 | 10.99 |
| 33063 | 3 | F | *Alouatta* | *seniculus* | 85.43 | 29.20 | 56.22 | 135.36 | 203.51 | 91.24 | 112.27 | 23.09 | .32 | 8.35 |
| 123282 | 1 | U | *Ateles* | *geoffroyi* | 51.50 | 16.01 | 35.49 | 89.36 | 120.56 | 47.22 | 73.34 | 16.02 | .34 | 10.31 |
| 176649 | 1 | U | *Ateles* | *geoffroyi* | 53.90 | 17.53 | 36.37 | 86.60 | 120.05 | 47.54 | 72.51 | 14.10 | .37 | 11.13 |
| 172171 | 1 | F | *Ateles* | *geoffroyi* | 65.30 | 20.25 | 45.05 | 98.73 | 151.49 | 66.40 | 85.09 | 13.64 | .31 | 8.57 |
| 14484 | 1 | F | *Ateles* | *geoffroyi* | 50.22 | 13.73 | 36.50 | 89.88 | 111.09 | 32.24 | 78.85 | 11.03 | .43 | 12.84 |
| 172170 | 1 | U | *Ateles* | *geoffroyi* | 54.73 | 18.23 | 36.50 | 84.57 | 121.03 | 51.88 | 69.15 | 15.42 | .35 | 10.59 |
| 123283 | 1 | M | *Ateles* | *geoffroyi* | 45.02 | 13.51 | 31.51 | 83.64 | 110.19 | 38.65 | 71.54 | 12.10 | .35 | 11.07 |
| 29844 | 1 | M | *Ateles* | *geoffroyi* | 44.61 | 15.50 | 29.11 | 91.55 | 119.25 | 40.56 | 78.69 | 12.86 | .38 | 12.43 |
| 11074 | 1 | F | *Ateles* | *sp.* | 54.78 | 20.73 | 34.06 | 88.36 | 125.57 | 50.42 | 75.16 | 13.20 | .41 | 12.68 |
| 123282 | 2 | U | *Ateles* | *geoffroyi* | 48.61 | 16.01 | 32.59 | 84.29 | 115.72 | 43.49 | 72.23 | 12.06 | .37 | 11.53 |
| 176649 | 2 | U | *Ateles* | *geoffroyi* | 53.50 | 16.92 | 36.58 | 89.74 | 118.41 | 41.19 | 77.22 | 12.52 | .41 | 12.38 |
| 172171 | 2 | F | *Ateles* | *geoffroyi* | 62.40 | 21.52 | 40.89 | 97.97 | 139.72 | 54.85 | 84.87 | 13.10 | .39 | 11.39 |
| 14484 | 2 | F | *Ateles* | *geoffroyi* | 38.98 | 11.61 | 27.37 | 80.44 | 100.77 | 31.61 | 69.15 | 11.29 | .37 | 12.18 |
| 172170 | 2 | U | *Ateles* | *geoffroyi* | 51.98 | 18.56 | 33.43 | 85.91 | 124.47 | 52.23 | 72.24 | 13.67 | .36 | 11.03 |
| 17220 | 2 | M | *Ateles* | *geoffroyi* | 52.75 | 16.13 | 36.62 | 110.69 | 134.16 | 36.42 | 97.74 | 12.95 | .44 | 13.34 |
| 17222 | 2 | F | *Ateles* | *geoffroyi* | 64.82 | 24.11 | 40.71 | 100.53 | 133.05 | 45.78 | 87.27 | 13.26 | .53 | 15.31 |
| 123283 | 2 | M | *Ateles* | *geoffroyi* | 50.75 | 17.79 | 32.97 | 102.39 | 127.00 | 36.51 | 90.49 | 11.91 | .49 | 15.19 |
| 29844 | 2 | M | *Ateles* | *geoffroyi* | 45.45 | 16.48 | 28.97 | 85.05 | 120.91 | 48.78 | 72.13 | 12.92 | .34 | 11.00 |
| 11074 | 2 | F | *Ateles* | *sp.* | 58.65 | 23.22 | 35.43 | 101.00 | 138.00 | 51.35 | 86.65 | 14.35 | .45 | 13.77 |
| 123282 | 3 | U | *Ateles* | *geoffroyi* | 36.16 | 12.89 | 23.27 | 67.15 | 94.30 | 36.08 | 58.22 | 8.92 | .36 | 12.51 |
| 176649 | 3 | U | *Ateles* | *geoffroyi* | 41.67 | 15.41 | 26.26 | 88.99 | 108.79 | 30.60 | 78.19 | 10.80 | .50 | 16.94 |
| 172171 | 3 | F | *Ateles* | *geoffroyi* | 53.58 | 20.12 | 33.45 | 84.87 | 125.46 | 51.16 | 74.30 | 10.57 | .39 | 12.21 |
| 14484 | 3 | F | *Ateles* | *geoffroyi* | 34.19 | 9.85 | 24.34 | 74.56 | 90.94 | 27.00 | 63.94 | 10.62 | .36 | 12.59 |
| 172170 | 3 | U | *Ateles* | *geoffroyi* | 42.34 | 17.04 | 25.29 | 72.52 | 103.19 | 41.31 | 61.88 | 10.64 | .41 | 14.05 |
| 17220 | 3 | M | *Ateles* | *geoffroyi* | 39.44 | 13.27 | 26.17 | 86.53 | 110.73 | 37.61 | 73.12 | 13.41 | .35 | 11.88 |
| 17222 | 3 | F | *Ateles* | *geoffroyi* | 50.99 | 21.69 | 29.30 | 89.04 | 126.27 | 47.78 | 78.49 | 10.55 | .45 | 14.73 |
| 106781 | 1 | F | *Hylobates* | *muelleri* | 69.05 | 28.41 | 40.64 | 111.74 | 147.85 | 53.10 | 94.76 | 16.98 | .54 | 15.56 |
| 103725 | 1 | F | *Hylobates* | *muelleri* | 54.86 | 22.55 | 32.31 | 89.77 | 127.40 | 51.67 | 75.73 | 14.04 | .44 | 13.70 |
| 103726 | 1 | M | *Hylobates* | *muelleri* | 68.75 | 28.11 | 40.64 | 109.50 | 153.45 | 58.81 | 94.64 | 14.86 | .48 | 13.90 |
| 106328 | 1 | F | *Hylobates* | *muelleri* | 47.57 | 16.34 | 31.23 | 85.79 | 117.96 | 45.92 | 72.04 | 13.75 | .36 | 11.30 |
| 106781 | 2 | F | *Hylobates* | *muelleri* | 87.25 | 35.45 | 51.80 | 119.24 | 159.99 | 58.92 | 101.07 | 18.17 | .60 | 16.14 |
| 103725 | 2 | F | *Hylobates* | *muelleri* | 76.93 | 32.14 | 44.79 | 112.27 | 155.41 | 59.34 | 96.07 | 16.20 | .54 | 15.25 |
| 103726 | 2 | M | *Hylobates* | *muelleri* | 80.54 | 35.95 | 44.60 | 118.42 | 171.52 | 69.94 | 101.58 | 16.84 | .51 | 14.49 |
| 106328 | 2 | F | *Hylobates* | *muelleri* | 52.03 | 20.44 | 31.59 | 86.73 | 128.78 | 57.24 | 71.54 | 15.19 | .36 | 11.29 |
| 106781 | 3 | F | *Hylobates* | *muelleri* | 59.69 | 26.72 | 32.97 | 95.85 | 127.09 | 45.11 | 81.98 | 13.87 | .59 | 18.47 |
| 103725 | 3 | F | *Hylobates* | *muelleri* | 54.59 | 25.69 | 28.89 | 94.07 | 126.29 | 44.82 | 81.47 | 12.60 | .57 | 18.68 |
| 106328 | 3 | F | *Hylobates* | *muelleri* | 44.42 | 18.25 | 26.17 | 78.20 | 111.44 | 46.92 | 64.51 | 13.69 | .39 | 13.10 |
| 102722 | 1 | F | *Symphalangus* | *syndactylus* | 162.08 | 56.00 | 106.08 | 181.21 | 308.26 | 159.00 | 149.27 | 31.94 | .35 | 7.44 |
| 102191 | 1 | F | *Symphalangus* | *syndactylus* | 132.75 | 39.90 | 92.85 | 170.58 | 226.44 | 88.36 | 138.08 | 32.50 | .45 | 9.97 |
| 102193 | 1 | M | *Symphalangus* | *syndactylus* | 160.04 | 53.16 | 106.88 | 198.63 | 253.43 | 84.85 | 168.57 | 30.06 | .63 | 13.20 |
| 100048 | 1 | M | *Symphalangus* | *syndactylus* | 275.06 | 88.21 | 186.85 | 263.06 | 378.38 | 159.43 | 218.95 | 44.11 | .55 | 9.68 |
| 201316 | 1 | U | *Symphalangus* | *syndactylus* | 143.12 | 44.07 | 99.04 | 170.40 | 231.51 | 93.06 | 138.46 | 31.95 | .47 | 10.24 |
| 102724 | 2 | M | *Symphalangus* | *syndactylus* | 219.01 | 74.50 | 144.51 | 213.65 | 328.15 | 152.05 | 176.11 | 37.55 | .49 | 9.34 |
| 102729 | 2 | M | *Symphalangus* | *syndactylus* | 220.48 | 71.58 | 148.90 | 210.82 | 313.23 | 137.16 | 176.07 | 34.75 | .52 | 9.85 |
| 102189 | 2 | M | *Symphalangus* | *syndactylus* | 144.98 | 39.82 | 105.16 | 172.17 | 235.43 | 92.54 | 142.89 | 29.28 | .43 | 9.12 |
| 102722 | 2 | F | *Symphalangus* | *syndactylus* | 187.08 | 76.57 | 110.51 | 202.42 | 344.47 | 179.68 | 164.78 | 37.64 | .43 | 8.88 |
| 106582 | 2 | F | *Symphalangus* | *syndactylus* | 192.42 | 71.88 | 120.54 | 204.73 | 294.34 | 124.45 | 169.89 | 34.84 | .58 | 11.69 |
| 102191 | 2 | F | *Symphalangus* | *syndactylus* | 193.88 | 66.62 | 127.27 | 224.81 | 289.43 | 99.93 | 189.50 | 35.31 | .67 | 13.25 |
| 102193 | 2 | M | *Symphalangus* | *syndactylus* | 211.27 | 78.07 | 133.20 | 218.39 | 290.03 | 108.35 | 181.68 | 36.72 | .72 | 14.11 |
| 201316 | 2 | U | *Symphalangus* | *syndactylus* | 191.52 | 68.14 | 123.38 | 214.55 | 297.86 | 119.92 | 177.94 | 36.61 | .57 | 11.41 |
| 102197 | 2 | F | *Symphalangus* | *syndactylus* | 165.28 | 49.69 | 115.59 | 208.21 | 259.61 | 87.92 | 171.69 | 36.52 | .57 | 11.60 |
| 102189 | 3 | M | *Symphalangus* | *syndactylus* | 153.70 | 61.81 | 91.90 | 178.80 | 253.26 | 106.35 | 146.91 | 31.89 | .58 | 12.88 |
| 102193 | 3 | M | *Symphalangus* | *syndactylus* | 198.37 | 73.04 | 125.33 | 216.17 | 283.34 | 103.91 | 179.43 | 36.74 | .70 | 14.05 |
| 102197 | 3 | F | *Symphalangus* | *syndactylus* | 141.09 | 45.91 | 95.19 | 177.67 | 222.08 | 78.62 | 143.46 | 34.21 | .58 | 12.79 |

## Appendix G: Angle Measurements (Degrees)

| AMNH Cat. # | Tooth | Sex | Genus | species | Protoconid Enamel Angle | Metaconid Enamel Angle | Hypoconid Enamel Angle | Entoconid Enamel Angle | Protoconid Dentine Angle | Metaconid Dentine Angle | Hypoconid Dentine Angle | Entoconid Dentine Angle |
|---|---|---|---|---|---|---|---|---|---|---|---|---|
| 33074 | 1 | F | *Alouatta* | *sp.* | 94.10 | 68.61 | 84.47 | 113.53 | 94.34 | 68.47 | 89.16 | 110.19 |
| 129415 | 1 | M | *Alouatta* | *seniculus* | 101.23 | 68.81 | 88.35 | 104.10 | 102.45 | 64.30 | 87.29 | 107.85 |
| 73553 | 1 | F | *Alouatta* | *seniculus* | 82.68 | 73.15 | 95.73 | 108.55 | 96.12 | 73.90 | 87.76 | 103.24 |
| 73548 | 1 | F | *Alouatta* | *seniculus* | 90.73 | 67.40 | 95.97 | 107.18 | 96.55 | 63.16 | 98.10 | 104.10 |
| 239857 | 1 | F | *Alouatta* | *seniculus* | 95.88 | 59.19 | 101.51 | 103.50 | 98.11 | 64.55 | 98.52 | 99.54 |
| 32145 | 1 | M | *Alouatta* | *seniculus* | 91.94 | 69.39 | 93.47 | 107.85 | 103.16 | 59.15 | 89.78 | 110.26 |
| 23347 | 1 | U | *Alouatta* | *seniculus* | 90.16 | 64.73 | 98.29 | 108.60 | 95.67 | 62.41 | 93.00 | 110.22 |
| 33074 | 2 | F | *Alouatta* | *sp.* | 96.62 | 68.45 | 83.17 | 113.45 | 95.01 | 76.71 | 86.28 | 104.09 |
| 94139 | 2 | F | *Alouatta* | *seniculus* | 87.60 | 83.77 | 83.61 | 106.76 | 87.03 | 80.98 | 90.66 | 104.79 |
| 73553 | 2 | F | *Alouatta* | *seniculus* | 85.37 | 85.24 | 88.31 | 105.01 | 93.64 | 80.12 | 86.84 | 104.91 |
| 73548 | 2 | F | *Alouatta* | *seniculus* | 95.46 | 75.26 | 90.86 | 99.96 | 92.64 | 77.95 | 92.96 | 97.22 |
| 239857 | 2 | F | *Alouatta* | *seniculus* | 89.71 | 80.55 | 95.85 | 95.46 | 94.24 | 75.22 | 94.16 | 97.81 |
| 33063 | 2 | F | *Alouatta* | *seniculus* | 92.48 | 79.44 | 87.05 | 105.52 | 96.28 | 74.87 | 82.55 | 111.10 |
| 32145 | 2 | M | *Alouatta* | *seniculus* | 97.47 | 72.29 | 91.68 | 100.78 | 89.01 | 76.37 | 92.78 | 103.93 |
| 23347 | 2 | U | *Alouatta* | *seniculus* | 92.42 | 69.58 | 93.40 | 107.11 | 95.91 | 60.78 | 96.44 | 108.38 |
| 33074 | 3 | F | *Alouatta* | *sp.* | 87.46 | 91.70 | 93.42 | 89.57 | 87.86 | 93.88 | 86.16 | 94.26 |
| 94139 | 3 | F | *Alouatta* | *seniculus* | 62.91 | 112.16 | 75.53 | 114.43 | 77.46 | 98.73 | 73.25 | 113.74 |
| 73553 | 3 | F | *Alouatta* | *seniculus* | 84.40 | 97.74 | 82.30 | 97.64 | 85.16 | 95.52 | 76.88 | 104.43 |
| 239857 | 3 | F | *Alouatta* | *seniculus* | 90.33 | 92.41 | 79.98 | 100.30 | 87.76 | 94.04 | 77.11 | 102.51 |
| 33063 | 3 | F | *Alouatta* | *seniculus* | 96.96 | 90.42 | 77.35 | 100.64 | 99.39 | 85.30 | 78.27 | 103.07 |
| 123282 | 1 | U | *Ateles* | *geoffroyi* | 85.36 | 97.87 | 93.18 | 87.73 | 93.74 | 91.17 | 93.29 | 88.16 |
| 176649 | 1 | U | *Ateles* | *geoffroyi* | 92.91 | 77.58 | 90.80 | 102.21 | 100.36 | 75.02 | 81.60 | 107.84 |
| 172171 | 1 | F | *Ateles* | *geoffroyi* | 85.66 | 90.30 | 86.29 | 99.50 | 85.61 | 83.01 | 86.03 | 107.59 |
| 14484 | 1 | F | *Ateles* | *geoffroyi* | 93.97 | 73.89 | 87.48 | 106.57 | 101.98 | 79.90 | 78.06 | 102.19 |
| 172170 | 1 | U | *Ateles* | *geoffroyi* | 97.85 | 77.33 | 69.46 | 116.50 | 93.17 | 76.81 | 78.76 | 112.99 |
| 123283 | 1 | M | *Ateles* | *geoffroyi* | 96.71 | 79.38 | 81.53 | 106.41 | 98.39 | 70.73 | 87.26 | 108.43 |
| 29844 | 1 | M | *Ateles* | *geoffroyi* | 97.64 | 70.43 | 94.41 | 103.87 | 98.91 | 72.45 | 91.97 | 102.57 |
| 11074 | 1 | F | *Ateles* | *sp.* | 103.78 | 81.76 | 75.38 | 106.08 | 94.50 | 79.69 | 90.48 | 103.72 |
| 123282 | 2 | U | *Ateles* | *geoffroyi* | 88.79 | 91.30 | 88.03 | 94.41 | 95.52 | 86.76 | 88.52 | 91.86 |
| 176649 | 2 | U | *Ateles* | *geoffroyi* | 91.46 | 89.15 | 85.06 | 102.28 | 92.67 | 82.24 | 83.05 | 112.42 |
| 172171 | 2 | F | *Ateles* | *geoffroyi* | 80.97 | 88.78 | 96.28 | 96.09 | 86.57 | 84.80 | 89.93 | 100.39 |
| 14484 | 2 | F | *Ateles* | *geoffroyi* | 97.81 | 84.90 | 74.44 | 106.81 | 102.92 | 84.30 | 67.71 | 108.75 |
| 172170 | 2 | U | *Ateles* | *geoffroyi* | 95.06 | 93.22 | 68.73 | 110.73 | 87.82 | 84.73 | 88.82 | 105.81 |
| 17220 | 2 | M | *Ateles* | *geoffroyi* | 81.23 | 89.80 | 92.16 | 98.84 | 81.89 | 84.58 | 99.68 | 95.56 |
| 17222 | 2 | F | *Ateles* | *geoffroyi* | 106.96 | 76.53 | 77.32 | 104.93 | 86.13 | 88.59 | 89.80 | 99.31 |
| 123283 | 2 | M | *Ateles* | *geoffroyi* | 100.63 | 81.35 | 85.01 | 100.19 | 98.88 | 77.51 | 86.00 | 103.23 |
| 29844 | 2 | M | *Ateles* | *geoffroyi* | 80.88 | 86.51 | 99.21 | 97.19 | 76.59 | 93.17 | 98.75 | 95.28 |
| 11074 | 2 | F | *Ateles* | *sp.* | 87.71 | 86.92 | 89.31 | 100.93 | 83.50 | 81.17 | 100.83 | 98.49 |
| 123282 | 3 | U | *Ateles* | *geoffroyi* | 97.47 | 96.95 | 83.24 | 85.27 | 99.20 | 90.21 | 82.90 | 91.03 |
| 176649 | 3 | U | *Ateles* | *geoffroyi* | 102.20 | 95.26 | 69.12 | 101.49 | 93.60 | 83.89 | 79.87 | 111.14 |
| 172171 | 3 | F | *Ateles* | *geoffroyi* | 95.86 | 93.02 | 90.88 | 85.93 | 84.66 | 87.62 | 88.52 | 102.24 |
| 14484 | 3 | F | *Ateles* | *geoffroyi* | 67.66 | 99.65 | 95.03 | 103.19 | 68.77 | 106.43 | 99.42 | 92.99 |
| 172170 | 3 | U | *Ateles* | *geoffroyi* | 89.04 | 92.77 | 77.73 | 106.36 | 81.70 | 86.91 | 88.31 | 109.01 |
| 17220 | 3 | M | *Ateles* | *geoffroyi* | 94.05 | 86.11 | 93.32 | 92.12 | 90.01 | 83.32 | 96.76 | 94.67 |
| 17222 | 3 | F | *Ateles* | *geoffroyi* | 86.95 | 86.10 | 86.38 | 105.49 | 84.48 | 83.93 | 92.90 | 104.72 |
| 106781 | 1 | F | *Hylobates* | *muelleri* | 79.44 | 85.45 | 96.79 | 99.99 | 87.78 | 87.96 | 81.90 | 105.21 |
| 103725 | 1 | F | *Hylobates* | *muelleri* | 73.72 | 85.15 | 89.63 | 112.81 | 87.22 | 82.75 | 83.00 | 108.56 |
| 103726 | 1 | M | *Hylobates* | *muelleri* | 81.51 | 87.04 | 85.53 | 107.25 | 83.05 | 80.88 | 86.21 | 112.26 |
| 106328 | 1 | F | *Hylobates* | *muelleri* | 85.63 | 87.89 | 90.66 | 98.23 | 89.09 | 85.55 | 86.68 | 101.24 |
| 106781 | 2 | F | *Hylobates* | *muelleri* | 91.01 | 86.04 | 89.48 | 95.47 | 88.82 | 86.99 | 84.40 | 100.36 |
| 103725 | 2 | F | *Hylobates* | *muelleri* | 93.01 | 82.78 | 77.93 | 107.24 | 92.12 | 88.26 | 78.57 | 104.10 |
| 103726 | 2 | M | *Hylobates* | *muelleri* | 84.82 | 86.65 | 85.54 | 105.20 | 86.59 | 81.47 | 90.55 | 104.03 |
| 106328 | 2 | F | *Hylobates* | *muelleri* | 86.32 | 94.02 | 80.32 | 102.04 | 96.23 | 87.11 | 77.17 | 102.79 |
| 106781 | 3 | F | *Hylobates* | *muelleri* | 99.01 | 86.07 | 78.48 | 96.46 | 99.17 | 88.58 | 77.50 | 94.98 |
| 103725 | 3 | F | *Hylobates* | *muelleri* | 97.96 | 70.72 | 80.04 | 111.28 | 94.48 | 69.85 | 83.21 | 112.49 |
| 106328 | 3 | F | *Hylobates* | *muelleri* | 96.26 | 97.98 | 77.93 | 90.66 | 99.12 | 90.62 | 78.00 | 94.40 |
| 102722 | 1 | F | *Symphalangus* | *syndactylus* | 85.74 | 89.34 | 76.87 | 109.59 | 89.72 | 78.93 | 85.09 | 107.75 |
| 102191 | 1 | F | *Symphalangus* | *syndactylus* | 80.60 | 83.73 | 88.47 | 108.85 | 86.52 | 82.28 | 82.83 | 109.55 |
| 102193 | 1 | M | *Symphalangus* | *syndactylus* | 86.03 | 90.54 | 76.99 | 107.36 | 90.31 | 85.28 | 77.86 | 107.63 |
| 100048 | 1 | M | *Symphalangus* | *syndactylus* | 89.57 | 85.13 | 76.02 | 110.55 | 90.58 | 79.64 | 78.95 | 111.86 |
| 201316 | 1 | U | *Symphalangus* | *syndactylus* | 89.44 | 85.14 | 84.87 | 103.65 | 85.69 | 81.09 | 89.42 | 105.68 |
| 102724 | 2 | M | *Symphalangus* | *syndactylus* | 89.45 | 79.22 | 82.86 | 109.90 | 93.89 | 77.16 | 80.57 | 109.56 |
| 102729 | 2 | M | *Symphalangus* | *syndactylus* | 91.90 | 81.46 | 80.16 | 112.08 | 90.83 | 79.36 | 79.21 | 114.56 |
| 102189 | 2 | M | *Symphalangus* | *syndactylus* | 85.71 | 77.95 | 89.62 | 109.24 | 82.96 | 80.52 | 90.69 | 106.59 |
| 102722 | 2 | F | *Symphalangus* | *syndactylus* | 92.02 | 89.27 | 66.67 | 115.95 | 92.49 | 77.91 | 78.01 | 112.74 |
| 106582 | 2 | F | *Symphalangus* | *syndactylus* | 79.73 | 88.88 | 83.06 | 109.27 | 89.68 | 89.02 | 75.68 | 106.54 |
| 102191 | 2 | F | *Symphalangus* | *syndactylus* | 81.28 | 83.75 | 78.57 | 117.28 | 79.49 | 85.68 | 85.83 | 110.82 |
| 102193 | 2 | M | *Symphalangus* | *syndactylus* | 90.03 | 88.55 | 79.43 | 103.08 | 93.42 | 87.17 | 75.65 | 104.44 |
| 201316 | 2 | U | *Symphalangus* | *syndactylus* | 94.65 | 74.75 | 81.00 | 112.71 | 91.86 | 75.26 | 84.42 | 112.05 |
| 102197 | 2 | F | *Symphalangus* | *syndactylus* | 83.10 | 79.80 | 90.60 | 111.38 | 92.02 | 71.21 | 84.28 | 115.50 |
| 102189 | 3 | M | *Symphalangus* | *syndactylus* | 90.58 | 81.99 | 80.32 | 109.03 | 92.47 | 79.89 | 80.26 | 108.59 |
| 102193 | 3 | M | *Symphalangus* | *syndactylus* | 93.38 | 89.37 | 78.24 | 100.57 | 96.32 | 87.98 | 73.04 | 104.36 |
| 102197 | 3 | F | *Symphalangus* | *syndactylus* | 93.24 | 82.97 | 74.95 | 115.91 | 95.18 | 82.53 | 76.93 | 112.03 |

## Appendix H: Enamel Intercuspal Distances (mm)

| AMNH Cat. # | Tooth | Sex | Genus | Species | Pr-Mt Enamel Cusp Dist | Pr-En Enamel Cusp Dist | Pr-Hy Enamel Cusp Dist | Mt-En Enamel Cusp Dist | Mt-Hy Enamel Cusp Dist | Hy-En Enamel Cusp Dist |
|---|---|---|---|---|---|---|---|---|---|---|
| 33074 | 1 | F | *Alouatta* | *sp.* | 2.42 | 5.24 | 3.47 | 3.85 | 4.09 | 3.60 |
| 129415 | 1 | M | *Alouatta* | *seniculus* | 3.41 | 5.83 | 4.05 | 3.65 | 4.76 | 4.08 |
| 73553 | 1 | F | *Alouatta* | *seniculus* | 3.00 | 5.80 | 3.89 | 4.18 | 5.21 | 4.71 |
| 73548 | 1 | F | *Alouatta* | *seniculus* | 3.19 | 6.11 | 4.31 | 4.13 | 5.33 | 4.80 |
| 239857 | 1 | F | *Alouatta* | *seniculus* | 2.67 | 5.56 | 4.49 | 3.70 | 4.98 | 4.30 |
| 32145 | 1 | M | *Alouatta* | *seniculus* | 3.21 | 5.68 | 3.77 | 3.70 | 4.86 | 4.49 |
| 23347 | 1 | U | *Alouatta* | *seniculus* | 2.84 | 5.61 | 4.00 | 3.78 | 4.90 | 4.55 |
| 33074 | 2 | F | *Alouatta* | *sp.* | 3.02 | 5.60 | 3.41 | 3.74 | 4.28 | 4.05 |
| 94139 | 2 | F | *Alouatta* | *seniculus* | 4.22 | 6.23 | 3.29 | 4.15 | 5.46 | 4.94 |
| 73553 | 2 | F | *Alouatta* | *seniculus* | 3.85 | 6.12 | 3.75 | 4.45 | 5.59 | 4.73 |
| 73548 | 2 | F | *Alouatta* | *seniculus* | 4.13 | 6.53 | 4.45 | 4.11 | 5.78 | 4.84 |
| 239857 | 2 | F | *Alouatta* | *seniculus* | 3.63 | 5.70 | 4.15 | 3.84 | 5.53 | 4.36 |
| 33063 | 2 | F | *Alouatta* | *seniculus* | 3.92 | 6.43 | 4.11 | 4.43 | 5.55 | 4.74 |
| 32145 | 2 | M | *Alouatta* | *seniculus* | 4.18 | 6.73 | 4.68 | 4.16 | 5.86 | 4.98 |
| 23347 | 2 | U | *Alouatta* | *seniculus* | 3.68 | 6.70 | 4.58 | 4.46 | 5.75 | 5.17 |
| 33074 | 3 | F | *Alouatta* | *sp.* | 3.45 | 4.96 | 3.65 | 3.66 | 5.14 | 3.58 |
| 94139 | 3 | F | *Alouatta* | *seniculus* | 3.64 | 5.05 | 2.21 | 5.13 | 5.04 | 4.02 |
| 73553 | 3 | F | *Alouatta* | *seniculus* | 4.50 | 6.13 | 3.68 | 4.80 | 6.09 | 4.43 |
| 239857 | 3 | F | *Alouatta* | *seniculus* | 4.11 | 6.15 | 3.95 | 4.75 | 5.68 | 4.08 |
| 33063 | 3 | F | *Alouatta* | *seniculus* | 3.86 | 5.86 | 3.92 | 4.44 | 5.16 | 3.58 |
| 123282 | 1 | U | *Ateles* | *geoffroyi* | 2.96 | 3.65 | 2.39 | 2.58 | 3.95 | 2.89 |
| 176649 | 1 | U | *Ateles* | *geoffroyi* | 2.91 | 4.23 | 2.56 | 2.51 | 3.77 | 3.40 |
| 172171 | 1 | F | *Ateles* | *geoffroyi* | 3.51 | 4.64 | 2.47 | 3.05 | 4.44 | 3.77 |
| 14484 | 1 | F | *Ateles* | *geoffroyi* | 2.26 | 3.87 | 2.50 | 2.58 | 3.25 | 2.85 |
| 172170 | 1 | U | *Ateles* | *geoffroyi* | 2.93 | 4.79 | 2.35 | 3.20 | 3.50 | 3.43 |
| 123283 | 1 | M | *Ateles* | *geoffroyi* | 2.58 | 4.27 | 2.72 | 2.96 | 3.52 | 2.91 |
| 29844 | 1 | M | *Ateles* | *geoffroyi* | 2.71 | 4.20 | 2.81 | 2.43 | 3.63 | 3.35 |
| 11074 | 1 | F | *Ateles* | *sp.* | 3.16 | 5.02 | 3.25 | 3.47 | 3.96 | 3.09 |
| 123282 | 2 | U | *Ateles* | *geoffroyi* | 3.41 | 4.56 | 2.83 | 3.11 | 4.48 | 3.48 |
| 176649 | 2 | U | *Ateles* | *geoffroyi* | 2.99 | 4.07 | 2.28 | 2.71 | 3.71 | 3.18 |
| 172171 | 2 | F | *Ateles* | *geoffroyi* | 3.51 | 4.36 | 2.28 | 2.52 | 4.47 | 3.97 |
| 14484 | 2 | F | *Ateles* | *geoffroyi* | 2.48 | 3.76 | 2.17 | 2.61 | 3.07 | 2.54 |
| 172170 | 2 | U | *Ateles* | *geoffroyi* | 3.27 | 4.38 | 1.94 | 3.12 | 3.65 | 3.29 |
| 17220 | 2 | M | *Ateles* | *geoffroyi* | 3.12 | 4.30 | 2.49 | 2.94 | 4.28 | 3.59 |
| 17222 | 2 | F | *Ateles* | *geoffroyi* | 3.48 | 5.23 | 3.27 | 3.17 | 4.02 | 3.42 |
| 123283 | 2 | M | *Ateles* | *geoffroyi* | 3.07 | 4.36 | 2.77 | 2.66 | 3.74 | 3.14 |
| 29844 | 2 | M | *Ateles* | *geoffroyi* | 2.77 | 3.94 | 2.56 | 2.64 | 4.06 | 3.43 |
| 11074 | 2 | F | *Ateles* | *sp.* | 3.24 | 4.44 | 2.51 | 2.86 | 4.18 | 3.63 |
| 123282 | 3 | U | *Ateles* | *geoffroyi* | 3.29 | 4.01 | 2.68 | 2.71 | 3.97 | 2.68 |
| 176649 | 3 | U | *Ateles* | *geoffroyi* | 3.15 | 3.86 | 1.94 | 2.54 | 3.33 | 2.72 |
| 172171 | 3 | F | *Ateles* | *geoffroyi* | 4.00 | 4.47 | 2.50 | 2.23 | 4.49 | 3.75 |
| 14484 | 3 | F | *Ateles* | *geoffroyi* | 2.48 | 3.18 | 1.51 | 2.45 | 3.36 | 2.93 |
| 172170 | 3 | U | *Ateles* | *geoffroyi* | 3.08 | 3.91 | 1.64 | 2.57 | 3.51 | 3.22 |
| 17220 | 3 | M | *Ateles* | *geoffroyi* | 2.98 | 3.87 | 2.51 | 2.27 | 3.76 | 3.09 |
| 17222 | 3 | F | *Ateles* | *geoffroyi* | 2.84 | 4.07 | 2.19 | 2.73 | 3.68 | 3.30 |
| 106781 | 1 | F | *Hylobates* | *muelleri* | 3.03 | 4.86 | 3.29 | 3.57 | 4.86 | 3.98 |
| 103725 | 1 | F | *Hylobates* | *muelleri* | 2.53 | 4.65 | 2.66 | 3.70 | 4.15 | 3.80 |
| 103726 | 1 | M | *Hylobates* | *muelleri* | 3.03 | 5.20 | 3.19 | 4.07 | 4.72 | 3.87 |
| 106328 | 1 | F | *Hylobates* | *muelleri* | 2.68 | 4.15 | 2.81 | 3.07 | 4.03 | 3.09 |
| 106781 | 2 | F | *Hylobates* | *muelleri* | 3.90 | 5.11 | 3.00 | 3.04 | 4.88 | 4.12 |
| 103725 | 2 | F | *Hylobates* | *muelleri* | 3.89 | 5.39 | 2.55 | 3.28 | 4.53 | 4.25 |
| 103726 | 2 | M | *Hylobates* | *muelleri* | 3.86 | 5.47 | 2.83 | 3.67 | 4.98 | 4.47 |
| 106328 | 2 | F | *Hylobates* | *muelleri* | 3.28 | 4.34 | 2.22 | 3.09 | 4.07 | 3.38 |
| 106781 | 3 | F | *Hylobates* | *muelleri* | 3.67 | 4.76 | 2.66 | 2.78 | 4.18 | 3.45 |
| 103725 | 3 | F | *Hylobates* | *muelleri* | 3.35 | 5.01 | 2.51 | 2.78 | 3.90 | 3.92 |
| 106328 | 3 | F | *Hylobates* | *muelleri* | 3.42 | 4.11 | 2.43 | 2.80 | 3.97 | 2.84 |
| 102722 | 1 | F | *Symphalangus* | *syndactylus* | 3.51 | 5.94 | 3.48 | 4.75 | 5.12 | 4.08 |
| 102191 | 1 | F | *Symphalangus* | *syndactylus* | 3.32 | 5.86 | 3.57 | 4.48 | 5.26 | 4.56 |
| 102193 | 1 | M | *Symphalangus* | *syndactylus* | 4.39 | 6.36 | 3.20 | 4.65 | 5.61 | 4.82 |
| 100048 | 1 | M | *Symphalangus* | *syndactylus* | 4.49 | 7.66 | 4.44 | 5.83 | 6.34 | 5.26 |
| 201316 | 1 | U | *Symphalangus* | *syndactylus* | 4.32 | 7.04 | 4.54 | 5.20 | 6.30 | 4.98 |
| 102724 | 2 | M | *Symphalangus* | *syndactylus* | 5.16 | 7.93 | 4.11 | 5.13 | 6.63 | 6.29 |
| 102729 | 2 | M | *Symphalangus* | *syndactylus* | 4.38 | 6.78 | 3.50 | 4.57 | 5.51 | 5.24 |
| 102189 | 2 | M | *Symphalangus* | *syndactylus* | 3.29 | 5.77 | 3.55 | 4.11 | 5.01 | 4.53 |
| 102722 | 2 | F | *Symphalangus* | *syndactylus* | 4.29 | 6.87 | 3.39 | 5.31 | 5.37 | 4.78 |
| 106582 | 2 | F | *Symphalangus* | *syndactylus* | 4.06 | 6.17 | 3.11 | 4.57 | 5.53 | 4.97 |
| 102191 | 2 | F | *Symphalangus* | *syndactylus* | 3.87 | 7.07 | 3.61 | 5.51 | 5.68 | 5.40 |
| 102193 | 2 | M | *Symphalangus* | *syndactylus* | 4.83 | 6.78 | 3.65 | 4.63 | 6.05 | 5.08 |
| 201316 | 2 | U | *Symphalangus* | *syndactylus* | 4.77 | 7.98 | 4.45 | 5.27 | 6.25 | 5.97 |
| 102197 | 2 | F | *Symphalangus* | *syndactylus* | 3.85 | 6.07 | 3.21 | 4.07 | 5.30 | 5.19 |
| 102189 | 3 | M | *Symphalangus* | *syndactylus* | 3.93 | 6.38 | 3.64 | 4.51 | 5.33 | 4.66 |
| 102193 | 3 | M | *Symphalangus* | *syndactylus* | 4.84 | 6.93 | 4.15 | 4.91 | 6.19 | 4.77 |
| 102197 | 3 | F | *Symphalangus* | *syndactylus* | 3.89 | 6.38 | 3.27 | 4.60 | 4.94 | 4.70 |

## Appendix I: Dentine Inter-Horn Distances (mm)

| AMNH Cat. # | Tooth | Sex | Genus | Species | Pr-Mt Dentine Horn Dist | Pr-En Dentine Horn Dist | Pr-Hy Dentine Horn Dist | Mt-En Dentine Horn Dist | Mt-Hy Dentine Horn Dist | Hy-En Dentine Horn Dist |
|---|---|---|---|---|---|---|---|---|---|---|
| 33074 | 1 | F | *Alouatta* | *sp.* | 2.53 | 5.06 | 3.44 | 4.12 | 3.54 | 3.65 |
| 129415 | 1 | M | *Alouatta* | *seniculus* | 3.13 | 5.82 | 4.04 | 4.55 | 3.73 | 3.99 |
| 73553 | 1 | F | *Alouatta* | *seniculus* | 3.35 | 5.86 | 4.07 | 4.99 | 3.97 | 4.06 |
| 73548 | 1 | F | *Alouatta* | *seniculus* | 3.10 | 5.85 | 4.43 | 5.11 | 3.76 | 4.50 |
| 239857 | 1 | F | *Alouatta* | *seniculus* | 2.99 | 5.48 | 4.32 | 4.90 | 3.48 | 4.07 |
| 32145 | 1 | M | *Alouatta* | *seniculus* | 3.37 | 5.96 | 3.98 | 4.59 | 3.49 | 4.43 |
| 23347 | 1 | U | *Alouatta* | *seniculus* | 2.80 | 5.49 | 3.78 | 4.48 | 3.60 | 4.18 |
| 33074 | 2 | F | *Alouatta* | *sp.* | 2.84 | 5.07 | 3.52 | 4.33 | 3.60 | 3.43 |
| 94139 | 2 | F | *Alouatta* | *seniculus* | 3.54 | 5.65 | 3.52 | 5.12 | 3.89 | 4.47 |
| 73553 | 2 | F | *Alouatta* | *seniculus* | 3.79 | 6.15 | 3.97 | 5.31 | 4.23 | 4.48 |
| 73548 | 2 | F | *Alouatta* | *seniculus* | 3.99 | 6.41 | 4.59 | 5.94 | 4.26 | 4.72 |
| 239857 | 2 | F | *Alouatta* | *seniculus* | 3.36 | 5.76 | 4.32 | 5.27 | 3.89 | 4.13 |
| 33063 | 2 | F | *Alouatta* | *seniculus* | 3.61 | 6.51 | 4.10 | 5.16 | 4.56 | 4.55 |
| 32145 | 2 | M | *Alouatta* | *seniculus* | 3.66 | 6.11 | 4.04 | 5.50 | 4.11 | 4.78 |
| 23347 | 2 | U | *Alouatta* | *seniculus* | 3.43 | 6.54 | 4.66 | 5.49 | 4.14 | 5.14 |
| 33074 | 3 | F | *Alouatta* | *sp.* | 3.25 | 4.76 | 3.30 | 4.72 | 3.70 | 3.22 |
| 94139 | 3 | F | *Alouatta* | *seniculus* | 3.46 | 5.41 | 2.67 | 4.81 | 4.72 | 4.00 |
| 73553 | 3 | F | *Alouatta* | *seniculus* | 4.13 | 6.20 | 3.63 | 5.73 | 5.03 | 4.27 |
| 239857 | 3 | F | *Alouatta* | *seniculus* | 4.02 | 6.17 | 3.86 | 5.68 | 4.97 | 4.03 |
| 33063 | 3 | F | *Alouatta* | *seniculus* | 3.55 | 5.98 | 4.21 | 5.05 | 4.53 | 3.48 |
| 123282 | 1 | U | *Ateles* | *geoffroyi* | 2.76 | 3.62 | 2.59 | 3.66 | 2.41 | 2.68 |
| 176649 | 1 | U | *Ateles* | *geoffroyi* | 2.73 | 4.25 | 2.53 | 3.37 | 2.62 | 3.06 |
| 172171 | 1 | F | *Ateles* | *geoffroyi* | 3.04 | 4.58 | 2.44 | 4.05 | 3.08 | 3.71 |
| 14484 | 1 | F | *Ateles* | *geoffroyi* | 2.40 | 3.65 | 2.32 | 2.98 | 2.36 | 2.38 |
| 172170 | 1 | U | *Ateles* | *geoffroyi* | 2.61 | 4.26 | 2.25 | 3.35 | 2.83 | 3.21 |
| 123283 | 1 | M | *Ateles* | *geoffroyi* | 2.28 | 4.21 | 2.88 | 3.40 | 2.87 | 2.94 |
| 29844 | 1 | M | *Ateles* | *geoffroyi* | 2.69 | 4.14 | 2.77 | 3.55 | 2.43 | 3.17 |
| 11074 | 1 | F | *Ateles* | *sp.* | 2.69 | 4.42 | 3.04 | 3.90 | 3.06 | 3.24 |
| 123282 | 2 | U | *Ateles* | *geoffroyi* | 3.13 | 4.44 | 3.13 | 4.20 | 2.97 | 3.07 |
| 176649 | 2 | U | *Ateles* | *geoffroyi* | 2.56 | 3.96 | 2.12 | 3.24 | 2.70 | 3.10 |
| 172171 | 2 | F | *Ateles* | *geoffroyi* | 3.14 | 4.35 | 2.45 | 4.10 | 2.73 | 3.59 |
| 14484 | 2 | F | *Ateles* | *geoffroyi* | 2.31 | 3.48 | 1.97 | 2.68 | 2.38 | 2.22 |
| 172170 | 2 | U | *Ateles* | *geoffroyi* | 2.71 | 3.86 | 2.09 | 3.49 | 2.51 | 3.20 |
| 17220 | 2 | M | *Ateles* | *geoffroyi* | 2.77 | 3.98 | 2.67 | 4.11 | 2.61 | 3.44 |
| 17222 | 2 | F | *Ateles* | *geoffroyi* | 2.70 | 4.06 | 2.65 | 3.91 | 2.96 | 3.07 |
| 123283 | 2 | M | *Ateles* | *geoffroyi* | 2.68 | 4.42 | 3.03 | 3.72 | 2.98 | 3.01 |
| 29844 | 2 | M | *Ateles* | *geoffroyi* | 2.82 | 3.81 | 2.41 | 4.11 | 2.72 | 3.35 |
| 11074 | 2 | F | *Ateles* | *sp.* | 2.85 | 4.25 | 2.89 | 4.28 | 2.75 | 3.71 |
| 123282 | 3 | U | *Ateles* | *geoffroyi* | 2.84 | 3.76 | 2.53 | 3.48 | 2.48 | 2.49 |
| 176649 | 3 | U | *Ateles* | *geoffroyi* | 2.48 | 3.73 | 1.94 | 3.06 | 2.53 | 2.86 |
| 172171 | 3 | F | *Ateles* | *geoffroyi* | 2.98 | 4.18 | 2.30 | 3.94 | 2.80 | 3.42 |
| 14484 | 3 | F | *Ateles* | *geoffroyi* | 2.17 | 2.76 | 1.84 | 3.31 | 2.43 | 2.38 |
| 172170 | 3 | U | *Ateles* | *geoffroyi* | 2.72 | 3.74 | 1.67 | 3.39 | 2.42 | 3.30 |
| 17220 | 3 | M | *Ateles* | *geoffroyi* | 2.69 | 3.85 | 2.68 | 3.80 | 2.46 | 3.10 |
| 17222 | 3 | F | *Ateles* | *geoffroyi* | 2.48 | 3.71 | 2.20 | 3.47 | 2.52 | 3.11 |
| 106781 | 1 | F | *Hylobates* | *muelleri* | 3.18 | 4.94 | 2.93 | 4.41 | 3.67 | 3.59 |
| 103725 | 1 | F | *Hylobates* | *muelleri* | 2.91 | 4.69 | 2.65 | 4.02 | 3.33 | 3.56 |
| 103726 | 1 | M | *Hylobates* | *muelleri* | 2.66 | 5.08 | 3.10 | 4.32 | 3.93 | 3.83 |
| 106328 | 1 | F | *Hylobates* | *muelleri* | 2.62 | 4.38 | 3.01 | 4.02 | 3.32 | 3.01 |
| 106781 | 2 | F | *Hylobates* | *muelleri* | 3.37 | 4.73 | 2.70 | 4.36 | 3.15 | 3.64 |
| 103725 | 2 | F | *Hylobates* | *muelleri* | 3.72 | 5.10 | 2.63 | 4.48 | 3.37 | 3.88 |
| 103726 | 2 | M | *Hylobates* | *muelleri* | 3.29 | 4.90 | 2.85 | 4.47 | 3.18 | 4.01 |
| 106328 | 2 | F | *Hylobates* | *muelleri* | 3.06 | 4.43 | 2.62 | 3.80 | 3.05 | 3.04 |
| 106781 | 3 | F | *Hylobates* | *muelleri* | 3.25 | 4.26 | 2.53 | 3.79 | 2.68 | 2.92 |
| 103725 | 3 | F | *Hylobates* | *muelleri* | 2.81 | 4.35 | 2.20 | 3.44 | 2.49 | 3.50 |
| 106328 | 3 | F | *Hylobates* | *muelleri* | 3.23 | 4.25 | 2.63 | 3.83 | 2.80 | 2.83 |
| 102722 | 1 | F | *Symphalangus* | *syndactylus* | 3.35 | 5.95 | 3.78 | 5.07 | 4.32 | 4.28 |
| 102191 | 1 | F | *Symphalangus* | *syndactylus* | 3.14 | 5.55 | 3.35 | 4.73 | 4.17 | 4.02 |
| 102193 | 1 | M | *Symphalangus* | *syndactylus* | 4.09 | 6.39 | 3.58 | 5.42 | 4.59 | 4.60 |
| 100048 | 1 | M | *Symphalangus* | *syndactylus* | 4.03 | 7.46 | 4.52 | 6.02 | 5.60 | 5.13 |
| 201316 | 1 | U | *Symphalangus* | *syndactylus* | 3.95 | 6.73 | 4.29 | 6.05 | 4.87 | 5.13 |
| 102724 | 2 | M | *Symphalangus* | *syndactylus* | 4.73 | 7.59 | 4.25 | 6.14 | 4.98 | 5.63 |
| 102729 | 2 | M | *Symphalangus* | *syndactylus* | 4.04 | 6.70 | 3.48 | 5.29 | 4.66 | 5.11 |
| 102189 | 2 | M | *Symphalangus* | *syndactylus* | 3.18 | 5.51 | 3.47 | 4.98 | 4.00 | 4.32 |
| 102722 | 2 | F | *Symphalangus* | *syndactylus* | 3.95 | 6.70 | 3.68 | 5.28 | 4.64 | 4.88 |
| 106582 | 2 | F | *Symphalangus* | *syndactylus* | 4.46 | 6.51 | 3.42 | 5.63 | 4.67 | 4.75 |
| 102191 | 2 | F | *Symphalangus* | *syndactylus* | 3.69 | 6.24 | 3.48 | 5.51 | 4.77 | 4.94 |
| 102193 | 2 | M | *Symphalangus* | *syndactylus* | 4.71 | 6.75 | 3.65 | 5.79 | 4.60 | 4.84 |
| 201316 | 2 | U | *Symphalangus* | *syndactylus* | 4.56 | 7.66 | 4.33 | 6.19 | 5.10 | 5.91 |
| 102197 | 2 | F | *Symphalangus* | *syndactylus* | 3.58 | 6.19 | 3.34 | 4.81 | 4.03 | 4.89 |
| 102189 | 3 | M | *Symphalangus* | *syndactylus* | 3.85 | 6.06 | 3.36 | 5.00 | 4.05 | 4.50 |
| 102193 | 3 | M | *Symphalangus* | *syndactylus* | 4.76 | 6.89 | 3.91 | 5.81 | 4.82 | 4.65 |
| 102197 | 3 | F | *Symphalangus* | *syndactylus* | 3.84 | 6.14 | 3.38 | 4.88 | 4.32 | 4.41 |

## Appendix J: Enamel Cusp and Dentine Horn Thickness (mm)

| AMNH Cat. # | Tooth | Sex | Genus | species | Pr Enamel Thickness | Mt Enamel Thickness | Hy Enamel Thickness | En Enamel Thickness | Pr Dentine Thickness | Mt Dentine Thickness | Hy Dentine Thickness | En Dentine Thickness |
|---|---|---|---|---|---|---|---|---|---|---|---|---|
| 33074 | 1 | F | *Alouatta* | *sp.* | .26 | .25 | .28 | .44 | 1.80 | 1.91 | 1.99 | 1.71 |
| 129415 | 1 | M | *Alouatta* | *seniculus* | .25 | .25 | .32 | .27 | 1.61 | 1.42 | 1.65 | 1.46 |
| 73553 | 1 | F | *Alouatta* | *seniculus* | .49 | .10 | .33 | .41 | 2.03 | 2.19 | 1.92 | 1.73 |
| 73548 | 1 | F | *Alouatta* | *seniculus* | .44 | .20 | .36 | .40 | 2.33 | 2.48 | 2.47 | 2.53 |
| 239857 | 1 | F | *Alouatta* | *seniculus* | .32 | .21 | .41 | .29 | 1.69 | 1.69 | 1.75 | 1.90 |
| 32145 | 1 | M | *Alouatta* | *seniculus* | .39 | .25 | .33 | .24 | 1.81 | 1.79 | 1.86 | 2.01 |
| 23347 | 1 | U | *Alouatta* | *seniculus* | .19 | .38 | .30 | .33 | 2.05 | 2.13 | 2.09 | 2.18 |
| 33074 | 2 | F | *Alouatta* | *sp.* | .35 | .42 | .43 | .68 | 1.87 | 2.15 | 2.10 | 2.50 |
| 94139 | 2 | F | *Alouatta* | *seniculus* | .64 | .22 | .26 | .47 | 1.99 | 2.86 | 2.57 | 2.85 |
| 73553 | 2 | F | *Alouatta* | *seniculus* | .49 | .18 | .28 | .29 | 2.22 | 2.60 | 2.45 | 2.89 |
| 73548 | 2 | F | *Alouatta* | *seniculus* | .44 | .47 | .48 | .37 | 2.57 | 2.51 | 2.50 | 2.48 |
| 239857 | 2 | F | *Alouatta* | *seniculus* | .37 | .43 | .34 | .45 | 2.13 | 2.09 | 2.14 | 2.19 |
| 33063 | 2 | F | *Alouatta* | *seniculus* | .37 | .34 | .43 | .25 | 2.23 | 2.34 | 2.42 | 2.45 |
| 32145 | 2 | M | *Alouatta* | *seniculus* | .62 | .39 | .36 | .31 | 1.76 | 1.94 | 2.05 | 2.06 |
| 23347 | 2 | U | *Alouatta* | *seniculus* | .36 | .45 | .30 | .23 | 2.42 | 2.41 | 2.71 | 2.87 |
| 33074 | 3 | F | *Alouatta* | *sp.* | .25 | .42 | .45 | .38 | 1.82 | 2.15 | 1.89 | 2.25 |
| 94139 | 3 | F | *Alouatta* | *seniculus* | .73 | .31 | .39 | .34 | 2.19 | 2.29 | 2.70 | 2.91 |
| 73553 | 3 | F | *Alouatta* | *seniculus* | .28 | .48 | .36 | .38 | 2.45 | 2.78 | 2.98 | 3.34 |
| 239857 | 3 | F | *Alouatta* | *seniculus* | .26 | .49 | .48 | .37 | 2.27 | 2.18 | 2.71 | 2.89 |
| 33063 | 3 | F | *Alouatta* | *seniculus* | .54 | .42 | .58 | .76 | 2.32 | 2.24 | 2.14 | 2.31 |
| 123282 | 1 | U | *Ateles* | *geoffroyi* | .31 | .10 | .33 | .26 | 1.28 | 3.57 | 3.27 | 1.54 |
| 176649 | 1 | U | *Ateles* | *geoffroyi* | .34 | .28 | .40 | .36 | 1.76 | 1.74 | 1.73 | 1.92 |
| 172171 | 1 | F | *Ateles* | *geoffroyi* | .40 | .29 | .38 | .29 | 2.00 | 1.90 | 1.85 | 1.89 |
| 14484 | 1 | F | *Ateles* | *geoffroyi* | .14 | .25 | .33 | .37 | 1.58 | 1.63 | 1.78 | 2.06 |
| 172170 | 1 | U | *Ateles* | *geoffroyi* | .43 | .27 | .26 | .17 | 1.45 | 1.28 | 1.45 | 1.56 |
| 123283 | 1 | M | *Ateles* | *geoffroyi* | .34 | .30 | .17 | .31 | 1.66 | 1.57 | 1.76 | 1.85 |
| 29844 | 1 | M | *Ateles* | *geoffroyi* | .22 | .31 | .26 | .31 | 2.00 | 1.88 | 2.06 | 2.20 |
| 11074 | 1 | F | *Ateles* | *sp.* | .41 | .38 | .26 | .40 | 14.11 | 1.55 | 2.03 | 1.98 |
| 123282 | 2 | U | *Ateles* | *geoffroyi* | .27 | .28 | .39 | .28 | 1.99 | 1.96 | 2.02 | 2.26 |
| 176649 | 2 | U | *Ateles* | *geoffroyi* | .34 | .37 | .38 | .42 | 1.74 | 1.78 | 1.83 | 2.09 |
| 172171 | 2 | F | *Ateles* | *geoffroyi* | .38 | .53 | .29 | .37 | 2.06 | 1.89 | 1.89 | 1.81 |
| 14484 | 2 | F | *Ateles* | *geoffroyi* | .24 | .26 | .44 | .33 | 1.94 | 1.90 | 2.04 | 2.30 |
| 172170 | 2 | U | *Ateles* | *geoffroyi* | .41 | .45 | .33 | .34 | 1.60 | 1.35 | 1.60 | 1.65 |
| 17220 | 2 | M | *Ateles* | *geoffroyi* | .28 | .36 | .28 | .51 | 1.76 | 1.55 | 1.76 | 1.71 |
| 17222 | 2 | F | *Ateles* | *geoffroyi* | .89 | .22 | .52 | .50 | 1.67 | 1.55 | 1.72 | 1.61 |
| 123283 | 2 | M | *Ateles* | *geoffroyi* | .34 | .52 | .31 | .34 | 1.75 | 1.64 | 1.77 | 1.92 |
| 29844 | 2 | M | *Ateles* | *geoffroyi* | .39 | .34 | .40 | .41 | 1.93 | 2.01 | 2.57 | 2.21 |
| 11074 | 2 | F | *Ateles* | *sp.* | .50 | .34 | .35 | .37 | 1.73 | 1.51 | 1.65 | 1.94 |
| 123282 | 3 | U | *Ateles* | *geoffroyi* | .31 | .37 | .35 | .30 | 2.09 | 2.18 | 2.25 | 2.62 |
| 176649 | 3 | U | *Ateles* | *geoffroyi* | .48 | .44 | .36 | .45 | 1.86 | 1.77 | 1.86 | 2.29 |
| 172171 | 3 | F | *Ateles* | *geoffroyi* | .56 | .79 | .59 | .48 | 2.05 | 1.89 | 2.00 | 2.20 |
| 14484 | 3 | F | *Ateles* | *geoffroyi* | .35 | .35 | .41 | .39 | 1.92 | 2.36 | 1.85 | 1.97 |
| 172170 | 3 | U | *Ateles* | *geoffroyi* | .38 | .31 | .40 | .59 | 1.69 | 1.57 | 1.75 | 1.85 |
| 17220 | 3 | M | *Ateles* | *geoffroyi* | .42 | .29 | .43 | .38 | 1.72 | 1.69 | 1.76 | 1.81 |
| 17222 | 3 | F | *Ateles* | *geoffroyi* | .57 | .45 | .49 | .43 | 1.83 | 1.54 | 1.55 | 1.97 |
| 106781 | 1 | F | *Hylobates* | *muelleri* | .47 | .39 | .39 | .36 | 1.91 | 2.33 | 2.46 | 2.30 |
| 103725 | 1 | F | *Hylobates* | *muelleri* | .24 | .30 | .25 | .27 | 2.71 | 2.75 | 2.81 | 2.64 |
| 103726 | 1 | M | *Hylobates* | *muelleri* | .18 | .44 | .32 | .42 | 1.79 | 2.03 | 2.22 | 2.10 |
| 106328 | 1 | F | *Hylobates* | *muelleri* | .39 | .37 | .16 | .22 | 2.17 | 2.45 | 2.48 | 2.40 |
| 106781 | 2 | F | *Hylobates* | *muelleri* | .31 | .50 | .62 | .46 | 2.72 | 2.88 | 2.68 | 2.50 |
| 103725 | 2 | F | *Hylobates* | *muelleri* | .36 | .41 | .35 | .67 | 3.02 | 2.97 | 3.43 | 2.71 |
| 103726 | 2 | M | *Hylobates* | *muelleri* | .56 | .43 | .54 | .77 | 2.32 | 2.46 | 2.63 | 2.36 |
| 106328 | 2 | F | *Hylobates* | *muelleri* | .34 | .25 | .35 | .37 | 2.75 | 2.97 | 2.81 | 2.65 |
| 106781 | 3 | F | *Hylobates* | *muelleri* | .58 | .50 | .61 | .66 | 2.67 | 2.72 | 2.51 | 2.28 |
| 103725 | 3 | F | *Hylobates* | *muelleri* | .75 | .61 | .77 | .78 | 2.59 | 2.38 | 2.70 | 2.65 |
| 106328 | 3 | F | *Hylobates* | *muelleri* | .25 | .40 | .16 | .31 | 2.59 | 2.62 | 2.61 | 2.47 |
| 102722 | 1 | F | *Symphalangus* | *syndactylus* | .50 | .38 | .32 | .65 | 3.48 | 3.68 | 2.43 | 2.37 |
| 102191 | 1 | F | *Symphalangus* | *syndactylus* | .26 | .29 | .53 | .41 | 1.89 | 1.92 | 2.21 | 2.23 |
| 102193 | 1 | M | *Symphalangus* | *syndactylus* | .48 | .34 | .30 | .41 | 2.04 | 2.07 | 2.24 | 2.34 |
| 100048 | 1 | M | *Symphalangus* | *syndactylus* | .52 | .38 | .51 | .45 | 2.54 | 2.52 | 2.77 | 2.88 |
| 201316 | 1 | U | *Symphalangus* | *syndactylus* | .54 | .52 | .70 | .76 | 2.67 | 2.83 | 3.05 | 3.15 |
| 102724 | 2 | M | *Symphalangus* | *syndactylus* | .54 | .61 | .82 | .76 | 4.39 | 4.43 | 4.38 | 4.41 |
| 102729 | 2 | M | *Symphalangus* | *syndactylus* | .44 | .47 | .56 | .51 | 3.52 | 3.49 | 3.66 | 3.44 |
| 102189 | 2 | M | *Symphalangus* | *syndactylus* | .32 | .45 | .29 | .38 | 2.10 | 2.09 | 2.34 | 2.47 |
| 102722 | 2 | F | *Symphalangus* | *syndactylus* | .89 | .75 | .83 | .87 | 3.18 | 3.03 | 3.26 | 3.14 |
| 106582 | 2 | F | *Symphalangus* | *syndactylus* | .44 | .52 | .74 | .54 | 3.49 | 3.75 | 3.51 | 3.36 |
| 102191 | 2 | F | *Symphalangus* | *syndactylus* | .76 | .50 | .72 | .98 | 2.66 | 2.85 | 2.89 | 2.79 |
| 102193 | 2 | M | *Symphalangus* | *syndactylus* | .59 | .74 | .72 | .75 | 3.09 | 3.06 | 3.18 | 2.98 |
| 201316 | 2 | U | *Symphalangus* | *syndactylus* | .89 | .83 | .80 | .81 | 3.74 | 3.80 | 3.73 | 3.90 |
| 102197 | 2 | F | *Symphalangus* | *syndactylus* | .66 | .62 | .71 | .54 | 3.09 | 3.07 | 3.16 | 3.24 |
| 102189 | 3 | M | *Symphalangus* | *syndactylus* | .51 | .70 | .62 | .59 | 3.18 | 3.13 | 3.29 | 2.90 |
| 102193 | 3 | M | *Symphalangus* | *syndactylus* | .85 | .81 | .81 | .73 | 3.29 | 3.16 | 4.32 | 4.54 |
| 102197 | 3 | F | *Symphalangus* | *syndactylus* | .76 | .70 | .72 | .55 | 3.00 | 3.11 | 3.15 | 3.01 |